Predictive numerical simulations for rebuilding freestream conditions in atmospheric entry flows

Andrea Francesco Cortesi

THÈSE

PRÉSENTÉE À

L'UNIVERSITÉ DE BORDEAUX

ÉCOLE DOCTORALE DE MATHÉMATIQUES ET D'INFORMATIQUE

par **Andrea Francesco CORTESI**

POUR OBTENIR LE GRADE DE

DOCTEUR

SPÉCIALITÉ : Mathématiques Appliquées et Calcul Scientifique

Simulations numériques prédictives pour la reconstruction des conditions en amont dans les écoulements de rentrée atmosphérique

---

Date de soutenance : 16 Février 2018

Devant la commission d'examen composée de :

Anne BOURDON ...	Directeur de Recherche, CNRS-LPP .	Examinateur
Pietro CONGEDO ..	CR-HDR, INRIA	Directeur
Didier LUCOR	Directeur de Recherche, CNRS-LIMSI	Rapporteur
Thierry MAGIN	Professeur, Von Karman Institute	Co-directeur
Pierre-Henri MAIRE .	Directeur de Recherche, CEA-CESTA	Examinateur
Nagi MANSOUR	Chief division scientist, NASA Ames .	Examinateur
Luc MIEUSSENS ...	Professeur, Université de Bordeaux ..	Président du jury
Massimiliano VASILE	Professeur, University of Strathclyde .	Rapporteur

– 2018 –

Résumé Une prédiction fidèle des écoulements hypersoniques à haute enthalpie est capitale pour les missions de rentrée atmosphérique. Cependant, la présence d'incertitudes est inévitable, sur les conditions de l'écoulement libre comme sur d'autres paramètres des modèles physico-chimiques. Pour cette raison, une quantification rigoureuse de l'effet de ces incertitudes est obligatoire pour évaluer la robustesse et la prédictivité des simulations numériques. De plus, une reconstruction correcte des paramètres incertains à partir des mesures en vol peut aider à réduire le niveau d'incertitude sur les sorties. Dans ce travail, nous utilisons un cadre statistique pour la propagation directe des incertitudes ainsi que pour la reconstruction inverse des conditions de l'écoulement libre dans le cas d'écoulements de rentrée atmosphérique. La possibilité d'exploiter les mesures de flux thermique au nez du véhicule pour la reconstruction des variables de l'écoulement libre et des paramètres incertains du modèle est évaluée pour les écoulements de rentrée hypersoniques. Cette reconstruction est réalisée dans un cadre bayésien, permettant la prise en compte des différentes sources d'incertitudes et des erreurs de mesure. Différentes techniques sont introduites pour améliorer les capacités de la stratégie statistique de quantification des incertitudes. Premièrement, une approche est proposée pour la génération d'un métamodèle amélioré, basée sur le couplage de *Kriging* et *Sparse Polynomial Dimensional Decomposition*. Ensuite, une méthode d'ajoute adaptatif de nouveaux points à un plan d'expériences existant est présentée dans le but d'améliorer la précision du métamodèle créé. Enfin, une manière d'exploiter les sous-espaces actifs dans les algorithmes de *Markov Chain Monte Carlo* pour les problèmes inverses bayésiens est également exposée.

Title Predictive numerical simulations for rebuilding freestream conditions in atmospheric entry flows

Abstract Accurate prediction of hypersonic high-enthalpy flows is of main relevance for atmospheric entry missions. However, uncertainties are inevitable on freestream conditions and other parameters of the physico-chemical models. For this reason, a rigorous quantification of the effect of uncertainties on the prediction of the model is mandatory to assess the robustness and predictivity of numerical simulations. Furthermore, a proper reconstruction of uncertain parameters from in-flight measurements can help in reducing the level of uncertainties of the output. In this work, we will use a statistical framework for direct propagation of uncertainties and inverse freestream reconstruction applied to atmospheric entry flows. We propose an assessment of the possibility of exploiting forebody heat flux measurements for the reconstruction of freestream variables and uncertain parameters of the model for hypersonic entry flows. This reconstruction is performed in a Bayesian framework, allowing to account for sources of uncertainties and measurement errors. Different tech-

niques are introduced to enhance the capabilities of the statistical framework for the quantification of uncertainties. First, an improved surrogate modeling technique is proposed, based on Kriging and Sparse Polynomial Dimensional Decomposition. Then, a method is proposed to adaptively add new training points to an existing experimental design to improve the accuracy of the trained surrogate model. A way to exploit active subspaces in Markov Chain Monte Carlo algorithms for Bayesian inverse problems is also proposed.

Keywords Hypersonic flows, Atmospheric entry, Freestream reconstruction, Bayesian inverse problems, Uncertainty Quantification, Surrogate models, Universal Kriging, Adaptive design of experiments, Active Subspaces

Mots-clés Écoulements hypersoniques, Rentrée atmosphérique, Reconstruction des conditions en amont, Problèmes inverses Bayesiens, Quantification des incertitudes, Métamodèles, Krigeage universel, Plan d'expériences adaptatif, Sous-espaces actifs

Laboratoire d'accueil Inria Bordeaux Sud-Ouest, Équipe CARDAMOM, 200 Avenue de la Vieille Tour, 33405 Talence

Résumé étendu

Introduction et objectifs

L'aérodynamique hypersonique joue un rôle principal dans la rentrée atmosphérique des véhicules spatiaux et une simulation aérothermique précise de l'écoulement d'entrée est cruciale pour la conception du véhicule et de la trajectoire d'entrée. Les écoulements d'entrée hypersoniques sont des phénomènes complexes, car le fort chauffage post-choc peut originer plusieurs phénomènes, comme la dissociation des molécules et d'autres réactions chimiques, la ionisation, les effets de non-équilibre chimique et thermique, le chauffage radiatif et les effets d'interaction avec la paroi, comme catalyse et ablation [Anderson, 2000; Sarma, 2000]. En raison de leur complexité, il est très difficile de reproduire les écoulements d'entrée dans des installations expérimentales, en particulier parce que la similitude expérimentale exacte ne peut pas être obtenue dans une situation générale de non-équilibre, sauf si un modèle en dimension réelle est utilisé. L'acquisition de mesures pendant un vol d'entrée réel peut fournir beaucoup de données utiles, mais cela est infaisable sur une base régulière, puisque chaque mission d'entrée implique des coûts économiques élevés. Par conséquent, les simulations numériques au moyen de la dynamique des fluides computationnelle (CFD) sont souvent la seule ressource disponible pour obtenir des données quantitatives sur les écoulements hypersoniques d'entrée [Longo, 2004; zur Nieden et Olivier, 2007].

Afin de produire des simulations précises et prédictives, il est essentiel de fournir des valeurs précises pour les conditions limites, comme la composition et l'état thermodynamique de l'atmosphère et la vitesse de vol. Malheureusement, les connaissances sur les propriétés atmosphériques et l'état thermodynamique sont généralement caractérisées par un haut degré d'incertitude, en particulier pour des autres planètes que la Terre. En plus, les fluctuations atmosphériques peuvent provoquer des écarts aléatoires par rapport aux modèles atmosphériques standards [Enzian *et al.*, 2002]. Pour améliorer les connaissances sur les conditions en amont, il est courant de reconstruire les paramètres atmosphériques à partir des données de vol lors de l'analyse post-vol. Cela permet d'améliorer les modèles atmosphériques pour la conception et l'analyse des missions EDL et de fournir des conditions limites d'entrée sig-

nificatives pour des simulations CFD prédictives. La reconstruction des conditions atmosphériques et l'état du véhicule sont également importants pour le contrôle et le guidage des véhicules opérationnels [Koppenwallner, 2007].

Les techniques classiques de reconstruction de la trajectoire d'entrée et des conditions atmosphériques sont des approches déterministes basées sur des accélérations linéaires et des rotations angulaires mesurées par des accéléromètres et des gyroscopes composant l'*Inertial Measurement Unit* (IMU), qui fait partie de l'instrumentation standard des véhicules d'entrée [Withers *et al.*, 2003]. Cependant, même si les données de vol inertielles sont idéales pour la reconstruction de la trajectoire d'entrée [Desai *et al.*, 2011], elles ne sont pas forcement suffisantes pour caractériser précisément l'environnement atmosphérique, puisqu'elles n'incluent aucune information directe sur l'écoulement d'air autour de la capsule [Van Hove et Karatekin]. Pour cette raison, sur certains autres véhicules d'entrée, un système dénommé *Flush Air Data System* (FADS) est également disponible [Cobleigh *et al.*, 1999], composé par des capteurs de pression (et d'autres capteurs dans certains cas) intégrés dans le bouclier thermique. Par conséquent, les mesures FADS consistent normalement en des données de pression à plusieurs points de l'avant-corps du véhicule. Ce système est capable de fournir des mesures complémentaires à celles de l'IMU, car elles contiennent des informations directes de l'écoulement et l'environnement atmosphérique auxquels la surface du véhicule est exposée. Sur certains véhicules d'entrée, le FADS peut également fournir des mesures de flux de chaleur. L'ensemble d'instrumentation RAFLEX (*Re-entry Aerodynamic Flow Experiment*) [Müller-Eigner et Koppenwallner, 2001], par exemple, est composé par plusieurs sondes capables de mesurer la pression et le flux de chaleur au même endroit. Néanmoins, au moins jusqu'à la connaissance de l'auteur, les mesures de flux de chaleur ne sont pas exploitées normalement pour la caractérisation atmosphérique et de la trajectoire, probablement en raison de la difficulté de réaliser à la fois des mesures précises [Loehle, 2016] et des simulations significatives du chauffage à la surface.

Les modèles numériques pour simuler des écoulements d'entrée atmopshérique nécessitent de nombreux paramètres d'entrée pour décrire les conditions limites et les propriétés du modèle, dont les valeurs doivent être indiquées avec précision pour avoir des prédictions significatives. Pourtant, certains paramètres décrivant les conditions limites, tels que les conditions atmosphériques, sont connus avec des incertitudes, puisque, comme on a vu, ils sont reconstruits à partir de mesures indirectes, et ces mesures sont intrinsèquement incertaines. Des autres entrées du modèle peuvent également être incertaines, en raison de leur variabilité intrinsèque ou du manque de connaissances de la parte de l'analyste. La quantification des incertitudes (UQ) est en train de gagner de plus en plus d'importance pour quantifier rigoureusement les incertitudes introduites dans les résultats des simulations numériques afin d'établir objectivement leurs capacités prédictives [Roy et Oberkampf, 2011]. L'un des

principaux objectifs de la UQ est de propager les incertitudes des différentes sources à travers le modèle de simulation afin d'obtenir des informations quantitatives sur la variabilité de certaines quantités d'intérêts (sorties).

Les objectifs de ce travail sont à la fois liés au domaine d'application des écoulements d'entrée hypersoniques, et en particulier à la reconstruction des conditions en amont, ainsi qu'aux outils mathématiques de quantification des incertitudes. Du point de vue de la reconstruction des conditions en amont pour les écoulements d'entrée hypersonique, le but de ce travail est d'évaluer la possibilité et l'utilité d'exploiter les mesures de flux thermique de surface, données par des capteurs de type FADS/RAFLEX avec aussi des mesures de pression, pour la caractérisation des quantités en amont, telles que la densité atmosphérique, la vitesse et les angles de vol, et d'autres paramètres incertains des modèles. Cela est fait dans un cadre statistique bayésien, comme dans [Tryoen *et al.*, 2014], qui permet de prendre en compte les erreurs de mesure et les incertitudes sur certains paramètres du modèle physico-chimique. D'un point de vue mathématique, le travail veut plutôt proposer des techniques qui pourraient améliorer l'analyse UQ directe et inverse. Comme, normalement, la propagation UQ devient exponentiellement plus exigeante en termes de coût de calcul en augmentant la taille de l'espace des paramètres d'entrée incertains [Donoho, 2000], des outils efficaces sont nécessaires pour fournir une solution aux problèmes de dimension moyenne à élevée sans nécessiter d'efforts de calcul exceptionnels. Donc, les principaux objectifs de ce sujet sont de fournir une technique améliorée pour la création d'un métamodèle, nécessitant un plus petit nombre de points d'entraînement, où le modèle CFD coûteux doit être exécuté, pour donner une prédiction précise de la quantité d'intérêt. En plus, une stratégie de réduction de la dimensionnalité des entrées récemment développée, basée sur des sous-espaces actifs [Constantine, 2015], est testée pour améliorer l'efficacité numérique des problèmes de propagation directe et inverse. Enfin, une technique d'échantillonnage adaptatif est proposée, afin d'augmenter le nombre de points d'apprentissage représentant les informations sur les gradients de la fonction et les erreurs de métamodélisation.

Travail effectué

Une technique de métamodélisation améliorée, dénommée PDD-UK, a été proposée. Elle consiste en l'utilisation des fonctions de base polynomiales sélectionnées par un algorithme de *sparse Polynomial Dimensional Decomposition* (PDD) adaptative [Tang *et al.*, 2016; Rahman, 2008] comme fonctions de régression pour un métamodèle de Krigeage universel (*Universal Kriging*, UK) [Cressie, 1993; Rasmussen et Williams, 2006]. Cette approche améliorée s'est avérée bien fonctionner sur les nombreux tests effectués, à la fois analytiques et issus d'applications dans le domaine de l'entrée atmosphérique, fournissant

une précision de métamodélisation améliorée par rapport au krigeage ordinaire et aussi au *sparse*-PDD. Ces tests ont montré que le métamodèle adaptatif proposé est capable de traiter des problèmes avec un nombre relativement élevé d'entrées incertaines, dans le cas où la contribution majeure à la variabilité de la sortie est donnée par un sous-ensemble limité d'entrées. Les tests effectués ont également montré que, pour obtenir les meilleurs résultats en termes de précision, il est nécessaire de choisir un ensemble adéquat de paramètres d'entrée (*i.e.* l'ordre polynomial maximal, l'ordre d'interaction, etc.). Cela peut nécessiter une analyse préliminaire avec des estimations d'erreur pour déterminer le meilleur ensemble de paramètres d'entrée.

Une nouvelle technique a été aussi développée pour ajouter de manière adaptative des nouveaux points d'entraînement à un plan expérimental (*experimental design*, ED) existant, dans le cas où l'on veut améliorer la précision du métamodèle construit sur ce premier ED. La technique repose sur la construction d'un maillage de Delaunay d'éléments simplexes où les points d'entraînement coïncident avec les sommets des éléments, et exploite des techniques derivées de l'adaptation de maillage anisotrope [Coupez, 2011; Coupez *et al.*, 2013]. La méthode est aussi capable de prendre en compte l'information sur la fonction d'intérêt acquise pendant la creation du premier métamodèle sur le plan expérimental initial. En particulier, la méthode tient compte des gradients de la fonction et des estimations locales de l'erreur de métamodélisation. La technique permet d'ajouter un nombre fixe de points d'entraînement, choisis par l'utilisateur, de sorte que le nouveaux ED fonctionne mieux qu'un plan *Latin Hypercubes* (LH) [McKay *et al.*, 1979] normal en termes d'erreur moyenne de métamodélisation. Le principal inconvénient de la méthodologie proposée est que la construction d'une grille de Delaunay devient très exigeante en termes de coût de calcul quand l'on augmente la dimensionnalité de l'espace d'entrée. Lorsqu'il n'est pas possible de diminuer la dimensionnalité des entrées par des techniques de réduction de dimensionnalité, cela devient un problème majeur qui peut empêcher l'utilisation de la méthodologie proposée.

Une manière émergente d'effectuer une réduction de dimensionnalité consiste à exploiter le sous-espace actif d'une fonction d'intérêt [Constantine, 2015]. Dans ce travail, ils sont exploités pour la réduction de dimensionnalité appliquée aux problèmes inverses bayésiens. Une nouvelle approche pour les utiliser dans cette situation est proposée et comparée à celle introduite dans [Constantine *et al.*, 2016b]. Les sous-espaces actifs se sont démontrés très efficaces pour la réduction de dimensionnalité pour la propagation directe des incertitudes et l'analyse de sensibilité, permettant d'obtenir des informations sur les structures à dimensionalité reduite cachées dans la fonction d'intérêt et de produire des densités de probabilité précises pour les sorties. Si la structure des fonctions d'intérêt permet l'existence de sous-espaces actifs, ils peuvent aussi être efficacement exploités pour des problèmes inverses bayésiens, mais avec la complication d'exiger une algorithme *Markov Chain Monte Carlo* (MCMC)

[Gilks *et al.*, 1996; Tarantola, 2005] supplémentaire pour échantillonner les variables physiques en partant des variables actives composant le sous-espace actif. Cependant, il faut noter que l'algorithme MCMC supplémentaire n'exige aucune évaluation du code de simulation coûteux ni du métamodèle.

La reconstitution de la densité freestream, des angles aérodynamiques et du coefficient catalytique Le problème inverse de reconstruction a été résolu dans un cadre bayésien pour le véhicule EXPERT (European eXPErimental Reentry Testbed) de l'Agence Spatiale Européenne [Muylaert *et al.*, 2007; Thoemel *et al.*, 2009], en exploitant les mesures de flux de chaleur sur la surface du nez du véhicule, ainsi que les mesures de pression disponibles classiquement. Au niveau actuel de précision pour les mesures de flux de chaleur (erreur de mesure élevée, de l'ordre de 10% de la valeur mesurée), ce type de données ne fournit pas suffisamment d'informations et donc ne permet pas de réduire les incertitudes les quantités par rapport aux reconstructions effectuées avec seulement des mesures de pression. La reconstruction de la vitesse et de la densité en amont a également été testée, en utilisant des mesures de pression et de flux de chaleur, pour la configuration expérimentale du cylindre HEG (*High Enthalpy shock tunnel Göttingen*) [Karl *et al.*, 2003]. L'utilisation de ce type de mesures done des résultats beaucoup plus incertains, c'est-à-dire avec une variation plus élevée, que la reconstruction classique par données inertielles (fournie par l'IMU) comme il est habituellement fait dans la littérature. Le seul scénario où les mesures de flux de chaleur deviendraient plus utiles est dans le cas d'un dysfonctionnement de l'IMU: en absence des données inertielles, une reconstruction relativement incertaine par flux thermique serait meilleure que l'impossibilité totale de reconstruire cette variable.

Publications

Papers submitted to scientific journals

- Cortesi, A. F., Constantine, P. G., Magin, T. E. et Congedo, P. M., submitted. Forward and backward uncertainty quantification with active subspaces: application to hypersonic flows around a cylinder. *Journal of Computational Physics*

- Cortesi, A. F., Jannoun, G. et Congedo, P. M., Submitted. Kriging-sparse polynomial dimensional decomposition surrogate model with adaptive refinement. *Journal of Computational Physics*

Papers in conference proceedings

- Cortesi, Andrea F. et Congedo, Pietro M., 2016b. A kriging-PDD surrogate model for low-cost sensitivity analysis. Dans *17th AIAA/ISSMO Multidisciplinary Analysis and Optimization Conference*, AIAA AVIATION Forum. American Institute of Aeronautics and Astronautics

- Cortesi, A. F., Congedo, P. M., Magin, T. E., Hove, B. Van et Karatekin, O., 2016. Rebuilding freestream atmospheric conditions using surface pressure and heat flux data. Dans *8th AIAA Atmospheric and Space Environments Conference*, AIAA AVIATION Forum. American Institute of Aeronautics and Astronautics

- Cortesi, A. F., Magin, T. E. et Congedo, P. M., 2015b. Surrogate model with conservative error measure for the stagnation heat flux in atmospheric entry flows. Dans *1st International Conference on Uncertainty Quantification in Computational Sciences and Engineering*, UNCECOMP 2015. ECCOMAS

Oral presentations at conferences (without proceedings)

- Cortesi, A. F., Jannoun, G. et Congedo, P. M., 2017. Adaptive refinement of the design of experiment for metamodels through anisotropic mesh adaptation. Dans *2nd International Conference on Uncertainty*

Quantification in Computational Sciences and Engineering, UNCECOMP 2017. ECCOMAS

- Cortesi, A. F. et Congedo, P. M., 2016a. A kriging-pdd surrogate model for uncertainty quantification. Dans *VII European Congress on Computational Methods in Applied Sciences and Engineering*, ECCOMAS 2016. ECCOMAS

- Cortesi, A. F., Magin, T. E. et Congedo, P. M., 2015a. About the Construction of a Robust Metamodel to Estimate the Stagnation Heat Flux for the EXPERT Vehicle. Dans *The 5th International ARA Days*

Acknowledgments

In this part of the work, I would like to express my gratitude to all the people who contributed to the realization of this work, with scientific and professional collaborations but also by motivating me throughout these Ph.D. years. Some of the following paragraphs, especially the less formal ones, will be in different languages, in order to allow all the concerned people to fully understand the message I am addressing to them.

The first person I would like to thank is, of course, my supervisor Pietro, who accorded me the opportunity to work on this interesting topic as his first Ph.D. student. I have always appreciated the trust that you gave to me and to my work. Thanks to your guidance, always present but never oppressive, you have been able to teach me a lot, not only from a strictly technical point of view. I am also very grateful for the chances I had to work in many collaborations and to attend several scientific manifestations. Secondly, I want to express my gratitude to my co-supervisor Thierry for his kind and constant support during this thesis work. Your enormous passion and dedication for the research in fluid dynamics and aerospace engineering has always been of great motivation, and your expertise has been very helpful during several phases of my research. Pietro and Thierry, in different but complementary ways, you both have been great mentors and I hope I have been able to make the most out of all you offered.

A further acknowledgment goes to the *Direction Générale de l'Armement* (DGA) for having made this Ph.D. possible with their financial support and to the reviewers and the members of the jury for having kindly dedicated their time to my discussion.

I would also like to thank Ghina Jannoun, Paul Constantine and Bart Van Hove for their collaboration concerning the content of respectively chapters 4, 5 and 6 of this manuscript, and the related submitted publications. Your suggestions and contributions have been fundamental to the production of these parts of the manuscript.

Moreover, an acknowledgement goes to all the other people I had the pleasure of working with during these three years. In particular, I would like to thank Nagi Mansour and Gianluca Iaccarino for giving me the big opportunity of visiting their teams during my stays respectively at NASA Ames and Stanford University. The exchanges we had during these experiences were surely

enriching and mind-opening, and your great experience allowed me to see the subjects of atmospheric entry and UQ from different and interesting points of view.

Je voudrais également adresser mes sincères remerciements à tous les nombreux membres de l'équipe CARDAMOM que j'ai eu le plaisir de rencontrer pendant ces années. L'ambiance de travail au sein de l'équipe a toujours été très motivante et enrichissante, et chaque matin on peut se considérer heureux d'y travailler. Cela est possible surtout grâce à la direction de notre chef d'équipe Mario, qui se montre toujours attentif et disponible. En particulier je veux citer et remercier les membres de la Team UQ: François, Mickaël et Nassim. Il a toujours été stimulant d'échanger avec vous sur des sujets scientifiques relatifs à la quantification d'incertitudes, mais on a aussi eu le plaisir de partager beaucoup des moments conviviaux, notamment lors des différentes missions et conférences auxquelles on a eu la chance d'aller ensemble.

Inoltre, vorrei ringraziare in modo speciale gli altri dottorandi italiani del team: Andrea, Luca e Umberto (Mathilde et Mahalia, vous aussi vous êtes incluses). Durante questi anni siete stati come la mia famiglia bordolese. Insieme abbiamo passato numerosi momenti di amicizia, in cui avete saputo portare molto buon umore, ma allo stesso tempo vi siete sempre dimostrati disponibili nei momenti di bisogno. Grazie!

Un grand merci aux autres amis français rencontrés à Inria Bordeaux: Léo, Carlo Faggio, Dr. Haine, Ulysse, Jo et Hicham (pas trop français en vrai mais bon ...). Les bons moments qu'on a partagés sont tellement nombreux que je n'arrive même pas à m'en souvenir en écrivant ces mots, et je suis sûr qu'on en gardera toujours des très bons souvenirs. Je me considère chanceux de vous avoir rencontrés !

Je tient aussi à remercier tous les amis du Leo Club Bordeaux International, en particulier Orane, Yoann et Darrène qui m'ont montré tout leur chaleureux accueil lors de mon arrivé à Bordeaux, et Anne-Cha, Marie, Émilie, Cyril et les autres membres du club avec qui j'ai partagé ma vie associative pendant ces années. Il faut qu'on soit fiers de tout ce qu'on a su réaliser ensemble!

Of course, a very big and special thanks goes to my girlfriend America, who I met during my stay in Bordeaux. You came into my life bringing your beautiful smile that was always there to encourage me during the most stressful moments of the redaction of this manuscript. Being at my side, you are motivating me every single day to work to become a better human, and I am very grateful and proud for having met you!

Last but not least, ci tengo a ringraziare la mia famiglia e in particolare i miei genitori, Franco e Vittoria, per avermi costantemente motivato, supportato e soprattutto sopportato durante questi 29 anni, e per avermi insegnato l'importanza di molti valori senza i quali oggi non sarei la persona che sono diventato. È a voi che dedico questo manoscritto, con la consapevolezza che ne sarete orgogliosi.

Contents

Introduction

Context

Relevance of space exploration

One driving force behind the advancement of aviation has always been the desire to fly higher and faster [Anderson, 2005, Chapter 1.11]. This has led to the beginning of the first space programs, whose intent was the exploration of space. The first main achievements of space programs occurred from the end of the '50s and throughout the '60s of the twentieth century, during the space race generated by the desire to demonstrate technological supremacy between the USA and the URSS during the Cold War. In 1957, the Russian satellite *Sputnik I* was the first artificial satellite to be sent to orbit around the Earth. A few years later, in 1961, the Russian Yuri Gagarin was the first man experiencing space flight, orbiting around the Earth and safely returning. At the same time, he has been the first human being in history to experience hypersonic flight during his earth reentry on the *Vostok* spacecraft. Another important landmark of that era, and maybe the most well-known, has been the first manned landing on the Moon and following reentry, with the Apollo 11 mission in 1969. Space missions produced many scientific and technological innovations, which yielded innovations that influenced directly the society and the life of many people. One example of these technological advances are applications related to artificial satellites: satellite communication and guidance, environmental and meteorological surveillance, disaster warning [Dick et Launius, 2007; ISECG, 2013]. Space mission themselves and the induced technological developments had of course also a strong economical impact for the countries involved in space programs.

For the first decades of human space flight, government space agencies, as the National Aeronautics and Space Administration (NASA) and the European Space Agency (ESA), have had the exclusive control on space programs for the development of spacecraft capable of delivering humans into space. However, more recently, private organizations have made considerable progress, with the goal of taking the lead in the future of space flight and space tourism. This new context is leading to further advances in the field of space missions, which will provide the technologies that will eventually lead to the development of a

space economy and the space-access market [Crawford, 2016]. One of the main objectives of this renovated interest for space missions consists in the exploration of Mars, which will eventually lead to the first manned landing on the planet. Martian missions are more complex from a technological point of view, leading also to socio-economical and socio-political difficulties [Shaghaghi et Antonakopoulos, 2012], due to the elevated associated economical cost and the necessity of building collaborations between different stakeholders to produce the necessary technological advances. The big technological challenges of a Martian manned mission space from making possible and safe such a long stay in a spatial environment of the human crew to the design of an adequate vehicle that could handle the difficult Entry, Descent and Landing (EDL) on Mars with manned vehicles [Braun et Manning, 2007].

Atmospheric entry and hypersonic flows

Hypersonic aerodynamics plays a big role in the atmospheric entry of space vehicles and an accurate aerothermal simulation of the entry flow is crucial in the design of the vehicle and the entry trajectory. In fact, aerodynamic flows in the hypersonic regime are characterized by the presence of a strong bow shock in front of the vehicle forebody, which converts a big part of the kinetic energy of the flow into thermal energy. This causes a huge increase in the temperature of the shock layer, the part of the fluid flow between the shock and the body. For this reason, the surface of the vehicle is exposed to a strong heating, requiring the presence of a Thermal Protection System (TPS, also called heat shield) which needs to be designed to protect the structure and internal components from excessive temperatures. Also the design and reconstruction of EDL trajectories is significantly affected by hypersonic aerodynamics. In fact, the aerodynamic drag produced during the hypersonic phase of the entry trajectory provides a major contribution to the deceleration of the capsule, influencing the design of the entry trajectory. Therefore, an accurate prediction of the aerodynamic and thermal loads is fundamental for the success of an entry mission.

Hypersonic entry flows are complex phenomena, because the strong post-shock heating is the origin of multiple features such as dissociation and other chemical reactions, ionization, chemical and thermal non-equilibrium effects, radiative heating and interaction effects with the wall such as catalysis and ablation [Anderson, 2000; Sarma, 2000]. As a consequence of their complexity, it is very difficult to reproduce entry flows in experimental facilities, especially because exact experimental similitude can not be obtained in a general non-equilibrium situation, unless a real-sized model is used. Acquiring measurements during real-world entry flight can provide useful data about the fluid flow, but it is infeasible on a regular basis, since every entry mission involves elevated economical costs. Therefore, numerical simulations by means of Com-

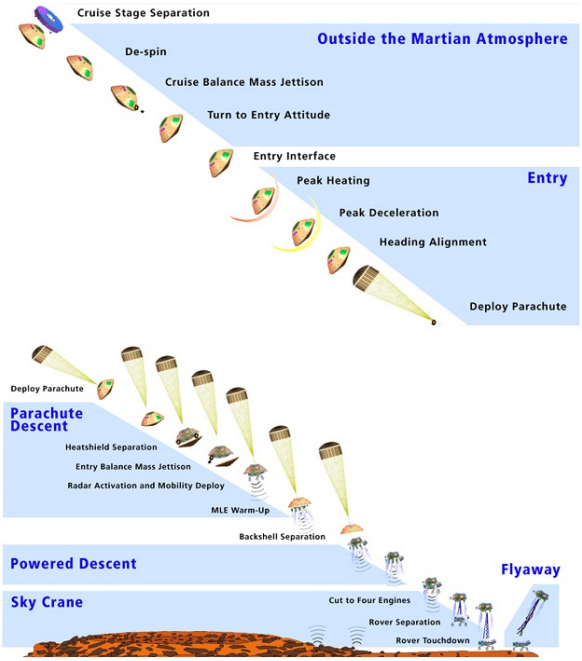

Figure 1: Representation of the main phases of an EDL mission. All the entry phase, from the entry interface to the parachute deployment, is usually characterized by hypersonic flows. Image credit: NASA [NASA, 2012].

putational Fluid Dynamics (CFD) are often the only available resource to get quantitative data about hypersonic entry flows [Longo, 2004; zur Nieden et Olivier, 2007].

The simulation of hypersonic entry flows has seen big advances in the literature [Sinha, 2010; Longo, 2004]. However, an accurate simulation of the complex phenomena occurring in the air flow around an entering vehicle is a challenging problem [Candler, 1998; Gnoffo, 1999]. Thermal loads are especially more challenging [Knight *et al.*, 2012, 2017; Bose *et al.*, 2013], because they require an accurate modeling of all the phisico-chemical phenomena they depend on (non-equilibrium effects, catalysis, ablation, radiation, *etc.*) [Sinha et Reddy, 2011] and also an accurate numerical resolution, with stable numerical schemes [Druguet *et al.*, 2005] and adequate computational grids [Saunders *et al.*, 2007].

Freestream reconstruction

In order to produce accurate and predictive simulations, it is essential to have accurate values for the boundary conditions, such as the composition and the thermodynamic state of the atmosphere at the freestream and flight speed. Unfortunately, the knowledge about atmospheric properties and thermodynamic

state is generally characterized by a high degree of uncertainty, especially away from Earth. Furthermore, the variability of atmospheric conditions, in particular density, has important implications for EDL mission planning, design and performance [Talay *et al.*, 1985], since entry velocities are reduced mainly by aerodynamic drag. In fact, atmospheric fluctuations can cause random deviations from standard-atmospheric models, which can be substantially different over altitudes of a few kilometers [Enzian *et al.*, 2002] (as shown in Figure 2). To improve the knowledge about freestream conditions, it is common prac-

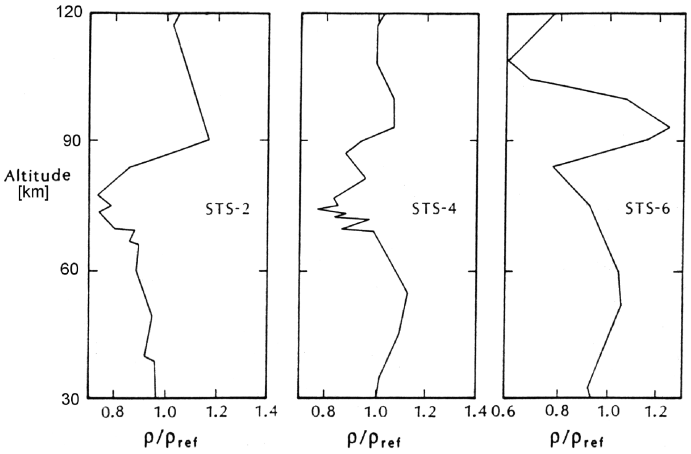

Figure 2: Deviations between atmospheric densities derived by Shuttle measurements and the 1962 U.S. standard atmosphere (from [Talay *et al.*, 1985]).

tice to rebuild atmospheric parameters from flight data in post-flight analysis. This enables the improvement of atmospheric models for design and analysis of EDL missions and provides critical input boundary conditions for predictive CFD simulations. The reconstruction of atmospheric conditions and the state of the vehicle is also important for the control and guidance of manned vehicles [Koppenwallner, 2007].

Classical reconstruction techniques of the entry trajectory and atmospheric conditions are deterministic approaches based on linear accelerations and angular rotations measured by accelerometers and gyros composing the Inertial Measurement Unit (IMU), which is part of the standard instrumentation on entry vehicles. Inertial measurements on an entering spherical probe have been used to characterize Earth's upper atmospheric density and temperature variations [Jones *et al.*, 1959]. They have been exploited also for the characterization of Martian atmosphere [Seiff et Reese, 1965] and for other planets [Seiff, 1991]. Moreover, the post-flight analysis of the entry phase of many different space missions relied mainly on inertial data to rebuild the entry trajectory and characterize the atmospheric freestream conditions. Examples in literature can be found for the Mars Pathfinder mission [Spencer *et al.*, 1999], the

Mars Exploration Rover mission [Desai *et al.*, 2003; Withers et Smith, 2006], the Phoenix mission [Blanchard et Desai, 2011; Desai et Knocke, 2007] and the Huygens mission [Kazeminejad *et al.*, 2007; Colombatti *et al.*, 2008], to cite some. They have been successfully used also in the presence of aerobraking for the Mars Odyssey mission [Tolson *et al.*, 2005, 2007, 2008]. A more modern formulation and review of IMU-based trajectory and atmosphere reconstruction approaches can be found in [Withers *et al.*, 2003], with an application to the Pathfinder EDL mission. However, while inertial flight data are ideally suited for the entry trajectory reconstruction [Desai *et al.*, 2011], they may not be sufficient to accurately characterize the atmospheric environment [Van Hove et Karatekin], since they do not include any direct information about the air flow around the capsule.

For this reason, on some other entry vehicles a Flush Air Data System (FADS) is also available, consisting of pressure ports (and other sensors in some cases) integrated into the heat shield [Cobleigh *et al.*, 1999]. Hence, FADS measurements normally consist of pressure data at several points of the vehicle forebody. This system is able to provide measurements that are complementary to those provided by IMU, since they contain direct information about the flow and the atmospheric environment to which the vehicle surface is exposed. FADS sensors were mounted on different entry vehicles, for exam-

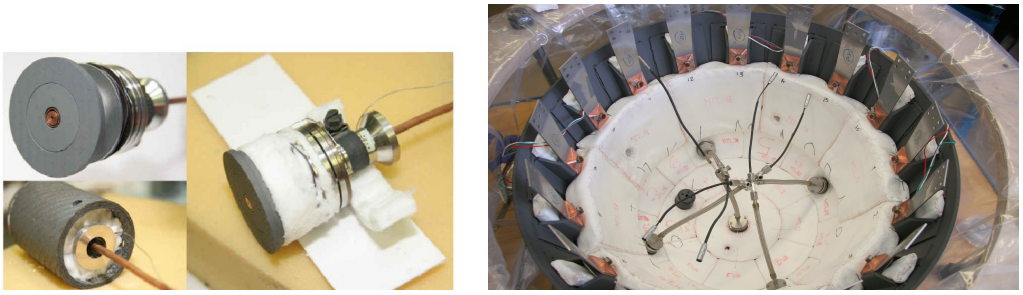

(a) (b)

Figure 3: Image of the FADS/RAFLEX probe (a) and their mounting inside the forebody of the EXPERT entry vehicle from European Space Agency (b) (taken from [Ratti *et al.*]).

ple Viking [Euler *et al.*, 1978] and Mars Science Laboratory (MSL) [Karlgaard *et al.*, 2014b] in case of Mars missions, or on the Space Shuttle, with the Shuttle entry air data system (SEADS) [Pruett *et al.*, 1983], for Earth entry missions. Freestream reconstruction techniques have been developed in the literature to exploit also surface pressure data, as a direct measurement of the flow given by the FADS. Often, these techniques do not take into account many high-temperature effects (*e.g.* chemical non-equilibrium, surface catalysis, ablation and radiative effects), and they usually rely on the calorically perfect

gas approximation. For example, results in [Müller-Eigner *et al.*, 1999; Koppenwallner, 2007] show how the Pitot pressure can be linked to the freestream pressure in the case of a supersonic flow, considering calorically perfect gas. [Häuser *et al.*, 2004] used several pressure measurements on the surface of the space vehicle to rebuild also the angle of attack and the yaw angle. In this context, they used the so called analytic sensor functions [Koppenwallner, 2003], based on the assumption of Newtonian flow. Moreover, an empirical correction was used to account for geometrical effects as well as flow viscosity and non-equilibrium phenomena. [zur Nieden et Olivier, 2007] proposed a more advanced curve-fit method as well as an analytically derived function for freestream reconstruction based on both FADS and IMU data. Other recent implementations of trajectory and freestream reconstruction exploiting FADS measurements can be found in [Karlgaard *et al.*, 2014b,a; Van Hove et Karatekin, 2017] for the entry of the MSL vehicle in Martian atmosphere. Other than in entry vehicles, FADS have been exploited for freestream rebuilding also in other contexts, for example on the X-34 transatmospheric vehicle [Whitmore et Ellsworth, 2008], for aeronautical applications like in tests on the F-14 [Larson *et al.*, 1987] and F-18 [Whitmore *et al.*, 1995] aircrafts or on mini air vehicles (MAV) [Samy *et al.*, 2010], and on vessels for nautical applications [Srivastava *et al.*, 2012; Srivastava et Meade, 2015]. Notice that both [Samy *et al.*, 2010] and [Srivastava *et al.*, 2012; Srivastava et Meade, 2015] used more advanced reconstruction techniques based on Neural Networks [Bishop, 1995].

In order to account for measurement errors, which intrinsically affect flight data, many trajectory and freestream reconstruction techniques have been developed in the literature to satisfy the need of accounting for these uncertainties in the rebuilt values. For example [Van Hove et Karatekin, 2017] used Monte Carlo methods to propagate uncertainties in the reconstruction inverse problem, in [Kutty, 2014] instead, uncertainties have been propagated by linear covariance mapping. [Christian *et al.*, 2007] proposed to use Kalman filtering to account for uncertainties in the freestream and trajectory rebuilding problem. A more advanced method for freestream characterization was discussed in [Dutta et Braun, 2014; Dutta *et al.*, 2013, 2014], where different statistical estimation methods, namely Extended Kalman filter, Unscented Kalman filter, and adaptive filter, were used to statistically estimate trajectories and freestream conditions from flight data, containing pressure measurements together with gyroscope, accelerometer and radar altimeter data, as well as to quantify uncertainties in these estimates. This method was applied in the context of post-flight analysis for Mars Science Laboratory (MSL) mission.

On some entry vehicles, flush-mounted sensors are able to provide also heat flux measurements. The Re-entry Aerodynamic Flow Experiment (RAFLEX) [Müller-Eigner et Koppenwallner, 2001] instrumentation package, for example, is composed by several flush-mounted probes that are able to measure pressure and heat flux at the same location. This system equips different vehicles, such

as MIRKA (Mikro-Rückkehrkapsel) [Müller-Eigner *et al.*, 1999] and EXPERT (European eXPErimental Re-entry Test-bed) [Thoemel *et al.*, 2009]. However, at least up to the author's knowledge, heat flux measurements normally are not exploited, probably due to the difficulty of realizing both accurate measurements [Loehle, 2016] and precise simulations of the heating. Some efforts in this direction can be found in the literature with the preliminary analysis of [Alekseev et Pavlov, 1998], which showed, by means of analytical correlations, that surface heat flux data were able to supplement standard trajectory and freestream reconstruction methods with additional information. Another use of heat flux measurements can be found in [Müller-Eigner *et al.*, 1999], where it has been used, together with dynamic pressure measurements, to determine the freestream velocity for MIRKA vehicle through an analytic relation.

Quantifying the uncertainties

Numerical models to simulate entry flows require many input parameter to describe boundary conditions and model properties, whose values must be accurately given in order to have significant predictions [Roy et Oberkampf, 2011]. However, some parameters describing boundary condition, such as freestream atmospheric conditions, are known within uncertainties, since, as seen, they are reconstructed from indirect measurements, and these measurements are intrinsically uncertain. Also many other model inputs may be uncertain, due to their intrinsic variability or lack of knowledge by the analyst. The thermo-physical models are mostly derived from a combination of theoretical and empirical assessments based on perhaps limited amount of experimental data. For example atmospheric chemistry parameters [Park *et al.*, 1994; Bose *et al.*, 2004] and wall chemistry parameters (catalysis) [Villedieu *et al.*, 2012; Sanson *et al.*, 2017b] may be known with uncertainties. The need for robust predictive simulations in the analysis and design process requires a rigorous quantification of how these uncertainties affect the output of the simulations. Uncertainty Quantification (UQ) is gaining increasing importance in rigorously quantifying the uncertainties introduced in the output of numerical simulations needed to establish objectively their predictive capabilities [Roy et Oberkampf, 2011]. One of the main goals of UQ is to propagate the different sources of uncertainties through the simulation model in order to obtain quantitative informations about the variability of some quantities of interests (outputs). Uncertainty quantification has been used in the literature in different applications in the field of entry flows [Bose *et al.*, 2006, 2013; Lockwood et Mavriplis, 2013; West et Hosder, 2015; Falchi *et al.*, 2017; Wang *et al.*, 2017] and hypersonic aerothermodynamics [Constantine *et al.*, 2011, 2015]. A statistical Bayesian framework has been tested for both direct and inverse uncertainty propagation in [Tryoen *et al.*, 2014], to account for measurement errors and other sources of uncertainties in inverse problems for atmospheric reconstruction. Bayesian inversion

has been used also in [Panesi *et al.*, 2011; Miki *et al.*, 2015] for the calibration of parameters of non-equilibrium thermochemical models for hypersonic flows and for shock tube experiments [Panesi *et al.*, 2012]. Atmospheric entry of space debris is another relevant application in the aerospace field that is seeing the development of a statistical uncertainty quantification framework to account for variability in the results of simulations [Sanson *et al.*, 2017a; Mehta *et al.*, 2016a,b, 2017].

Challenges and main objectives

The underlying objective motivating this work is to assess the possibility and the usefulness of exploiting surface heat flux measurements, given by FADS/RAFLEX-like sensors together with pressure measurements, for the characterization of freestream quantities, like atmospheric density, flight velocity and angles, and of other uncertain parameters in the physico-chemical model. Due to the high measurement errors associated with heat flux data and the presence of uncertainties in the complex computational model of the hypersonic flow, a Bayesian statistical framework is chosen to formulate the reconstruction problem, like in [Tryoen *et al.*, 2014]. From this choice, some challenges arise, which are related to numerical algorithms used both for the simulation of the flow and the solution of the inference problem. In fact, the solving algorithms for uncertainty problems require a fair amount of evaluations of the computational model. Therefore, CFD simulations should be able to provide reasonably accurate results without the constant monitoring of the user. Also, since CFD simulations are quite expensive from a computational point of view, it will be mandatory to use a surrogate model for the quantities of interest. Further challenges are related to the construction of an accurate surrogate model which is also efficient, in the sense that it requires the least amount possible of evaluations of the actual computational model, especially when considering a medium-to-large number of uncertain parameters. In fact, usually, UQ problems get exponentially more computationally demanding when increasing the size of the space of uncertain input parameters [Donoho, 2000], and efficient tools are needed to provide a solution for medium-to-high dimensional problems without requiring excessive computational efforts.

The other objectives of this work are therefore focused at tackling challenges related to the algorithmic development. Firstly, an automated strategy is needed for producing relatively accurate CFD simulations, that at the same time is not too computationally demanding, having in mind the UQ applications. From the point of view of the resolution of the uncertainty problem, instead, the work wants to seek for enhanced techniques that could improve the forward propagation and inverse reconstruction problems. Therefore, the main goals in this topic are to provide an improved surrogate modeling technique,

requiring a smaller number of training points, in which the CFD model needs to be run, able to provide an accurate prediction of the quantity of interest. In the following list, the main objectives are summarized for clarity.

1. Assess the capabilities of using surface heat flux measurements in atmospheric reconstruction for hypersonic entry flows
2. Set-up of a numerical framework for getting accurate numerical simulation of the flow under a UQ perspective
3. Formulate direct and inverse problems of uncertainty propagation for entry flow simulations in a statistical Bayesian framework
4. Develop an appropriate algorithmic framework for the construction of a robust and accurate surrogate model usable in the Bayesian UQ framework. It should be efficient, in the sense that it should require a limited number of training points to produce an accurate approximation of the computational model

Outline

The present work is divided in six chapters. The first two are mainly introductory about aspects related to the modeling and simulation of hypersonic flows and the formulation of the statistical uncertainty quantification framework, together with a review of some UQ tools. The first chapter also addresses the objective of setting-up a numerical framework for robust automated CFD simulations. The following three chapters deal with the development of algorithmic aspects for robust and accurate solutions of the UQ problem. The last chapter proposes an application to assess freestream reconstruction for entry flows of the EXPERT vehicle. Three appendix give further information about some topics mentioned in the core discussion but not completely clarified.

Chapter 1 is an introduction to hypersonic atmospheric entry flows. The purpose is to give an insight of the main phenomena that characterize this kind of flows, to provide mathematical models used to describe the physics and to show how numerical simulations can be performed. Since research activity in this field was not the main purpose of this work, the chapter serves as a description of existing models taken from the literature.

Chapter 2 acts an in introduction to Uncertainty Quantification, global Sensitivity Analysis and Bayesian inference. Forward and inverse uncertainty quantification problems are defined in a statistical framework. A review is given of different techniques to solve the UQ problems, with particular emphasis given on the tools that will be used in the following parts of the work.

Chapter 3 proposes a novel technique for the construction of a surrogate model of an expensive computational model. This technique is derived as the coupling between two other methods taken from the literature, namely *Universal Kriging* and *sparse Polynomial Dimensional Decomposition*. Firstly, a description of the two existing techniques is given. Then the coupling algorithm is proposed. The technique is assessed on different analytical test cases and engineering application cases.

Chapter 4 introduces a novel technique for the adaptation of the experimental design for the training of surrogate models. This technique is based on the idea of creating a simplex grid using the training points as nodes, and then exploiting an algorithm derived from anisotropic mesh refinement to add new training points.

Chapter 5 is about the application of dimension reduction by *active subspaces* in the context of uncertainty propagation and Bayesian inference. Firstly, the methodology is described, and then an application is proposed for the hypersonic high-temperature flow past a cylinder, with a first assessment of heat flux-based freestream reconstruction.

Chapter 6 presents results for assessment of freestream and model parameters rebuilding starting from surface pressure and heat flux measurements, in the case of entry flows of the EXPERT vehicle. Different configurations are tested, in order to rebuild freestream density, flight angles and catalytic recombination coefficient.

Conclusions contain a summary of the several accomplishments of the work and recommendations for future developments.

Appendix A introduces to the main ideas of classical freestream reconstruction techniques, namely the ones based on IMU data and the ones that exploit also pressure measurements from the FADS.

Appendix B provides in-depth details about Kriging (or Gaussian process regressions), such as their derivation, together with other technical details.

Appendix C is about the review of the techniques used in the work to estimate the surrogate modeling error, in order to assess their quality and accuracy.

Chapter 1

Physical context and numerical simulations of hypersonic entry flows

This first chapter is meant to be an introduction to the phenomenology and the models related to hypersonic entry flows. The physical and mathematical models used in this work to represent the phenomena are first described, and then the numerical methods employed to simulate them are provided. An automated mesh adaptation strategy is shown, which is meant to be used in the perspective of uncertainty quantification applications. Finally, some physical application cases in the atmospheric entry field are presented, and they will be used throughout the work.

1.1 Introduction

The main application field of this PhD work is about aerodynamic flows occurring during the atmospheric entry of a space vehicle. Along its entry trajectory, a space vehicle experiences many different flow regimes [Gnoffo, 1999]: from free molecular regime, where individual molecular impacts on the surface are important, to transitional regime, in which traditional no-slip boundary conditions are no longer valid, to continuum regime. In this work we will focus only on hypersonic flows where the continuum hypothesis is completely valid, and classical Navier-Stokes equations can be used to describe the fluid motion. Hypersonic entry flows involve complex physical phenomena, where several aspects (as fluids dynamics, thermodynamics, transport and chemistry) and their interaction need to be accounted for, in order to have a representative model [Anderson, 2000].

Conventionally, hypersonic flows are defined for Mach numbers of $M > 5$. However, this is more a rule of thumbs than an actual definition, as, more

precisely, hypersonic aerodynamics can be defined as the regime where certain physical phenomena in the flow become progressively more important as the Mach number is increased. Hypersonic flows are, in the first place, characterized by the presence of a strong *shock* in front of the object, due to the high Mach number. Across this strong bow shock, a large amount of kinetic energy is converted to internal energy of the gas, translating into a very high temperature in the post-shock region. This can cause several phenomena, that are normally referred to as *high-temperature effects*. In fact, if the temperature becomes high enough, it can excite vibrational energy within molecules and can cause dissociation and other chemical reactions, and even ionization. Therefore, hypersonic high-temperature flows are usually also *multicomponent*

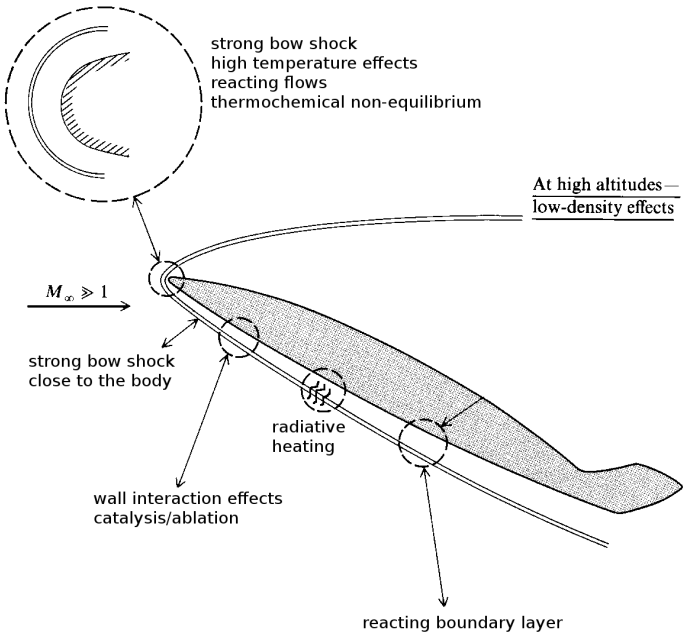

Figure 1.1: Representation of some physical phenomena involved in hypersonic atmospheric entry flows (modified from [Anderson, 2000]).

and *reacting* flows. If the time associated to vibrational excitation and chemical reactions is smaller in comparison to the time it takes for a fluid element to move through the flow field, the flow is in vibrational and chemical equilibrium. Otherwise, if the flow characteristic time is smaller than the one of molecular excitation and chemistry, *non-equilibrium* effects on thermodynamics and chemistry need to be accounted for, and the air mixture properties become function of the history of each fluid element [Gnoffo *et al.*, 1989]. In addition, closer to the vehicle body, the strong viscous dissipation occurring in hypersonic boundary layers can create very high temperatures and can cause

the boundary layer to become chemically reacting. Therefore, a hypersonic entry flow can be also characterized by chemically *reacting boundary layer* at the surface of the vehicle. For entry speeds of about 7 km/s, typical of LEO (Low Earth Orbit) return, the wall can be made of a *catalytic* material that tends to promote chemical recombination of atoms at the surface. Furthermore, for entry speed greater than 10 km/s, typical for example of Moon return missions, due to the strong heating, the surface of an entry vehicle is usually protected by an *ablative* thermal protection system (TPS), and the products of the ablation process are also present in the boundary layer. Moreover, a further effect arises when the shock layer temperature is high enough: the thermal radiation emitted by the gas becomes important and produces a *radiative heating*, which further increases the surface heating. All these various effects related to hypersonic entry flows are summarized in Figure 1.1.

In this chapter, the mathematical modeling of the physical phenomena is described, together with the numerical methods used to simulate the model. First, in Section 1.2, we briefly present the governing equations used for representing hypersonic entry flows and the thermodynamic, transport and chemical models used to compute the properties of the gas mixture. Some further details about catalysis and ablation gas-surface interactions are reported in Section 1.3. Then, Section 1.4 contains an overview on the numerical schemes used to solve the system of equations and their implementation in the COSMIC code, with an emphasis on the need for mesh adaptation (Sec. 1.5). Finally, the application cases on which hypersonic high-temperature flows are simulated are described in Section 1.6, which contains also the characterization of the uncertainties on some model parameters, which will be used for the following uncertainty quantification on the model outputs.

1.2 Governing equations and physico-chemical model

In this section, the governing equations and the physico-chemical models used to describe the hypersonic entry flows are presented. A first assumption that is made is that each species composing the fluid can be treated as a perfect gas in the range of thermodynamic conditions of interest to the proposed applications. A second hypothesis is that the fluid can be described as a continuum, meaning that the macroscopic quantities describing the flow can be identified with suitable average values of molecular quantities at any location in the flow. This allows to use Navier-Stokes equations as governing equations for the fluid flow. The continuum hypothesis is valid as long as there is a sufficient number of molecules within the smallest significant volume of the flow. This is true if the Knudsen number Kn, defined as the ratio between the mean free path and a suitable reference length, is $Kn < 0.01$. The application cases presented

in this work are all in the continuum regime and Navier-Stokes equations can be used without any issue. The flow is considered to be in local thermal equilibrium, which is a valid hypothesis for the range of considered freestream conditions, but chemical non-equilibrium is taken into account.

1.2.1 Conservation equations for a mixture of reacting perfect gases

Here we recall the governing equations describing the unsteady compressible flow of a mixture of reacting perfect gases in chemical non-equilibrium. The derivation of the governing equations in fluid dynamics can be found in many references [Anderson, 2000, 2010]. Usually, it is performed by means of the control volume method, that consists in applying the conservation principles on a suitable control volume in the flow field. However, the control volume approach is not linked to a specific physico-chemical model, therefore different physical and chemical models are needed to provide the missing description of transport terms and thermodynamic properties of the reacting gas. In this framework, statistical mechanics (suitably coupled with quantum mechanics) is able to provide the thermodynamic properties of the gas mixture (internal energy, specific heat) and kinetic theory is used to describe the transport properties (viscosity, thermal conductivity, diffusion). The model used in this work has been developed by Barbante in his PhD work, and more detail can be found in [Barbante, 2001].

Continuity

The equation that describes the global conservation of mass in the system is the so-called continuity equation, and it can be written in the classical form:

$$\frac{\partial \rho}{\partial t} + \nabla \cdot \left(\rho \boldsymbol{u}\right) = 0 \,, \tag{1.1}$$

where ρ is the air mixture density and $\boldsymbol{u}$ is the vector containing the components of the average mixture velocity.

Species continuity

For a non-equilibrium flow, in addition to the global continuity equation given by eq. (1.1), s species continuity equation are needed, one for each chemical species in the mixture. They can be written as:

$$\frac{\partial \rho_i}{\partial t} + \nabla \cdot \left(\rho_i \boldsymbol{u}\right) + \nabla \cdot \left(\rho_i \boldsymbol{\mathcal{V}}_i\right) = \dot{\omega}_i \qquad \text{for} \qquad i = 1, \ldots, s \,, \tag{1.2}$$

with ρ_i and $\dot{\omega}_i$ representing respectively the partial density of each mixture component and the rate of production due to chemical reaction for the i-th

species, and where $\boldsymbol{\mathcal{V}}_i$ is the diffusion velocity of each species, which satisfy the following property:

$$\sum_{i=1}^{s} \rho_i \boldsymbol{\mathcal{V}}_i = 0. \tag{1.3}$$

Momentum

The equation describing the conservation of momentum can be written as:

$$\frac{\partial \rho \boldsymbol{u}}{\partial t} + \nabla \cdot \left(\rho \boldsymbol{u} \otimes \boldsymbol{u}\right) = -\nabla p + \nabla \cdot \underline{\underline{\tau}}\,, \tag{1.4}$$

where p is the mixture pressure, $\underline{\underline{\tau}}$ the tensor of viscous stress. We assume that the plasma is quasi-neutral, that no external electromagnetic forcing is applied, and that the internal electric field for the ionized mixture arises from the so-called ambipolar diffusion constraint, *i.e.* the diffusion current is zero, and the magnetic field is negligible. We also assume the effects of gravitational forces to be negligible.

Energy

The total energy conservation equation for the mixture reads:

$$\frac{\partial \rho E}{\partial t} + \nabla \cdot \left[(\rho E + p)\boldsymbol{u}\right] - \nabla \cdot \left(\underline{\underline{\tau}} \cdot \boldsymbol{u}\right) + \nabla \cdot \boldsymbol{q} = 0\,, \tag{1.5}$$

where E is the total energy per unit mass, sum of the internal and kinetic energy $E = e + |\boldsymbol{u}|^2/2$, and $\boldsymbol{q}$ is the heat flux. Note that the assumptions on the electromagnetic and gravitational forces lead to a null work for this kind of forcing.

1.2.2 Physico-chemical Models

Here the different physical and chemical model used to compute the thermodynamic properties of the mixture and the transport terms are outlined. These models are necessary for the closure of the conservation equations.

Thermodynamic model: Perfect gas

As already stated, each species in the gas mixture is supposed to behave like a perfect gas, *i.e.* a gas where the effects of intermolecular forces are negligible. The well-known perfect gas equation of state, valid for each species, is:

$$p_i = \rho_i R_i T\,, \tag{1.6}$$

with $R_i = \mathcal{R}/M_i$ the specific gas constant for the i-th mixture component, which is the ratio between the universal gas constant $\mathcal{R}$ and the molar mass

M_i, p_i the partial pressure and T the temperature. From Dalton's law, we have that the mixture pressure is $p = \sum_{i=1}^{s} p_i$ and it follows that the mixture density is equally defined as $\rho = \sum_{i=1}^{s} \rho_i$. Mass fractions y_i are defined as the mass of i-th species per unit mass of mixture $y_i = \rho_i/\rho$ and concentrations x_i (mole fractions) are defined as the ratio between the number of moles of the i-th species and the total number of moles of the mixture $x_i = n_i/n$.

Statistical thermodynamics and quantum physics are used to define the internal energy and, subsequently, the thermodynamic properties of the gas mixture [Anderson, 2000, Chapter 11]. It can be shown that the internal energy of a species is related to the partition function $\mathcal{Q}$ [Mayer et Mayer, 1946]:

$$e_i = R_i T^2 \left(\frac{\partial \ln \mathcal{Q}_i}{\partial T} \right)_v , \tag{1.7}$$

and the enthalpy is defined as $h_i = e_i + R_i T$. Note that, form this theory, in agreement with the factorization property of the partition function, the internal energy for a molecule can be written as the sum of the energies related to different energy modes of the molecule itself:

$$e_i = \underbrace{e_{tr_i}}_{\text{translational}} + \underbrace{e_{rot_i}}_{\text{rotational}} + \underbrace{e_{vib_i}}_{\text{vibrational}} + \underbrace{e_{el_i}}_{\text{electronic}} + \underbrace{e_{0_i}}_{\text{zero-point}} . \tag{1.8}$$

The energies related to each different mode are expressed relatively to the value they assume at absolute zero, called the zero-point energy e_0 or ground state, so that the computed energy is not the absolute energy but instead the sensible one. The zero-point energy generally cannot be directly computed or measured. However, in a reacting mixture, it is necessary to establish a common level from which all the species energies are measured. Therefore, it follows that the zero-point energy of a species can be replaced by the heat of formation of the same species at the reference temperature, which are available in literature. Once an expression for the energy of each species is available, mixture energy per unit mass can be easily obtained from the energies of the different species:

$$e = \sum_{i=1}^{s} y_i \, e_i . \tag{1.9}$$

From the mixture energy and the enthalpy, it is possible to compute the specific heats of the reacting gas mixture. In the case of chemical equilibrium flow, the specific heats are function of two thermodynamic variables, for example (p, T), since the mixture composition depends also on two thermodynamic

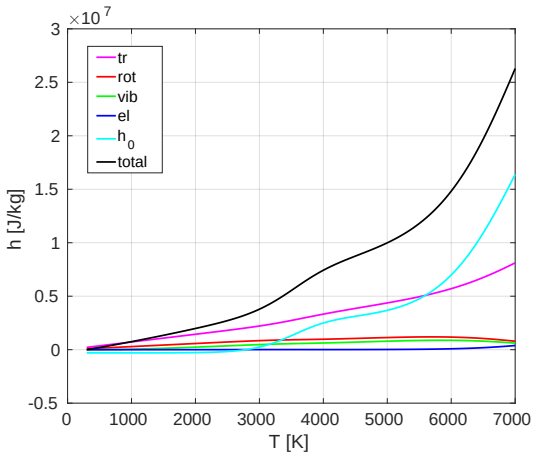

Figure 1.2: Enthalpy for five species air [Park *et al.*, 2001] as a function of the temperature (in black) and decomposition in translational, rotational, vibrational, electronic and zero point contributions. Figure obtained by means of the Mutation++ library [Magin *et al.*, 2006a]

variables, and they can be expressed as:

$$c_p = \left(\frac{\partial h}{\partial T}\right)_p = \sum_{i=1}^{s}\left[\left(\frac{\partial y_i}{\partial T}\right)_p h_i + y_i\left(\frac{\partial h_i}{\partial T}\right)_p\right] \tag{1.10}$$

$$c_v = \left(\frac{\partial e}{\partial T}\right)_v = \sum_{i=1}^{s}\left[\left(\frac{\partial y_i}{\partial T}\right)_v e_i + y_i\left(\frac{\partial e_i}{\partial T}\right)_v\right]. \tag{1.11}$$

Instead, in the other limit case of a frozen mixture, where chemical composition does not change, heat fluxes are function only of temperature (through the energy and the enthalpy):

$$c_p^{(fr)} = \sum_{i=1}^{s} y_i\left(\frac{\partial h_i}{\partial T}\right)_p \tag{1.12}$$

$$c_v^{(fr)} = \sum_{i=1}^{s} y_i\left(\frac{\partial e_i}{\partial T}\right)_v. \tag{1.13}$$

Finally, in the intermediate case of chemical non-equilibrium, the chemical composition is function not only of two thermodynamic variables, but also of the previous flow history and the position. Therefore, specific heats are not uniquely defined and the only specific heat that is logical to consider is the frozen one.

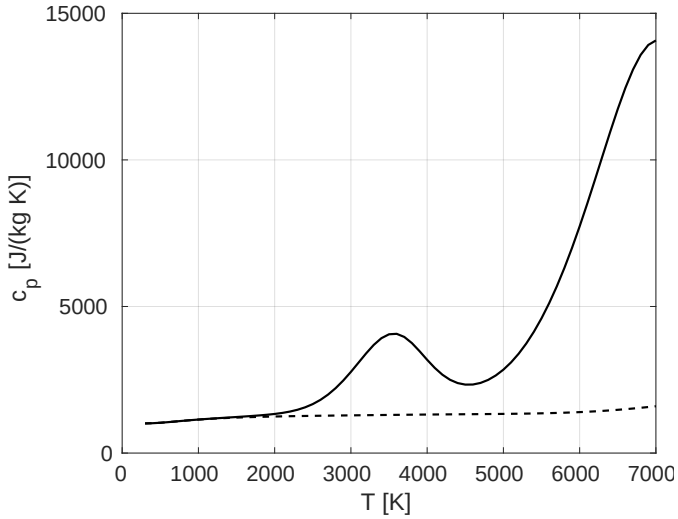

Figure 1.3: Comparison between equilibrium (solid line) and frozen (dashed line) specific heats at constant pressure of 1 atm for the five species air mechanism described in [Park *et al.*, 2001]. Figure obtained by means of the Mutation++ library [Magin *et al.*, 2006a].

Chemical production term

Here we show how to find an expression for chemical production term $\dot{\omega}_i$ for each species. Let us start by considering an elementary reaction (identified with index r), which is a reaction that takes place in only one step. It can be formally written as:

$$\sum_{i=1}^{s} \nu'_{ir} X_i = \sum_{i=1}^{s} \nu''_{ir} X_i \ , \tag{1.14}$$

where X_i is the symbol for the i-th species, and ν'_{ir} and ν''_{ir} are respectively the stoichiometric coefficients for the i-th reactant and product. An elementary reaction can proceed in both directions (forward and backward reactions) and is always reversible. When the forward and backward reactions are in perfect balance, the reaction is said to be in chemical equilibrium. The net rate of production of the i-th species by the r-th elementary reaction can be expressed as [Barbante et Magin, 2004]:

$$\dot{\omega}_i^{(r)} = M_i(\nu''_{ir} - \nu'_{ir}) \left[k_{fr} \prod_{j=1}^{s} \left(\frac{\rho_j}{M_j} \right)^{\nu'_{jr}} - k_{br} \prod_{j=1}^{s} \left(\frac{\rho_j}{M_j} \right)^{\nu''_{jr}} \right]. \tag{1.15}$$

Since this equation must be valid also at the equilibrium, and the forward k_{fr} and backward k_{br} reaction rates are linked by the equilibrium constant K_{er} through the following expression: $k_{fr} = K_{er} k_{br}$. This ensures that the chemical composition is correctly computed when the flow is locally in equilibrium

conditions. K_{er} is linked to the Gibbs free energy and for a perfect gas it is a function only of temperature. Referring to the elementary reaction r, K_{er} reads [Anderson, 2000]:

$$\log K_{er} = -\sum_{i=1}^{s} \frac{(\nu''_{ir} - \nu'_{ir})\hat{g}_i}{\mathcal{R}T} - \log(\mathcal{R}T) \sum_{i=1}^{s} (\nu''_{ir} - \nu'_{ir}) \ , \tag{1.16}$$

where $\hat{g}_i$ is the Gibbs free energy per unit mole of species i and is equal to $\hat{g}_i = \hat{h}_i - T\hat{s}_i$, with $\hat{h}_i$ and $\hat{s}_i$ respectively the enthalpy and entropy of species i per unit mole. In theory, it is possible to derive the forward reaction rate k_{fr} from kinetic theory, doing several assumptions. In practice this approach is not always possible, and a semi-empirical formulation, called Arrhenius formulation, is used instead to compute the forward rate:

$$k_{fr} = A_r T^{\nu_r} e^{-\frac{E_{dr}}{kT}} \ , \tag{1.17}$$

with k the Boltzmann constant. $A_r > 0$ is a constant pre-exponential factor, ν_r a positive or negative exponent and E_{dr} is the activation energy for the r-th reaction. These parameters values are usually computed by fitting experimental data, and different values can be found in literature. Therefore, they can be affected by uncertainties, especially the pre-exponential coefficient A_r.

If N_r elementary reaction involving the i-th species take place, the production term for this species is obtained by summing over the contribution of all the reactions:

$$\dot{\omega}_i = \sum_{r=1}^{N_r} \dot{\omega}_i^{(r)}. \tag{1.18}$$

Air mixture mechanism

Air at ambient temperature is a mixture of molecular nitrogen (N_2), molecular oxygen (O_2), argon (Ar), carbon dioxide (CO_2) and other minor components. For the applications of interest in this work, air can be assumed to be made by just the two dominant species, with a composition of 79% N_2 and 21% O_2 in volume.

As temperature increases, different chemical reactions start to take place, modifying in this way the mixture composition (see Figure 1.4). A suitable set of chemical reactions is needed to represent all the chemical phenomena, like dissociation, exchange reactions and ionization. In this work we will mainly use the air model from [Park *et al.*, 2001] for 5 species air (N_2,O_2,N,O,NO), which is valid for lower entry speeds, where the post-shock temperature increase is not sufficient to cause ionization. The chemical reactions taking place in this five species model are reported in Table 1.1.

A brief comparison between the 5 species and an 11 species model is proposed in 3.6.1 for the HEG cylinder test case, described in 1.6.1.

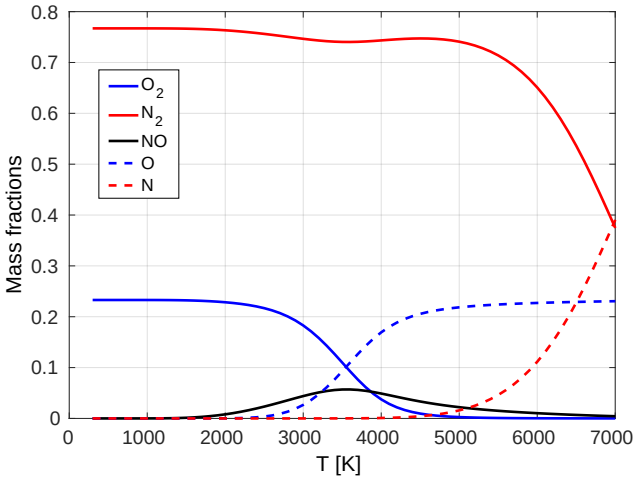

Figure 1.4: Mass concentrations at constant pressure of 1 atm for the five species air mechanism described in [Park *et al.*, 2001]. Figure obtained by means of the Mutation++ library [Magin *et al.*, 2006a].

Reaction number	Reaction
1-3	$N_2 + M \rightarrow 2N + M$ where $M = N_2, NO, O_2$
4,5	$N_2 + M \rightarrow 2N + M$ where $M = O, N$
6-10	$O_2 + M \rightarrow 2O + M$ where $M = N_2, NO, O_2, O, N$
11-15	$NO + M \rightarrow N + O + M$ where $M = NO, N, O, N_2, O_2$
16	$N_2 + O \rightarrow NO + N$
17	$NO + O \rightarrow O_2 + N$

Table 1.1: Reactions constituting the chemical mechanism for the five species air model.

Transport fluxes

Transport fluxes, namely the diffusion flux $\boldsymbol{J}_i = \rho_i \boldsymbol{\mathcal{V}}_i$, the stress tensor $\underline{\underline{\tau}}$ and the heat flux $\boldsymbol{q}$ and the related transport coefficients, are computed by the kinetic theory of gases [Chikhaoui *et al.*, 1997]. The starting point of the theory is the Boltzmann equation, which describes a mixture from the molecular point of view. Then, the Chapman-Enskog method [Chapman et Cowling, 1970] for the solution of the Boltzmann equation gives the transport fluxes of mass, momentum and energy as linear functions of the macroscopic variables gradients

through some proportionality scalar quantities, the transport coefficients.

Diffusion is a very important phenomenon in reacting flows, for example for an accurate computation of the heat flux experienced by a space entry vehicle. Often in literature, diffusion is approximated by Fick's law or some modified version [Ramshaw, 1990]. However, in the model of [Barbante, 2001], a more rigorous form of the diffusion flux for the i-th species has been used:

$$\boldsymbol{J}_i = -\rho_i \left(\sum_{j=1}^{s} D_{ij} \nabla x_j \right) , \tag{1.19}$$

where the baro and thermal diffusion effects are neglected. D_{ij} are the multicomponent diffusion coefficients, which also account for the diffusion caused by the ambipolar electric field that arises for the presence of ionized species in the mixture.

The viscous stress tensor in the Chapman-Enskog approximation can be written as:

$$\underline{\underline{\tau}} = \mu \left(\nabla \boldsymbol{u} + \nabla \boldsymbol{u}^T \right) + \left(\eta + \frac{2}{3} \mu \right) \nabla \cdot \boldsymbol{u} \underline{\underline{I}} , \tag{1.20}$$

with μ the shear viscosity coefficient and η the volume viscosity coefficient. The volume viscosity is usually neglected in multicomponent flow modeling, the main reason being that the necessary data to correctly computing it are lacking.

Finally, the approximation of the heat flux reads:

$$\boldsymbol{q} = -\lambda \nabla T + \sum_{i=1}^{s} h_i \boldsymbol{J}_i , \tag{1.21}$$

where λ is the coefficient of thermal conductivity and thermal diffusion is neglected. Notice that in this work we neglect the effect of the radiative heat flux, because it is not an influent phenomenon at entry speed taken into account. For more information about the derivation of the transport fluxes and the definitions of the transport coefficients, see [Barbante, 2001; Anderson, 2000]

1.3 Gas-surface interactions

This section is about the interaction arising in hypersonic entry flows between the high-temperature reacting gas and the wall of the vehicle. The section is divided in two parts. The first is about the interaction seen by the fluid point of view when reusable materials are used for the wall, and some details are given by catalysis and the relative wall boundary condition used for the simulations of the flow. The second part instead is about the interaction seen by the wall material point of view in case of ablative materials, and introduces

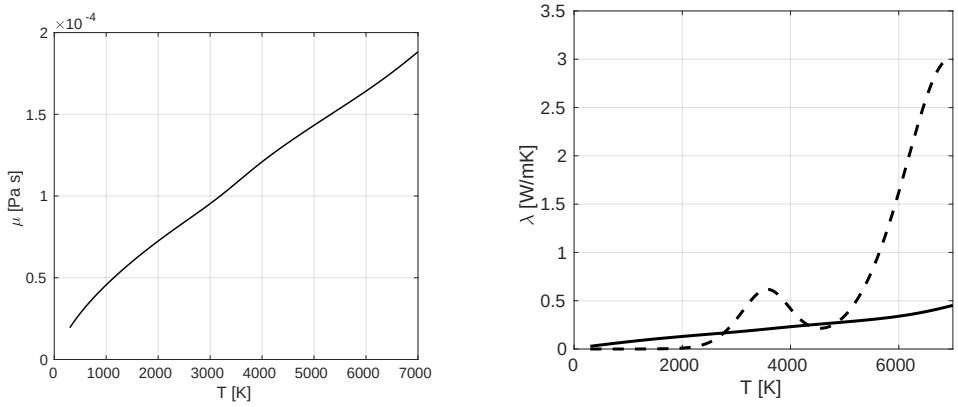

(a) (b)

Figure 1.5: Plot of the viscosity coefficient (a) and the coefficient of thermal conductivity (b) at the pressure of 1atm for the five species air air mechanism described in [Park *et al.*, 2001]. In figure (b) the solid line represents the equilibrium coefficient of thermal conductivity of the mixture, and the dashed line the reactive thermal conductivity. Figure obtained by means of the Mutation++ library [Magin *et al.*, 2006a].

the concept of ablation. While the ablation of the heat shield is not taken into account in the flow numerical simulations performed in this work, the decoupled simulation of the phenomena is used as test case for one of the uncertainty quantification tools developed later in this work.

1.3.1 Reusable material: catalytic wall

In a typical hypersonic reentry flow, due to the high post-shock temperatures, the gas surrounding an aerospace vehicle is dissociated. In such circumstances, atomic species can recombine not only in the boundary layer for the temperature reduction, but also at the vehicle surface, because the heat shield material can act as a catalyzer and promote some chemical reactions without altering its own chemical composition. The releasing of reaction energy due to the catalytic recombinations can increase the thermal load, therefore is important to account for these effects in an entry flow simulation.

The wall shows different behaviors with respect to catalytic recombination depending on the composition of the material. When the material is completely inert and does not promote atomic recombination, the wall is called *non-catalytic*. Instead, when it promotes the recombination of all the impinging atoms, the wall is said to be *fully catalytic*. Note that the definition of fully catalytic wall as the wall that promotes the recombination of all the impinging

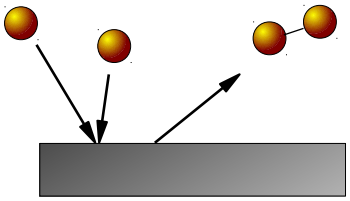

Figure 1.6: Simple graphical representation of the catalysis phenomenon.

atoms is not correct. A more rigorous definition of fully catalytic wall is a material that allows the local gas composition to be equal to the equilibrium one. In the literature such a wall is often known as *local equilibrium* wall. Finally, a *partially catalytic* wall promotes just a partial recombination and sits in between the other two definitions.

Thanks to a catalytic wall model, it is possible to determine the rate of production or destruction of each species due to the surface reactions by summing up over all the elementary reactions. Since diffusion is the mechanisms that feeds particles from the gas to the surface, at steady state the net amount of species i produced or destroyed by catalytic reactions has to be balanced by the diffusion flux:

$$\boldsymbol{J}_i|_w \cdot \boldsymbol{n}_w = \dot{\omega}_i^{(cat)}. \tag{1.22}$$

A possible approach to define the wall production rate $\dot{\omega}_i^{(cat)}$ is by assuming that the impinging species recombine with a certain recombination probability γ_i, also called effective catalytic recombination property (in the following, it will be often referred to as catalytic coefficient), defined as the ratio between the number flux of the i-th species recombining at the surface $\mathcal{M}_i^{rec}$ and the number flux of the imping at the surface $\mathcal{M}_i^{(in)}$:

$$\gamma_i = \frac{\mathcal{M}_i^{(rec)}}{\mathcal{M}_i^{(in)}}. \tag{1.23}$$

Since the net flux $\boldsymbol{J}_i|_w \cdot \boldsymbol{n}_w$ is equal to the difference between the impinging flux and the flux leaving the surface $\mathcal{M}_i^{(out)}$, multiplied by the species mass m_i, we have that

$$\begin{aligned}\dot{\omega}_i^{(cat)} &= m_i\big(\mathcal{M}_i^{(in)} - \mathcal{M}_i^{(out)}\big) = m_i\big(\mathcal{M}_i^{(in)} - (\mathcal{M}_i^{(in)} - \mathcal{M}_i^{(rec)})\big) \\ &= \gamma_i m_i \mathcal{M}_i^{(in)}.\end{aligned} \tag{1.24}$$

Kinetic theory provides an expression for the impinging flux $\mathcal{M}_i^{(in)}$, thanks to the Chapman-Enskog method:

$$\mathcal{M}_i^{(in)} = n_i\sqrt{\frac{kT_w}{2\pi m_i}} + \frac{1}{2m_i}\boldsymbol{J}_i|_w \cdot \boldsymbol{n}_w\ , \tag{1.25}$$

where T_w is the wall temperature, n_i the species number density and k the Boltzmann constant.

1.3.2 Ablative material: ablation

Non-reusable thermal protection materials constituting the heat shield of an entering vehicle are normally subject to the ablation phenomenon [Lachaud *et al.*, 2011]. This means that the virgin material, as heated, undergoes thermal degradation, caused by sublimation and pyrolysis, and ultimately recession. On the other hand, the ablation process is able to divert a significant part of the convective and radiative heat flux away from the heat shield.

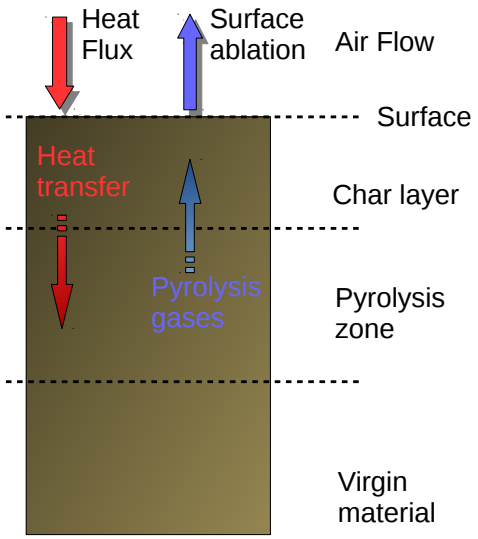

Figure 1.7: Simple graphical representation of the ablation phenomenon.

Figure 1.7 simply resumes the main physical aspects related to the ablation of a sacrificial heat shield material [Moyer et Rindal, 1968]. In the pyrolysis zone, the virgin material (or rather one or more components of the original composite) thermally decomposes and progressively carbonizes, releasing pyrolysis gases and leaving a porous residue, which for most materials of interest is a carbonized char. The pyrolysis gases released by solid pyrolysis convect and diffuse to the surface through the porous char. Reactions within the pyrolysis gaseous mixture and between pyrolysis gases and the char may take place, with possible effects like erosion or deposition of an additional residue upon it (so called coking phenomenon). Further reactions of the pyrolysis gases with boundary layer gases may occur when boundary layer gases penetrate into the pores of the charred material by forced convection or due to fast diffusion at low pressures. In the ablation zone at the surface, the charred

material is removed by ablation and the initial surface recedes. Depending on entry conditions, ablation can be caused by chemical reactions, phase change, or mechanical erosion.

The complete physical and mathematical description of porous ablative materials is quite complex, and here we will give only the basic volume-averaged conservation equations. Their form is somehow related with the one of conservation equations presented for hypersonic flows, but additional terms account for the effect of fluid motion in porous media and reactions between solid and gaseous phases. More details about the description of the phenomena can be found in [Lachaud *et al.*, 2011; Moyer et Rindal, 1968]. Let us take into account a carbon-phenolic low-density ablating material, and let us assume that it is composed by three phases: solid carbon fibers, solid phenolic matrix and gaseous phase in the pores produced by pyrolysis. The mass conservation for gaseous phase can be written as:

$$\frac{\partial}{\partial t}(\epsilon_g \rho_g) + \nabla \cdot (\epsilon_g \rho_g \mathbf{u}_g) = \Pi \,, \tag{1.26}$$

where ρ_g is the gas density, ϵ_g its volume fraction and $\mathbf{u}_g$ the average gas velocity. The pyrolysis gas production term Π is usually obtained by fitting experimental data with Arrhenius laws, like the ones presented in (1.15) and (1.17). The species conservation for the gaseous phase equation, expressed in terms of mass fractions y_i for each one of the s species, reads:

$$\frac{\partial}{\partial t}(\epsilon_g \rho_g y_i) + \nabla \cdot (\epsilon_g \rho_g y_i \mathbf{u}_g) + \nabla \cdot \boldsymbol{J}_i = \pi_i M_i + \epsilon_g \omega_i M_i \,, \tag{1.27}$$

with $\boldsymbol{J}_i$ the diffusion flux of the i-th species, π_i the production of the i-th species, M_i its molar mass and ω_i the production term due to reactions between pyrolysis gases. Solid phase mass conservation is used to compute the effective density of the matrix, after changes due to pyrolysis, and it is modeled in the following way:

$$\frac{\partial}{\partial t}(\epsilon_m \rho_m) = -\Pi \,, \tag{1.28}$$

with ρ_m is the solid matrix density and ϵ_m its volume fraction. The momentum conservation in porous media is used to obtain the average gas velocity:

$$\mathbf{u}_g = -\frac{1}{\epsilon_g \mu} \frac{1 + \beta/p}{1 + Fo} \underline{\underline{K}} \cdot \nabla p \,, \tag{1.29}$$

where μ is the viscosity, β the Klinkenberg coefficient to account for slip effects at the pore scale when the Knudsn number is not small, p the pressure, Fo the Forchheimer number that accounts for high velocity effects at the pore scale, $\underline{\underline{K}}$ the second-order permeability tensor, for the general case of anisotropic

material. Finally, energy conservation, under the assumption of thermal equilibrium between gaseous and solid phases, can be written as

$$\frac{\partial}{\partial t}(\rho_a e_a) + \nabla \cdot (\epsilon_g \rho_g h_g \mathbf{u}_g) + \nabla \cdot \sum_{i=1}^{s} h_i \boldsymbol{J}_i = \\ = \nabla \cdot (\underline{\underline{\lambda}} \cdot \nabla T) + \mu \epsilon_g^2 (\underline{\underline{K}}^{-1} \cdot \mathbf{u}_g) \cdot \mathbf{u}_g \ , \qquad (1.30)$$

where e_a is the energy of the whole ablative material, written as $\rho_a e_a = \epsilon_g \rho_g e_g + \epsilon_m \rho_m h_m + \epsilon_f \rho_f h_f$, with h the enthalpy and the subscript f referring to the non-pyrolyzing fibers. T is the temperature and $\underline{\underline{\lambda}}$ the second order conductivity tensor, accounting for conductivity in the solid, in the gas and effective radiative heat transfer.

The coupling between the fluid flow and surface ablation is important to accurately predict surface thermal loads [Gnoffo *et al.*, 2009], but at the same time is quite complex and computationally expensive. The accounting of ablation phenomena and their coupling with the hypersonic fluid flow is beyond the purposed of this work. However, the sensitivity analysis of the temperature of an ablating material with respect to uncertainties in the parameters describing the material itself will be used as an application case to test one of the uncertainty quantification tools developed in this work. The application will be briefly described in Section 1.6.3.

1.4 COSMIC code

The governing equations for a mixture of reacting gases, as presented in Section 1.2, are a set of hyperbolic-parabolic partial differential equations. They can be rewritten in compact form as

$$\frac{\partial r^\epsilon \boldsymbol{U}}{\partial t} + \nabla \cdot (r^\epsilon F) + \nabla \cdot (r^\epsilon H) = r^\epsilon \boldsymbol{S} \ , \qquad (1.31)$$

where $\boldsymbol{U} = (\rho, \rho_i, \rho u, \rho v, \rho E)$ is the vector of conserved variables, F are the convective fluxes, H the transport fluxes and $\boldsymbol{S}$ the source terms, respectively defined as:

$$F = \begin{bmatrix} \rho u & \rho v \\ \rho_i u & \rho_i v \\ \rho u^2 + p & \rho v u \\ \rho u v & \rho v^2 + p \\ (\rho E + p) u & (\rho E + p) v \end{bmatrix} \quad \boldsymbol{S} = \begin{Bmatrix} 0 \\ \dot{\omega}_i \\ 0 \\ 0 \\ 0 \end{Bmatrix}$$

$$H = \begin{bmatrix} 0 & 0 \\ \rho_i \mathcal{V}_{i_x} & \rho_i \mathcal{V}_{i_y} \\ -\tau_{xx} & -\tau_{yx} \\ -\tau_{xy} & -\tau_{yy} \\ -\tau_{xx} u - \tau_{xy} v + q_x & -\tau_{yx} u - \tau_{yy} v + q_y \end{bmatrix} .$$

The term r^ϵ, with $\epsilon = 0$ for bi-dimensional flows and $\epsilon = 1$ for axisymmetric ones, is used to automatically account for the modifications to the equations when changing coordinate system. The set of equations we have to solve is very complex, and in practical applications it is impossible to find analytical solutions. Therefore we have to rely on a numerical method implemented in a computer code to simulate the flow. At this purpose, in this work we use the code COSMIC [Barbante, 2001] from Von Karman Institute for Fluid Dynamics, which contains implementations of different finite volumes numerical schemes to simulate 2D or axisymmetric reacting flows. It is coupled with the library Pegase [Bottin *et al.*, 1999] for the computation of the thermodynamic and transport properties of the reacting mixture. In the following, some details about the COSMIC code and the used numerical schemes are reported.

Note that, in this work, we are only interested in steady state solutions of the flow. Nevertheless, the equations are kept unsteady and the simulation is run until the steady state, because in this way the governing equations are always hyperbolic-parabolic and a unique numerical technique can be used for their solution.

1.4.1 Numerical schemes

Since we are interested in hypersonic applications, where the flow field is characterized by a strong shock in front of the object, it is better to use a numerical method which is based on the integral form of the equation, rather than on the differential one in equation 1.31. This is because the differential form is valid only if the solution is continuous and differentiable, while the integral form admits also *weak solutions* with the presence of discontinuities (as shocks). The integral formulation of the governing equation is obtained by integrating equation 1.31 on the fixed domain and applying the Gauss theorem on the terms containing a divergence:

$$\frac{\partial}{\partial t}\int_\Omega r^\epsilon \boldsymbol{U}\,\mathrm{d}\Omega + \int_\Gamma r^\epsilon F\cdot\boldsymbol{n}\,\mathrm{d}\Gamma + \int_\Gamma r^\epsilon H\cdot\boldsymbol{n}\,\mathrm{d}\Gamma = \int_\Omega r^\epsilon \boldsymbol{S}\,\mathrm{d}\Omega\,, \tag{1.32}$$

where Ω is the computational domain, $\Gamma = \partial\Omega$ its boundary and $\boldsymbol{n}$ the normal. This equation is mathematically equivalent to eq. 1.31 for continuous solutions, but it admits also discontinuous solutions. From this integral form of the governing equations, it is possible to introduce the spatial and time numerical discretizations.

Spatial discretization: Finite Volumes

The integral form of governing equations 1.32 is discretized with the finite volumes technique. First of all, consider a structured computational grid discretizing the domain, like in Figure 1.8. Then equation 1.32 can be applied to

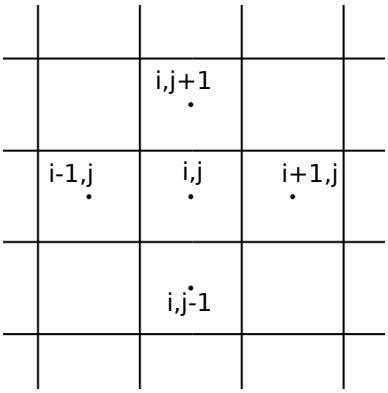

Figure 1.8: Example of structured mesh.

each cell composing the grid, indicated with the indices i and j.

$$r_{ij}^{\epsilon}\Omega_{ij}\frac{\partial U_{ij}}{\partial t}+\sum_{k=1}^{4}\int_{\Gamma_{ij}^{k}} r_{k}^{\epsilon}F_{k}\cdot\boldsymbol{n}_{k}\,\mathrm{d}\Gamma_{ij}^{k}+\sum_{k=1}^{4}\int_{\Gamma_{ij}^{k}} r_{k}^{\epsilon}H_{k}\cdot\boldsymbol{n}_{k}\,\mathrm{d}\Gamma_{ij}^{k}=\int_{\Omega_{ij}} r^{\epsilon}\boldsymbol{S}\,\mathrm{d}\Omega_{ij}\ , \tag{1.33}$$

where the unknowns U_{ij} are the average values of the conserved quantities on each cell. The surface integrals have been replaced by the sum over the four faces constituting the interfaces of each cell. The spatial numerical discretization consists then in finding suitable expressions for the convective and the transport fluxes across the cell interfaces and for the volume integral of the source term.

The discretization of the transport fluxes and the source terms is quite straightforward, and involves for example, the discretization of the gradients of some variables at the cell interface and the details can be found in [Barbante, 2001].

The convective fluxes, instead, are more difficult and delicate to discretize. In fact they are nonlinear, and this nonlinearity is responsible for the appearance of shocks in the solution. A good numerical method has to capture the shock accurately in a monotone way, *i.e.* without generating numerical oscillations. For the discretization of convective fluxes, two of the numerical schemes implemented in COSMIC are used: Hybrid Upwind Splitting (HUS) and Artificially Upstream Flux vector Splitting (AUFS) schemes.

Hybrid Upwind Splitting scheme

The Hybrid Upwind Splitting (HUS) scheme [Coquel et Liou, 1995] is an attempt of combining rigorously the two families of flux difference schemes (FDS) and flux vector splitting (FVS) schemes (see for example [LeVeque, 2002, Chapter 4] for more details about the definition of the two families) with the aim to

create a scheme that keeps only the good properties of the two families. The combination of a FDS and a FVS scheme is done at the level of the determination of the numerical convective flux: the FDS scheme takes care of the contact discontinuity and the FVS scheme of the shocks or of the rarefaction waves. In the code COSMIC, the hybridization of Van Leer [Van Leer, 1979, 1982] and Osher [Osher et Solomon, 1982] schemes has been used.

If we call $\mathcal{F}_{HUS}(U_L, U_R)$ the approximated numerical flux for the HUS scheme, that is a function of the conserved variable vector U_L and U_R at the left and right state, meaning at the two cells sharing the considered interface, its expression can be written as:

$$\mathcal{F}_{HUS}(U_L, U_R) = \underbrace{\mathcal{F}^+_{VL}(U_L) + \mathcal{F}^-_{VL}(U_R)}_{\text{Van Leer scheme}} + \begin{cases} \mathcal{F}^-_{VL}(U^*_L) + \mathcal{F}^-_{VL}(U^*_R) & \text{if} \quad V^*_n > 0 \\ -\mathcal{F}^+_{VL}(U^*_L) + \mathcal{F}^+_{VL}(U^*_R) & \text{otherwise} , \end{cases} \tag{1.34}$$

where $\mathcal{F}^+_{VL}(U_L)$ and $\mathcal{F}^-_{VL}(U_R)$ are the split fluxes of the Van Leer scheme. The HUS scheme has the following interpretation: it is basically equal to the Van Leer scheme plus an anti-diffusive term expressed in term of the Van Leer flux. The anti-diffusive contribution allows the exact capturing of contact discontinuities and the good resolution of boundary layers and, thus, a good computation of the thermal loads. The scheme requires the determination of the intermediate points U^*_R and U^*_L and the corresponding velocity normal to the interface V^*_n, this is done by means of the Riemann invariants (see [Barbante, 2001, Chapter 3.5] for more details).

MUSCL approach The numerical method described up to now is only first order accurate, because the left and right states correspond to the cell center values. However, the use of a higher order scheme is very handy to obtain an accurate solution while reducing the computational cost. As observed by [Van Leer, 1977], it is possible to build a higher accuracy scheme by replacing the left and right states constant on the cells with a piecewise polynomial representation. In particular, a piecewise linear representation is second order accurate, a quadratic representation third order accurate and so on. This procedure of generating higher order upwind schemes via variable extrapolation is called MUSCL approach (Monotone Upstream-centred Schemes for Conservation Laws). In Cosmic, we are using second order accurate numerical schemes.

TDV approach and limiters The MUSCL extrapolation method is able to produce a higher accuracy scheme, but it has also the drawback of allowing the appearance of spurious oscillations in the solution, especially across shocks. The reason is related to the fact that the interpolated value of U depends on the difference of the solution between different cells (or the gradient in a

broader sense), and this can cause problems near discontinuities, where the gradients tends to infinity. Therefore, oscillations can be avoided by a suitable limitation of the gradients. The idea is to switch on the limiter in regions of strong gradients, thus preventing oscillations, at the price of reducing the local accuracy to roughly first order, and to switch it off in regions of smooth flow, to recover second order accuracy. A criteria for the definition of the limiting functions is given by the Total Variation Diminishing (TVD) approach [Hirsch, 1990]. In particular, in the simulations performed with COSMIC, we will use a Van Albada limiter [Van Albada *et al.*, 1982].

Carbuncle fix Most numerical schemes have been originally developed for 1D conservation laws, and then extended to 2D and 3D by projecting the solution along the normal to the interface and computing the 1D fluxes along this direction. In 1D configurations usually the schemes behave in a physically correct way for a wide range of conditions. However, when extended to two or more dimensions, some pathologic behaviors may appear [Quirk, 1994]. One of these pathologies, the so-called *carbuncle phenomenon*, appears when computing high Mach number flows over blunt body configurations. Therefore it is of main relevance in this work. The carbuncle phenomenon is an alteration of the flow characterized by an area of recirculation near the stagnation point and a protrusion of the bow shock which, therefore, appears oblique near the stagnation line [Sermeus, 2013, Chapter 6]. This phenomenon shows up with most shock-capturing schemes that are able to exactly capture a contact discontinuity [Pandolfi et D'Ambrosio, 2001]. Instead, FVS schemes, such as Van Leer scheme, and shock-fitting schemes [Paciorri et Bonfiglioli, 2009] are free of carbuncle.

In COSMIC, an empirical ad-hoc shock-fix for the HUS scheme is implemented to prevent the appearance of carbuncle. Since the basic Van Leer scheme is free of carbuncle, the shock-fix is obtained by multiplying the anti-diffusive contribution by a suitable coefficient which has to be less than one when a shock parallel to the grid is detected [Barbante, 2001, Section 3.7].

AUFS scheme

Another numerical scheme implemented in the COSMIC code and used in some parts of this work is the Artificially Upstream Flux vector Splitting (AUFS) scheme by [Sun et Takayama, 2003]. This is an accurate FVS scheme that is able to exactly resolve stationary 1D contact discontinuities, and it avoids the carbuncle problem in multi-dimensional computations. In this work, a modified preconditioned version of the AUFS scheme, recently developed and implemented by [Bellas-Chatzigeorgis *et al.*, 2017], has been used.

Time discretization

After having introduced the spatial discretization for all the terms, equation (1.33) is reduce to a system of first-order ordinary differential equations in time:

$$\frac{\partial \boldsymbol{U}_{ij}}{\partial t} = -\frac{1}{r^{\epsilon}_{ij}\Omega_{ij}}\boldsymbol{R}_{ij}(\boldsymbol{U}) \,, \tag{1.35}$$

where $\boldsymbol{R}_{ij}$ is called the residual, and it consists in the sum of all the fluxes and source terms for the cell i, j. For a steady state computation, no interest is given to the transient and the time evolution is just a convenient way of preserving the same mathematical characteristics for the governing equations through all Mach numbers. Therefore, the objective is to decrease the residual to zero as quickly as possible.

For this reason, in this work only an implicit scheme is used for time discretization, meaning that both terms of equation (1.35) are taken at the same time level. Hence, after having discretized the time derivative, the solution is found by solving a nonlinear system, since the residual $\boldsymbol{R}_{ij}$ is nonlinear in the unknown. More details about the implicit time solver implemented in COSMIC can be found in [Barbante, 2001, Chapter 3.9].

1.5 Mesh adaptation for CFD simulations

Practitioners and experts of hypersonic flows simulations know the importance of using a good computational grid in order to obtain accurate results. Often, a good computational grid is the result of some grid adaptation tool but also of the expertise and the monitoring of an expert user [Saunders *et al.*, 2007; Candler *et al.*, 2009].

As it will be more clear from Chapter 2, to perform an uncertainty quantification study on a computational model, it is necessary to evaluate some output quantity at several (also thousands) configurations of the uncertain variables. This translates in having to perform many simulations with different values of input parameters, for example of freestream values. It is clear, that in this case, the monitoring of the convergence of the solution is much more difficult, and it can be impossible to think about doing non-automated interventions to improve the quality of the mesh. However, for uncertainty quantification it is very important to have sufficiently accurate and reliable evaluations of the outputs, otherwise fluctuations caused by numerical errors could be misinterpreted as variations due to input uncertainties.

Note that uncertainty propagation through a CFD code is often performed by using a fixed mesh, since a converged mesh in nominal conditions can be reasonably considered as converged also if some variations of the operating conditions are taken into account. This approach is usually sufficient in the absence of shock waves and in non-hypersonic flows [Kawai et Shimoyama, 2014;

Salehi *et al.*, 2017], but it has been used also for hypersonic flows [Hosder *et al.*, 2006; Constantine *et al.*, 2015]. However, as it will be shown in the following, this can yield highly inaccurate results in hypersonic reacting flows over blunt bodies. In fact, in the numerical simulation of hypersonic flows by means of a second-order accuracy cell-centered finite-volume discretization method, and in general of shock-capturing methods, it is known that a proper alignment between the shock and the discretization grid is essential to get a meaningful solution [Bonfiglioli *et al.*, 2013; Onofri *et al.*, 2011]. As suggested in [Bonfiglioli *et al.*, 2013], the main cause of poor heating predictions is thought to be lack of a truly multidimensional shock-capturing scheme, able to produce solutions that are insensitive to the relative orientation of the control volume faces with respect to the shock. This becomes especially more challenging for UQ applications, where, to make the required simulations more affordable, one would prefer using grids that are automatically generated and not excessively refined. However, in when considering uncertainties on some input parame-

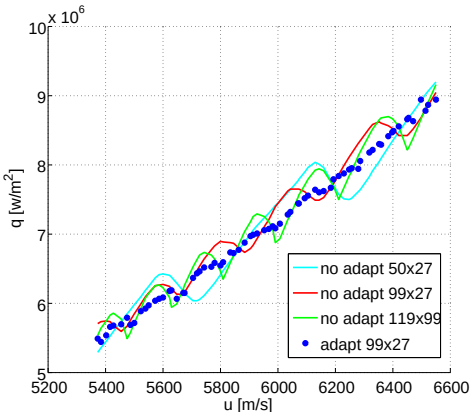

Figure 1.9: Example of problem caused by using a fixed nominal mesh when perturbing the freestream conditions: stagnation heat flux for the HEG cylinder (Sec. 1.6.1) versus 10% variation of the freestream velocity. Results obtained with COSMIC using second order HUS scheme with Van Albada limiter and carbuncle fix. Comparison between different fixed grids and mesh adaptation.

ters, the values of freestream conditions, such as freestream velocity, may be subject to variations, which leads to different shock stand-off distances for each sample of input parameters. This can lead to a mesh/shock misalignment and bad simulation results, causing poor heat flux trends, as clearly noticeable in figure 1.9. From this same figure, it can be noticed that using a more refined nominal mesh for all the simulations at different input values does not solve this problem, at least for the computational code employed in this work. But it is essential to adopt a simple mesh adaptation technique to realign the shock

to the mesh for each different freestream configuration.

Different solutions for mesh adaptation in case of shock-capturing simulations have been proposed in the literature [Hartmann et Houston, 2002; Wang et Mavriplis, 2009; Frauholz *et al.*, 2012], which are meant to be used with different numerical approaches than the one adopted in this work, and which are able to work in complex configurations. Here we describe briefly the adaptation technique adopted in this work,which is a very simple tool that uses basic algorithms well-known to practitioner in the hypersonic flows field. However, it is important to stress out the fact that here the process needs to be automated and can not be directly monitored by the user, because several simulations need to be run. The different steps of the algorithm used for computations of the HEG cylinder configuration with the HUF numerical scheme are summarized in Algorithm 1. A first solution is computed on the nominal

Algorithm 1 Mesh adaptation algorithm to automatically ensure a good alignment between the shock and the mesh.

Starting from a nominal mesh and a starting solution computed at nominal condition,

1. Compute a CFD solution with the value of input parameters for a specific sample in the stochastic space
2. Find the shock position by looking at the jump in Mach number in the flow field
3. Adapt the mesh solving the solution of 1D linear elasticity equations along the radial directions, imposing a rigid constraint on a row of nodes corresponding to the shock position, and also at the wall surface and outer bound shape

Repeat this steps until the maximum number of iterations is reached.

mesh, and the shock position is found by looking at the Mach number in the flow field. Then, the adaptation is performed by solving 1D linear elasticity equations along the radial directions. The alignment to the shock is enforced by imposing a rigid constraint on a row of nodes corresponding to the shock position, and also the wall surface and outer bound shape are constrained in the same way. No forcing is considered. If a small refinement near the shock is needed, two rows of nodes are added by splitting existing cells close to the shock during the first iteration.

Axisymmetric simulations of the flow around the forebody of the EXPERT entry vehicle (see Section 1.6.2) have instead been performed using the AUFS numerical scheme. A slightly different adaptation strategy empirically proved to be more suitable for this case: after a first computation on the nominal mesh, the computational grid is refined around the shock position, and successively

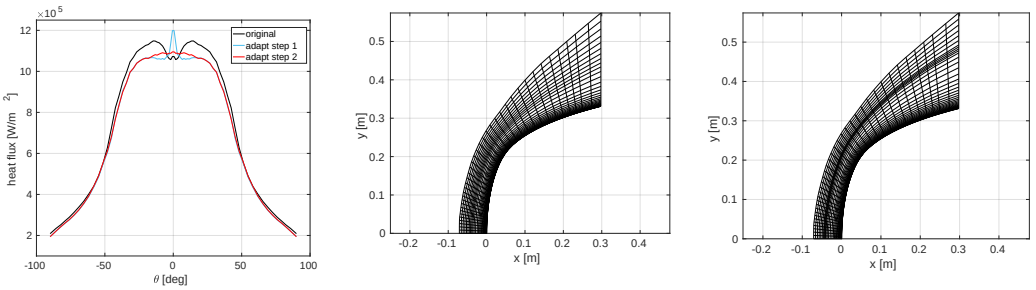

(a) (b) (c)

Figure 1.10: Surface heat flux prediction for the EXPERT vehicle (a). Notice that the original computational grid and the one generated by the first adaptation steps present bad solutions, especially in the region near the stagnation, while the last adaptation shows a better trend, with just some small local oscillations. Original (b) and final (c) computational grid are shown too.

regularized by means of a laplacian smoothing, without changing the position of the boundary layer and near-shock cells. Then a second computation is performed on the new grid, following by one iteration of Algorithm 1, in order to obtain the final grid for the considered input parameters combination.

1.6 Description of the application cases

In this section, three application cases are described. They will be used in the following parts of this work to test some of the developed tools for Uncertainty Quantification and Bayesian inference. The first is about the simulation of the hypersonic flow past a cylinder in an experimental configuration. The second instead, represents a real entry configuration for the EXPERT vehicle. Finally, an ablation problem of the TACOT material is presented.

1.6.1 HEG cylinder

This first application case deals with the hypersonic high-temperature reacting flow around a cylinder. The reference configuration chosen in this work is the experimental configuration used at the HEG facility (High Enthalpy shock tunnel Göttingen), which has been described and tested in [Karl *et al.*, 2003]. It has also been used in [Knight *et al.*, 2012] to assess and compare the prediction capabilities of different CFD codes. An image of the experimental setup is reported in Figure 1.11. The nominal freestream conditions chosen for the numerical simulations are the ones referred to as *HEG I configuration* in [Knight *et al.*, 2012], and they are reported in Table 1.2. The simulation

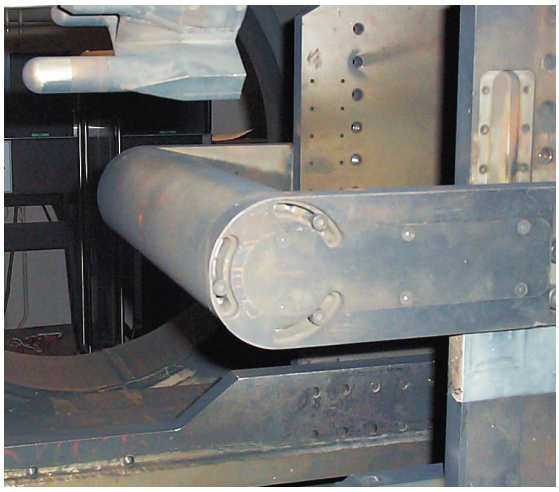

Figure 1.11: Image of the cylindrical experimental model in the HEG facility (taken from [Karl *et al.*, 2003]).

problem consists in computing the quantities of interest, namely the pressure p_{st} and heat flux q_{st} at the stagnation point,

The set of governing equations and physico-chemical models used to describe the phenomena is the one described in Section 1.2. Two-dimensional Navier-Stokes equations are combined with the chemical mechanism introduced by Park et al. [Park *et al.*, 2001] applied to a mixture of five species air (N, O, NO, N_2 and O_2). Five species are sufficient to represent the main chemical phenomena involved in the flow for the considered configuration, as will be motivated in Section 3.6.1. To obtain the numerical results, we use the numerical method described in Section 1.4, in particular the HUS scheme with carbuncle fix, together with the mesh adaptation technique in Section 1.5 used to obtain meaningful results. Figure 1.12a shows an example of solution temperature field together with a label for each boundary. Supersonic inflow and outflow boundary conditions are imposed respectively on boundaries 1 and 2. On boundary 3, a solid wall with no-slip condition boundary is imposed. Furthermore, the catalyticity of the vehicle surface is taken into account, and it is modeled as a catalytic wall at imposed wall temperature T_w, with recombination coefficient $\gamma = 1$. Finally, on boundary 4 a planar symmetry condition is imposed.

Verification and validation

The COSMIC code has been extensively tested in [Barbante, 2001]. Here, a further test is proposed on the HEG cylinder configuration, especially to check the grid refinement and the mesh adaptation technique.

A structured mesh of 99×26 cells has been chosen as nominal grid. The

Quantity	Value
u_∞ [m/s]	5956
ρ_∞ [kg/m^3]	1.547e-3
p_∞ [Pa]	476
T_∞ [K]	901
M_∞	8.98
$Y[N_2]_\infty$	0.75430704
$Y[O_2]_\infty$	0.00713123
$Y[NO]_\infty$	0.01026010
$Y[N]_\infty$	6.5e-7
$Y[O]_\infty$	0.22830098
T_w [K]	300

Table 1.2: Nominal freestream conditions and wall temperature for the simulation configuration.

number of nodes should be a good compromise between solution accuracy and computational efficiency, since the simulation needs to be repeated several times for the UQ study. Figure 1.13 shows the comparison of a zoom between the starting nominal mesh close to the symmetry axis and the same area of the mesh adapted for input conditions corresponding to one of the samples in the stochastic space. One example of the solution temperature field obtained at the end of the adaptation process is shown in figure 1.12a together with the temperature profile on the stagnation line in figure 1.12b.

To assess the effectiveness of the mesh adaptation algorithm, several computations are repeated by perturbing the freestream velocity, which is assumed to vary randomly in the interval of $\pm 10\%$ of its nominal value. Three steps of the mesh adaptation algorithm are performed for each input condition starting from the nominal mesh. The obtained evolution of the pressure and heat flux at the stagnation point is plotted with respect to the freestream velocity (Figure 1.14). Furthermore, we compare the results obtained with adaptation with the ones of different fixed meshes. Note that the comparison is done also with computations performed on 119×99 mesh, which is a mesh size used in [Knight *et al.*, 2012]. Finally, also results obtained with first-order HUS scheme are compared. From the comparison (Figure 1.14b), it can be observed the necessity to adapt the mesh over each different condition, while the use of a fixed mesh yields a large numerical error and wrong heat flux trends. Instead, as known, the stagnation pressure is much less affected by this issue (Figure 1.14a). Also the first-order solution does not present the numerical oscillations, but its accuracy is not sufficient for a grid of this size. As a consequence, it is possible to state that the Algorithm 1 allows an automatic mesh adaptation, and the highest influence on the output value is caused by the proper align-

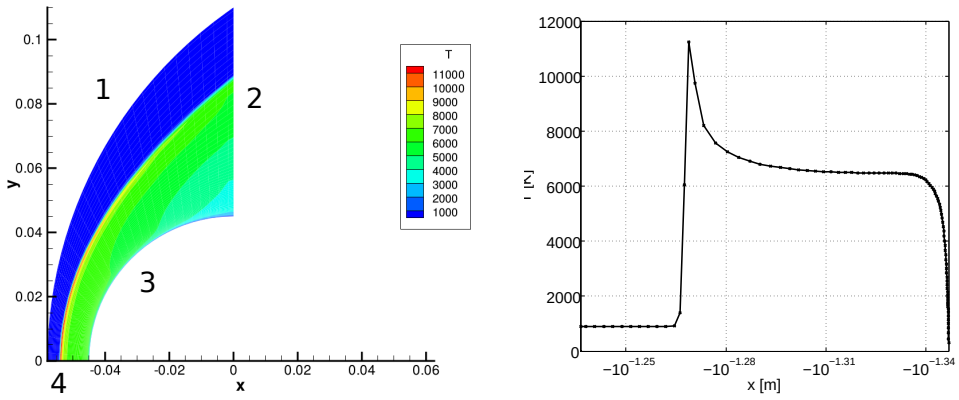

(a) Temperature field (b) Temperature

Figure 1.12: Solution temperature field (a) around the cylinder computed on the adapted mesh and temperature profile (b) on the stagnation line.

ment between the shock and the grid, rather than the grid refinement itself. From these results, it is possible to estimate that the numerical error due to mesh alignment associated to the output value of the heat flux is contained in the ±2% interval. An example the comparison of heat flux solution on the cylinder surface before and after mesh adaptation is shown in figure 1.15. A non negligible difference in heat flux values, especially close the stagnation point, is noticeable.

Furthermore, a comparison with the experimental data presented in [Karl *et al.*, 2003; Knight *et al.*, 2012] is used to validate the simulations at nominal conditions. The nominal mesh with three steps of the adaptation algorithm is used to compute the solution. In Figure 1.16, the pressure and heat flux at the wall of the cylinder are compared with experimental data. For the sake of comparison, for the heat flux some simulations from [Knight *et al.*, 2012] are reported too, together with a computation performed with COSMIC code on a finer 119x99 mesh. It can be noticed that the agreement is very good for the pressure, and quite good for the heat flux, but worse than the pressure, as expected due to the known difficulties in the simulation of the heat flux at the wall for hypersonic flows. Other codes, such as the one of Nompelis [Knight *et al.*, 2012] show better performance, while the refined mesh does not improve substantially the result. However, results can be considered satisfying, especially near the stagnation, which is where we will focus for the UQ study.

Characterization of the uncertainties

For this study case, aleatory uncertainties have been considered on the freestream conditions and also on parameters of the chemistry model. In particular, the

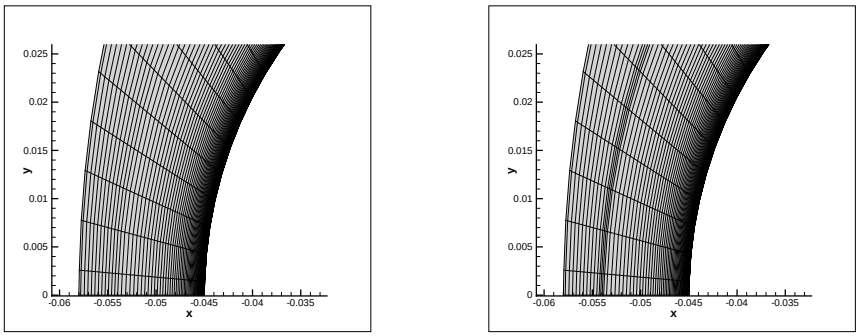

(a) Starting mesh (b) Adapted mesh

Figure 1.13: Comparison between a zoom of the starting nominal mesh close to the symmetry axis (left) and the same area of the adapted mesh for one of the training points (right).

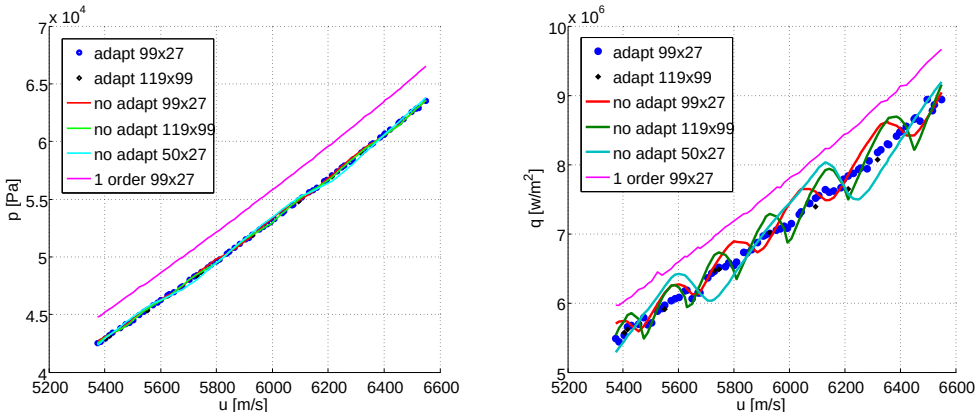

(a) Pressure (b) Heat flux

Figure 1.14: Comparison between numerical results obtained with grids of increasing size, to test the mesh convergence.

freestream density and velocity have been considered uniformly distributed on a $\pm 20\%$ interval around the nominal condition, as described in Table 1.3. These uncertainties have been chosen quite arbitrarily, and they mainly constitute a prior belief of a relatively wide range of possible values for these two inputs, as their calibration is proposed in Chapters 3 and 5 by means of Bayesian calibration.

Concerning the air chemical model, seventeen (17) uncertain variables are considered for this test case, which are the pre-exponential factors A_r of the Arrhenius rate coefficients k_r of all the reactions constituting the chemical mechanism. Other parameters, such as the activation energy, are supposed to

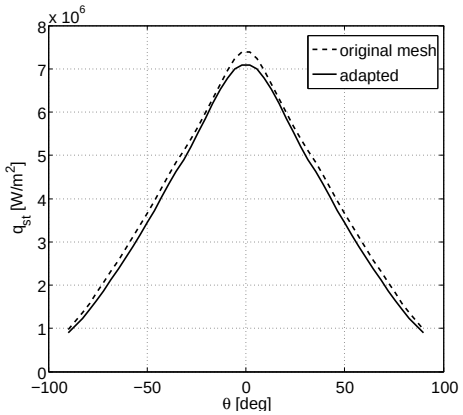

Figure 1.15: Solution heat flux around the cylinder surface computed on the original mesh compared to the one obtained at the end of the adaptation profile, for a speed of 5929 m/s.

Variable	Distribution	Minimum	Maximum
ρ_∞, kg/m^3	Uniform	$1.237 \cdot 10^{-3}$	$1.856 \cdot 10^{-3}$
u_∞ m/s	Uniform	4764.8	7147.2

Table 1.3: Uniform uncertainties on freestream conditions for the HEG cylinder.

be known with a higher accuracy and so are considered fixed to their nominal values. Pre-exponential factors are supposed to be distributed with a log-normal distribution (as in [Bose *et al.*, 2004; Bellas-Chatzigeorgis *et al.*, 2013]) centered on their mean values and standard deviations given in Table 1.4. This corresponds to a normal uncertainty on their exponent. Later, in Section 3.6.1, a preliminary sensitivity study is used to reduce the number of chemistry uncertainties for the HEG cylinder, and finally, in the CFD-based uncertainty analysis, only the six most influent pre-exponential factors uncertainties will be kept.

Another source of uncertainty in the problem of freestream calibration is related with the experimental measurement errors associated to pressure and heat flux data at the stagnation point. Experimental data are here considered to be affected by Gaussian noise, as it will be more clear in Chapter 2. The standard deviation model for the stagnation pressure noise is $\sigma_p = 0.02\, p^*_{\text{st}}$, and the standard deviation model for stagnation heat flux is $\sigma_q = 0.1\, q^*_{\text{st}}$; where p^*_{st} and q^*_{st} are the measured values. The differences in noise levels model the engineers' trust in the sensors for pressure and heat flux; in other words, we expect roughly 2% error in pressure measurements and 10% error in heat flux measurements.

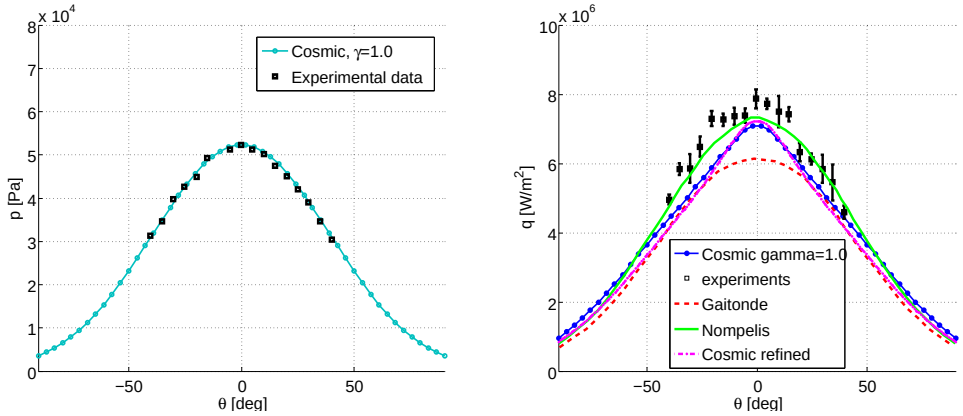

(a) Pressure (b) Heat flux

Figure 1.16: Comparison between numerical and experimental data for the nominal conditions.

1.6.2 EXPERT vehicle

The second application proposed in this work is about the atmospheric entry flow around the forebody of the EXPERT (European eXPErimental Reentry Testbed) vehicle from the European Space Agency [Muylaert *et al.*, 2007; Thoemel *et al.*, 2009]. We focus on the part of the entry trajectory where the hypothesis of continuum regime is valid. Two specific points of the en-

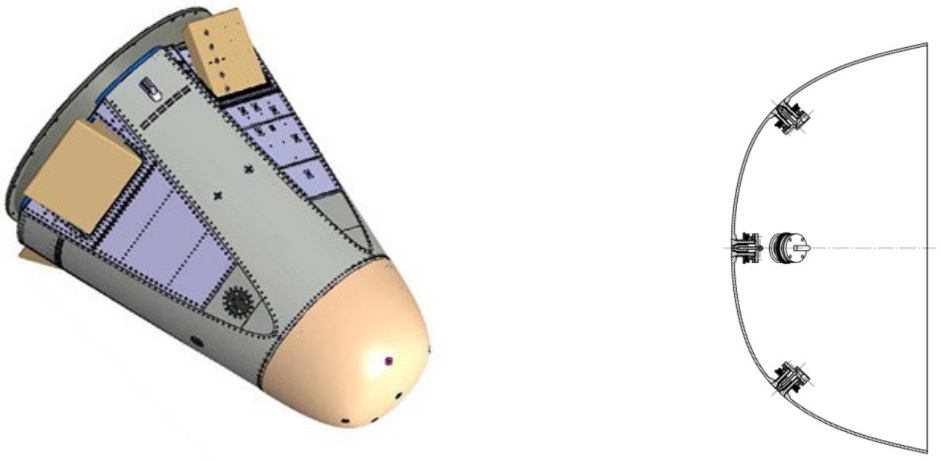

(a) (b)

Figure 1.17: Representation of th EXPERT vehicle and detail about the location of the nose sensors.

Variable	Reaction	Deviation σ
1-3	$N_2 + M \rightarrow 2N + M$ where $M = N_2, NO, O_2$	0.11
4,5	$N_2 + M \rightarrow 2N + M$ where $M = O, N$	0.15
6-10	$O_2 + M \rightarrow 2O + M$ where $M = N_2, NO, O_2, O, N$	0.10
11-15	$NO + M \rightarrow N + O + M$ where $M = NO, N, O, N_2, O_2$	0.12
16	$N_2 + O \rightarrow NO + N$	0.10
17	$NO + O \rightarrow O_2 + N$	0.10

Table 1.4: Standard deviations of the pdfs for the reaction rate coefficients preexponential factors.

try trajectory are considered for the freestream calibration (see Figure 1.18). The first, at a higher altitude, known to exhibit chemical non-equilibrium effects, while the second, situated in a lower part of the trajectory, close to the peak heating point, where the chemistry tends to be at equilibrium. Nominal freestream conditions for both trajectory points are reported in Table 1.5

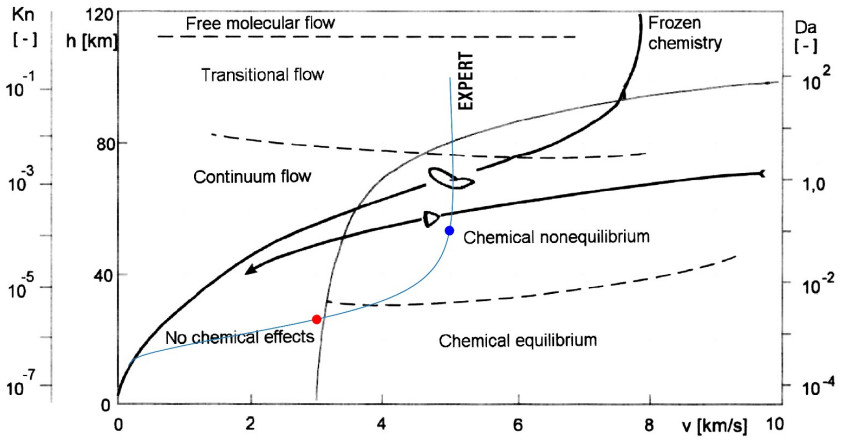

Figure 1.18: Aerodynamic and kinetic flow regimes in the altitude-velocity map (from [zur Nieden et Olivier, 2007]), with, in blue, an approximate representation of the ballistic entry trajectory of the EXPERT vehicle. The blue and red dots represent the two trajectory points where the UQ analysis is carried out

Axisymmetric Navier-Stokes governing equations are used to describe the flow, together with the same physico-chemical models (Section 1.2) used for

Altitude, Km	T_∞, K	p_∞, Pa	ρ_∞, kg/m^3	u_∞ m/s	M_∞
60	245.5	20.3	2.8806e-04	4868.6	15.5
30	220	1200	0.0190	3657.3	12.3

Table 1.5: Freestream conditions for two points of the trajectory of the EXPERT vehicle.

the HEG cylinder. The equations are combined with the chemical mechanism introduced by Park et al. [Park *et al.*, 2001] applied to a mixture of five species air (N, O, NO, N_2 and O_2). COSMIC code is used to simulate the flow, using AUFS numerical scheme, and the mesh adaptation technique described in Section 1.5 is adopted. The simulation problem consists of computing the quantities of interest, which correspond to the pressure and heat flux measured by five sensors integrated in the nose heat shield. As it can be seen from figure 1.17, the first sensor is located at the center of the nose of the vehicle, which, in our axisymmetry hypothesis, coincides with the stagnation point, the others are disposed at an angle of (approximatively) 45 degrees from the center line. In practice, the solution, computed with the finite volume code, is available at the nodes of the computational grid, and it is interpolate to the desired locations.

Figure 1.19 shows the $n \times m$ nominal computational grid, with labels for the bounds, and the solution temperature field computed for the 60km trajectory point. Supersonic inflow and outflow boundary conditions are again imposed

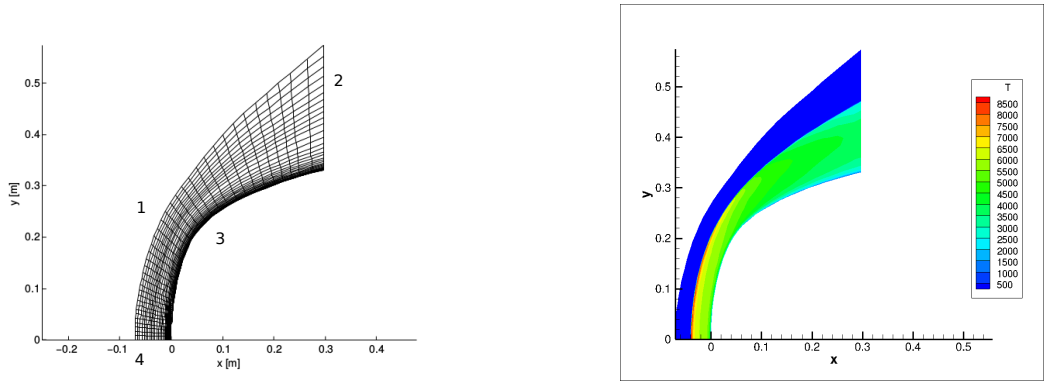

(a) (b)

Figure 1.19: Nominal computational grid (a) and nominal temperature field for the 60km trajectory point (b) of the EXPERT vehicle.

respectively on boundaries 1 and 2. On boundary 3, a partially catalytic wall at radiative equilibrium and with no-slip condition is imposed. The nominal

value of recombination probability is taken as $\gamma = 0.0015$. Finally, on boundary 4 the axisymmetry condition is imposed.

Characterization of the uncertainties

For the EXPERT entry problem, uncertainties are taken into account on the uncertain freestream conditions that we will try to rebuild by means of Bayesian inference and also on some parameters of the air chemistry mechanism. Concerning the freestream conditions, at each different calibration problem treated in Chapter 6, a uniformly distributed prior uncertainty in the $\pm 20\%$ interval around the nominal condition is considered on the quantity we wish to rebuild. The relatively wide uncertainty rage is chosen arbitrarily to allow the rebuilt parameters to be mainly informed by the measurements rather than by the priors, as it will be more clear in Section 2.5. Furthermore, an uncertainty on the catalytic recombination coefficient γ is taken into account. It is a uniform uncertainty of $\pm 33\%$ around the nominal value of 0.0015, as proposed by [Villedieu *et al.*, 2012]. Finally, as for the HEG cylinder, centered log-normal uncertainties are considered on the pre-exponential factors of the Arrhenius reaction rate coefficients. As in [Tryoen *et al.*, 2014], the standard deviation values reported in Table 1.6 are chosen.

Gas reaction	Distribution of $\log_{10} A_r$	σ_r
$NO + O \rightarrow N + O + O$	Normal	0.12
$NO + N \rightarrow N + O + N$	Normal	0.12
$O_2 + N_2 \rightarrow 2O + N_2$	Normal	0.10
$O_2 + O \rightarrow 2O + O$	Normal	0.10

Table 1.6: Uncertainties on gas reaction rates for EXPERT reentry.

As for the HEG cylinder, experimental data are considered to be affected by Gaussian measurement noise. Pressure measurements are assumed to be affected by a noise with standard deviation $\sigma_p = 0.02\, p^*_{\text{st}}$, and the standard deviation value for heat flux measurements is assumed to be $\sigma_q = 0.1\, q^*_{\text{st}}$; where p^*_{st} and q^*_{st} are measured values.

1.6.3 TACOT material ablation

A third application case related to atmospheric entry problems is here presented. It does not concern a hypersonic flow simulation, but it is focused instead on the analysis of the temperature of an ablative material at a fixed position and imposed time during the ablation process. In particular, we consider the unidirectional ablation of a 7.21 cm thick TACOT (Theoretical Ablative Composite for Open Testing) material [Lachaud *et al.*, 2010], a low

density carbon-phenolic created from literature data, exposed to a constant heat flux for one minute before radiatively cooling down. This rectangular incoming flux is an interesting case to test the surrogate modeling method proposed in Chapter 3. While this case does not represent a real ablation pro-

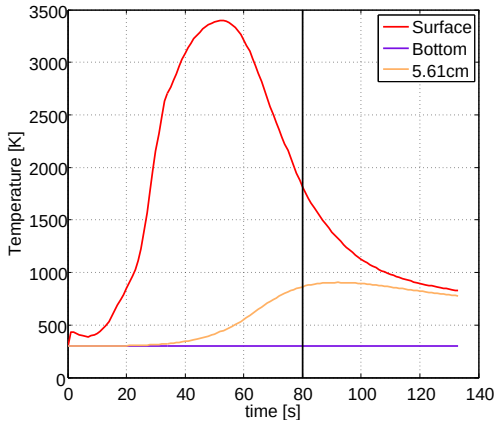

Figure 1.20: Temperature trend of the reference point at 5.61cm inside TACOT material compared to the one of the heated surface, obtained with nominal material parameters. The black vertical line indicates the reference time at which the sensitivity analysis is carried out.

cess of a TPS material occurring during the atmospheric entry of a spacecraft, it is however quite close to an ablation test in the Plasmatron facility [Bottin *et al.*, 2000] of the Von Karman Institute for Fluid Dynamics.

The quantity of interest is chosen to be the temperature of the material at a position $x = 5.61$ cm, meaning 1.6 cm inside from the heated surface, at the time $t = 80$ s over 120 s of simulation (see Figure 1.20). The measuring position corresponds to the location of a sensor, and it is deep enough into the material so that it does not reach the surface because of the recession caused by ablation. Computational simulations have been performed with the PATO code [Lachaud et Mansour, 2014], on the one-dimensional computational grid shown in figure 1.21. Note that the grid shows a strong refinement near the heated surface. Figure 1.20 shows the nominal temperature trend of the reference point used for the test case, located at 5.61 cm inside the TACOT material (in orange). It is compared to the temperature trend of the heated surface (in red) and the one of the bottom of the material (in blue). Concerning the uncertainty characterization, uncertainties are considered on 27 input parameters related to the physical and chemical properties of the different components constituting the virgin composite material and the char. A uniform distribution is associated to each uncertain variable, with values reported in Table 1.7. The definition of some terms can be found in Section 1.3.2, for the others the reader is referred to [Lachaud *et al.*, 2011].

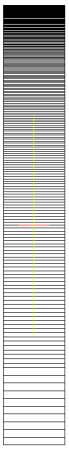

Figure 1.21: Computational grid used for the 1D simulation of the ablation of the TACOT material by means of the PATO code.

Referring to the conservation equations introduced in 1.3.2, uncertainties are assigned to the densities of both fiber ρ_f and matrix ρ_m of the composite material, and also to their volume fractions ϵ_f and ϵ_m. Uncertain are also the permeabilities K, heat capacities c_p, emissivities C_e, C_r reflectivities and conductivities λ in the i,j and k directions of both the virgin material and the char, denoted with the subscripts v and c respectively. Finally, uncertainties are accounted on pre-exponential factors, enthalpies and activation energies of Arrhenius forward rates of reactions 1 and 2 of the chemical mechanism described in [Lachaud *et al.*, 2011, Table 2] and on carbon, oxygen and hydrogen mass fractions y_i in the gaseous phase.

1.7 Conclusions

In this section we firstly introduced the phenomenology related to hypersonic entry flows. Then, we have provided the description of the models and the computational schemes used in this work to perform numerical simulations. Governing equations for hypersonic reacting flows were given, together with the closure physico-chemical models. The computational code used in the rest of the work to perform CFD simulations was described. Emphasis was given to the importance of mesh adaptation in case of simulations of hypersonic reacting flows. Finally, all the application cases used throughout the work were detailed, namely the flow around the HEG cylinder configuration and the node of the EXPERT vehicle, and the ablation of a TACOT material.

Variable	Description	Minimum	Maximum
ρ_f	Fiber density	1520	1680
ϵ_f	Fiber volume fraction	0.095	0.105
ρ_m	Matrix density	1140	1260
ϵ_m	Matrix volume fraction	0.095	0.105
K_v	Permeability of the virgin material	1.52e-11	1.68e-11
K_c	Permeability of the char	1.9e-11	2.1e-11
y_C	Carbon fraction	0.1854	0.2266
y_H	Hydrogen fraction	0.6111	0.7469
y_O	Oxygen fraction	0.1035	0.1265
A_1	Pre-exponential factor reaction 1	10800	13200
e_1	Activation energy reaction 1	64017.801	78243.979
h_1	Pyrolysis enthalpy reaction 1	-4.4e6	-3.6e6
A_2	Pre-exponential factor reaction 2	4.479993e8	5.475547e8
e_2	Activation energy reaction 2	1.529775e5	1.869725e5
h_2	Pyrolysis enthalpy reaction 2	-4.4e6	-3.6e6
c_{p_v}	Heat capacity virgin	0.95	1.05
λ_{i_v}	Conductivity i virgin	0.95	1.05
λ_{j_v}	Conductivity j virgin	0.95	1.05
λ_{k_v}	Conductivity k virgin	0.95	1.05
C_{e_v}	Emissivity virgin	0.95	1.05
C_{r_v}	Reflectivity virgin	0.95	1.05
c_{p_c}	Heat capacity char	0.95	1.05
λ_{i_c}	Conductivity i char	0.95	1.05
λ_{j_c}	Conductivity j char	0.95	1.05
λ_{k_c}	Conductivity k char	0.95	1.05
C_{e_c}	Emissivity char	0.95	1.05
C_{r_c}	Reflectivity char	0.95	1.05

Table 1.7: Uncertainties characterization for PATO: minimum and maximum of the uniform distribution associated to each uncertain input.

Chapter 2

Uncertainty Quantification, Sensitivity Analysis and Bayesian inference

In this chapter, the statistical framework for direct and inverse uncertainty quantification and global sensitivity analysis is introduced. A definition and classification of uncertainties is given, together with the definitions of forward and inverse uncertainty quantification problems. A brief review presents different techniques in the literature, with emphasis given on the ones that will be exploited in the following parts of the present work.

2.1 Introduction

Simulation of several engineering systems requires numerical resolution of complex computational models, which often involve a large number of physical parameters. In some practical cases, it can be difficult, or even impossible, to obtain enough experimental data to adequately calibrate the parameters of the physical model and furthermore, in general, experimental data, when available, is intrinsically affected by measurement errors. The need for robust predictive simulations in the analysis and design process requires rigorous quantification of how these uncertainties affect the values of quantities of interest. This is valid, obviously, also for atmospheric entry problems, where complex multidisciplinary models are used to model the complex phenomena related to hypersonic entry flows, and where it can be difficult to obtain accurate data about the atmospheric environment and its chemical behavior.

Techniques to define the quality of numerical simulations have been organized in the framework of so-called *verification and validation* [Oberkampf et Roy, 2010; Stern *et al.*, 2001]. The aim of verification is to check that the

equations of the simulation model are being solved correctly. This is done firstly by assessing the convergence and then by quantifying the errors of the numerical algorithms used to solve the governing equations. Validation, instead, verifies if the correct set of equations, constituting the mathematical model, is used to describe the physics by comparing the numerical predictions to reality, *i.e.* to experimental data. There is a growing recognition of the fact that validation can not be carried out without accounting for uncertainties present in both experimental measurements and numerical computations [Roy et Oberkampf, 2011]. Furthermore, information on the uncertainties in simulations is critical in the decision-making process for the design and analysis of physical and engineering systems. Without estimating the uncertainty associated to a prediction, the decision-making process could be misleading, which could cause inadequate safety, reliability and performance of the system. For these reasons, Uncertainty Quantification (UQ) is gaining increasing importance to rigorously quantify the uncertainties introduced in the output of numerical simulations to assess their predictive capabilities.

One of the main goals of UQ is to propagate the different sources of uncertainties through the simulation model in order to obtain quantitative information about the variability of some quantities of interests (outputs) [Glimm et Sharp, 1999]. The first step necessary for this process is to identify and characterize all the different sources of uncertainties. In section 2.2, a brief overview is given about this important topic. In this work we will mainly focus on the effect of uncertainties associated to model input data, such as boundary freestream conditions and physical model parameters, where some physically-sound assumptions on their probability density function (PDF) are done. In this probabilistic uncertainty quantification framework, the problem of uncertainty propagation consists in computing the PDFs of the outputs given the distributions of the uncertain input parameters. Several approaches have been developed to solve this problem, which are reviewed in section 2.3, in which the description of two popular classes of methods, namely sampling techniques and spectral methods, is given, due to their use in this work.

Another objective of UQ can be to rank the uncertain inputs according to their influence on the variability of the quantity of interest. This type of problem is called Sensitivity Analysis (SA). In Section 2.4 more details are given about the formulation of this problem and some classes of SA methods that can be found in literature.

A way to reduce the variability of the output of a simulation is to reduce the uncertainty of some input parameter, especially of the ones who presented higher relative weights in sensitivity analysis. Often, the lack of direct experimental data and the difficulty of characterizing uncertainties on aleatory parameters leads to the choice of associating them with analytical probability distributions (Gaussian, uniform) specified by expert opinions, which can lead to poor estimates. In this context, it is possible to improve the characterization

of uncertain parameters by inferring their PDFs from experimental measurements available on some quantities of interest. Probabilistic approaches such as Bayesian inference (see Section 2.5) are able to treat these problems by taking into account also the error intrinsically associated to experimental data. Uncertainty propagation and Bayesian calibration can be seen as two major types of problems in uncertainty quantification. The first is a forward UQ problem, since the various sources of uncertainty are propagated through the model to predict the uncertainty in the system response, while the other is an inverse problem, since the input model parameters are the solutions of a calibration done by exploiting measurements of some model outputs. The relations and differences between forward problem of uncertainty propagation and the inverse problem associate to Bayesian inference are graphically displayed in figure 2.1.

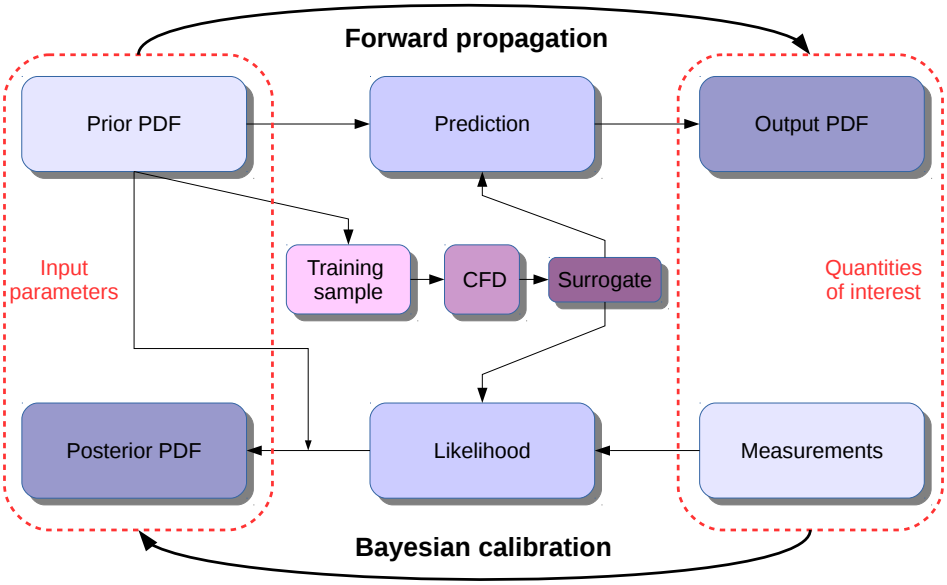

Figure 2.1: Diagram explaining inputs, outputs and different actors in the forward uncertainty propagation and Bayesian calibration problems.

2.2 Sources of uncertainties: identification and characterization

A proper identification, characterization and description of the uncertainties is crucial to obtain reliable uncertainty quantification results. Furthermore, the presence of different types of uncertainties may lead, as here briefly described, to the use different approaches and tools for their description and,

subsequently, for the following UQ analysis.

Uncertainties are often classified in two categories [Iaccarino, 2014]: aleatory or epistemic. *Aleatory* (or stochastic) uncertainty measures the physical variability in the system under analysis, or in other words the intrinsic variation of a quantity. It is not strictly related to a lack of knowledge and it can not be reduced or completely eliminated, but given sufficient samples of the stochastic process, can be characterized by a random variable (RV) and its probability density function. For example, the operating conditions of an engineering system normally are assumed as aleatory sources of uncertainties. *Epistemic* (or reducible) uncertainty, instead, is an uncertainty due to lack of knowledge. This kind of uncertainties can arise from assumptions in the physical and mathematical modeling of the phenomena, and can be reduced for example by improving the physical models. This type of uncertainty is usually represented as an interval (with no associated PDF) or, as done in the probabilistic Bayesian approach to uncertainty [Gelman *et al.*, 2003], as a PDF (usually uniform) representing the degree of belief of the analyst on the true value. Other approaches to treat epistemic uncertainties are fuzzy set [Shafer, 1976] and possibility and evidence theory [Zimmermann, 1996]. An example of sources of epistemic uncertainty are turbulence or chemical kinetics model assumptions. Notice that the two categories constituting this classification are not neatly separated, but sometimes complex uncertainties may result of an interaction between aleatory and epistemic effects.

In scientific computing, sources of uncertainties can be further divided in three categories [Oberkampf et Roy, 2010]: model inputs, model form and poorly-characterized numerical approximation errors. Model input uncertainties are used to describe variability in things such as geometry, constitutive model parameters, and initial and boundary conditions, and can come from a range of sources including experimental measurement, theory, other supporting simulations, or expert opinion. Input parameter uncertainties can be classified as aleatory, epistemic, or a mixture of the two. The characterization of the numerical approximation errors is done with verification. When numerical approximation errors can be exactly estimated, their uncertainty can, in principle, be eliminated, given that sufficient computing resources are available. If this is not feasible, they should generally be converted to epistemic uncertainties due to the uncertainties associated with the error estimation process itself [Roy et Oberkampf, 2011]. Model form uncertainties are related to assumptions embodied in the mathematical model. The characterization of model form uncertainty is commonly estimated using model validation. Model form uncertainties are usually treated as epistemic [Ferson *et al.*, 2008].

In this work, the attention is focused on uncertainties related to boundary conditions (freestream conditions) and input parameters of the physico-chemical model (chemical mechanism of the air mixture and catalysis). They may be considered as both aleatory or epistemic uncertainties, since they rep-

resent both the intrinsic variability of the atmosphere/materials and the lack of knowledge related to improvable measurements. However, we decided to adopt a Bayesian stochastic framework for their description, which is considered to naturally be the more suitable for treating this kind of uncertainties. Therefore, in this framework, uncertain variables are described as random variables and their PDFs represent the degree of belief of the true value on the part of the analyst, given by expert opinion.

2.3 Forward uncertainty propagation

In a probabilistic framework, the problem of uncertainty propagation consists in the computation of PDFs of some output quantity of interest given the probability distributions of the uncertain inputs (figure 2.2), in order to get mean values, variances, confidence intervals and other statistical indicators of the output or the likelihood of a certain outcome.

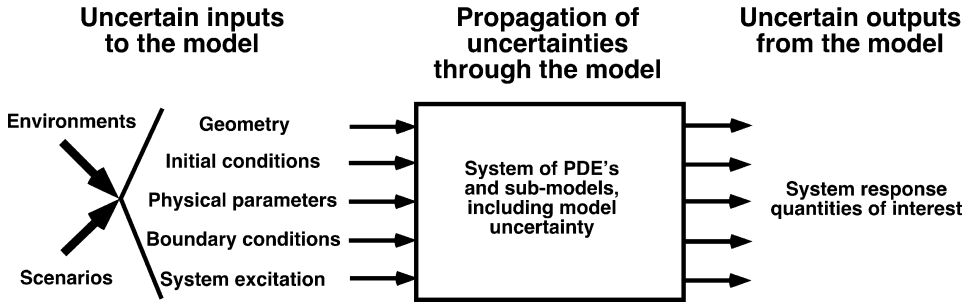

Figure 2.2: Propagation of uncertainties associated to model input parameters to obtain output uncertainties (taken from [Oberkampf et Roy, 2010]).

Let us describe this problem from a mathematical point of view. In the adopted probabilistic (statistical) framework, it is possible to consider the d-dimensional vector of input uncertainties $\mathbf{x} \in \mathbb{R}^d$ as a random variable $\mathbf{X}$, with joint probability density function $\sigma_{\mathbf{X}}(\mathbf{x})$ defined in a probability space $(\mathbb{R}^d, \mathcal{B}_d, \Sigma_{\mathbf{X}})$, where $\mathcal{B}_d$ is the Borel σ-algebra of the event space $\mathbb{R}^d$ and $\Sigma_{\mathbf{X}}$ is its probability measure [Delmas, 2010]. The response of the model $y = f(\mathbf{x})$, with $y \in \mathbb{R}$, is consequently described by a random variable $Y = f(\mathbf{X})$. The upper-case letters, $\mathbf{X}$ and Y, denote a list of input random variables (random vector) and a scalar random output, respectively, while the lower-case letters $\mathbf{x}$ and y represent the realizations. The model response Y is assumed to have finite variance, hence it belongs to the Hilbert space $L^2(\mathbb{R}^d, \Sigma_{\mathbf{X}})$ of square-integrable functions with respect to the measure $\Sigma_{\mathbf{X}}$. This space is known to be equipped with the inner product $\langle \cdot, \cdot \rangle_{L^2}$, defined as

$$\langle g(\mathbf{X}), h(\mathbf{X}) \rangle_{L^2} = \int_{-\infty}^{\infty} g(\mathbf{x}) h(\mathbf{x}) \sigma_{\mathbf{X}}(\mathbf{x}) \, \mathrm{d}\mathbf{x} \, , \tag{2.1}$$

which also induces the norm $\|g(\mathbf{X})\|_{L^2}^2 = \langle g(\mathbf{X}), g(\mathbf{X})\rangle_{L^2}$.

Performing uncertainty propagation through the model $Y = f(\mathbf{X})$ means to characterize the random variable Y and its variability, which usually requires the computation of n-th order statistical moments about a constant $c \in \mathbb{R}$ (that is equal to the mean for centered moments), that can be written in the form:

$$\mathbb{E}[(Y - c)^n] = \int_{-\infty}^{\infty} (f(\mathbf{x}) - c)^n \sigma_{\mathbf{X}}(\mathbf{x})\, \mathrm{d}\mathbf{x}. \tag{2.2}$$

The previous expression can be generally written as an expectation of a generic function $g(\cdot)$ of the input:

$$\mathbb{E}[g(\mathbf{x})] = \int_{-\infty}^{\infty} g(\mathbf{x}) \sigma_{\mathbf{X}}(\mathbf{x})\, \mathrm{d}\mathbf{x}. \tag{2.3}$$

In most applications, the integral in (2.3) cannot be evaluated analytically. For this reason, several techniques have been proposed in the literature to solve the uncertainty propagation problem [Lucor, 2011; Geraci, 2013; Iaccarino, 2014]. A big distinction is usually done between *non-intrusive* and *intrusive* approaches: non-intrusive approaches require only multiple runs of the existing deterministic numerical code, which can be used as a black-box, while intrusive methods require to reformulate entirely the theoretical formulation of the problem and a deep modification of the numerical code. Being able to use the computer code as a black-box presents a big advantage for many applications, as very complex physical models (highly nonlinear models, multiphysics, coupled problems, ...) can be used in the uncertainty propagation without having to modify the computational code. Another advantage is that the different deterministic simulations can be easily performed in parallel. These features make non-intrusive methods very attractive for UQ problems in industrial applications and when complex computational models are involved. However, a drawback of non-intrusive methods is that their numerical cost directly increases with the number of deterministic simulations that need to be performed to construct the approximation. This number can become very large, since most of non-intrusive methods suffer from the so-called *curse of dimensionality* [Donoho, 2000]. This means that the number of required evaluations of the computational model increases exponentially with the dimension of the input stochastic space, *i.e.* with the number of independent input random variables.

The more straightforward family of non-intrusive methods for uncertainty propagation are *sampling techniques*, like Monte Carlo approach [Caflisch, 1998], which focus on stochastic integration methods to compute the integrals in eq. (2.3). However they are characterized by a slow convergence rate, and therefore are often associated to high computational costs, especially when the evaluation of the function of interest requires expensive numerical simulations

(see Section 2.3.1 for more details). On the other hand, deterministic numerical integration techniques such as *quadrature rules* [Smolyak, 1963] try to solve the integral in a deterministic way. *Stochastic collocation* methods [Babuska *et al.*, 2007; Xiu et Hesthaven, 2005][Witteveen et Iaccarino, 2012, 2013] rely instead on a global or piecewise interpolation of the function of interest given its evaluation in a set of deterministic collocation points. The interpolation is then exploited for the characterization of the statistics of the output.

Another family of UQ methods are stochastic *spectral approaches* (see [Le Maître et Knio, 2010] for an extensive review), like the well-known Polynomial Chaos expansion [Xiu, 2010] or Polynomial Dimensional Decomposition [Rahman, 2008]. These methods aim at giving an approximated representation of the output random variable as a functional expansion on an orthogonal functional basis of the stochastic space (see section 2.3.2 for more details). Inside this family of methods, several techniques have been developed to determine the (deterministic) expansion coefficients. *Stochastic Galerkin* approaches [Xiu et Karniadakis, 2002; Le Maître *et al.*, 2001; Xiu *et al.*, 2002], which are intrusive, rely on the weak formulation of the stochastic problem in a similar mathematical framework as deterministic Galerkin methods. Spectral methods can be implemented also in many non-intrusive ways, like *non-intrusive spectral projection* [Reagan *et al.*, 2003; Congedo *et al.*, 2011], *collocation* [Xiu, 2009] and *regression* [Blatman et Sudret, 2010a] to cite some. More recently, also some semi-intrusive implementations of spectral approaches have been proposed [Abgrall et Congedo, 2013; Geraci *et al.*, 2016], which only require some minor modifications to the existing computational code.

A further family of approaches for uncertainty propagation has been initially developed with the aim of alleviating the high computational cost associated to sampling methods. It is based on the idea of constructing approximation models, known as *surrogate models* (also referred to as metamodels or response surfaces) [Simpson *et al.*, 2001; Hastie *et al.*, 2009], which are mathematical models that mimic the behavior of the computational model as accurately as possible, while being cheaper to evaluate. Surrogate models are built exploiting the information about the computational model on a limited number of points, called training points, where the expensive computational model needs to be evaluated, and therefore they are normally considered as non-intrusive techniques. The problem of building accurate and computationally efficient surrogate models is not trivial, hence several efforts have been and are still carried out in literature in this direction. Once a sufficiently accurate surrogate model of the function of interest is available, it can be exploited to compute predictions, rare events and statistics of the output at a reduced computational cost. Surrogate models are useful mathematical tools that are also used in other applications, like global optimization [Jones *et al.*, 1998] and statistical learning [Rasmussen et Williams, 2006]. Among the many surrogate modeling techniques available in literature, it is possible to mention least-

squares regressions [Hastie *et al.*, 2009], polynomial response surface methods [Box et Draper, 1987; Jones, 2001], radial basis functions [Powell, 1987; Buhmann, 2003], artificial neural networks [Bishop, 1995] and Kriging [Cressie, 1993] (or Gaussian process regressions [Rasmussen et Williams, 2006]). Also the previously mentioned spectral expansions and stochastic collocation interpolations can be considered as surrogate models of the function of interest. The fact that non-intrusive surrogate models suffer from the curse of dimensionality makes more challenging the construction of a good surrogate for a medium-to-high number of input dimensions, that is at the same time accurate and efficient, requiring an as-small-as-possible number of training point to be built. This is the direction where the recent research on surrogate models is focused, with the use of sparse representations [Blatman et Sudret, 2010a; Tang *et al.*, 2016] or dimensional reduction techniques [Constantine, 2015; Tripathy *et al.*, 2016]. Chapters 3 and 5 of the present work also focus respectively on the construction of an efficient surrogate model and on dimension reduction.

Two popular classes of UQ methods are described more formally in the two following subsections, because of their relevance for the rest of the work. In particular, more details about sampling techniques are given in 2.3.1, and about spectral approaches in 2.3.2. For the same reason, Kriging surrogate models will be extensively discussed in Section 3.2.1 and Appendix B.

2.3.1 Sampling techniques

Sampling techniques are the simplest available approach to propagate input uncertainties through a numerical simulation. A useful characteristic of sampling techniques is that their rate of convergence is independent of the problem dimensionality. The Monte Carlo method (MC) and its variants [Hammersley et Handscomb, 1964] are the most popular sampling approach. It consists in drawing independent random samples $\mathbf{x}_i$ from the joint PDF of the input parameters and evaluating the model output for each sample. All the results are then used to characterize the statistics of the output. It is possible to use sampling expected values as MC estimators of the real expectations:

$$\mathbb{E}[f(\mathbf{x})] \approx \frac{1}{N} \sum_{i=1}^{N} f(\mathbf{x}_i) \,, \tag{2.4}$$

with N the number of samples. The method has many advantages, being simple, robust, versatile and universally applicable, and it is non-intrusive, not requiring any modification to the existing deterministic computational code, which can be used as a black-box. However, while it converges to the exact solution as the number of samples goes to infinity, its convergence is very slow, since its convergence rate is only of the order $O(N^{-1/2})$ [Fishman, 1996]. Therefore several thousands (or even millions) of samples, and hence of numerical simulations, are required to obtain accurate estimations, making it

too expensive in order to be used in problems where the evaluation of the output involves the solution of complex systems of partial differential equations, like in CFD. It is competitive with respect to other methods only in case of high-dimensional input probability spaces, since its order of convergence is independent of the number of random parameters.

Latin Hypercube sampling (LHS) [McKay *et al.*, 1979] is one of the most popular methods that have been developed to partially accelerate the convergence of Monte Carlo approaches. It is based on dividing the range of each input parameter in intervals of equal probability, and then on drawing random samples from each one of the equiprobability interval. The convergence is faster than simple Monte Carlo [Stein, 1987], since LHS provides an optimal coverage of the input space [Helton et Davis, 2003]. Another popular improvement over Monte Carlo sampling methods is the family of quasi-Monte Carlo (qMC) methods [Caflisch, 1998]. In qMC methods, the random generation of samples is substituted by a low-discrepancy sequence, for example the well known low discrepancy sequence introduced by [Sobol', 1967]. In Figure 2.3, a comparison between MC and LHS sampling points is shown by drawing 50 samples from a uniformly-distributed two-dimensional stochastic vector.

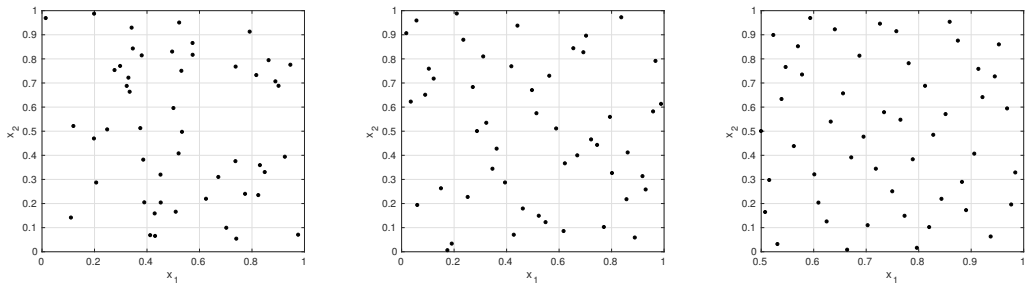

(a) Monte Carlo (b) Latin Hypercube (c) quasi Monte Carlo

Figure 2.3: Plots of 50 samples drawn from a uniformly-distributed two-dimensional stochastic vector with Monte Carlo and Latin Hypercubes and quasi Monte Carlo sampling methods.

2.3.2 Spectral approaches

Let us consider again the problem of propagating the multidimensional uncertain random input $\mathbf{X}$, with joint probability density function $\sigma_{\mathbf{X}}(\mathbf{x})$ defined in the probability space $(\mathbb{R}^d, \mathcal{B}_d, \Sigma_{\mathbf{X}})$, through the model $Y = f(\mathbf{X})$. Let us suppose the output random variable to have finite variance and therefore to belong to the space $L^2(\mathbb{R}^d, \Sigma_{\mathbf{X}})$ of square-integrable random variables, which is equipped with the previously defined inner product and the induced L^2 norm. Let us suppose, for simplicity, that the components of the input random vector

are independent, therefore the joint PDF can be written

$$\sigma_{\mathbf{X}}(\mathbf{x}) = \prod_{i=1}^{d} \sigma_{X_i}(x_i) \ , \tag{2.5}$$

with $\sigma_{X_i}(x_i)$ the marginal PDF of the i-th component. Spectral approaches are available also for mutually dependent inputs, but the formulation is more complex [Le Maître et Knio, 2010]. Spectral methods for UQ [Xiu, 2010] aim at reconstructing the functional dependence of the solution on the input uncertainties. This functional dependence is typically expressed in terms of a series expansion:

$$f(\mathbf{X}) = \sum_{k=0}^{\infty} C_k \psi_k(\mathbf{X}) \ , \tag{2.6}$$

where the ψ_k are suitably selected functionals of the input random variables which constitute a multi-dimensional orthogonal basis of the Hilbert stochastic space, and the C_k are deterministic expansion coefficients. After computing the coefficients, the expansion can be exploited to determine the statistics of the output, either analytically, by manipulation of the expansion coefficients or via sampling. Therefore the problem is shifted to the computation of the series coefficients.

A well know spectral method for uncertainty quantification is Polynomial Chaos (PC) expansion. It was first introduced by [Ghanem et Spanos, 1991] for Gaussian random variables, then [Xiu et Karniadakis, 2002] introduced generalized Polynomial Chaos (gPC) for inputs distributed with other PDFs. Generalized PC uses orthogonal polynomials from the Askey family [Xiu et Karniadakis, 2002] as basis for the spectral decomposition. This polynomials are orthogonal with respect to the measure associated to the probability space of the input variable:

$$\int \psi_j(\mathbf{x})\psi_k(\mathbf{x})\, \sigma_{\mathbf{x}}(\mathbf{x})\, \mathrm{d}\mathbf{x} = \delta_{jk} \qquad \text{with} \qquad \delta_{jk} = \begin{cases} 1, & \text{if } j = k \\ 0, & \text{otherwise.} \end{cases} \tag{2.7}$$

A traditional way to write a gPC decomposition of a d-dimensional function $f(\mathbf{x})$ of maximum polynomial order p is:

$$\begin{aligned} f(\mathbf{x}) \approx c_0\Gamma_0 + \sum_{i_1=1}^{d} c_{i_1}\Gamma_1(x_{i_1}) + \sum_{i_1=1}^{d}\sum_{i_2=1}^{i_1} c_{i_1,i_2}\Gamma_2(x_{i_1}, x_{i_2}) + \\ + \cdots + \sum_{i_1=1}^{d}\sum_{i_2=1}^{i_1}\cdots\sum_{i_p=1}^{i_{p-1}} c_{i_1\ldots i_p}\Gamma_p(x_{i_1}, \ldots, x_{i_p}) \ , \end{aligned} \tag{2.8}$$

where the polynomial chaoses Γ_p of order p are various combinations of tensor products of sets of univariate orthonormal polynomials $\psi(x_i)$. This representation shows spectral (exponential) convergence with respect to the polynomial

order p in the L^2 norm [Wan et Karniadakis, 2005; Lucor, 2011] for smooth functions of interest. It can be noticed that the gPC expansion is organized with respect to an increasing degree of multivariate polynomials, and not to an increasing order of parameter interactions. The total number of terms in the expansion P is linked to the dimensionality of the input and the imposed maximum polynomial order:

$$P + 1 = \frac{(d+p)!}{d!\,p!}. \tag{2.9}$$

As previously seen, several intrusive and non-intrusive approaches exist in the literature to compute the expansion coefficient of stochastic spectral methods. A review of these approaches and more details about PC expansions can be found in [Le Maître et Knio, 2010]. Notice that another polynomial spectral expansion method is present in the literature, the so-called Polynomial Dimensional Decomposition (PDD) [Rahman, 2008]. It will be extensively described in Section 3.2.2, since it plays a fundamental role in the improved metamodeling strategy proposed in Chapter 3.

2.4 Global Sensitivity Analysis

In uncertainty quantification, it is important to determine which uncertain inputs have the biggest impact on the variability of the model output. This can be useful for example to reduce the dimensionality of the input by discarding those variables whose relative impact on the output is negligible or to know on which variables is more effective to reduce the uncertainty in order to reduce the variance of the function of interest.

Sensitivity Analysis (SA) is the mathematical discipline that studies variations in the output of a mathematical model with respect to some input parameters. There are two categories of methods for sensitivity analysis: local SA and global SA. Local SA is focused on the local variation of the model with respect to the inputs. The impact on the output of small perturbations of input parameters around nominal values is studied. This deterministic approach consists in calculating or estimating the partial derivatives of the model at a specific nominal point, hence relying on the use of gradients of the function of interest. Instead, global SA takes into account the global influence of input parameters and their interactions on the output quantity of interest, by considering the entire input domain rather than considering gradients at a specific nominal point. In contrast to local SA, global sensitivity methods are developed in a statistical framework. Global SA has been largely studied and many approaches have been proposed in literature.

We will restrict on the sensitivity with respect to the global variability of the model output, usually measured by its variance. Several types of indices

have been introduced to measure variance-based sensitivity. Screening methods, such as Morris method [Morris, 1991], are qualitative methods useful for studying sensitivities on models containing a high number of input variables. Other quantitative measures are, for example, Standard Regression Coefficients (SSC) [Saltelli *et al.*, 2008, Chapter 1.2.5], based on the analysis of a fitted linear model, or graphical regression methods. [Iooss et Lemaître, 2015; Borgonovo et Plischke, 2016] give a overview on global and local SA methods.

In the following section we will focus on global SA using Sobol' indices [Sobol', 1993] to determine input variables (or groups of variables) mostly responsible of the variance in the model output [Homma et Saltelli, 1996]. The Sobol' sensitivity indices are obtained from a functional decomposition of the output with respect to its variance (ANOVA decomposition). Several methods had been developed to compute these indices directly through sampling using Monte-Carlo and quasi-Monte-Carlo (QMC) methods or by building a metamodel to approximate the ANOVA decomposition and then compute the indices from the metamodel with lower computational cost.

2.4.1 ANOVA decomposition and Sobol' sensitivity indices

Let us suppose to write the set of uncertain input parameters in a d-dimensional input random variable $\mathbf{X} = \{x_1, \dots, x_d\}$ with a joint probability density function (PDF) $\sigma_{\boldsymbol{X}}(\boldsymbol{x})$ defined in the probability space $(\mathbb{R}^d, \mathcal{B}_d, \Sigma_{\mathbf{X}})$. The assumption of independence of the components of this random vector implies that its PDF can be written as

$$\sigma_{\boldsymbol{X}}(\mathbf{x}) = \prod_{i}^{d} \sigma_{X_i}(x_i), \tag{2.10}$$

where $\sigma_{X_i}(x_i)$ is the marginal PDF of x_i. Let us suppose that the response of the system is represented by a multivariate function of interest $y = f(\mathbf{x})$.

It is possible to represent the function of interest $f(\mathbf{x})$ by the following functional decomposition:

$$\begin{aligned} f(\mathbf{x}) &= f_0 + \sum_{s=1}^{d} \sum_{i_1<\cdots<i_s}^{d} f_{i_1\dots i_s}(x_{i_1}, \dots, x_{i_s}) \\ &= f_0 + \sum_{1\le i\le d}^{d} f_i(x_i) + \sum_{1\le i<j\le d}^{d} f_{ij}(x_i, x_j) + \cdots + f_{1,2,\dots,d}(x_1, x_2, \dots, x_d)\ , \end{aligned} \tag{2.11}$$

which can be rewritten in compact form exploiting a multi-index notation:

$$y = f_0 + \sum_{j=1}^{\mathcal{M}} f_{s_j}(\boldsymbol{x}_{s_j}) \qquad \text{with} \quad \mathcal{M} = 2^d - 1. \tag{2.12}$$

This representation is called ANOVA (Analysis of Variance) decomposition [Sobol', 2001, 1993] if, for any $j \in 1, \ldots, \mathcal{M}$, the following condition is respected

$$\int f_{s_j}(\boldsymbol{x}_{s_j})\, \sigma_{X_i}(x_i)\, \mathrm{d}x_i = 0 \qquad \text{for} \quad x_i \in \{\boldsymbol{x}_{s_j}\}. \tag{2.13}$$

From this definition, it follows that all of the terms of the ANOVA decomposition are orthogonal. It follows also that the expectation of any component function, excluding f_0, is zero:

$$\mathbb{E}[f_{i_1 \ldots i_s}(x_{i_1}, \ldots, x_{i_s})] = 0. \tag{2.14}$$

From this property, it can be noticed that the term f_0 represents the mean of the function. The ANOVA expansion decomposes the original high-dimensional space into a union of several low-dimensional spaces that are orthogonal between each other.

Assuming that $f(\mathbf{x})$ is square integrable, then also all the component functions $f_{i_1 \ldots i_s}$ of the ANOVA decomposition are square integrable, hence the variance D of the function can be computed as

$$D = \int f^2(\mathbf{x})\, \sigma_X(\mathbf{x}) \mathrm{d}\mathbf{x} - f_0^2 = \sum_{s=1}^{d} \sum_{i_1 < \cdots < i_s}^{d} \int f^2_{i_1 \ldots i_s} \sigma_{X_{i_1 \ldots i_s}} dx_{i_1} \ldots dx_{i_s} \ , \tag{2.15}$$

and the so-called conditional variances of each component function is defined as

$$D_{i_1 \ldots i_s} = \mathrm{Var}[f_{i_1 \ldots i_s}] \equiv \int f^2_{i_1 \ldots i_s}\, \sigma_{X_{i_1 \ldots i_s}}\, \mathrm{d}x_{i_1} \ldots \mathrm{d}x_{i_s} \ , \tag{2.16}$$

where $p_{X_{i_1 \ldots i_s}}$ is the joint probability distribution of the set of variables $(x_{i_1}, \ldots, x_{i_s})$. Hence the following property is valid

$$D = \sum_{s=1}^{d} \sum_{i_1 < \cdots < i_s}^{d} D_{i_1 \ldots i_s} \ , \tag{2.17}$$

which means that the total variance is the sum of the conditional variances associate to every component function of the ANOVA expansion.

The ANOVA decomposition is closely related to the Sobol' sensitivity indices (SI), which are global sensitivity indices defined as the ratios

$$S_{i_1 \ldots i_s} = \frac{D_{i_1 \ldots i_s}}{D}. \tag{2.18}$$

They express the sensitivity of the output with respect to an input variable or set of variables as the ratio between their contribution to the output variance, expressed by their conditional variance, and the total output variance itself. The integer s is often called the order or the dimension of the index, thus

indices accounting for the contribution of a single variable are called first-order indices, while higher order indices account for interaction effects between sets of variables. From this definition, it is possible to see that all the $S_{i_1 \dots i_s}$ are non negative and that they sum up to the unity:

$$\sum_{s=1}^{d} \sum_{i_1 < \cdots < i_s}^{d} S_{i_1 \dots i_s} = 1. \tag{2.19}$$

Furthermore, it is also possible to define the total Sobol' sensitivity indices, which summarizes the total impact related to a variable x_i on the output variance. Indeed, it is defined as the sum of all the sensitivity indices containing x_i. In a multi-index notation, it can be written as

$$S_i^{tot} = \sum_{\boldsymbol{s}_j \ni i} S_{\boldsymbol{s}_j} \ , \tag{2.20}$$

with $\boldsymbol{s}_j = (i_1, \dots, i_s)$. The sensitivity indices are useful to compare the impact on the function variance of input variables or set of variables. In uncertainty quantification, they are used to state the sensitivity of the quantity of interest to each source of uncertainty, and to rank the random inputs according to their impact on the solution variance. The input variable x_i is influential on the output variance if the first-order Sobol' index S_i associated to that variable is important, while it can be considered as a non-influential parameter if S_i and S_{T_i} are small. Moreover, if the first-order index S_i is close to the total index S_{T_i}, it means that the variable x_i has a negligible interaction with the other uncertain parameters.

2.4.2 Computing Sobol' indices

The evaluation of the integrals involved in the computation of Sobol' sensitivity indices can be performed with Monte Carlo (MC) techniques, as described for example in [Sobol', 2001].

Consider an arbitrary subset of the input variables $z = (x_{k_1}, \dots, x_{k_m})$ of dimension m, with $1 \leq m \leq d-1$. Calling w the set of dimension $d-m$ of complementary variables, we have that $\mathbf{x} = (z, w)$. Let $K = (k_1, \dots, k_m)$, with $1 \leq k_1 < \cdots < k_m \leq d$. The variance corresponding to the subset z is defined as

$$D_z = \sum_{s=1}^{m} \sum_{(i_1 < \cdots < i_s) \in K} D_{i_1 \dots i_s}. \tag{2.21}$$

Similarly, the variance D_w can be introduced. Then the total variance corresponding to the subset z is

$$D_z^{tot} = D - D_w. \tag{2.22}$$

From these definitions and equation (2.11) it can be proven that [Sobol', 2001, Sec. 8]

$$D_z = \int f(x) f(z, w')\, \sigma_x \sigma_w \, \mathrm{d}x \mathrm{d}w' - f_0^2 \tag{2.23}$$

and a similar formula can be written for D_w

$$D_w = \int f(x) f(z', w)\, \sigma_x \sigma_z \, \mathrm{d}x \mathrm{d}z' - f_0^2. \tag{2.24}$$

Therefore, it can be seen that for computing the sensitivity indices S_z and S_z^{tot}, the following four integrals need to be estimated:

$$f_0 = \int f(x) \sigma_x \mathrm{d}x \qquad D + f_0^2 = \int f(x)^2 \sigma_x \mathrm{d}x \tag{2.25}$$

$$D_z + f_0^2 = \int f(x) f(z, w') \sigma_x \sigma_w \mathrm{d}x \mathrm{d}w' \qquad D_w + f_0^2 = \int f(x) f(z', w) \sigma_x \sigma_z \mathrm{d}x \mathrm{d}z'.$$

A Monte Carlo method can be used to estimate those integrals. Consider two independent random samples ξ and ξ' of the joint PDF of the inputs, and let $\xi = (\eta, \zeta)$ and $\xi' = (\eta', \zeta')$. Each Monte Carlo point requires three evaluations of the model: $f(\eta, \zeta))$, $f(\eta, \zeta'))$ and $f(\eta', \zeta))$. A further evaluation must be added for each subset of variables for which the SI is desired. This fact makes the process very computationally demanding, especially when the evaluation of expensive codes is concerned. After n_s trials, Monte Carlo estimates of mean, variance and sensitivity indices are computed from equation (2.4):

$$f_0 \approx \frac{1}{n_s} \sum_{i=1}^{n_s} f(\xi_i) \qquad D \approx \frac{1}{n_s} \sum_{i=1}^{n_s} f(\xi_i)^2 - f_0^2 \tag{2.26}$$

$$D_z \approx \frac{1}{n_s} \sum_{i=1}^{n_s} f(\xi_i) f(\eta_i, \zeta_i') - f_0^2 \qquad D_w \approx \frac{1}{n_s} \sum_{i=1}^{n_s} f(\xi_i) f(\eta_i', \zeta_i) - f_0^2.$$

The total sensitivity index can be obtained exploiting eq. (2.22). It can be noticed that, when dealing with small sensitivity indices, this MC-based algorithm may be spoiled by loss of accuracy. Some computational tricks [Sobol' et Myshetskaya, 2008] are available to improve the accuracy in these cases.

The main drawback of this method is that, as for all MC based techniques, its convergence is quite slow, thus requiring several thousands evaluations of the model. In many engineering applications, where the evaluation of the quantities of interest involves expensive solutions of systems of PDEs describing the physical phenomena, those methods become prohibitively expensive. One possible way to reduce the computational cost of the evaluation of the sensitivity indices can be through the use of a surrogate model to accelerate the model prediction, as in [Iooss *et al.*, 2006], where a response surface surrogate model has been used to predict the model output at the MC samples, or

in [Marseguerra *et al.*, 2003], where instead a neural network surrogate model has been preferred, or in [Marrel *et al.*, 2009] where Gaussian process surrogate (see Section 3.2.1) has been used. In this case, the evaluation of the true value of the function of interest is substituted by the evaluation of its surrogate model for each MC sample of the uncertain parameters. Thus the only expensive solutions of the true model required are the ones necessary for the evaluation of the training points for the metamodel. Generally speaking, an accurate estimation of the sensitivity indices obtained by means of a metamodel can be obtained only if the metamodel is accurately representative of the function of interest.

The use of other kinds of surrogate models, such as spectral methods like Polynomial Chas expansion and Polynomial Dimension Decomposition (see Sections 2.3.2 and 3.2.2) allows to compute Sobol' indices analytically from the coefficients of the polynomial expansion which constitutes the surrogate model. A discussion for gPC can be found in [Crestaux *et al.*, 2009; Sudret, 2008], while for PDD it will be discussed in Section 2. This is indeed an advantage from the point of view of computational cost, since SIs are obtained by analytical manipulations of the expansion coefficients instead of evaluating (with the actual model or with the metamodel) the output in thousands of MC sampling points.

2.5 Bayesian setting for inverse UQ problems

This section is focused on the inverse UQ problem of rebuilding some non-observable uncertain input parameters $\boldsymbol{m}$ starting from experimental (*i.e.* noisy) measurements $\boldsymbol{d}$ of some observable quantities of interest. We also want to be able to account for other stochastic input uncertainties $\boldsymbol{c}$ of the physical model $y = f(\boldsymbol{m}, \boldsymbol{c})$. The Bayesian setting [Calvetti et Somersalo, 2007] allows to rigorously treat inverse problems with noisy data and uncertain forward models. Notice that the output of the inverse problem in this stochastic framework is no more a single deterministic value but a probability distribution that summarizes all available information about measurements and uncertain parameters.

Let us collect all the uncertain inputs in the vector $\mathbf{x} = \{\boldsymbol{m}, \boldsymbol{c}\} \in \mathbb{R}^d$. In the Bayesian setting, both the uncertain inputs and the measured quantities are random variables, denoted respectively with the upper-case letters $\mathbf{X}$ and $\mathbf{D}$. The probability density of the uncertain input $\mathbf{X}$, denoted with $\sigma(\mathbf{x})$, represents the degree of belief about possible values of $\mathbf{X}$ before observing the data. For this reason, it is called the *prior* PDF. The actual measured data $\boldsymbol{d}$ is an observed realization of $\mathbf{D}$. Solving the reconstruction problem in the Bayesian sense means to find the conditional probability distribution of the

variable $\mathbf{X}$ given the observed data $\boldsymbol{d}$:

$$\begin{aligned} \text{given:} \quad & \sigma(\mathbf{x}) \text{ and } \boldsymbol{d} \\ \text{find:} \quad & \sigma^{\text{pos}}(\mathbf{x}|\boldsymbol{d}). \end{aligned} \tag{2.27}$$

The conditional probability distribution $\sigma^{\text{pos}}(\mathbf{x}|\boldsymbol{d})$ is called the posterior distribution of $\mathbf{X}$, and it expresses what we know about $\mathbf{X}$ after observing the realization of the measurements $\boldsymbol{d}$. *Bayes rule* is used to define the posterior probability density $\sigma^{\text{pos}}(\mathbf{x}|\boldsymbol{d})$ for the uncertain input quantities given measurements of the quantities of interest [Kaipio et Somersalo, 2005]:

$$\sigma^{\text{pos}}(\mathbf{x}|\boldsymbol{d}) = \frac{\ell(\boldsymbol{d}|\mathbf{x})\,\sigma(\mathbf{x})}{\int \ell(\boldsymbol{d}|\mathbf{x})\,\sigma(\mathbf{x})\,\mathrm{d}\mathbf{x}}. \tag{2.28}$$

The conditional probability $\ell(\boldsymbol{d}|\mathbf{x})$ is called the *likelihood* function, because it expresses the likelihood of a measurement outcome given a realization $\mathbf{x}$ of the inputs.

The construction of the likelihood models the information about the measurement noise and other modeling uncertainties. Often in the classical literature [Kaipio et Somersalo, 2005], measurement errors are considered as additive noise $\boldsymbol{H}$ (with realization η), mutually independent of $\mathbf{X}$:

$$\mathbf{D} = f(\mathbf{X}) + \boldsymbol{H}. \tag{2.29}$$

The probability density $p_{\boldsymbol{H}}(\boldsymbol{\eta})$ of the noise $\boldsymbol{H}$ is assumed to be known. In this case the likelihood distribution becomes:

$$\ell(\boldsymbol{d}|\mathbf{x}) = \prod_{j=1}^{n_m} \ell_{d_j}(d_j|\mathbf{x}) = \prod_{j=1}^{n_m} p_{H_j}(d_j - f_j(\mathbf{x}))\ , \tag{2.30}$$

where $p_{H_j}(\eta_j)$ is the Gaussian probability density representing the noise associated to the j-th measured quantity, and n_m is the number of independent measurements. In the present work, we will assume measurement errors as Gaussian noise with zero mean and a standard deviation that quantifies the experimental error. With this additive noise model, the likelihood models the discrepancy between the model output $\boldsymbol{f}(\mathbf{x})$ and the measured data, which is equal to the measurement error if the model is considered to be exact.

Modeling the prior density $\sigma(\mathbf{x})$ consists in writing in a formal way the qualitative prior belief on the unknown parameters. The prior is usually chosen by expert judgment or defined on previous analysis and uncertainty characterization (see [Kaipio et Somersalo, 2005, Chapter 3] for more details about different prior models). In the absence of additional information, one may simply choose a prior that is uninformative. In this work, we will be always considering the

prior belief that input random parameters are independent, hence their joint prior $\sigma(\mathbf{x})$ is the product of the univariate prior of each stochastic variable:

$$\sigma(\mathbf{x}) = \prod_{i=1}^{d} \sigma_{X_i}(x_i). \tag{2.31}$$

In order to compute means, moments and other statistical indicators of the posterior, often the only possible way is by drawing samples [Stuart, 2010]. This because the normalization integral in the expression for the posterior distribution (2.28) is difficult to be evaluated in the case of general prior and likelihood models. The most common class of sampling methods used at this purpose are Markov Chain Monte Carlo methods, which are introduced in the next section.

2.5.1 Markov Chain Monte Carlo

The most common class of sampling methods for characterizing the posterior distribution, defined in eq. (2.28), are Markov Chain Monte Carlo (MCMC) methods [Gilks *et al.*, 1996; Tarantola, 2005]. They are a broad class of methods used to draw samples from a probability density by constructing a Markov chain whose stationary distribution converges to the desired posterior. Several implementations of MCMC exist in literature, that differ in the way they construct a Markov chain such that the stationary distribution is exactly the distribution of interest.

A well-known implementation of MCMC is the Metropolis-Hastings algorithm [Hastings, 1970]. For this algorithm, at each step k, the next sample (state) of the chain $\mathbf{x}_{k+1}$ is chosen by firstly sampling a *candidate* point $\tilde{\mathbf{x}}$ from a *proposal* distribution $q(\cdot, \mathbf{x}_k)$ that may depend on the current state $\mathbf{x}_k$. The candidate point has then to pass and acceptance test, and it is accepted with a probability $\alpha(\mathbf{x}_k, \tilde{\mathbf{x}})$, where

$$\alpha(\mathbf{x}_k, \tilde{\mathbf{x}}) = \min\left\{1, \frac{\pi(\tilde{\mathbf{x}})q(\mathbf{x}_k, \tilde{\mathbf{x}})}{\pi(\mathbf{x}_k)q(\tilde{\mathbf{x}}, \mathbf{x}_k)}\right\}, \tag{2.32}$$

where $\pi(\cdot)$ is the target distribution from which one wants to sample, and in the case of inverse problems it coincides with the posterior given by eq. (2.28). If the candidate point is accepted, then the chain moves to the next state $\mathbf{x}_{k+1} = \tilde{\mathbf{x}}$, otherwise the chain does not move, and $\mathbf{x}_{k+1} = \mathbf{x}_k$. This algorithm converges theoretically to the target distribution independently on the choice of the proposal distribution, but a good proposal is fundamental to have a good convergence in a reasonable time (see [Gilks *et al.*, 1996, Chapers 1 and 3] for more details). To give an example, here the Metropolis-Hastings algorithm with single-site updating and Gaussian proposal density is reported in Algorithm 2. It will be used in applications in following parts of this work

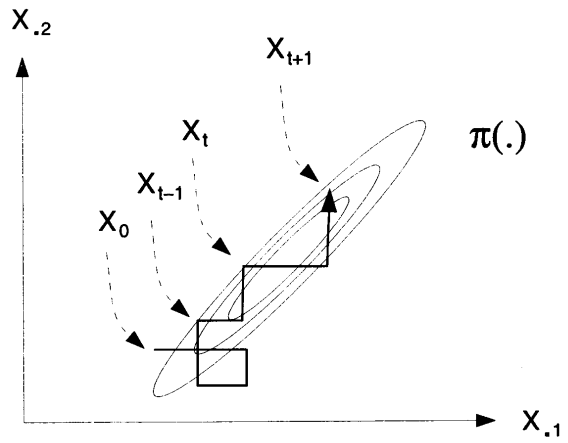

Figure 2.4: Illustration of the single-site updating Metropolis-Hastings MCMC (taken from [Gilks *et al.*, 1996]).

to draw samples from posterior distributions. An illustration of the algorithm is also given in Figure 2.4.

Once the MCMC algorithm has run, samples can be exploited to characterize the joint posterior distribution of the unknowns. The marginal distribution of the inferred parameters $\boldsymbol{m}$ given the measurements

$$\sigma^{\text{pos}}(\boldsymbol{m}|\boldsymbol{d}) \propto \int \sigma^{\text{pos}}(\boldsymbol{m}, \boldsymbol{c}|\boldsymbol{d}) d\boldsymbol{c} \tag{2.34}$$

can be directly estimated by kernel density estimation (KDE) [Silverman, 1986] from the MCMC sample. Given such sample, it is also possible to compute posterior statistics of the parameters, such as moments, quantiles. Sampling means and variances of the rebuilt quantities can be estimated exploiting eq. (2.4),

$$\mu(m_i) = \frac{1}{N_{MCMC} - b} \sum_{k=b+1}^{N_{MCMC}} m_i^k \tag{2.35}$$

$$\sigma^2(m_i) = \frac{1}{N_{MCMC} - b - 1} \sum_{k=b+1}^{N_{MCMC}} (m_i^k - \mu(m_i))^2. \tag{2.36}$$

Note that, in this sampling expectations, the first b iterations of the chain have been neglected. It is a common practice to discard the first iterations of a chain, called *burn-in* [Brooks *et al.*, 2011], since they can be strongly influenced by the starting values and so they may not provide correct information about the posterior. Burn-in is a simple way to account for the dependence of the chain on the starting value, but it is not very efficient, since it obliges to discard many sampling points.

Algorithm 2 A Metropolis-Hastings MCMC algorithm with single-site updating and Gaussian proposal density (see [Tryoen *et al.*, 2014])

Initialize the chain state $\mathbf{x}^{k=0} \in \mathbb{R}^d$.
For $k = 1, 2, \ldots, N_{\text{MCMC}}$:
For each input random variable x_i, $i = 1, \ldots, d$:

1. Draw a candidate $\tilde{x}_i$ from a Gaussian proposal distribution centered at x_i^k and with standard deviation ω_i
2. Call the candidate sample vector $\tilde{\mathbf{x}}^{k,i} = (\mathbf{x}_{/x_i}^{k-1}, \tilde{x}_i)$
3. Evaluate the acceptance rate:

$$\alpha(\mathbf{x}^{k-1}, \tilde{\mathbf{x}}^{k,i}) = \min\left\{1, \frac{\ell(\boldsymbol{d}|\tilde{\mathbf{x}}^{k,i})\, \sigma_{\mathbf{x}}(\tilde{\mathbf{x}}^{k,i})}{\ell(\boldsymbol{d}|\boldsymbol{x}^{k-1})\, \sigma_{\mathbf{x}}(\mathbf{x}^{k-1})}\right\} \tag{2.33}$$

4. Draw $u^{k,i} \sim \mathcal{U}(0,1)$ from a uniform distribution in [0,1]
5. Perform the acceptance test: if $u^{k,i} < \alpha(\mathbf{x}^{k-1}, \tilde{\mathbf{x}}^{k,i})$ then $x_i^k = \tilde{x}_i$, else $x_i^k = x_i^{k-1}$.

In order to have a chain that is representative of the real posterior distribution, the proposal distribution widths ω_i, of the Gaussian proposal in Algorithm 2, have to be chosen carefully. If the proposal distribution widths are too large, most of the proposed moves will be rejected, and the chain will not move very often. On the other hand, if they are too small, most proposed values will be accepted but the chain will explore very slowly the entire support of the posterior. Adaptive strategies exist to choose proper values of ω_i [Gilks *et al.*, 1996]. An efficient way to verify if a good value for ω_i has been chosen is to plot the empirical autocorrelation at lag s, denoted by $\beta(s)$, for each component of the input vector. The autocorrelation quantifies the interdependence of the iterations of the chain, therefore a proper value for the proposal distribution width implies a quick decay of the autocorrelation with the lag.

MCMC algorithms produce a Markov Chain that converges to a stationary distribution that coincides with the posterior distribution, independently of the initial state. However, to obtain good inference results from sequences of MCMC samples, it is necessary that the chain has converged to the true posterior. Theory guarantees this condition as the number of iterations approaches infinity, however, run the MCMC algorithm for a sufficiently high number of iterations to ensure a reasonable approximation. Unfortunately, no universal rule exists to, so the convergence must be assessed for each MCMC estimation with convergence diagnostics [Brooks *et al.*, 2011].

The most simple and straightforward approach for assessing convergence is based on visual inspection of plots of chain traces and histograms of the MCMC sample [Lynch, 2007, Chapter 6]. Often, the lack of convergence is caused by poor mixing of the chain, which is the degree to which the Markov chain explores the support of the posterior distribution. Poor mixing can arise from inappropriate choice of proposal distributions or from attempting to estimate models with highly correlated variables. If the plot of the trace of values for each variable exhibits asymptotic stationary behavior over the last set of iterations, meaning that variance and the mean value of the sample stays relatively constant, this can be considered as a satisfactory proof for convergence. Another similar approach is to plot a histogram for every set of iterations of arbitrary size after the burn-in. If the histograms are not visibly different between the intervals, it is another reasonable evidence for convergence. There exist other more formal and rigorous statistical approaches to assess convergence of a MCMC chain [Raftery et Lewis, 1970; Cowles et Carlin, 1996], but they will not be used in this work. With most diagnostics methods, convergence cannot be guaranteed. While the evidence for lack of convergence implies lack of convergence, the absence of this evidence does not guarantee convergence in the chain. However, if one or more criteria provide good convergence results, this can assure the users that their sample will provide valid inferences.

It is well known that MCMC-based methods struggle to produce accurate estimates when the parameter space dimension is large. In effect, the Markov chain must explore the high dimensional space to reveal all regions of high posterior probability. Such exploration suffers from the *curse of dimensionality* [Donoho, 2000], where the cost of thorough parameter space exploration scales exponentially with the dimension of the space.

2.5.2 Accelerating MCMC with surrogate models

As seen in Algorithm 2, MCMC methods, as all sampling methods, require several thousand of model evaluations to achieve convergence. Furthermore, unlike in standard MC methods, the evaluation in different samples from the same chain can not be run in parallel, since the acceptance of a new sample requires to know the evaluation of the likelihood at the previous. This makes impossible the direct application of MCMC methods to expensive computational modes, like in CFD applications. One possible way to reduce the computational cost in such cases is to replace the expensive model evaluation by the use of a surrogate model [Marzouk *et al.*, 2007; Birolleau *et al.*, 2014]. In this case, in the likelihood expression (2.30) the exact model evaluation $f(\mathbf{x})$ is replaced by the prediction given by the surrogate model $\hat{f}(\mathbf{x})$.

When replacing the actual model $f(\mathbf{x})$ with the surrogate $\hat{f}(\mathbf{x})$, the model

for the measurement errors given in eq. (2.29) becomes:

$$\boldsymbol{D} = \hat{\boldsymbol{f}}(\mathbf{X}) + \boldsymbol{H} + \boldsymbol{\Delta}(\mathbf{x}) \,, \tag{2.37}$$

where $\boldsymbol{\Delta}(\mathbf{x})$ is the term that accounts for the discrepancy between the actual model and the surrogate, *i.e.* the surrogate modeling error. If this error is small enough with respect to the measurement errors, that is when the surrogate is converging to the actual function of interest, it is safe to neglect the surrogate modeling error from the likelihood without loss of accuracy, as done for example in [Marzouk et Najm, 2009] or [Constantine *et al.*, 2011].

2.6 Conclusions

This chapter introduced direct uncertainty propagation and global sensitivity analysis. A brief review was given on the literature related to this subject, introducing to different techniques related to the statistical (Bayesian) approach to uncertainties. Some more insights have been given about the tools that will be exploited in the following part of the work, like sampling methods, statistical spectral methods for UQ and surrogate models, ANOVA decomposition and global sensitivity analysis. Also the inverse UQ problem has been formulated in a Bayesian framework, and MCMC algorithms have been described to sample from the posterior distribution of the inferred parameters.

Chapter 3

Improved surrogate model: coupled Kriging-PDD

In this chapter, an improved surrogate modeling strategy is proposed. It relies on the coupling between Universal Kriging and Polynomial Dimensional Decomposition. Firstly, the two starting-point techniques are recalled and detailed, then the coupling algorithm is described. Finally, the strategy is assessed on several analytical functions of increasing dimensionality and used to propagate uncertainties for engineering applications in the field of atmospheric entry, namely the hypersonic flow around the HEG cylinder and the unidimensional ablation of a piece of TACOT material.

3.1 Introduction

In the previous chapter, it has been shown that a common practice for UQ problems involving the evaluations of expensive computational models is to resort using a surrogate model to replace evaluations of the actual model. Training an accurate but at the same time computationally efficient surrogate is not a trivial task. Problems arise especially when the dimensionality of the input tends to increase, due to the so-called *curse of dimensionality*, that causes the number of required training points to increase exponentially with the dimension of the input. In this chapter, a technique to build an improved surrogate model is introduced, which tries to improve the accuracy of existing classes of surrogates while remaining usable for medium-to-high dimensions. It consists in coupling two different metamodeling strategies, Universal Kriging and Polynomial Dimensional Decomposition, in order to reduce the effects of some of their limitations. First, in Section 3.2, the two basic surrogate models will be described. Then, in 3.3 the coupling strategy is described. In Section 3.4, the coupling strategy is assessed on several test functions of increasing dimensionality, and finally in Sections 1.3.2 and 3.6, two applications

are proposed in the atmospheric entry context.

3.2 Starting point: existing metamodels

Let us suppose to have a d dimensional vector $\mathbf{x} \in \mathbb{R}^d$ of uncertain input parameters, with $\mathbf{x} = \{x_1, \ldots, x_d\}$. In a probabilistic (statistical) framework, it is possible to consider this vector as a random variable, defined in a probability space $(\mathbb{R}^d, \mathcal{B}_d, \Sigma_{\mathbf{X}})$, where $\mathcal{B}_d$ is the Borel σ-algebra of the event space $\mathbb{R}^d$ and $\Sigma_{\mathbf{X}}$ is its probability measure. We refer to the joint probability density function of the input vector as $\sigma_{\mathbf{x}}(\mathbf{x})$. The assumption of independence of the components of this random vector implies that its PDF can be written as

$$\sigma_{\mathbf{x}}(\mathbf{x}) = \prod_{i=1}^{d} \sigma_{x_i}(x_i) \ , \tag{3.1}$$

where $\sigma_{x_i}(x_i)$ is the marginal PDF of each component x_i. Let us suppose that the response of the computational model $y = f(\boldsymbol{x})$ is represented by a scalar function of interest, hence $y \in \mathbb{R}$.

3.2.1 Universal Kriging

A very popular technique for building surrogate models is Kriging [Sacks *et al.*, 1989b; Cressie, 1993]. Its name is due to [Matheron, 1971], who firstly formalized the idea introduced by [Krige, 1951] in the geostatistics literature. It can be also seen as an implementation of the so-called Gaussian Process regressions [Rasmussen et Williams, 2006] in *supervised learning*, referring to the *statistical learning* literature.

The main idea of Kriging method is to consider the output of the deterministic model $f(\mathbf{x})$ as a realization of a Gaussian stochastic process $F(\mathbf{x})$. In Universal Kriging (UK), the stochastic process is written in the form of the sum of a deterministic linear regression model and a stochastic departure term [Dubourg, 2011]:

$$F(\mathbf{x}) = \sum_{j=1}^{n} \beta_j h_j(\mathbf{x}) \ + Z(\mathbf{x}) = \boldsymbol{h}^T(\mathbf{x})\boldsymbol{\beta} + Z(\mathbf{x}) \ , \tag{3.2}$$

where $h_j(\mathbf{x})$ are n linearly independent known regression functions, β_j are unknown weights, and $Z(\mathbf{x})$ is a stationary Gaussian process with zero mean function

$$\mathbb{E}[Z(\mathbf{x})] = 0 \qquad \forall \mathbf{x} \in \mathbb{R}^d \ , \tag{3.3}$$

and a stationary autocovariance function

$$\mathbb{E}[Z(\mathbf{x}), Z(\mathbf{x}')] = \sigma^2 k(\mathbf{x} - \mathbf{x}') \qquad \forall \mathbf{x}, \mathbf{x}' \in \mathbb{R}^d. \tag{3.4}$$

The autocovariance $\sigma^2 k(\mathbf{x}-\mathbf{x}')$ is assumed to be known. Normally, in the case of computer models this is not the case, therefore it needs to be modeled empirically by choosing among a family of correlation models, such as exponential, Gaussian or Matèrn correlation functions (see [Picheny, 2009] or Appendix B.4), and estimating the unknown *hyperparameters*, namely the covariance magnitude σ^2 and the correlation lengths $\boldsymbol{\theta}$, from the training set $\mathbf{x}_{obs} = \{\mathbf{x}_i : i = 1, \dots, N_s\}$ (see Appendix B.5). The idea behind this model is that the departure of the response of the actual model from the regression, even if deterministic, can be seen as a sample path of a suitable stochastic process. Notice that the hypothesis of a stationary covariance is not strictly necessary, but it is often done in the classical literature on Kriging interpolation. There are examples of Kriging metamodels with non-stationary covariance models in the Kriging literature [Xiong *et al.*, 2007], and in the statistical learning literature this hypothesis is often not done, to enable more complex kernel structures (see for example [Duvenaud, 2014]). However, the use of non-stationary kernels is beyond the purpose of this work.

The Gaussian process assumption in Eq. (3.2) holds for both the unobserved values $f(\mathbf{x})$ and the observations of the model at the training points $\boldsymbol{f}_{obs} = (f(\mathbf{x}_1), \dots, f(\mathbf{x}_{N_s}))^T$. Thanks to this, it is possible to write the joint normal PDF of the observed and unobserved values:

$$\begin{Bmatrix} F(\mathbf{x}) \\ F(\mathbf{x}_{obs}) \end{Bmatrix} \sim \mathcal{N}\left(\begin{Bmatrix} \boldsymbol{h}^T(\mathbf{x})\boldsymbol{\beta} \\ H\boldsymbol{\beta} \end{Bmatrix}, \sigma^2 \begin{bmatrix} 1 & \boldsymbol{c}^T(\mathbf{x}) \\ \boldsymbol{c}(\mathbf{x}) & C \end{bmatrix} \right), \tag{3.5}$$

where $\boldsymbol{h}(\mathbf{x}) = (h_1(\mathbf{x}), \dots, h_n(\mathbf{x}))^T$ is the vector of basis functions, H is a $N_s \times n$ matrix whose elements are the evaluation of the j-th basis function at the i-th training point $H_{ij} = h_j(\mathbf{x}_i)$, $\boldsymbol{c}(\mathbf{x})$ is a vector of length N_s whose elements $c_i = k(\mathbf{x}-\mathbf{x}_i)$ contain the correlations between the point $\mathbf{x}$ and each training point $\mathbf{x}_i$, and C is a $N_s \times N_s$ matrix of correlations among training points $C_{ij} = k(\mathbf{x}_i - \mathbf{x}_j)$.

The aim of Kriging is to build a *linear predictor* of the function of interest $F(\mathbf{x})$. This means that the predictor $\hat{F}(\mathbf{x})$ is written as a linear combination of the observations $\boldsymbol{F}_{obs} = (F(\mathbf{x}_1), \dots, F(\mathbf{x}_{N_s}))^T$ of the actual model at the N_s training points:

$$\hat{F}(\mathbf{x}) = \sum_{i=1}^{N_s} F(\mathbf{x}_i) a_i(\mathbf{x}) = \boldsymbol{a}^T(\mathbf{x}) \boldsymbol{F}_{obs}. \tag{3.6}$$

where $a_i(\mathbf{x})$ are unknown weights. We want the predictor to be the *best linear unbiased predictor* (BLUP) of the quantity of interest. This means that it has to minimize the mean-squared error (MSE) between the model and the predictor

$$\mathrm{MSE}(\mathbf{x}) = \mathbb{E}\left[\left(F(\mathbf{x}) - \hat{F}(\mathbf{x}) \right)^2 \right], \tag{3.7}$$

while respecting the constraint of unbiasedness:

$$\mathbb{E}\left[F(\mathbf{x}) - \hat{F}(\mathbf{x}) \right] = 0. \tag{3.8}$$

Note that these expectations are taken with respect to the joint Gaussian PDF of the observed and unobserved values. Therefore, the optimization problem consists in finding the optimal set of weights $\boldsymbol{a}^*(\mathbf{x})$ of the linear predictor with respect to the following optimization problem

$$\begin{aligned} \boldsymbol{a}^*(\mathbf{x}) = \arg\min_{\boldsymbol{a}} \ & \mathbb{E}\Big[\big(F(\mathbf{x}) - \boldsymbol{a}^T(\mathbf{x})\boldsymbol{f}_{obs}\big)^2\Big] \\ \text{subject to} \quad & \mathbb{E}\big[F(\mathbf{x}) - \boldsymbol{a}^T(\mathbf{x})\boldsymbol{f}_{obs}\big] = 0. \end{aligned} \tag{3.9}$$

By solving the optimization problem and replacing the optimal $\boldsymbol{a}^*(\boldsymbol{x})$ in (3.6) (see Appendix B.2), it is possible to obtain the mean of the best unbiased linear predictor, that is used as a surrogate model $\hat{f}(\mathbf{x})$ of the original computational model $f(\mathbf{x})$:

$$\begin{aligned} f(\mathbf{x}) \approx \hat{f}(\mathbf{x}) = \mu_k(\mathbf{x}) = \mathbb{E}[\hat{F}(\mathbf{x})] = \\ = \boldsymbol{h}^T(\mathbf{x})\boldsymbol{\beta} + \boldsymbol{c}(\boldsymbol{x})^T C^{-1}(\boldsymbol{f}_{obs} - H\boldsymbol{\beta}) \ , \end{aligned} \tag{3.10}$$

with

$$\boldsymbol{\beta} = (H^T C^{-1} H)^{-1} H^T C^{-1} \boldsymbol{f}_{obs}. \tag{3.11}$$

It is also possible to have an expression for the MSE between the model and the predictor, which can be used as a local model-based error estimate

$$\begin{aligned} s_k^2(\mathbf{x}) = \mathbb{E}\big[(\hat{F}(\mathbf{x}) - F(\mathbf{x}))^2\big] = \\ = \sigma^2\Big(1 + \boldsymbol{u}(\mathbf{x})^T (H^T C^{-1} H)^{-1} \boldsymbol{u}(\mathbf{x}) - \boldsymbol{c}(\mathbf{x})^T C^{-1} \boldsymbol{c}(\mathbf{x})\Big) \ , \end{aligned} \tag{3.12}$$

where

$$\boldsymbol{u}(\boldsymbol{x}) = H^T C^{-1} \boldsymbol{c}(\mathbf{x}) - \boldsymbol{h}(\mathbf{x}). \tag{3.13}$$

More details about Universal Kriging can be found in Appendix B.

Remark 1. Let us suppose to apply the predictor at a location $\mathbf{x} = \mathbf{x}_i$ coinciding to the one of a training point. Then $c(\mathbf{x}_i)$ coincides to the i-th column $C_{:i}$ of C. If a covariance model without nugget effect is used, for which $k(\mathbf{x}, \mathbf{x}) = 1$, then it is possible to show [Lophaven *et al.*, 2002] that the Kriging predictor is an interpolation of the training data

$$\hat{f}(\mathbf{x}_i) = f_i^{obs} = f(\mathbf{x}_i). \tag{3.14}$$

It can be also shown that the prediction error at the training point is null

$$s_k^2(\mathbf{x}_i) = 0 \ , \tag{3.15}$$

meaning that observations are supposed to be error-free.

Including numerical simulation errors in the metamodel training

Often, when dealing with the construction of surrogate models for computer codes, the output of the computational model is considered to be exact, hence to coincide with the actual model output. In other words, the training data are considered to be *noiseless*. When choosing a correlation model for noiseless data, it is assumed that $k(\mathbf{x}, \mathbf{x}) = 1$. As shown in Remark 1, in these cases, the Kriging predictor behaves like an interpolation of the function of interest at the training data.

In this work, instead, as discussed in Section 1.5, the results of the numerical simulations can be affected by some numerical error, since the heat flux value is very sensitive to the mesh-shock alignment, and it is very difficult to properly align the shock and the mesh when automatically performing an high number of simulations on each sampling point. Hence, to account for the noise on the training data, it is possible to add a (small) nugget effect (Appendix B.4.4) to the autocorrelation model of the Gaussian process [Neal, 1997]:

$$\mathbb{E}[Z(\mathbf{x}), Z(\mathbf{x}')] = \sigma^2 k(\mathbf{x} - \mathbf{x}') + \sigma_n^2 \delta(\mathbf{x} - \mathbf{x}') \qquad \forall \mathbf{x}, \mathbf{x}'. \tag{3.16}$$

In such cases, the C matrix of correlations between training points can be rewritten as:

$$C_{(n)} = C + \frac{\sigma_n^2}{\sigma^2} I \,, \tag{3.17}$$

where I is the identity matrix. This translates in the fact that the Kriging surrogate model is no more an exact interpolation of the training data, but becomes a regression. Furthermore, the predictive variance is no more equal to zero at the training points, but has a positive value equal to σ_n^2.

It has to be noticed that the Kriging process implemented in the ForK library [Lockwood] used in this work (as in many other practical implementations), includes also the nugget effect variance in the covariance model even for noiseless data. From a theoretical point of view, this should not be correct, but in practice this can often be useful, since a small nugget effect can improve the conditioning [Gramacy et Lee, 2012; Andrianakis et Challenor, 2012] of the numerical problem related to the inversion of the matrix C.

Ordinary Kriging

In real-world applications, often the Universal Kriging is not used, because it can be difficult to determine relevant basis functions for the regression term in Equation (3.2) without the proper *a priori* knowledge about the evolution of the quantity of interest. Hence, one is limited to use the simpler technique called *Ordinary Kriging* [Lophaven *et al.*, 2002], in which the regression functions are chosen as $y_1(\boldsymbol{x}) = 1$ and $y_j(\boldsymbol{x}) = 0$ for $j \neq 1$, which means that only a constant regression term is kept and then only β_1 needs to be determined.

In Ordinary Kriging, the stochastic process can be written in the form of the sum of a constant deterministic mean model and a stochastic departure term, as follows

$$F(\boldsymbol{x}) = \beta + Z(\boldsymbol{x}). \tag{3.18}$$

In this way, the mean of the stochastic predictor, that can be used as surrogate model, simplifies to:

$$f(\boldsymbol{x}) \simeq \hat{f}(\boldsymbol{x}) = \mu_k(\boldsymbol{x}) = \left(\boldsymbol{c}(\boldsymbol{x}) + \frac{\mathbf{1}\big(1 - \mathbf{1}^T C^{-1}\boldsymbol{c}(\boldsymbol{x})\big)}{\mathbf{1}^T C^{-1}\mathbf{1}}\right)^T C^{-1}\boldsymbol{f}_{obs}\ , \tag{3.19}$$

where $\mathbf{1}$ is unity vector.

This fact simplifies the method but can limit the power of the metamodeling technique, thus requiring a higher number of training points in order to obtain a representation of the output function with a certain level of accuracy.

3.2.2 Sparse adaptive Polynomial Dimensional Decomposition

In this subsection, the adaptive sparse-Polynomial Dimensional Decomposition (sPDD) implementation used in this work is detailed. This adaptive strategy to build a PDD metamodel with the sparse approach has been recently proposed by [Tang *et al.*, 2016]. In the original paper, the technique is addressed primarily to problems of global sensitivity analysis, but it can be employed also as a surrogate model for other applications. In this manuscript, this technique is used as a component of the improved surrogate developed in the present chapter, and it is also retained as a reference for assessing the performances of the proposed approach.

Classical PDD representation

Let us briefly recall the ANOVA representation of a multivariate function. More details about it can be found in Section 2.4.1, or for example, in [Sobol', 1993, 2001]. In general, the multivariate function of interest can be represented by the following expansion:

$$f(\mathbf{x}) = f_0 + \sum_{s=1}^{d} \sum_{i_1<\cdots<i_s}^{d} f_{i_1\ldots i_s}(x_{i_1}, \ldots, x_{i_s}). \tag{3.20}$$

This representation is called ANOVA decomposition if, for any component function $f_{i_1\ldots i_s}(x_{i_1}, \ldots, x_{i_s})$, the orthogonality condition in equation (2.13) is respected.

At this point, the component functions of the ANOVA decomposition of the function of interest are not determined yet. Polynomials can be efficiently

used to represent the component functions in the ANOVA expansion. In literature several metamodeling techniques are used at this purpose. Two of the most well known are generalized Polynomial Chaos expansion (Section 2.3.2) and Polynomial Dimensional Decomposition (PDD). As in [Tang *et al.*, 2016], the PDD is here preferred for its closer structure with respect to ANOVA decomposition. Let us consider an orthogonal set of univariate polynomials $\{\psi^j(x_i); j = 0, 1, \dots\}$ in the Hilbert space $\mathcal{L}_2$. The orthogonality condition means that for any couple of polynomials in the set:

$$\int_{\mathbb{R}} \psi^j(x_i)\, \psi^k(x_i)\, \sigma_{x_i}(x_i)\, \mathrm{d}x_i = \gamma_{j,x_i}\, \delta_{jk} \quad \text{with} \quad \delta_{jk} = \begin{cases} 1, & \text{if } j = k \\ 0, & \text{otherwise} \end{cases}, \tag{3.21}$$

where j and k are the orders of the polynomials for the variable x_i and with the normalization constant γ_{j,x_i} determined as

$$\gamma_{j,x_i} = \int_{\mathbb{R}} \left(\psi^j(x_i)\right)^2 \sigma_{x_i}(x_i)\, \mathrm{d}x_i. \tag{3.22}$$

As for generalized Polynomial Chaos, polynomials from the Askey family [Xiu et Karniadakis, 2002] can be used as orthogonal basis with respect to the PDFs of the input variables. As known in literature (see [Rahman, 2008] for example), specific orthogonal polynomials are associated to common input probability distributions also for PDD. For example uniform distributions can be associated to Legendre polynomials and Gaussian distributions to Hermite polynomials.

Let us consider a T-dimensional component function of the ANOVA decomposition, with $1 \leq T \leq d$. It is possible to write it in the compact form

$$f_{i_1,i_2,\dots,i_T}(x_{i_1}, x_{i_2}, \dots, x_{i_T}) = f_{\boldsymbol{i}_T}(\mathbf{x}_T). \tag{3.23}$$

The assumption of independence between the components of the random input vector allows the tensorized polynomial

$$\Psi^{\boldsymbol{j}_T}_{\boldsymbol{i}_T}(x_{i_1}, x_{i_2}, \dots, x_{i_T}) = \prod_{k=1}^{T} \psi^{j_k}(x_{i_k}) \qquad \text{with} \quad \boldsymbol{j}_T = \{j_1, j_2, \dots, j_T\} \tag{3.24}$$

to be a multivariate basis in the T-dimensional space. Exploiting the zero-mean property (eq. (2.14)) of ANOVA expansion, each T-dimensional component function can be expanded by tensor product as in [Rahman, 2008]:

$$f_{i_1,i_2,\dots,i_T}(x_{i_1}, x_{i_2}, \dots, x_{i_T}) = \sum_{j_T=1}^{\infty} \cdots \sum_{j_1=1}^{\infty} C^{j_1,j_2,\dots,j_T}_{i_1,i_2,\dots,i_T} \prod_{k=1}^{T} \psi^{j_k}(x_{i_k}). \tag{3.25}$$

In compact form, this is equivalent to:

$$f_{\boldsymbol{i}_T}(\mathbf{x}_T) = \sum_{j_T,\dots,j_1}^{\infty} C^{\boldsymbol{j}_T}_{\boldsymbol{i}_T} \Psi^{\boldsymbol{j}_T}_{\boldsymbol{i}_T}(\mathbf{x}_T). \tag{3.26}$$

In practice, this infinite expansion must be truncated, leaving m terms for each dimension, where m is the maximum polynomial order taken into account.

$$f_{i_1,i_2,\dots,i_T}(x_{i_1},x_{i_2},\dots,x_{i_T}) \approx \sum_{j_T=1}^{m}\cdots\sum_{j_1=1}^{m} C_{i_1,i_2,\dots,i_T}^{j_1,j_2,\dots,j_T}\prod_{k=1}^{T}\psi^{j_k}(x_{i_k}). \tag{3.27}$$

Thus, repeating the same process for every component function of the ANOVA decomposition, the polynomial dimensional decomposition $f_m(\mathbf{x})$ of order m of the function of interest $f(\mathbf{x})$ can be written as follows:

$$\begin{aligned} f(\mathbf{x}) \approx & \hat{f}(\mathbf{x}) = f_m(\mathbf{x}) = \\ = & f_0 + \sum_{i=1}^{d}\sum_{j=1}^{m} C_i^j\psi^j(x_i) + \sum_{i_1<i_2}^{d}\sum_{j_2=1}^{m}\sum_{j_1=1}^{m} C_{i_1,i_2}^{j_1,j_2}\psi^{j_1}(x_{i_1})\psi^{j_2}(x_{i_2}) + \\ & + \sum_{i_1<i_2<i_3}^{d}\sum_{j_3=1}^{m}\sum_{j_2=1}^{m}\sum_{j_1=1}^{m} C_{i_1,i_2,i_3}^{j_1,j_2,j_3}\psi^{j_1}(x_{i_1})\psi^{j_2}(x_{i_2})\psi^{j_3}(x_{i_3}) + \\ & + \dots + \sum_{i_1<\dots<i_d}^{d}\sum_{j_d=1}^{m}\cdots\sum_{j_1=1}^{m} C_{i_1,i_2,\dots,i_d}^{j_1,j_2,\dots,j_d}\prod_{k=1}^{d}\psi^{j_k}(x_{i_k}). \end{aligned} \tag{3.28}$$

Hence, the total size P of the m-th order PDD expansion of an q-dimensional function is $P = (1+m)^d$.

Remark 2. Notice that the PDD and PC expansions, even if they share the same orthogonal polynomial basis, when truncated do not lead to the same representation of the function. In fact, the terms in a p-th order PC approximation, given in Eq. (2.8) and here recalled for clarity

$$\begin{aligned} f(\mathbf{x}) \approx & c_0\Gamma_0 + \sum_{i_1=1}^{d} c_{i_1}\Gamma_1(x_{i_1}) + \sum_{i_1=1}^{d}\sum_{i_2=1}^{i_1} c_{i_1,i_2}\Gamma_2(x_{i_1},x_{i_2}) + \\ & + \dots + \sum_{i_1=1}^{d}\sum_{i_2=1}^{i_1}\cdots\sum_{i_p=1}^{i_{p-1}} c_{i_1\dots i_p}\Gamma_p(x_{i_1},\dots,x_{i_p}) \ , \end{aligned} \tag{3.29}$$

are organized with respect to the increasing order of polynomials. In contrast, the terms in the PDD approximation, given in Eq. (3.28), are organized with respect to the degree of interaction between input variables. Therefore, significant differences in terms of accuracy and convergence properties may arise when truncating the expansions. In this way, the PDD is able to give the priority to exploit low-order parameter interactions, following the principle where low-order ANOVA component functions are dominant for most engineering cases. For this reason, PDD is preferred over Polynomial Chaos (PC) expansion in this work. In fact, as pointed out in [Yadav et Rahman, 2014],

if a (stochastic) function is highly nonlinear, but contains rapidly diminishing interaction effects of multiple variables, the PDD approximation is expected to be more effective than the PC approximation, as the lower-variate interaction terms of the PDD approximation can be just as nonlinear by selecting appropriate values of maximum polynomial degree in the PDD. However, many more terms and expansion coefficients must be included in the PCE approximation to capture such a high nonlinearity.

Computation of the expansion coefficients

As for other spectral approaches for UQ, different methods are available to compute the coefficients of the PDD expansion. As in [Tang *et al.*, 2016], a regression approach is preferred with respect to a projection approach. Projection approaches require the computation of d-dimensional integrals. Usually, they are computed by multidimensional quadrature rules or by sampling methods. Quadrature rules, however, suffering from the curse of dimensionality, become too expensive for high-dimensions, while sampling methods are costly since their convergence rate is slow. A regression approach is instead supposed to be more suitable for problems with a moderate-to-high number of input variables, since it allows to choose more flexibly the location and the number of sampling points. Nevertheless, it has the characteristic of creating a metamodel which does not exactly interpolate the training points, but acts like a regression.

For regression methods, the sampling points (or experimental design) are chosen as a set of samples of the input random vector, for examples by Latin Hypercube [McKay *et al.*, 1979] or quasi Monte Carlo (qMC) sampling [Caflisch, 1998]. It is possible to denote the training set as $\mathcal{X} = (\mathbf{x}^1, \mathbf{x}^2, \dots, \mathbf{x}^N)^T$. Its size N needs to be larger than the PDD expansion size P, so that the problem is not under-determined. It is common to choose $2P \leq N \leq 3P$. The model output at each training point is collected in the vector $\mathcal{Y} = (y^1, y^2, \dots, y^N)^T$.

For convenience, it is possible to rewrite the PDD expansion in a vectorial form:

$$f_m(\mathbf{x}) = \boldsymbol{C}^T \boldsymbol{\psi}(\mathbf{x}) \,, \tag{3.30}$$

where $\boldsymbol{C} = (C_0, \dots, C_{P-1})^T$ is a vector containing all of the P expansion coefficients and $\boldsymbol{\psi}(\mathbf{x}) = (\boldsymbol{\psi}_0, \dots, \boldsymbol{\psi}_{P-1})$ contains all the multivariate basis polynomials including $\psi_0 = 1$.

The idea of regression methods is to compute the expansion coefficients by minimizing the error in $\mathcal{L}_2$ norm between the surrogate model and the actual model evaluations at the training points. This means that the coefficients are solution of the following optimization problem:

$$\boldsymbol{C} = \arg\min_{\tilde{\boldsymbol{C}}} \sum_{i=1}^{N} \left(y^i - \tilde{\boldsymbol{C}}^T \boldsymbol{\psi}(\mathbf{x}^i) \right)^2 . \tag{3.31}$$

The solution of the least-squares regression (LSR) problem (3.31) can be found by using a variational approach:

$$\frac{\partial}{\partial C_j}\left[\sum_{i=1}^{N}\left(y^i - \boldsymbol{C}^T\boldsymbol{\psi}(\mathbf{x}^i)\right)^2\right] = 0 \qquad \text{for} \qquad j = 0, \ldots, P-1. \tag{3.32}$$

This leads to the solution the following linear system:

$$A^T A\, \boldsymbol{C} = A^T \mathcal{Y}\ , \tag{3.33}$$

where A is a $N \times P$ matrix whose elements $A_{ij} = \psi_j(\mathbf{x}^i)$ are the evaluations of the j-th polynomial at the i-th training point.

Global Sensitivity Indices with PDD

The Sobol' global sensitivity indices can be obtained in a straightforward way with PDD by analytical manipulation of the expansion coefficients, as it is possible also for generalized Polynomial Chaos. PDD (eq. (3.28)) has the advantage of being organized with respect to an increasing order of parameter interactions, while the gPC formulation (eq. (2.8)) is organized with respect to an increasing degree of multivariate polynomials. For this reason, in order to compute the Sobol' indices for PC, additional reordering of the PC terms is needed, with respect to the random variables they depend on.

Let us now see how to get the variance-based sensitivity indices form PDD coefficients. Exploiting the orthogonality of the polynomial basis, the variance of the model output can be computed as:

$$\mathrm{Var}[f_m(\mathbf{x})] = \mathbb{E}[f_m^2(\mathbf{x})] - f_0^2 = \sum_{j=1}^{P-1} C_j^2 \gamma_j. \tag{3.34}$$

If using normalized polynomials, all the normalization coefficients are equal to 1, and the variance reduces to the sum of all expansion coefficients. It is then straightforward to write the variance-based global sensitivity indices by using the PDD expansion coefficients:

$$S_{i_1,\ldots,i_T} = \frac{\mathrm{Var}[f_{i_1,\ldots,i_T}]}{\mathrm{Var}[f_m(\mathbf{x})]} = \frac{1}{\mathrm{Var}[f_m(\mathbf{x})]} \sum_{j \subseteq (i_1,\ldots,i_T)} C_j^2 \gamma_j. \tag{3.35}$$

The total sensitivity index S_i^{tot} is simply obtained by summing all the indices $S_{i_1,\ldots,i_T}$ that involve a contribution of the variable x_i.

Adaptive dimension reduction for the model representation

For practical problems, in particular the ones with a moderate-to-large number of stochastic input variables, the size of the PDD expansion becomes really big, therefore requiring a very high number training points to solve the

least-squares regression problem (3.31). Since the actual model needs to be evaluated at each training point, this makes the problem not feasible in case of problems involving expensive computer codes. For this reason, techniques for an adaptive dimension reduction of the representation have been proposed [Yadav et Rahman, 2014; Tang *et al.*, 2016]. In the following, we will focus on the implementation by [Tang *et al.*, 2016], which is based on three levels of dimension reduction. Its first step consists in applying a truncation to the interaction dimensionality, a widely used approach for the ANOVA component functions. Then two additional levels of dimension reduction are considered: an adaptive ANOVA decomposition, and a stepwise regression to retrieve the most significant polynomials using a variance-based or an error-based selection criterion

Truncated ANOVA: Since the lower-order interaction terms often have the greater impact on the output [Sobol', 2001], the ANOVA expansion can be truncated at a maximum dimension of component functions $\nu < d$, called the truncation dimension

$$f(\mathbf{x}) = f_0 + \sum_{T=1}^{\nu} \sum_{i_1<\cdots<i_T}^{d} f_{i_1,i_2,\ldots,i_T}(x_{i_1}, x_{i_2}, \ldots, x_{i_T}). \tag{3.36}$$

This reduces to ν the maximum interaction dimensionality taken into account in the truncated ANOVA expansion.

Adaptive ANOVA: Even considering a truncated ANOVA expansion with small dimension ν, for problems with a high dimension of the stochastic space d, the computation of all the terms in the decomposition can be still very expensive. This problem can be addressed by using the adaptive ANOVA decomposition, which can be written:

$$f(\mathbf{x}) = f_0 + \sum_{T=1}^{\nu} \sum_{i_1<\cdots<i_T}^{D_T} f_{i_1,i_2,\ldots,i_T}(x_{i_1}, x_{i_2}, \ldots, x_{i_T}). \tag{3.37}$$

In adaptive ANOVA, $D_T < d$ is the active dimension of the component function of T-th order.

In this adaptive approach, it is considered $D_1 = d$. The active dimension for higher order terms is determined with a variance-based criterion, which is used for choosing the active dimension D_2, and, for simplicity, then we set $D_T = D_2$ for $T \geq 3$. The criterion consists in computing the first-order terms variances

$$\mathrm{Var}(f_i(\mathbf{x})) = \sum_{j=1}^{m} (C_i^j)^2 \gamma_i^j \qquad \text{for} \qquad i = 1, \ldots, d\,, \tag{3.38}$$

and the total first order variance

$$\mathrm{Var}_{1st}(f(\mathbf{x})) = \sum_{i=1}^{d} \mathrm{Var}(f_i(\mathbf{x})) = \sum_{i=1}^{d}\sum_{j=1}^{m} (C_i^j)^2 \gamma_i^j. \tag{3.39}$$

Then, assuming the sensitivity indices to be monotonically-decreasing ordered with respect to i, it is possible to choose the active dimension D_2 for second order ANOVA functions such as:

$$\sum_{i=1}^{D_2} \mathrm{Var}(f_i(\mathbf{x})) \geq p\, \mathrm{Var}_{1st}(f(\mathbf{x}))\ , \tag{3.40}$$

where p is a user-defined constant parameter $\in [0, 1]$, usually chosen to be very close to 1.

Sparse PDD representation: Even with an adaptive-truncated ANOVA expansion, the computational cost required to compute the classical PDD expansion for each component function can still be very high for high-dimensional inputs. However, in many real-world problems the contribution of some polynomial terms is negligible with respect to the accuracy of the metamodel or their impact on the global variance [Blatman et Sudret, 2010a]. This fact can be exploited to build a sparse PDD representation without compromising the accuracy of the UQ result.

The global adaptive sparse PDD algorithm can be described combining the two adaptive ANOVA steps and a sparse PDD representation:

1. Construct a full set of PDD representation (given the maximum polynomial order m) for all the first-order ANOVA component functions

$$f(\mathbf{x}) \simeq f_0 + \sum_{i=1}^{d} f_i(x_i) = f_0 + \sum_{i=1}^{d}\sum_{j=1}^{m} C_i^j \psi_j(x_i). \tag{3.41}$$

   Compute then the first-order terms variances and the total first-order variance (eq. (3.38) and (3.39)), and determine the active dimension D_2 for second order ANOVA functions with the criterion in equation (3.40).

2. Reduce the size of the first order PDD expansion expressed in equation (3.41), eliminating the less important terms with respect to the chosen criteria (variance-based or error-based). The obtained first-order reduced basis is denoted by $\{\psi_{\alpha^1}\}$

3. After defining a truncation dimension ν, enrich the model by adding significant higher-order PDD polynomials $\{\psi_{\alpha^{2+}}\}$ to the reduced first-order basis, by means of Algorithm 3 or 4, obtaining the final basis $\{\psi_{\alpha^F}\}$.

In [Tang *et al.*, 2016] two different algorithms were proposed to choose the most relevant polynomial terms to be added to the sparse basis: the first based on the variance (Algorithm 3) and the second on the metamodeling error (Algorithm 4). The common idea is that new terms are added to the existing polynomial set by adding recursively one new polynomial candidate from the set of higher-order ANOVA functions. During this recursive procedure, the polynomial terms that are quantified as irrelevant to the output are discarded. In the variance-based algorithm the terms are chosen according to their relative

Algorithm 3 Variance-based adaptive PDD by stepwise regression

Initialization of the first-order PDD basis $\{\psi^w\} = \{\psi_{\alpha^1}\}$
for $\psi_{\alpha_i} \in \{\psi_{\alpha^{2+}}\}$ **do**
  Add ψ_{α_i} into $\{\psi^w\}$, namely $\{\psi^w\} = \{\psi^w, \psi_{\alpha_i}\}$
  Solve the regression system to determine the PDD coefficients
  Compute the total variance $\mathrm{Var}(f^w(\mathbf{x})) = \sum_k (C_{\alpha_k})^2 \gamma_{\alpha_k}$
  for $\psi_{\alpha_j} \in \{\psi^w\}$ **do**
    if $(C_{\alpha_j})^2 \gamma_{\alpha_j} / \mathrm{Var}(f^w(\mathbf{x})) < \theta$ **then**
      Eliminate this polynomial: $\{\psi^w\} = \{\psi^w\} \backslash \psi_{\alpha_j}$
    end if
  end for
end for
Solve the final regression system based on the constructed basis $\{\psi^F\}$

contribution to the total variance associated to the output function of interest: if the ratio between the contribution of the term and the total variance is lower than a certain threshold θ (for example a typical value is $\theta = 10^{-5}$), the term is discarded. This algorithm, firstly introduced by [Tang *et al.*, 2016], proved to be very effective for the computation of the sensitivity indices. The error-based algorithm [Blatman et Sudret, 2010b; Tang *et al.*, 2016], instead, selects the most relevant terms according to their contribution to the global metamodeling accuracy computed with *leave-one-out cross-validation* (LOOCV) error (see Appendix C.2 for more details about this technique). This second criterion states that, if the decrease of the model accuracy is smaller than threshold ε_{Q^2} when excluding the polynomial term in consideration, it is then possible to eliminate this term from the basis. This second criterion is more effective for the construction of a surrogate model with higher accuracy with respect to the previous criterion. Note that the initialization of the first order multivariate PDD bases (Operation 1) can be also realized by this second criterion.

Remark 3. [Tang *et al.*, 2016] pointed out a disadvantage of Algorithm 4, compared to Algorithm 3, consisting in the fact that it requires the solution of a bigger number of regression systems. For instance, in order to select significant polynomials from the set $\{\Psi\}$ whose cardinality is denoted by $|\Psi|$, we need

Algorithm 4 Error-based adaptive PDD by stepwise regression

Initialization of the first order PDD basis $\{\psi^w\} = \{\psi_{\alpha^1}\}$
for $\psi_{\alpha_i} \in \{\psi_{\alpha^{2+}}\}$ **do**
  Add ψ_{α_i} into $\{\psi^w\}$, namely $\{\psi^w\} = \{\psi^w, \psi_{\alpha_i}\}$
  Solve the regression system to determine the PDD coefficients
  Evaluate the metamodel accuracy Q_i^2 by LOOCV error
  if $Q_i^2 \geq Q_{tgt}^2$ **then**
    exit
  end if
  for $\psi_{\alpha_j} \in \{\psi^w\}$ **do**
    Solve the regression system with the polynomial basis $\{\psi^w\} \backslash \psi_{\alpha_j}$
    Evaluate the accuracy of the metamodel $Q_{i\backslash\alpha_j}^2$ without ψ_{α_j}
    if $Q_i^2 - Q_{i\backslash\alpha_j}^2 < \varepsilon_{Q^2}$ **then**
      Eliminate this polynomial: $\{\psi^w\} = \{\psi^w\} \backslash \psi_{\alpha_j}$
    end if
  end for
end for
Solve the final regression system based on the constructed basis $\{\psi^F\}$

to solve $|\Psi| + 1$ least-squares systems, while Algorithm 3 requires only one. Although the cost of resolving a linear system is negligible compared to the one of a deterministic model simulation, the difference in computational cost between the two algorithms becomes visible when high-dimensional problems are treated.

3.3 Coupling strategy (PDD-UK)

As pointed out by [Kersaudy *et al.*, 2015], often the lack of *a priori* knowledge on the function of interest does not allow a choice for appropriate basis functions for the regression term in Universal Kriging (equation (3.2)). For this reason, often in real-world applications, the simpler Ordinary Kriging is preferred to Universal Kriging. In Ordinary Kriging, as seen in Section 1, the regression term is replaced by a constant mean term, whose value is learned by the training process. In a previous work, the blind-Kriging method [Joseph *et al.*, 2008] was developed in the attempt to find a representative set of basis functions for the unknown quantity of interest by exploiting a Bayesian selection technique. More recently, [Kersaudy *et al.*, 2015] proposed to use a sparse Polynomial Chaos (PC) expansion computed with least-angles regression (LARS) algorithm to obtain a set of relevant regression functions to build an Universal Kriging surrogate model.

The idea here is to take inspiration by [Kersaudy *et al.*, 2015], but using

instead the final basis obtained with the adaptive sparse PDD algorithm (Sec. 3.2.2) as regression functions for the Universal Kriging surrogate model. This is a very sparse representation of the function of interest that is able to achieve a good metamodeling accuracy and to discard the stochastic variables whose influence on the output value is negligible. The use of the most influential PDD polynomials as basis for the Universal Kriging improves the quality of the final metamodel by adding the most relevant information about the trends of the quantity of interest to the regression term. To be concise, we will denote this

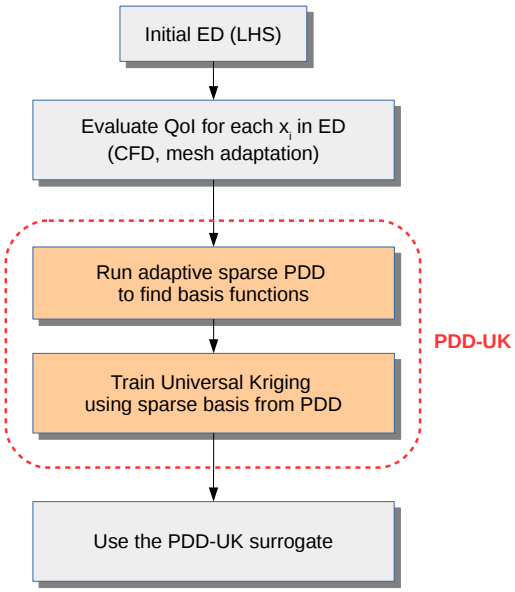

Figure 3.1: Diagram showing the coupling strategy behind the PDD-UK surrogate modeling technique.

coupled metamodeling method as PDD-UK technique. The algorithm used here to couple Universal Kriging with the sparse-PDD basis functions is the following:

1. Build an experimental design (set of training points)
2. Train an adaptive sparse PDD metamodel (see Section 2):

$$\hat{f}(\boldsymbol{x}) = f_0 + \sum_{\alpha \in \alpha^F} C_\alpha \psi_\alpha \qquad \text{with} \quad C_\alpha \psi_\alpha = C_{i_\alpha}^{j_\alpha} \psi_{j_\alpha}(x_{i_\alpha}) \,, \tag{3.42}$$

where i_α and j_α are respectively multi-indices. This allows to obtain a set of relevant basis function $\{\psi_{\alpha^F}\}$ describing the main trends of the QoI. Notice that also $\psi_0 = 1$ must be kept in the set of basis function for the Universal kriging.

3. Train the Kriging surrogate, with Universal Kriging technique, using the final basis functions of the sparse PDD $\{\psi_{\alpha^F}\}$ as regression functions

$$F(\boldsymbol{x}) = \sum_{j \in \alpha^F} \beta_j \psi_j + Z(\boldsymbol{x}). \tag{3.43}$$

The coupling algorithm is resumed in Figure 3.1.

Notice that the original coupling algorithm of Kersaudy and coworkers is more complex. In fact, for each step of the cycle used to enrich the sparse PC basis, they build a coupled UK metamodel and compute cross-validation error for each metamodel. Then, they chose the final surrogate as the best with respect to the LOOCV error. Even if this approach could lead to further improvements of the quality of the metamodel, it seems quite complex and computationally expensive, especially for high dimensional functions where a lot of polynomial terms are required in the sparse PDD representation. However, this difference in the implementation does not change the main idea of the coupling process, and this feature could always be added later.

3.3.1 Parameters of interest

In this section, an overview is given on the user-defined parameters of the coupled strategy, with their role and suggestions on a possible range of values. They are all listed in Table 3.1.

Name	Possible values	Role
m	$[1, \infty]$	maximum polynomial degree for PDD
ν	$[1, d]$	maximum size of ANOVA interaction for PDD
p	$[0, 1]$	variance threshold for adaptation in sparse-PDD
ϵ or θ	$[0, 1]$	error threshold for adaptation in sparse-PDD
Q^2_{tgt}	$[0, 1]$	accuracy threshold for adaptation in sparse-PDD

Table 3.1: Parameters chosen by the user in the algorithm for the construction of the PDD-UK surrogate.

One of the most relevant is the maximum polynomial order m, since it strongly influences the accuracy of the intermediate sparse PDD surrogate, and hence the amount of information added to the final coupled surrogate model. As it has been shown in Chapter 3, it's value needs to be chosen according to the function of interest, and, if necessary, a preliminary test can be carried out. A bad value can spoil the convergence of the final surrogate model. The value on ν, the maximum size of ANOVA interaction terms, is easier to determine, as it can be left equal to the number of variables for smaller input, or fixed to 3 or 4 for higher inputs, following the principle that

in most application cases, most relevant interactions occur at lower interaction orders. For the sensitivity of the sparse-PDD to the thresholds p, ϵ, θ and Q^2_{tgt} one can refer to [Tang *et al.*, 2016]. Author's experience would suggest to fix them to standard values and concentrate mostly on m and ν to improve the convergence of the surrogate model.

3.3.2 Exploiting active dimensions in Kriging

In cases where just a subset of the input variables contributes to the variation of the output, it could be possible to reduce the size of the input to facilitate the training of the surrogate model, thus reducing the computational cost and improving its quality. The simple strategy that can be exploited in the proposed framework consists in building the final PDD-UK considering as input variables of the Universal Kriging just the ones whose total sensitivity indices, computed with the preliminary sparse-PDD, are non-null. In this way, all the inputs which show an irrelevant contribution to the output are neglected, simplifying the training problem and the fitting of the hyperparameters. This simple sensitivity-based dimension reduction strategy will be just tested here for the 100-dimension Sobol' function 3.4.5 and the TACOT ablation engineering case 1.3.2.

Other techniques for the input size reduction and their coupling with Kriging surrogate models have been developed in literature. Two examples are the Active Subspaces method [Constantine *et al.*, 2014] and anchored-ANOVA [Margheri et Sagaut, 2016], but the in-deep analysis and comparison are not object of study in this chapter. We will talk about Active Subspaces in Chapter 5.

3.4 Analytical test cases

The PDD-UK will be used in this section to build surrogate models for different analytical test functions, verify the convergence of the metamodeling errors with the size of the Experimental Design and compare results with the ones obtained with Ordinary Kriging and sparse-PDD. Clearly, a comparison with Universal Kriging is not done, because in real-world it would be difficult to choose appropriate regression functions without a proper *a priori* knowledge about the function or a further processing step like done with PDD-UK. Furthermore, the sensitivity of the coupled method with respect to some parameters of the sparse adaptive selection of the PDD basis function will be analyzed. In Table 3.2, the characteristics of the test function used in the work are reported for clarity. Test 2 is a 2D function built with the purpose of testing the coupled metamodel and later the adaptation approach. Test 3, 4, 5 are well known test functions for metamodels for UQ and optimization

taken from literature.

Name	Input dim.	Domain	Function
TEST 1	1	$[-1, 1]$	$f(\boldsymbol{x}) = g(10x - 2)\cos(5x^2)$
TEST 2	2	$[-1, 1]$	$f(\boldsymbol{x}) = g(10x_1 - 2)\cos(5x_1^2)\cos(x_2^2)(3 - x_2)^2$ with $g(s) = \frac{s\lvert s\rvert}{1+s^2}$
TEST 3	3	$[-\pi, \pi]$	$f(\boldsymbol{x}) = \sin x_1 + a\sin^2 x_2 + bx_3^4 \sin x_1$
TEST 4	8	$[0, 1]$	$f(\boldsymbol{x}) = \prod_{i=1}^{8} \frac{\lvert 4x_i-2\rvert+c_i}{1+c_i}$
TEST 5	100	$[0, 1]$	$f(\boldsymbol{x}) = \prod_{i=1}^{100} \frac{\lvert 4x_i-2\rvert+c_i}{1+c_i}$

Table 3.2: Test functions used for the assessment of the UK-PDD method

3.4.1 TEST 1: 1D test function

This first test case deals with a test function described in [Chkifa *et al.*, 2013]:

$$f(x) = g(10x - 2)\cos(5x^2) \quad \text{with} \quad g(s) = \frac{s|s|}{1 + s^2}. \tag{3.44}$$

The function is evaluated in the domain $x \in [-1, 1]$. It is plotted for clarity in Figure 3.2a. We mainly use this simple 1D test to draw in Figure 3.2b a visual

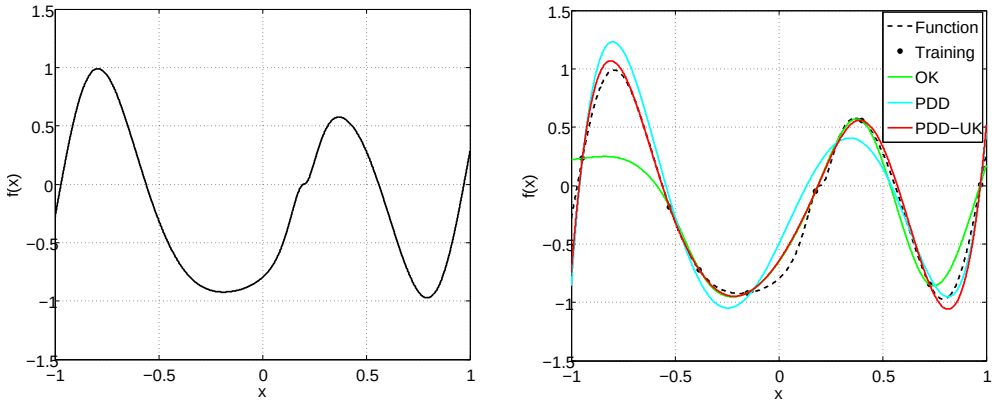

(a) Test function (b) Metamodels

Figure 3.2: TEST 1: Visual comparison between the actual 1D test function 3.2a and the surrogate models 3.2b.

comparison between the original test function and different surrogate models trained on 8 LHS training points.

From the plot, it is clear that the Ordinary kriging with Matérn kernel (in green), while representing a good surrogate model in regions rich of training

points thanks to its interpolation characteristic, it is not able to capture the trend of the function at the first peak. Instead PDD with $m = 5$ (in blue) captures very well the trends of the function, but does not give a very accurate surrogate model of the function. The PDD-UK (in red) is able to couple the good aspects of the two previous techniques: as the Ordinary Kriging, it passes exactly through the training points, and in addition it captures pretty well the first peak thanks to trend information given by the PDD polynomials.

3.4.2 TEST 2: 2D test function

For this test case, we introduce the following bivariate function, which has been derived from the univariate test case [Chkifa *et al.*, 2013] already used in TEST 1:

$$f(\boldsymbol{x}) = g(10x_1 - 2)\cos(5x_1^2)\cos(x_2^2)(3 - x_2)^2 \quad \text{with} \quad g(s) = \frac{s|s|}{1 + s^2}. \tag{3.45}$$

The function is evaluated in the domain $\boldsymbol{x} \in [-1, 1]^2$, and it is plotted for clarity in Figure 3.3. This function can be used as first simple case to test

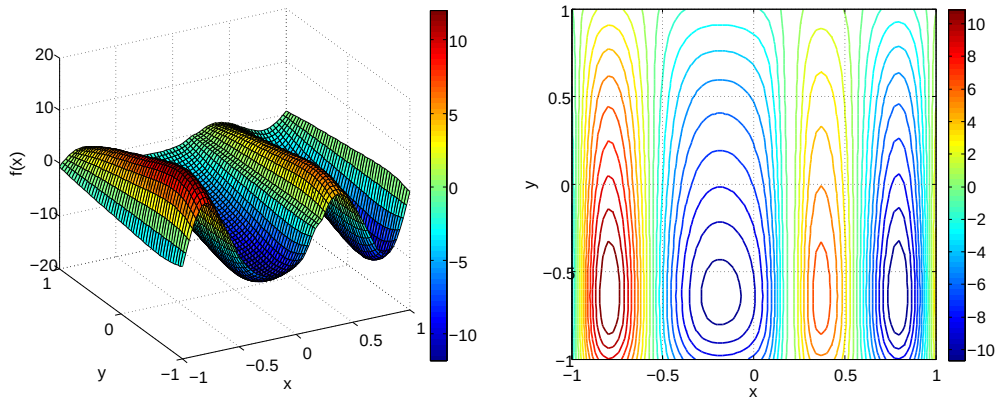

(a) (b)

Figure 3.3: TEST 2: Three-dimensional plot (a) and 2D contour (b) of the 2D test function in equation (3.45).

the convergence of the coupled PDD-UK method when increasing the size of the experimental design. The convergence test is performed by increasing the number of training points, chosen with Latin Hypercube sampling, and by computing the RMSE between the metamodels and the true function evaluated in 100000 LHS test points. Computations are repeated fifteen times for each size of the experimental design, in order to account for the variability of the LHS experimental design. The tested surrogate models are: Ordinary Kriging

with exponential kernel function, sparse PDD with $m = 5$ and the coupled PDD-UK. Results are reported in Figure 3.4.

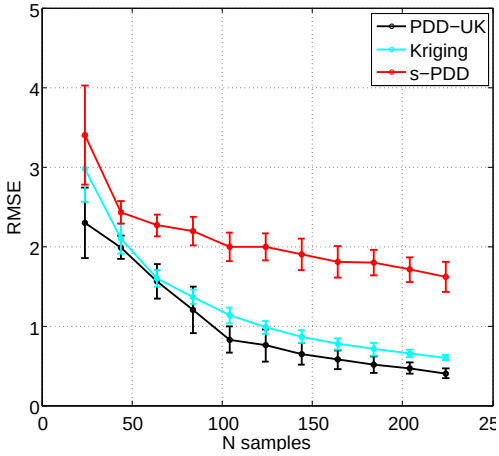

Figure 3.4: TEST 2: Mean RMSE convergence comparison between Ordinary Kriging, sparse PDD and coupled PDD-UK metamodels, $m = 5$, $\varepsilon_{Q^2} = 10^{-8}$

First of all, it can be seen that the RMSE of the coupled metamodel decreases monotonically with the increase of the number of training points. Its mean value, computed on the fifteen different numerical experiments, is always lower than the ones of the two starting metamodels. For this particular case, the OK metamodel performs better than the sparse PDD, but the PDD-UK is still able to improve the results of the Ordinary Kriging exploiting the function trends.

3.4.3 TEST 3: Ishigami function

The well-known Ishigami function is considered another analytical example to verify the convergence of the method and to test the sensibility to the parameter m of the PDD, since sometimes it could be difficult to determine *a priori* a good value of maximum polynomial order. This function, which is widely used for benchmarking in global sensitivity analysis, depends on three independent input parameters and can be written as:

$$f(\boldsymbol{x}) = \sin x_1 + a \sin^2 x_2 + b x_3^4 \sin x_1, \tag{3.46}$$

where the input random variables $\boldsymbol{x} = \{x_1, x_2, x_3\}$ are uniformly distributed over $[-\pi, \pi]$. The constants are set to $a = 7$ and $b = 0.1$, as done for example in [Tang *et al.*, 2016; Kersaudy *et al.*, 2015]. As training sets, we use Latin Hypercube designs of different sizes. Each training plan is used to build an Ordinary Kriging metamodel, a sparse-PDD and a coupled PDD-UK surrogate. The obtained metamodels are tested on a LHS plan of 100000 points.

A low maximum PDD order of $m = 3$ is initially considered and the two variance-based (v) and error-based (e) selection algorithms are compared. Table 3.3 reports values of RMSE, MSE_r and Q^2 (see Appendix C for their definitions) for all the surrogates. Firstly, it can be noticed from this compar-

N_s		OK	s-PDDe	PDD-UKe	s-PDDv	PDD-UKv
40	RMSE	2.19369	3.93583	3.14090	103.9839	-
	MSE_r	0.35438	1.09102	0.70760	1.0050	-
	Q^2	0.413350	0.534050	0.864321	-	-
80	RMSE	1.62157	2.92508	1.04595	74.7111	-
	MSE_r	0.19322	0.62815	8.0481e-2	1.00314	-
	Q^2	0.798325	0.527088	0.940881	-	-
160	RMSE	1.0656	2.53986	0.47179	7.54097	-
	MSE_r	8.27647e-2	0.47480	1.6393e-2	1.12117	-
	Q^2	0.897168	0.519746	0.973951	0.855120e-1	-
320	RMSE	0.66843	2.6088	0.34148	4.09612	-
	MSE_r	3.29050e-2	0.50122	8.58841e-3	0.79921	-
	Q^2	0.959829	0.633514	0.990904	0.572308	-
640	RMSE	0.442623	2.537008	0.227492	3.910519	0.369953
	MSE_r	1.442877e-2	0.474011	3.811484e-3	0.782575	1.007985e-2
	Q^2	0.981296	0.560523	0.995585	0.532891	0.986737

Table 3.3: TEST 3: Actual error measures for the Ordinary Kriging, Sparse-PDD with error-based (e) and variance-based (v) selection algorithms and coupled PDD-UK surrogate models of the Ishigami function, $m = 3$, $\theta = 10^{-5}$, $\varepsilon_{Q^2} = 10^{-8}$.

ison that the variance-based adaptation approach for the sparse-PDD always produces a less accurate surrogate model with respect to the error based one. For this reason, it can happen that the set of basis functions given to the Universal Kriging in the coupled approach, in the case of variance-based approach, is not enough representative of the actual function trends for the method to converge. Hence no results are obtained for the coupled method. The error based approach, instead, is always able produce a representative set of basis functions and the coupled method is then able to converge. When considering the small value of $m = 3$ for the maximum PDD order, OK performs better than sparse-PDD for the Ishigami function. Except for the 40 points training plan, the coupled method always delivers a better surrogate model than the Ordinary Kriging and the sparse-PDD, having a smaller metamodeling error (RMSE and MSE_r) and higher LOOCV metamodeling accuracy Q^2. This means that the additional information in the regression part of the Kriging surrogate is actually able to improve the representation of the function, or, seen from the opposite point of view, that the Kriging departure term is able to improve the representation given only by the sparse-PDD regression. The

behavior in the case of 40 points training plan is likely to be caused by the fact that this set of points is too small to give enough information for the PDD to produce an accurate enough set of basis functions.

The same analysis is repeated when considering a higher maximum PDD order of $m = 10$. In Table 3.4 results are shown. When using the error-based adaptive approach, sparse-PDD surrogates are this time better than the Ordinary Kriging ones. The coupled PDD-UK approach is always able to further reduce the metamodeling error. However, it is important to mention that, as pointed out in [Tang *et al.*, 2016], the computational cost associated with the error-based criterion can be way higher than the one needed to perform the variance-based criterion because a higher number of regression systems need to be solved to build the sparse representation. While this can be negligible for simple low-dimensional cases such as the Ishigami function, it can be relevant for higher-dimensional problems.

N_s		OK	s-PDDe	PDD-UKe	s-PDDv	PDD-UKv
40	RMSE	2.193697	3.68578	2.19369	-	-
	MSE_r	0.354380	1.00000	0.354380	-	-
	Q^2	0.413350	-	0.413350	-	-
80	RMSE	1.621572	1.08661	1.00083	50.22814	1.625250
	MSE_r	0.19322	8.69541e-2	7.376024e-2	1.30340	0.194121
	Q^2	0.798325	0.994236	0.995617	0.999215	0.792188
160	RMSE	1.06008	0.636108	0.35959	5.358411	1.0424
	MSE_r	8.2764e-2	2.9793e-2	9.5226e-3	2.114611	8.00259e-2
	Q^2	0.897168	0.995448	0.998263	0.999857	0.912285
320	RMSE	0.668438	0.32831	8.42948e-2	5.51245	0.63282
	MSE_r	3.2905e-2	7.93837e-3	5.233157e-4	2.23793	2.94929e-2
	Q^2	0.959829	0.998906	0.999896	0.999981	0.963671
640	RMSE	0.442623	7.291311e-2	1.559595e-2	5.161115	0.321574
	MSE_r	1.442877e-2	3.915368e-4	1.791371e-5	1.961754	7.615962e-3
	Q^2	0.981296	0.999900	0.999994	0.999978	0.989006

Table 3.4: TEST 3: Error measures and accuracies for the Ordinary Kriging, Sparse-PDD with error-based (e) and variance-based (v) selection algorithms and coupled PDD-UK surrogate models of the Ishigami function, $m = 10$, $\theta = 10^{-5}$, $\varepsilon_{Q^2} = 10^{-8}$.

The comparison between the $m = 3$ and the $m = 10$ cases shows, as it could be expected, that this parameter has a high influence also on the quality of the final coupled metamodel, hence it must be chosen wisely. When no information at all is available about the trends of the function to guide the choice of this parameter, a preliminary convergence study of the sparse-PDD algorithm varying m could be usefully performed on the available design of experiments to help to choose a good value. This means repeating the training

of different sparse-PDD (or better of different PDD-UK) varying the value of m, and choosing as surrogate the one which shows lower metamodeling error.

A further test of the convergence of the PDD-UK method can be performed on the sensitivity indices associated to the Ishigami function, since analytical values are known in literature (see for example [Tang *et al.*, 2016, Sec. 5.1]). A comparison with the numerical values obtained with the three metamodeling techniques under analysis and direct Monte Carlo sampling (MC) (Section 2.4.2) is reported in Table 3.5. Values for PDD are directly computed with the expansion coefficients (see 2), Monte Carlo sampling is performed to obtain the sensitivities from the two other Kriging-based techniques. The size of the training set is fixed at 200 points to be consistent with the results in [Tang *et al.*, 2016, Tab. 3].

SI	Exact	Kriging	s-PDDv	PDD-UKv	s-PDDe	PDD-UKe	MC
S_1	0.3138	0.3558	0.3133	0.3486	0.3126	0.3137	0.3147
S_2	0.4424	0.4804	0.4397	0.4949	0.4448	0.4431	0.4419
S_3	0	0.0063	0	0.0064	0	0.0046	0.0045
S_{12}	0	0.0053	0	0.0035	0	-0.0002	0
S_{13}	0.2436	0.1462	0.2470	0.1426	0.2423	0.2386	0.2389
S_{23}	0	0.0031	0	0.0022	0	0.0001	0
S_{123}	0	0.0029	0	0.0018	0.0023	0.0001	0
f_0	3.5	3.4861	3.5023	3.4785	3.4983	3.4946	3.4955
D	13.845	11.8388	13.9338	12.7512	13.8550	13.8793	13.8720
Q^2		0.91604	0.99959	0.92383	0.99991	0.99996	
Eval.		200	200	200	200	200	6×100000

Table 3.5: TEST 3: numerical mean f_0, variance D, metamodel accuracy Q^2 and sensitivity indices S of the Ishigami function obtained with different metamodeling techniques and comparison with exact values and Monte Carlo results. For PDD, these values have been used $m = 10$, $\nu = 3$, $\varepsilon_{Q^2} = 10^{-8}$, $\theta = 10^{-3}$.

A general good convergence is shown for the first order sensitivity indices, while the convergence of the second order indices is more difficult for the sampling-based computations, especially when they have really small (or null) values. This because there is an intrinsic difficulty in the MC computation of small sensitivity indices [Sobol' et Myshetskaya, 2008], and also because the computation of high-order indices depends on the estimated values for lower-order indices [Sobol', 1993], hence it can be spoiled by a loss of accuracy (see for example the negative index in Tab. 3.5 for PDD-UKe).

Note that, in practical applications, the direct MC approach on the actual function would be drastically more expensive than the others, due to the high number of model evaluations required. Therefore, the metamodel-based tech-

niques represent a very attractive option, due to the good trade off between accuracy and efficiency.

3.4.4 TEST 4: 8D Sobol' function

To test the approach on a higher-dimensional problem, the eight-dimensional Sobol' function is considered [Tang *et al.*, 2016]. Its expression is:

$$f(\boldsymbol{x}) = \prod_{i=1}^{8} \frac{|4x_i - 2| + c_i}{1 + c_i} \,, \tag{3.47}$$

where the components of the input vector $\boldsymbol{x}$ are uniformly distributed over $[0, 1]$ and the vector of positive coefficients is $\boldsymbol{c} = \{1, 2, 5, 10, 20, 50, 100, 500\}$.

SI	Exact	Kriging (MC)	s-PDD	PDD-UK (MC)	MC
S_1	0.603	0.654	0.632	0.607	0.603
S_2	0.268	0.265	0.284	0.269	0.271
S_3	0.067	0.045	0.048	0.072	0.069
S_4	0.020	0.015	0.018	0.025	0.022
S_5	0.0055	0.004	0.006	0.010	0.009
S_6	0.000	0.002	0.002	0.005	0.003
S_7	0.000	0.002	0.003	0.004	0.003
S_8	0.000	0.001	0.003	0.004	0.002
f_0	1.0000	1.0064	0.9988	0.9960	0.9998
D	0.1380	0.1185	0.1307	0.1302	0.1378
Q^2		0.9394	0.9896	0.9913	
Eval.		150	150	150	100000

Table 3.6: TEST 4: numerical mean, variance, metamodel accuracy and sensitivity indices of the 8-dimensional Sobol function obtained with different metamodeling techniques and comparison with exact values and Monte Carlo results, $m = 4$, $\nu = 2$.

A first comparison between Ordinary Kriging, variance-based sparse PDD and the coupled PDD-UK method can be performed on the first order sensitivity indices obtained with the three surrogate modeling techniques. Results are reported in Table 3.6, and a further comparison is done with analytical (exact) results and values obtained with a classical Monte Carlo sapling performed on the original function.

Results show a general good convergence of all methods. It can be noticed that, while being slightly more accurate in some cases, especially for the most influent indices, the coupled PDD-UK approach is not able to outperform the sparse-PDD in the approximation of the sensitivity indices, as observed also

for the Ishigami function. Hence, in general, it is not necessary to perform the MC sampling on the final UK-PDD surrogate to obtain the SIs, but one could simply rely on the use of the PDD coefficients computed during the intermediate construction of the sparse-PDD surrogate to compute the sensitivities. In this way the SIs would come almost effortlessly and with a good accuracy.

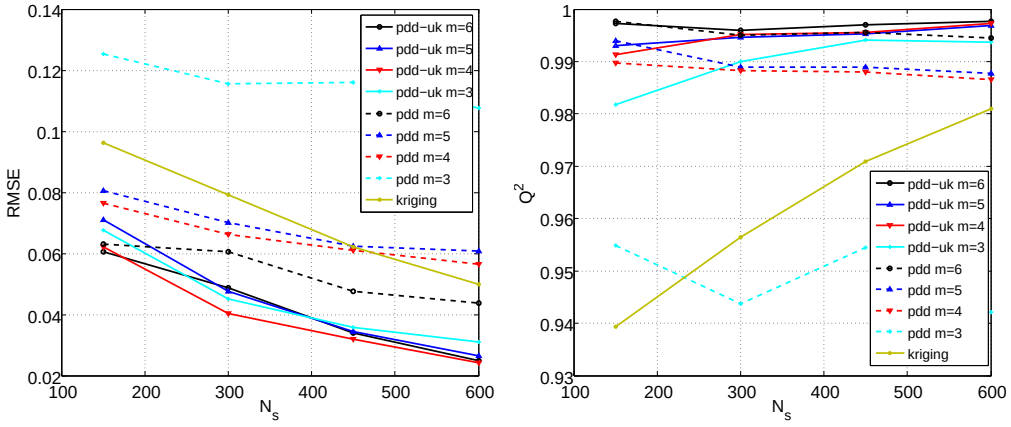

(a) RMSE (b) Q^2

Figure 3.5: TEST 4: Actual (RMSE) and cross-validation (Q^2) error measures when increasing the number of training points. Results are plotted for the Ordinary Kriging, Sparse-PDD and coupled PDD-UK surrogate models of the 8-dimensional Sobol function at different values of m. Error-based adaptive algorithm.

A second convergence test is performed by plotting the trends of the RMSE and Q^2 when increasing the size of the training plan N_s at different values of the maximum polynomial degree m. Values are compared for the sparse-PDD method, the Ordinary Kriging and the coupled UK-PDD method. Results are shown in Figure 3.5. The comparison shows that the convergence of the sparse-PDD is not monotone with the value of m, as already remarked in [Tang *et al.*, 2016], and this reflects on the convergence of the coupled method. In this context, the more complex and expensive coupling strategy developed in [Kersaudy *et al.*, 2015] could reduce the sensitivity of the final PDD-UK metamodel to the maximum polynomial order m, but with an increasing computational effort, which could not always be justified, as in general all the coupled metamodels at different values of m are better than the single sparse-PDD ones (in the RMSE sense, which is the actual metamodeling error estimate). Another option could be to test the convergence of sparse-PDD with respect to m before training the coupled PDD-UK surrogate.

It is also important to notice that the Q^2 accuracy, and so the cross-validation error, being only an estimate of the true error, sometimes are not

able to capture properly the difference in accuracy of different metamodels, especially when they are relatively close. This is a known fact [Goel *et al.*, 2009; Meckesheimer *et al.*, 2002], which must be kept into account in application where it is not possible to compute the RMSE.

3.4.5 TEST 5: 100D Sobol' function

A high-dimensional test case is proposed here with the 100-dimensional Sobol function. The model is the same as in the previous test case 3.4.4, but with different parameter values, namely $c_i = i^2$. This means that the influence of the variables on the output decays quite rapidly with their index. For this high-dimensional test case, the error-based algorithm is computationally too expensive, hence computations are performed only with the variance-based selection algorithm for PDD. A convergence study is performed by gradually increasing the number of Latin Hypercube training points. The maximum polynomial order m is fixed to 4, since, as pointed out in [Tang *et al.*, 2016], for $m = 3$ the accuracy of the metamodel for the sparse PDD tends to decrease when increasing the size of the design of experiments, and some preliminary tests showed that the coupled approach was not always able to produce good results in this case.

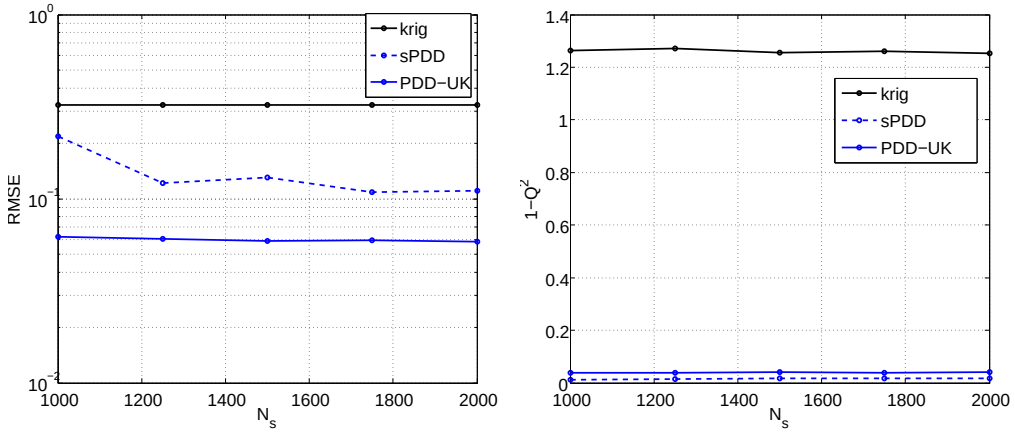

(a) RMSE (b) $1 - Q^2$

Figure 3.6: TEST 5: Actual (RMSE) and cross-validation ($1 - Q^2$) error measures when increasing the number of training points. Results are plotted for the Ordinary Kriging, Sparse-PDD and coupled PDD-UK surrogate models of the 100-dimensional Sobol function. Variance-based adaptive algorithm.

In Figure 3.6, errors estimates are reported for the three metamodeling methods at different sizes of the DoE. First of all, it has to be noticed that

the error associated to the Ordinary Kriging is quite large, as the number of training points used is quite limited with respect to the number of input variables, and in general it is not easy to build an accurate Ordinary Kriging surrogate model with a high-dimensional input. However the sparse PDD is able to produce far better results, since the adaptive procedure allows to recognize the most influencing variables and neglect the others. The coupled approach is able to exploit the sparse functional basis taken from the sPDD and so that also its metamodeling error is relatively small.

It is possible to remark that the RMSE associated to both the sPDD and the PDD-UK decreases when increasing the number of training points, while the cross-validation error increases slightly. As observed in [Tang *et al.*, 2016], the Q^2 error estimate could not always be the most appropriate way to compare metamodels accuracy, since it directly depends on the design of experiments and its size. Unfortunately, when the computation of the RMSE is unaffordable, one must rely on some error estimate as the LOOCV, to state the accuracy of the surrogate.

Finally, an example of the possible advantages of the simple dimensionality reduction proposed in Section 3.3.2 for high-dimensional cases is here presented. In Table 3.7 a comparison is proposed, for the experimental design with 2000 points, between the RMSEs of the RMSE of a normal PDD-UK surrogate and the one of a PDD-UK with the kriging built only on the variables that have a positive contribution to the output variance, according to the sparse-PDD adaptation process. Results are compared also with the ordinary Kriging and sparse-PDD. In the case under analysis, reducing in such way the dimensionality of the problem means that the final kriging step of the PDD-UK is trained on only 24 over 100. It is possible to notice that this leads to a further improvement of the metamodeling accuracy, with a further reduction of RMSE.

Kriging	s-PDD	PDD-UK	PDD-UK reduced
0.3229	0.11021	5.8727E-002	1.7138E-002

Table 3.7: TEST 5: comparison of RMSE between ordinary Kriging, spare PDD, PDD-UK and PDD-UK with reduction of the input dimension, 2000 training points.

3.5 Engineering application: Ablative material TACOT

A higher dimensional engineering case is here proposed with the analysis of the temperature of an ablative material at a fixed position and imposed time of

an ablation process. In particular, let us consider the unidirectional ablation of a 7.21cm thick TACOT (Theoretical Ablative Composite for Open Testing) material (previously described in section 1.6.3), exposed to a constant heat flux for one minute before radiatively cooling down. This rectangular incoming flux is an interesting case to test the metamodeling method here proposed.

Uncertainties are considered on 27 input parameters related to the physical and chemical properties of the material. An uniform distribution is associated to each uncertain variable, with values reported in Table 1.7. The quantity of interest, as seen in Section 1.3.2 is the temperature of the material at a position $x = 5.61$cm, meaning 1.6cm from the heated surface, at the time $t = 80$s over 120s of simulation (see Figure 1.20), performed with the PATO code [Lachaud et Mansour, 2014].

Here again, PDD-UK surrogate models are built on experimental design of increasing size (200, 300, 400, 500, 600 and 700 training points) to verify the convergence of the coupled method. In order to reduce the computational effort while not affecting the metamodeling accuracy, the PDD-UK is built just on the input variables which are not completely neglected in the the sparse-PDD regression, as tested on the 100-dimensional Sobol function in Sec. 3.4.5. This leads to considering only 18 input dimensions in the final metamodel.

N_s	OK	s-PDD 1	PDD-UK 1	s-PDD 2	PDD-UK 2
200	2.4191	3.8836	3.8798	2.9348	2.5952
300	1.5707	3.3070	2.7257	2.6766	1.4420
400	1.2439	3.0733	1.8667	2.6449	1.1829
500	0.9394	1.9956	0.6890	2.6574	0.8736
600	0.7055	1.6047	0.4821	2.5490	0.6620
700	0.5779	1.3625	0.4470	2.5658	0.5427

Table 3.8: PATO, RMSE comparison of the ordinary Kriging, sparse-PDD and PDD-UK metamodels. For the PDD, the following parameters values have been used: $\nu = 2$, $m = 4$ for case 1, $\nu = 1$, $m = 2$ for case 2.

The comparison between the three metamodeling techniques is reported in Table 3.8. First of all, it can be noticed that each one of the three techniques converges when increasing the size of the Latin Hypercubes Experimental Design. For the smaller design with size of 200 samples, the best performing surrogate is Ordinary Kriging. Since more than 100 basis functions are kept in sparse PDD representation with $\nu = 2$, $m = 4$, the computation of the coefficients and so the choice of the rejected basis function can not be accurate enough for the smaller designs, hence also the coupled PDD-UK metamodel suffers the inaccurate choice of regression functions, and results less accurate than Ordinary Kriging. However, when enough training points are considered, the metamodeling error of the PDD-UK becomes the smaller of the three tech-

niques. The convergence of the method for smaller DoE could be improved by reducing the number of terms kept in the final regression by reducing the maximum polynomial order and the order of interaction, as shown in the case 2, with $\nu = 1$, $m = 2$.

N_s	OK	s-PDD	PDD-UK
200	2.4191	2.4103	1.6193
300	1.5707	2.2190	0.8193
400	1.2439	1.8097	0.5365
500	0.9394	1.4698	0.4777
600	0.7055	1.3344	0.4235
700	0.5779	1.1882	0.4232

Table 3.9: PATO, RMSE comparison of the ordinary Kriging, sparse-PDD and PDD-UK metamodels, with optimized parameter m for the PDD at each training set. $\nu = 2$ have been used

The RMSE values obtained for optimized values of ν and m parameters is reported in table 3.9. The maximum ANOVA interaction is set $\nu = 2$, and m is kept equal to one for the smaller training plans and then increased to two at 700 training points. Note the consistent gain in accuracy obtained with the coupled metamodel for smaller experimental design, while for the larger the error seems to be at convergence.

3.6 Study Case: HEG cylinder

In this Section, a forward UQ study and sensitivity analysis are performed on the hypersonic flow around a cylinder described in Section 1.6.1. The goal is to see how uncertainties on the freestream conditions and chemical model parameter influence the pressure and heat flux at the stagnation point. The tools introduced in the chapter, especially sparse-PDD and the PDD-UK method developed in this section, will be exploited at this purpose.

3.6.1 Preliminary analysis of the atmospheric chemical model

Before performing the UQ study on the COSMIC computational model, a preliminary study on the chemical model is performed using a simplified and less expensive computational model. First of all, a comparison between two chemical mixture is performed to choose the best to represent the phenomena. Then, a global sensitivity analysis is performed on the chosen model to reduce

the number of uncertain chemical parameter that are taken into account in the final study.

Choice of the number of species

A first step in the analysis of the atmospheric chemistry model is to verify which species are mostly influential in the post shock region, to be able to

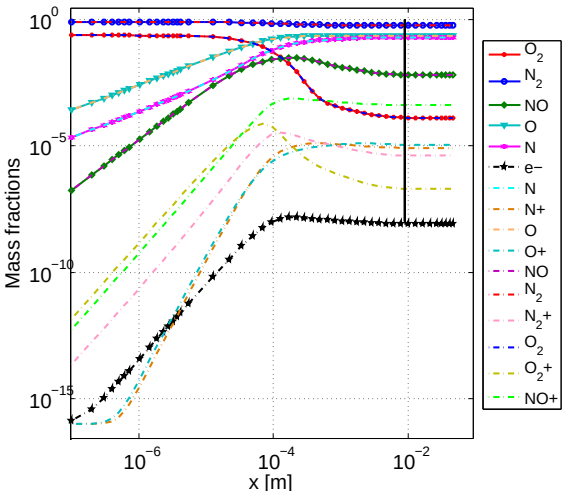

Figure 3.7: Comparison of mass fraction post-shock variations between air 5 and air 11 mixtures.

choose the simpler mixture that represents the phenomena. Here, the Park's air model [Park *et al.*, 2001] with 5 species (air5) is compared to the one with 11 species (air11). Since, in [Knight *et al.*, 2012], every simulation is performed with just 5 species air model, we are expecting to observe a good agreement between the two different mixtures.

For this analysis, a simpler simulation of the post-shock flow field is performed by means of the Shocking code (details about this code are provided in [Magin *et al.*, 2006b]), which computes the downstream flow field using the 1D conservation equations of mass, momentum and global energy plus the conservation of vibrational energy of the nitrogen molecules. This code is not able to account for the deceleration due to the body and the stand-off distance is imposed a priori to an approximate value equal to 9.5 mm.

The comparison between the two gas mixtures is done by looking at the differences between mass fractions of the common species and by checking if a strong presence of ionized species, typical of air11 mixture, is observed, especially at the position corresponding to the stand off distance. As it can be noticed from Figure 3.7, the two mixtures behave practically in the same way in all the post-shock region, and the mass fractions of ionized species, and

especially of electrons, are very small with respect to the ones of the species composing the air5 mixture. Hence it is safe to continue the analysis on the simpler air5 mixture, knowing that the main chemical characteristics of the flow are correctly described.

Global Sensitivity Analysis on the chemical model

Here, the two Quantities of Interest chosen for the sensitivity analysis on the air5 model are the mass fractions of nitrogen $[\mathrm{N}]_w$ and oxygen $[\mathrm{O}]_w$ at a distance from the shock corresponding to the stand-off distance d_{so} between the shock and the cylinder wall. These two QoIs are chosen since they have a major influence in the recombination of atoms at the surface of a reusable thermal protection material.

Seventeen (17) uncertain variables are considered for this problem, which are the pre-exponential factors A_r of the forward reaction rate coefficients in the Arrhenius formulation. Other parameters such as the activation energy are supposed to be known with a higher accuracy, so they are supposed fixed. The uncertain parameters are supposed to be distributed with a log-normal distribution centered on their mean values and with standard deviations given in Table 1.4. This corresponds to consider a normal uncertainty on their exponent. The freestream variables are fixed to their nominal values described in Table 1.2, and the standoff distance is taken $d_{so} = 0.0095$m. Latin hypercube sampling is used to select 20000 sampling points in the stochastic input space, and the Shocking code is run for each sample to get the values of the outputs for each input condition. Then, a sparse PDD surrogate is built on the QoIs in order to get their first-order sensitivity indices.

In Tables 3.10 and 3.11, the sorted first order sensitivity indices obtained for the two quantities of interest are shown. These tables illustrate the hierarchy of the uncertain Arrhenius coefficients with respect to the their contribution to the variance of the outputs. It can be noticed that the first two reactions, namely the dissociation of NO with third body being respectively O and N, contribute to about the 98% of the variance of the QoIs in this particular configuration. For this reason, it is important to take into account at least the uncertainties associated to these two reactions in the following UQ analysis performed by means of the CFD tool. For sake of completeness, we consider also the four following reactions, thus arriving to 99.7% of the output variance contribution.

3.6.2 UQ propagation through the CFD model

Since the number of important chemical species has been chosen, as well as the influential uncertainties to consider for the chemical model, it is possible to continue with the UQ study on the computational model of the flow around the

Variable	Reaction	SI 1st order	% Variance
13	$NO + O \rightarrow N + O + O$	0.5128	0.51287
12	$NO + N \rightarrow N + O + N$	0.4636	0.97657
16	$N_2 + O \rightarrow NO + N$	0.9996e-2	0.98656
4	$N_2 + O \rightarrow 2N + O$	0.4294e-2	0.99086
5	$N_2 + N \rightarrow 2N + N$	0.3559e-2	0.99442
14	$NO + N_2 \rightarrow N + O + N_2$	0.3412e-2	0.99783
9	$O_2 + O \rightarrow 2O + O$	0.6639e-3	0.99849
10	$O_2 + N \rightarrow 2O + N$	0.5532e-3	0.99905
11	$NO + NO \rightarrow N + O + NO$	0.3693e-3	0.99942
1	$N_2 + N_2 \rightarrow 2N + N_2$	0.2516e-3	0.99967
6	$O_2 + N_2 \rightarrow 2O + N_2$	0.1309e-3	0.99980
17	$NO + O \rightarrow O_2 + N$	0.1051e-3	0.99990
7	$O_2 + NO \rightarrow 2O + NO$	0.5214e-4	0.99996
3	$N_2 + O_2 \rightarrow 2N + O_2$	0.1544e-4	0.99997
2	$N_2 + NO \rightarrow 2N + NO$	0.1157e-4	0.99998
15	$NO + O_2 \rightarrow N + O + O_2$	0.6492e-5	0.99999
8	$O_2 + O_2 \rightarrow 2O + O_2$	0.6155e-5	1.0000

Table 3.10: Sorted first-order sensitivity Indices for HEG cylinder chemistry, QoI $[N]_w$.

cylinder. We consider in total 8 uncertain input parameters: the freestream density and velocity, characterized by uniform probability densities described in Table 1.3, and the preexponential factors A_r for the rate coefficients of 6 elementary chemical processes (dissociation of N_2 and NO and exchange reaction of formation of NO). The choice of the atmospheric model and uncertain variables is based on the analysis presented in the previous Section 3.6.1, and the chosen uncertain chemical parameters are reported for clarity in Table 3.12. The output of the simulations, namely the stagnation pressure and heat flux, are evaluated on a 576 points Latin Hypercube experimental design in the 8-dimensional input space by exploiting the COSMIC code.

Global Sensitivity Analysis

Here, sparse PDD is used to perform a global Sensitivity Analysis of the two functions of interests. As seen, the method can easily provide the first order Sobol' Sensitivity Indices, which are used to hierarchically rank the input variables according to their contribution to the variance of the output. Computations are performed considering a maximum ANOVA order of interaction $\nu = 3$ and a maximum polynomial order $m = 4$ for both quantities of interest. The obtained Sobol' indices are given in Table 3.13 for the pressure and 3.14

Variable	Reaction	SI 1st order	% Variance
13	$NO + O \rightarrow N + O + O$	0.5165	0.51652
12	$NO + N \rightarrow N + O + N$	0.4683	0.98489
4	$N_2 + O \rightarrow 2N + O$	0.3978e-2	0.98887
14	$NO + N_2 \rightarrow N + O + N_2$	0.3450e-2	0.99232
5	$N_2 + N \rightarrow 2N + N$	0.3284e-2	0.99560
16	$N_2 + O \rightarrow NO + N$	0.1997e-2	0.99760
9	$O_2 + O \rightarrow 2O + O$	0.8116e-3	0.99841
10	$O_2 + N \rightarrow 2O + N$	0.6824e-3	0.99909
11	$NO + NO \rightarrow N + O + NO$	0.3827e-3	0.99948
1	$N_2 + N_2 \rightarrow 2N + N_2$	0.2328e-3	0.99971
6	$O_2 + N_2 \rightarrow 2O + N_2$	0.1435e-3	0.99985
7	$O_2 + NO \rightarrow 2O + NO$	0.6008e-4	0.99991
17	$NO + O \rightarrow O_2 + N$	0.3895e-4	0.99995
3	$N_2 + O_2 \rightarrow 2N + O_2$	0.1665e-4	0.99997
2	$N_2 + NO \rightarrow 2N + NO$	0.1420e-4	0.99998
15	$NO + O_2 \rightarrow N + O + O_2$	0.7047e-5	0.99999
8	$O_2 + O_2 \rightarrow 2O + O_2$	0.6463e-5	1.0000

Table 3.11: Sorted first-order sensitivity Indices for HEG cylinder chemistry, QoI $[O]_w$.

Variable	Index	Gas reaction	Density of $\log_{10} A_r$	σ_r
A_1	13	$NO + O \rightarrow N + O + O$	Normal	0.12
A_2	12	$NO + N \rightarrow N + O + N$	Normal	0.12
A_3	16	$N_2 + O \rightarrow NO + N$	Normal	0.10
A_4	4	$N_2 + O \rightarrow 2N + O$	Normal	0.15
A_5	5	$N_2 + N \rightarrow 2N + N$	Normal	0.15
A_6	14	$NO + N_2 \rightarrow N + O + N_2$	Normal	0.12

Table 3.12: Uncertainties on gas reaction rates. The index is referred to the notation used in Section 3.6.1.

for the heat flux.

What can be noticed from these results is that the 20% uncertainty on the velocity value has the greatest impact on both outputs. Especially for the heat flux, where the theory suggests a dependence with the cube of the velocity, this variable is responsible of more than the 96% of the total output variance. Uncertainties on the chemistry play a very small role in the variance of the output for both quantities, and values of their sensitivity indices are mostly related to numerical noise. This was expected for the stagnation pressure, since

Variable	SI 1st order	% Variance	Total SI
u_∞	0.7970115	0.7970115	0.802208
ρ_∞	0.2027181	0.9997297	0.208394
A_5	0.8159018E-04	0.9998113	0.520080E-06
A_6	0.7354608E-04	0.9998848	0.510802E-07
A_2	0.4810281E-04	0.9999329	0.261344E-06
A_3	0.4020067E-04	0.9999731	0.170147E-05
A_4	0.2178639E-04	0.9999949	0.175886E-06
A_1	0.5055511E-05	1.000000	0.376313E-06

Table 3.13: Sorted first order and total Sensitivity Indices for HEG cylinder simulation, QoI p_{st}.

Variable	SI 1st order	% Variance	Total SI
u_∞	0.9644307	0.9644307	0.965089
ρ_∞	0.3547857E-01	0.9999093	0.375331E-01
A_6	0.3577629E-04	0.9999450	0.465707E-05
A_5	0.2533707E-04	0.9999704	0.474139E-05
A_1	0.1540559E-04	0.9999858	0.104035E-04
A_2	0.5799109E-05	0.9999916	0.353491E-05
A_3	0.5159200E-05	0.9999967	0.260056E-04
A_4	0.3205809E-05	0.9999999	0.626155E-05

Table 3.14: Sorted first order and total Sensitivity Indices for HEG cylinder simulation, QoI q_{st}.

it is known to be mainly dependent on the free stream density and velocity. For the heat flux, this can be explained firstly by the fact that the 20% uniform uncertainty on the velocity causes big variations of the heat flux. Furthermore, in the considered configuration the Mach number is relatively small, and only molecular oxygen dissociates. In addition, the imposed value of $\gamma = 1$ for the catalicity is forcing chemical equilibrium at the wall. Therefore, the fact that small sensitivity indices are associated to the chemistry should not be surprising. Also Total SIs are reported for both QoIs in Tables 3.13 and 3.14. The fact that their values are quite similar to the ones of the first order indices means that the interaction between variables is not very strong.

Forward uncertainty propagation

To perform the uncertainty propagation, PDD-UK surrogate models for the stagnation pressure and heat flux are trained. Different surrogate models are built on experimental design of increasing size (72, 144, 288 and 576 training

points) to state the convergence of the metamodeling technique in this application. Exploiting the very reduced cost of evaluating the surrogate model, a Monte Carlo sampling technique can be applied to the PDD-UK metamodels in order to perform a forward uncertainty propagation and estimate the probability densities of the statistics of the quantities of interest.

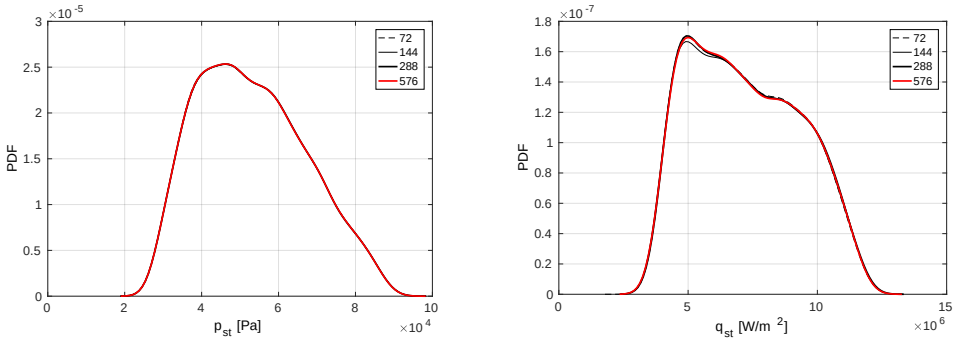

(a) Pressure

(b) Heat flux

Figure 3.8: Kernel density estimates of the probability density functions of stagnation pressure and heat flux computed on the MC sample propagated through PDD-UK metamodels. Comparisons are proposed for results obtained with different surrogates trained on experimental design of increasing size.

Figure 3.8 shows the kernel density estimates (KDE) [Silverman, 1986] of the output PDFs. The comparison between surrogates built on different training sets shows a very good convergence of the technique, even for the smaller experimental design. Notice that in this 8-dimensional application, only two dimensions play an important role on the variation of the outputs, as seen from the sensitivity analysis. Therefore the task to build a surrogate model is simpler than on a problem where all the inputs are relevant.

	μ	σ	σ/μ
p_{st} [Pa]	53088	13925	0.262
q_{st} [W/m^2]	7.2093 e6	2.0703 e6	0.287

Table 3.15: Sampling estimates of mean value, standard deviation and coefficient of variation for the pressure and heat flux. Values are computed propagating 100000 Latin Hypercube samples on the PDD-UK response surfaces for the quantities of interest.

Table 3.15 reports sampling estimates of mean value, standard deviation and coefficient of variation for the pressure and heat flux computed on the

surrogates built on 576 training point. Notice that, considering uniform uncertainties of 20% on the freestream density and velocity, the resulting variations of the stagnation pressure and heat flux are respectively of about 26% and 29%.

3.7 Conclusions

In this chapter, an improved surrogate modeling strategy has been proposed, that uses basis functions chosen by an adaptive sparse-PDD algorithm as regression functions for a Universal Kriging surrogate. This improved surrogate has proven to perform better, in the sense of metamodeling accuracy, than both adaptive sparse-PDD and Ordinary Kriging on several analytical test cases and engineering applications, allowing to efficiently perform sensitivity analysis and uncertainty propagation. However, since PDD-UK requires additional complexity of having to perform a MC sensitivity estimation, the original sparse-PDD technique seems to be more suited, especially in the cheaper-to-train variance-based approach, if the only purpose is the computation of Sobol' sensitivity indices. The reason is that sparse-PDD, due to its close link with ANOVA decomposition, allows a straightforward and more accurate computation of the indices, especially for higher-order ones and when small sensitivity values are involved. However, as stated before, the PDD-UK metamodel presents a higher LOO cross-validation accuracy, hence the method can be useful if the application requires a good surrogate model of the actual function, such as forward and inverse uncertainty propagation. Furthermore, another feature of the PDD-UK metamodel that can be advantageous over the sparse-PDD in some applications, is that, being a Gaussian process, it can be exploited in several techniques that have been developed based on this hypothesis, such as with Expected Improvement (EI) and Efficient Global Optimization (EGO) algorithms [Jones *et al.*, 1998] and the *a priori* optimal design methods called Integrated Mean Square Error (IMSE) and Maximum Mean Square Error (MMSE) [Sacks *et al.*, 1989a] .

This surrogate modeling strategy will be exploited in the following parts of this manuscript to train surrogate models for quantities of interest, both in forward and inverse UQ applications. In next chapter, it will further coupled with an adaptation technique to enrich the experimental design, to further improve the accuracy of the surrogate.

Chapter 4

Novel adaptive refinement of the Experimental Design by mesh adaptation

In this chapter, a novel strategy is introduced to adaptively add new points to an existing set of training points. The proposed method is based on the idea of building a Delaunay triangulation of simplex elements using the existing training points as nodes of the grid, and exploiting an error criterion to add new points on the edges that maximize the criterion. Different computational algorithms that implement this concept are proposed and compared. Then the method is tested on several analytical functions and on an application case, coupled with the PDD-UK surrogate model introduced in the previous chapter.

4.1 Introduction

One important aspect in the accuracy of surrogate models is the choice of a good set of training points, also called Experimental Design (ED) or Design of Experiments (DoE), or simply design. Often in literature, and as done also in the previous parts of the work, points are chosen according to space-filling criteria, such as Latin Hypercubes (LH) designs [McKay *et al.*, 1979] (briefly described in Chapter 2). This kind of ED, being fast to generate, is widely used with fairly good results, also for practical applications. However, in some applications, the total number of available evaluations of the actual numerical model can be limited by its elevated computational cost, and a surrogate model built on a first relatively small space-fulling ED could show a lower accuracy than desired. For this reason, methods have been developed for efficiently adding training points to the initial ED, without discarding the previous model evaluations or to produce more optimal ED from scratch. For

example a nested Latin Hypercube sampling was introduced in [Wang, 2003] to enrich an existing LHS with new training points, while keeping its space-filling properties. However, this method does not rely on the information about the function of interest obtained by evaluating it in the initial set of training points and by training an initial surrogate model. Many other methods have been introduced to directly create an ED that is optimal with respect to some criterion. [Sacks *et al.*, 1989a,b] proposed optimal designs that minimize the Integrated Mean Squared Error (IMSE) for Gaussian Process metamodels, and [Sacks *et al.*, 1989b] proposed also an adaptive sampling strategy minimizing the maximum mean squared error (MMSE). Though the IMSE and MMSE based designs are optimized using some information from the function, they are strongly model-based, meaning that their performance still depends on parameters associated with Kriging surrogate modeling techniques, as the covariance model and the selected hyperparameters. [Shewry et Wynn, 1987; Currin *et al.*, 1991] proposed optimal designs that maximize the entropy, also based on Gaussian process surrogates. Both these designs are more efficient than LH designs, in the sense that they are able to produce surrogate models with lower prediction error, but at the same time they are much more expensive to compute, especially when increasing the number of dimensions or of points. An early review of such techniques can be found in [Koehler et Owen, 1996]. Another review and comparison can be found in [Bursztyn et Steinberg, 2006], where also an alternative technique is proposed for regression models based on the so called alias matrix [Draper et Guttman, 1992]. [Park, 1994] proposed a combination between Latin Hypercubes and optimal designs, introducing optimal LH designs (OLHD), which are LH designs that are nearly optimal at minimizing the IMSE or maximizing the entropy. Other methods have been presented in the literature, which aim at sequentially adding new points to an existing ED to globally enhance the surrogate accuracy. This class of methods is usually called adaptive sampling (also known as sequential sampling). For example, sequential versions of the IMSE, MMSE and maximum entropy design exist [Jin *et al.*, 2002]. In [Jin *et al.*, 2002], two sequential sampling approaches are also proposed: the Maximin Scaled Distance approach and the cross-validation approach. Both approaches exploit the information from the existing metamodel trained on the first ED and are not limited to the Kriging method. Another strategy for sequential design can be found in [Crombecq *et al.*, 2011], named the LOLA-Voronoi strategy, which involves a combination of Voronoi Tessellations, for domain exploration, and local linear approximation (LOLA) for exploitation of local information about the function. [Xu *et al.*, 2014] employed Voronoi tessellations for dividing the domain into smaller regions and then placed samples based on cross validation errors. [Ajdari et Mahlooji, 2014] proposed the so-called Delaunay-hybrid adaptive sequential design (DHASD) which employs Delaunay triangulation for exploration of the domain and cross validation error for exploitation of the

information about the function. More recent surveys on adaptive Design of Experiments can be found in [Liu *et al.*, 2017; Garud *et al.*, 2017]. Notice that adaptive sampling techniques discussed in this section aim at enhancing surrogate quality globally. Thus, they differ from adaptive sampling techniques for surrogate-assisted optimization, like the well-known Expected Improvement (EI) [Jones *et al.*, 1998; Jones, 2001]. However, EI has also been reformulated for global fit problems, as in [Loeppky *et al.*, 2010]. [Quan, 2014] proposed a review of DoE for computer experiment based on EI, introducing developments focused on batch methods (parallel computations of several new training points) combining EI and space filling criteria in order to construct efficient experimental designs.

In this chapter we want to propose and assess an adaptation method that does not strictly depend on the chosen surrogate modeling technique and that is able to account for the information about the function of interest, gained by evaluating the model in the first set of training point and by having trained a first surrogate model. Another requirement of the technique is to be able to add several new training points in a single run, making it suited for parallel (batch) evaluation of the computational model in the new points. The main idea of the adaptation method proposed in this work is to build a Delaunay grid [Delaunay, 1934] of simplex elements in the stochastic space of the input parameters, considering the training points as nodes of the elements, to be able, in this way, to exploit for the adaptation an approach derived from a mesh adaptation technique. The points insertion method is adapted from the work in [Coupez, 2011; Coupez *et al.*, 2013], where an anisotropic mesh adaptation technique was introduced. New training points are added along the edges of the grid according to the optimization of an error criterion. The possibility of adding nodes just on the edges can sound limiting, and surely it leads to a non optimality of the methodology, but at the same time, in practical applications, it can help avoid an excessive clustering of new points around the area which defines the optimum of the adaptation criterion. The real drawback of the technique is the fact that it relies on the notion of edges of a mesh, and, as known, the construction of an n-dimensional Delaunay triangulation for higher dimensional spaces can become very costly. Although the adaptive sampling strategy proposed does not depend directly on the adopted surrogate modeling method, it will be coupled with the PDD-UK surrogate model introduced in the previous chapter, and a model-based surrogate modeling error estimate will be used for convenience in the adaptation criterion. The coupling between the adaptation process and the metamodeling process is represented in Figure 4.1. It is important to notice that, after the ED adaptation phase, the surrogate model is re-trained completely, accounting for the information added by the new training points, meaning that the sparse-PDD is run again to select basis functions and the hyperparameters for the UK are re-optimized.

The chapter is structured as follows. Section 4.2 describes the basic idea

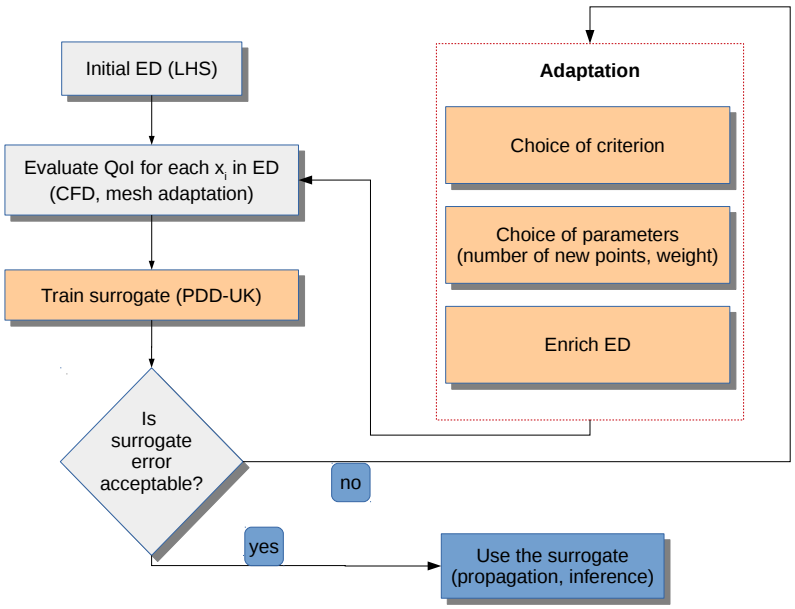

Figure 4.1: Diagram describing the link between metamodeling and adaptation process, including the PDD-UK metamodel presented in Chapter 3 and the DoE adaptation technique presented in this chapter. The aspects developed in this work are highlighted with orange-colored boxes.

behind this approach and introduces the criterion used to decide where to add new training points to an existing design. Section 4.3 introduces the algorithms used to add a fixed number of new training points, imposed by the user according to the available computational resources. In Section 4.4, an extrapolation method is presented to deal with high dimensional problems. The method and the different algorithms are tested on several test functions in Section 4.6. Finally, in section 4.7, an application to the HEG cylinder case study is presented.

4.2 Basic Idea

A first simple implementation of the algorithm is directly derived from the work of [Coupez, 2011; Coupez *et al.*, 2013] on anisotropic adaptive meshing. This will be the starting point to create the final "operating" algorithm. With the original algorithm from Coupez and coworkers, the total number of mesh nodes is fixed and does not change during the adaptive process. Therefore, the number of nodes of the mesh does not increase, but nodes are only moved in the remeshing process. The algorithm controls an error criterion along the edges while respecting a fixed number of nodes in the mesh. A threshold global

error is used to compute stretching and shrinking factors of the edges in order to adapt the mesh by moving the existing nodes. In this work, instead, the interest is basically in adding new points to the existing experimental design. To do this, we decided to explore the idea of considering the existing training points as nodes of a mesh of simplex elements. New points are added in such a way that they minimize an error criterion computed on the constructed mesh. Unlike in the original method of [Coupez, 2011; Coupez *et al.*, 2013], old mesh nodes will not be allowed to move all over the domain, since they coincide with training points where the expensive computational model has already been evaluated. Therefore, as it will be described in what follows, the algorithm will be adapted to a node insertion approach.

Let us consider a scalar function of interest $f(\mathbf{x})$, with $\mathbf{x} \in \mathbb{R}^d$, and let us denote $\boldsymbol{g}(\mathbf{x}) = \nabla f(\mathbf{x})$ the gradient of the function. Let us suppose to construct a Delaunay mesh of simplex elements using the training points as element nodes. The number of total edges constituting the mesh is denoted by n_e. The error measure on each edge e_k, with $k = 1, \ldots, n_e$, can be quadratically defined, in analogy with the work in [Coupez *et al.*, 2013], as the projected gradient on that edge. Hence, the edge based error criterion is expressed as the following quantity:

$$e_k = \sqrt{\sum_{j=1}^{d} \left((g_j(\mathbf{x}^{k^{(2)}}) - g_j(\mathbf{x}^{k^{(1)}}))(x_j^{k^{(2)}} - x_j^{k^{(1)}}) \right)^2} \tag{4.1}$$

where $\mathbf{x}^{k^{(1)}}$ and $\mathbf{x}^{k^{(2)}}$ are the coordinates of the two nodes of the k-th edge, and $g_j(.)$ is the j-th component of the gradient of the function of interest. In practice, since the gradient of the actual model usually is not known in the case of UQ applications, one could generally exploit the metamodel to compute numerical gradients at the training points. For a Kriging surrogate model, as for polynomial based metamodels and other surrogates, an analytical gradient can be (tediously) computed. Then, a stretching factor s_k can be defined for each edge, starting from the computed error value e_k and a target value e_tgt:

$$s_k = \left(\frac{e_{tgt}}{e_k} \right)^{\frac{1}{2}}. \tag{4.2}$$

If the stretching factor is smaller than one, it means that the error is higher than the target value, hence it is necessary to add a number n_k of nodes evenly spaced along the edge. This number is computed as:

$$N_k = \left\lfloor \frac{1}{s_k} \right\rfloor = \lfloor n_k \rfloor \tag{4.3}$$

where $\lfloor n_k \rfloor$ denotes the *floor* of the quantity n_k, meaning the closer integer smaller or equal than n_k. The resulting algorithm is described in Algorithm

Algorithm 5 Basic algorithm

```
Build the triangulation
Compute e_k for each edge k = 1 ... n_e
Compute s_k = (e_tgt/e_k)^{1/2} and N_k = ⌊1/s_k⌋
for each edge k do
    if N_k > 0 then
        add N_k evenly spaced new points along the edge
        add the new points to the DoE
    end if
end for
```

5. This procedure can then be repeated several times in an iterative cycle to increase sequentially the number of added training points. An illustration of the node insertion approach along an edge e_k is illustrated in figure 4.2.

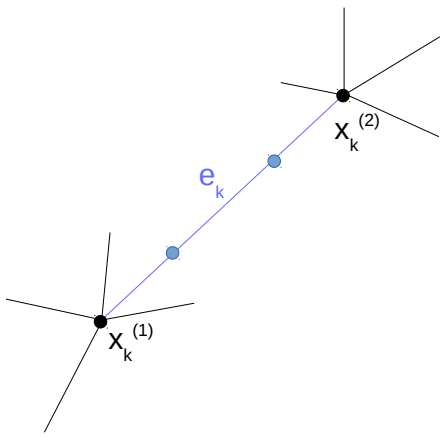

Figure 4.2: Graphical representation of the adaptation model: adding two evenly spaced nodes to the edge e_k.

With this algorithm, the user has no direct control on the number of points added to the experimental design, and the relation between N_k and the imposed target error is not intuitive, neither it is intuitive to assign an appropriate value to e_t to obtained a desired global metamodeling accuracy. A way to improve this algorithm is to give the user the possibility to control directly the number of added training points.

4.2.1 Including metamodeling error into the error indicator

In order to improve this adaptation approach, it is useful to add some information about the accuracy of the metamodel to the error criterion. This is useful, first of all, to add new training point where the metamodel is supposed to be less accurate, and secondly because we do not want to put too much confidence in gradients values where the metamodel is not accurate, since gradients are computed numerically starting from the metamodel itself. Therefore, it is interesting to refine also in regions where the gradient-based criterion is estimated to be small, if the metamodeling error is high, since it is not possible to trust completely the computed gradient value. Hence, a weighted combination of metamodeling error and gradient error indicators is developed in this section. Since we will couple this adaptation strategy with the metamodeling technique introduced in Chapter 3, which is based on universal Kriging, the model-based error estimate associated with this technique will be exploited. However, it is important to notice that this adaptation method can be applied to whatever surrogate modeling technique, if a proper local metamodeling error estimation is available.

A simple local model-based error estimator for Kriging surrogate models is given by the Gaussian process predictive variance (see Eq. (3.12)). Notice however, that in absence of nugget effect this indicator is zero at the training points, since the metamodel is an exact interpolation and that at these points the exact function value is known. Hence, a possible way to account for the metamodeling error in the computation of e_k is to consider its value computed at the center of each k-th edge, denoted $\mathbf{x}^{c_k} = (\mathbf{x}^{k^{(1)}} + \mathbf{x}^{k^{(2)}})/2$. Therefore, denoting $e_k^{(m)}$ the edge-centered metamodeling error, we have:

$$e_k^{(m)} = \sqrt{s_k^2(\mathbf{x}^{c_k})}. \tag{4.4}$$

This value can now be re-scaled and summed to the existing gradient based error criterion e_k, defined in Eq. (4.1), to obtain a weighted error criterion $e_k^{(w)}$:

$$e_k^{(w)} = \alpha \frac{e_k}{\max_k (e_k)} + (1-\alpha)\frac{e_k^{(m)}}{\max_k (e_k^{(m)})} \tag{4.5}$$

where the weight α can be adjusted to control the relative influence of the two criteria. Note that other ways to include a metamodeling error estimate in the error criterion are available. For example, one possibility, not explored in this work because considered too computationally demanding, could be to consider the integral of the predictive variance along the edge as metamodeling error measure. Another metamodeling error measure, this time available at each node, can be the point-wise leave-one-out cross-validation error.

4.3 Adding a fixed number of training points

Having the possibility to choose the number of added nodes can be advantageous, because in this way the user will be able to fix this value according to the available computational resources. For example, it becomes easier to parallelize, according to the available resources, the task of computing the actual value of the function of interest, which can involve expensive simulations.

Two different strategies for the implementation of this feature are available. The first, denoted *brute approach*, is a more rigorous mathematical formulation of the problem, but it translates in a more difficult and expensive solving algorithm, while the second, called *fast approach* tackles the problem directly on the computational algorithm, resulting in a faster procedure. The two approaches will be detailed in the next subsections.

4.3.1 Brute approach

A first rigorous attempt to insert a fixed number of nodes is developed. It consists in formulating the adaptation problem as finding the best combination of positions of a fixed number N_a of new nodes on the n_e edges in order to minimize an imposed error criterion. We seek to solve the following optimization problem:

$$N_k^* = \arg\min(\varphi(N_k)) \qquad \text{with} \qquad \varphi(N_k) = \sum_{k=1}^{n_e} \frac{1}{2} \frac{e_k}{(N_k+1)^2} \tag{4.6}$$

$$\text{subject to:} \quad N_a = \sum_{k=1}^{n_e} N_k$$

where e_k is the edge error and N_k is the number of nodes added on each edge. The cost functions is designed in such a way that new points are added with priority along edges where the error is higher. This optimization problem can be quite tricky to solve, due to the discrete nature of the design variables ($N_k \in \mathbb{N}$). However, it can be noticed that, when $N_a < n_e$, it is possible to consider in the optimization just the N_a edges associated to a higher error value, so the problem becomes:

$$N_k^* = \arg\min(\varphi(N_k)) \qquad \text{with} \qquad \varphi(N_k) = \sum_{k=1}^{N_a} \frac{1}{2} \frac{e_k}{(N_k+1)^2} \tag{4.7}$$

$$\text{subject to:} \quad N_a = \sum_{k=1}^{N_a} N_k$$

At this point, a possible approach to solve the problem through the use of brute force consists in seeking among all possible permutations of N_a nodes

on N_a edges the one that minimizes $\varphi(N_k)$. As it can be easily seen, this approach is convenient just for small enough values of N_a (*i.e.* $N_a \leq 10$), since the number of total cases to be explored n_t increases quickly:

$$n_t = \frac{(N_a + N_a - 1)!}{(N_a - 1)! N_a!} \tag{4.8}$$

The method showed to be powerful and very accurate for low dimensions problems. However, it might be difficult to implement and expensive to solve for increasing size of the dimensional space.

Improved numerical algorithm

A simple and efficient algorithm to find a solution for the optimization problem in equation (4.6) can be built by exploiting the structure of the objective function. In fact, it is constructed as the sum of the different edge errors, which are constant known values during the optimization process, divided by a monotone function of the number of new training points points added along that edge. It is possible to imagine to add one new point at the time: the contribution to the total error of the edge where the point is added will be divided by 2^2, while the ones of the other edges will remain the same. Of course, in this situation the solution that guarantees a higher decrease in the value of the total objective function consists in adding one point along the edge where e_k is higher. If a second point needs to be added, it is possible to follow the same process and add the new point on the edge where $\frac{e_k}{(N_k+1)^2}$ is maximum. This can be be iterated until the total desired number of new training point has been reached and the constraint is satisfied. This procedure is resumed in Algorithm 6.

Algorithm 6 Improved brute algorithm

1: Build the triangulation
2: Compute e_k for each edge $k = 1 \dots n_e$
3: Initialize $N_k = 0$ and $e_{tmp_k} = e_k$ for all $k = 1 \dots n_e$
4: **while** $\sum_{k=1}^{N_e} N_k < N_a$ **do**
5: Find the edge where e_{tmp_k} is maximum
6: Update $N_k = N_k + 1$ and $e_{tmp_k} = e_{tmp_k}/(N_k + 1)^2$
7: **end while**
8: **for** each edge k **do**
9: **if** $N_k > 0$ **then**
10: add N_k evenly spaced new points along the edge
11: add the new points to the DoE
12: **end if**
13: **end for**

This algorithm has been introduced just lately in our research, therefore it has not been thoroughly tested, but it should be able to give the exact same results as what we called the "brute" approach, but at a significantly reduced computational cost. Note that other optimization approaches could be explored, for example genetic algorithms with discrete design variables. We tested an implementation of this method but without obtaining the desired results.

4.3.2 Fast approach: edge-based length distribution method

The second approach consists in rewriting the optimization problem and modifying the iterative cycle of the original Algorithm 5 so that it adds, at each iteration, a fixed number of points N_a imposed by the user. While this insertion technique does not necessarily converge, from a strict and rigorous mathematical point of view, to the actual optimal solution, it highly decreases the computational cost, especially for higher values of N_a.

First of all, note that the optimization problem can be stated also with respect to the stretching factors s_k associated to the edges of the mesh, since the number of points added on each edge can be related to the stretching factors (and hence to the error estimates) through the relation $N_k = \lfloor s_k^{-1} \rfloor$:

$$\begin{aligned} &\text{minimize} \qquad \varphi(s_k) = \sum_{k=1}^{n_e} \frac{1}{2} \frac{e_k}{\left(\lfloor s_k^{-1} \rfloor + 1\right)^2} \\ &\text{subject to} \quad N_a = \sum_{k=1}^{n_e} \lfloor s_k^{-1} \rfloor. \end{aligned} \tag{4.9}$$

It can be noticed, however, that also in this case, although the design variable is continuous, there is a function in the constraint that transforms it into an integer, and so the same difficulties of the previous approach arise. In practice, to overcome this problem, we decided to relax this constraint by removing the floor operator. Therefore, the rigorous formulation is replaced by a weaker and more empirical formulation defined in the following way:

$$\begin{aligned} &\text{minimize} \qquad \varphi(s_k) = \sum_{k=1}^{n_e} \frac{1}{2} s_k^2 e_k \\ &\text{subject to} \quad N_{tot} = \sum_{k=1}^{n_e} s_k^{-1} \end{aligned} \tag{4.10}$$

where $N_{tot} = N_s + N_a$, and N_s is the number of current training points. At this point, it is possible to find a solution of the optimization problem by exploiting the Lagrangian formalism:

$$\mathcal{L}(s_k, \lambda) = \frac{1}{2} \sum_{k=1}^{n_e} s_k^2 e_k + \lambda \Big(\sum_{k=1}^{n_e} s_k^{-1} - N_{tot} \Big). \tag{4.11}$$

By putting to zero the derivatives of the Lagrangian, the following system is obtained:

$$\begin{aligned}\frac{\partial \mathcal{L}}{\partial s_k} &= s_k e_k - \lambda s_k^{-2} = 0 \\ \frac{\partial \mathcal{L}}{\partial \lambda} &= \sum_{k=1}^{n_e} s_k^{-1} - N_{tot} = 0\end{aligned} \tag{4.12}$$

which leads to:

$$s_k = \left(\frac{\lambda}{e_k}\right)^{\frac{1}{3}} \tag{4.13}$$

with the multiplier

$$\lambda = \left(\frac{\sum_{k=1}^{n_e} e_k^{\frac{1}{3}}}{N_{tot}}\right)^3. \tag{4.14}$$

This process will add new points where it is most needed *i.e.* where the error is most important. However, clearly, the generated solution will not necessarily respect the exact number of nodes as a truncation to the integer part of s_k^{-1} is applied. Consequently, the solution of problem (4.10) will result in an adaptation algorithm that adds a number of points not necessarily equal to N_a, since the rigorous formulation has been replaced by a weaker one. Therefore, in order to meet the constraint on the number of nodes, a correction part has been implemented in Algorithm 7. It consists in repeating the cycle of node insertion where the estimated error is most important as long as the target number of nodes has not been reached. The implementation of the algorithm is described in Algorithm 7.

4.4 Extrapolation technique for high dimensional inputs

A drawback of the direct derivation of the adaptation methodology from the mesh adaptation technique is that, in order to be able to adapt in the whole domain, it is necessary to have nodes (training points) also in each vertex of the hypercube representing the domain when each input is uniformly distributed. However, this can be really limiting when the size of the input variables increases, since the number of vertices of the hypercube rapidly increases as 2^d, and subsequently the number of extra training points in which is necessary to evaluate the function of interest augments.

A possible simple solution for this problem, inspired by the work of [Witteveen et Iaccarino, 2012] on simplex stochastic collocation, can be to consider only training points inside the domain and then exploit an extrapolation to cover the remaining part up to the corners and the bounds. The extrapolation procedure can be structured as follows. First, a metamodel is trained on the

Algorithm 7 Fixed N_a adaptation, fast approach

Calculate e_k for each edge $k = 1 \dots n_e$
Compute $\lambda = \left(\sum_{k=1}^{n_e} \frac{e_k^{1/3}}{N_{tot}}\right)^3$, where $N_{tot} = N_t + N_a$ and $s_k = \left(\frac{\lambda}{e_k}\right)^{1/3}$
Compute $N_k = \lfloor \frac{1}{s_k} \rfloor$
while $k \leq n_e$ and $\sum_k n_{p_k} < N_a$ **do**
  if $(N_k > 0)$ **then**
    for $j = 1 : N_k$ **do**
      $n_{p_k} = n_{p_k} + 1$
      if $\sum_k n_p = N_a$ **then**
        EXIT
      end if
    end for
  end if
  $k = k + 1$
end while
if $\sum_k n_{p_k} < N_a$ **then**
  Compute $s_k^{new} = \frac{1}{s_k} - N_k$
  Sort the edges k according to their value of s_k^{new} in decreasing order and compute $N_k^{new} = \lfloor \frac{1}{s_k^{new}} \rfloor + 1$
  while $k \leq n_{edges}$ and $\sum_k n_{p_k} < N_a$ **do**
    if $(N_k^{new} > 0)$ **then**
      for $j = 1 : N_k + 1$ **do**
        $n_{p_k} = n_{p_k} + 1$
        if $\sum_k n_p = Na$ **then**
          EXIT
        end if
      end for
    end if
    $k = k + 1$
  end while
end if
for each edge k where $n_{p_k} > 0$ **do**
  add n_{p_k} evenly spaced new points along the edge
end for

initial design of experiments, which can be a Latin Hypercube or quasi Monte Carlo design. Then, the triangulation of the domain is built including also the corners in the set of nodes. It is important to note that the true function values are not computed at the corner points. Thus, two different types of edges will be considered: the interpolation edges, constructed by joining two

training nodes, and the extrapolation edges, for which at least one of the two nodes is a corner of the domain (Figure 4.3). At this point, it is important

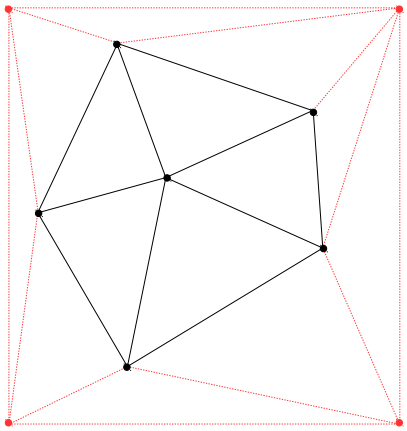

Figure 4.3: Example of the extrapolation technique: the black solid lines represent the edges where the real function value is known for both nodes, while red dashed lines represent extrapolated edges, where the function values is extrapolated in at least one of the nodes.

to highlight the fact that, since the actual value of the QoI is not known on the extrapolation edges, one could be less confident about the gradient value computed in the error criteria. Hence, when computing the global error, it is possible to put a smaller weight (or even a null weight) on the gradient part, with respect to the interpolation edges. Then the procedure for adding the new nodes is exactly the same as described in Algorithm 7. While the normal approach is supposed to work at least as fine, or even better than the extrapolation one for smaller sizes of the input, this last should behave better when the number of input variables starts to increase, and the number of corners becomes comparable to the size of a DoE to get a sufficiently good metamodel of the QoI.

4.5 Parameters of interest

In this section, as also done in the previous chapter, a brief overview is given on the parameters of the adaptation algorithm that need to be set by the user, with their role and suggestions on a possible range of values.

Most of the parameters whose value needs to be imposed by the user in the global algorithm, accounting for both the PDD-UK surrogate model and the adaptation technique, as in Figure 4.1, are related to the sparse PDD algorithm, and a discussion can be found in Section 3.3.1. Concerning the adaptation algorithm, the two main parameters that need to be assigned are

Name	Possible values	Role
N_a	$[1, \infty]$	fixed number of added points in refinement algorithm
α	$[0, 1]$	error weight in refinement algorithm

Table 4.1: Parameters chosen by the user in the algorithm for the adaptation of the ED.

the number of added points N_a, and the error weight α. The normal operational use of the adaptation algorithm would be perform only one or very few iterations of the adaptation, and choose N_a to add a number of nodes according to the available computational resources, if the accuracy of the metamodel trained on the initial experimental design is not satisfactory. A comparison of computations at different values of α is proposed in Section 4.6.

4.6 Numerical experiments

In this section the proposed strategy to adaptively add new points to the Experimental Design is assessed. Firstly, the fast approach is compared to the more rigorous one to verify its robustness. Then, several iterations of the adaptation algorithm are applied to different test functions to test its convergence in RMSE sense. It has to be noticed that in a normal application, just few iterations of the algorithm are likely to be performed, since, if the adequate computational power is available to evaluate the QoI in a lot of training points, it would be more advisable to generate a bigger Experimental Design from the beginning. Notice that for each new ED, the surrogate model is trained completely from scratch, meaning that both the basis functions and the hyperparameters are recomputed.

4.6.1 Comparison between brute and fast approach

In this first part of the results related to the adaptation strategy, a comparison between the optimal but computationally expensive approach presented in Sec. 4.3.1 and the faster one described in 4.3.2 is presented. The analysis is performed on the following 2D test function, derived from the 1D test case in Table 3.2: The function is evaluated in the domain $\boldsymbol{x} \in [-1, 1]$.

In Figure 4.5, results obtained starting from an initial LHS design of 24 points (20 actual LHS points plus the four corners of the bidimensional domain) are compared. Comparisons between the brute (a,c,e) and the faster approach (b,d,f) are performed for three different values of α, *i.e.* 0.2, 0.5 and 0.8. Note that curves relative to different values of N_a are shown in different colors. As it is possible to notice, the obtained solutions are, most of the times, practically identical between the two algorithms for both different values of the parameters

N_a and α. Sometimes, as it can be seen in Figure 4.5b for $N_a = 2$, the convergence performance of the faster algorithm is better, even if the reasons are not clear.

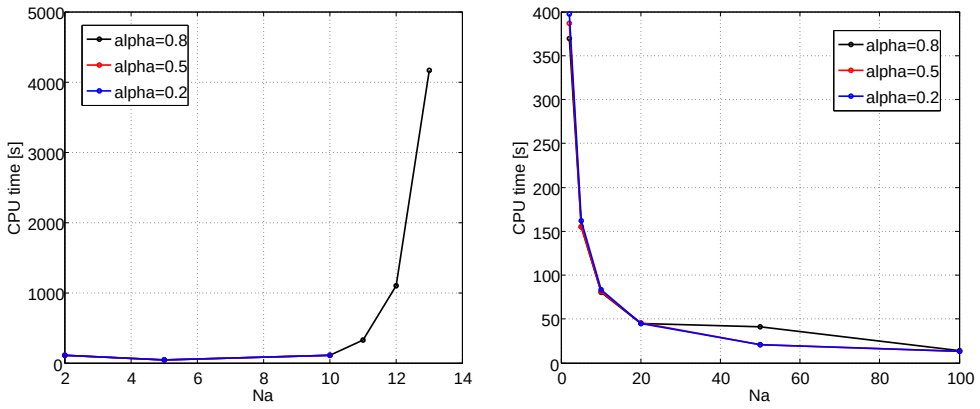

(a) brute (b) fast

Figure 4.4: 2D testcase: Comparison between the computational cost of brute and fast approach, initial DoE of 24 points

Concerning the computational cost of the two algorithms, figure 4.4 shows the trend of the CPU time when increasing the value of points added at each iteration N_a for different values of α. It can be seen that, as expected, the fast algorithm outperforms the brute approach for $N_a > 10$. In fact the brute approach becomes almost unusable in this conditions. Another possible remark is that, for the fast algorithm, the computational time decreases with N_a, because less iterations of the adaptation algorithm are required, which includes also the construction of the Delaunay triangulation of the domain. This difference in computational cost is expected to increase with the size of the input space.

The same convergence analysis can be repeated for a bigger training plan, this time of 44 training points. The behavior, as shown in Figure 4.6, is generally the same, with the fast algorithm performing at least as good as the other one.

4.6.2 Convergence

As stated in the previous section, the fast algorithm is able to perform adequately well and allows a bigger flexibility and lower computational cost with respect to the so-called brute approach. Using this assumption, the fast algorithm is then retained for the following analysis. The adaptive part of the algorithm is then tested on TEST 2, 3 and 4 (see Table 3.2). Note that the

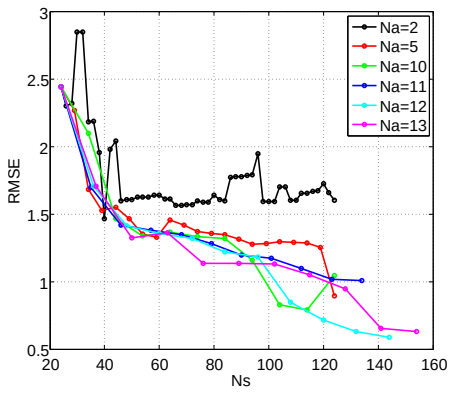

(a) brute, $\alpha = 0.8$

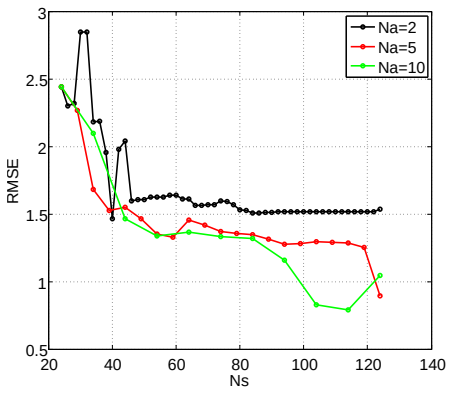

(b) fast, $\alpha = 0.8$

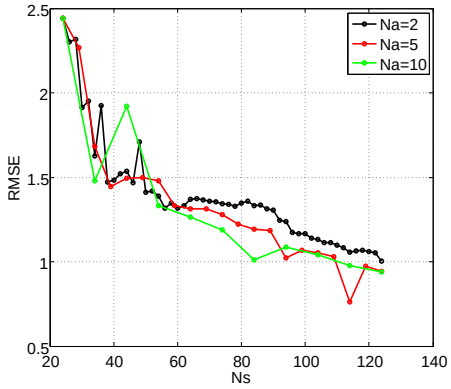

(c) brute, $\alpha = 0.5$

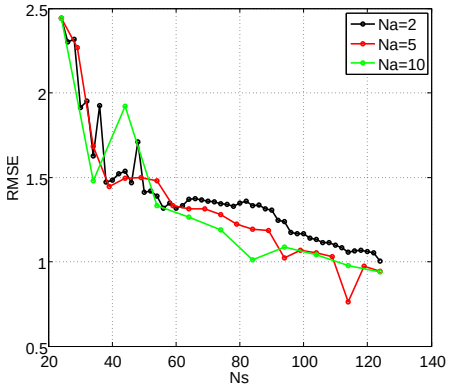

(d) fast, $\alpha = 0.5$

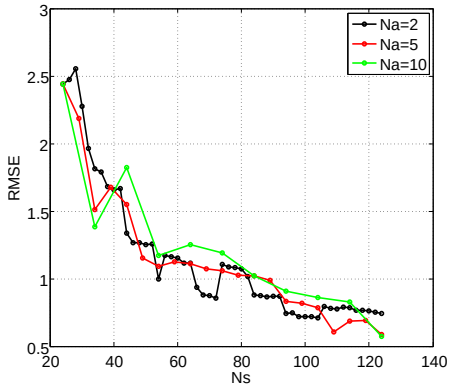

(e) brute, $\alpha = 0.2$

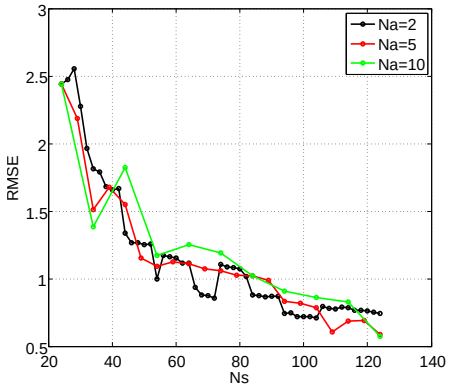

(f) fast, $\alpha = 0.2$

Figure 4.5: 2D testcase: Comparison between brute and fast approach, initial DoE of 24 points

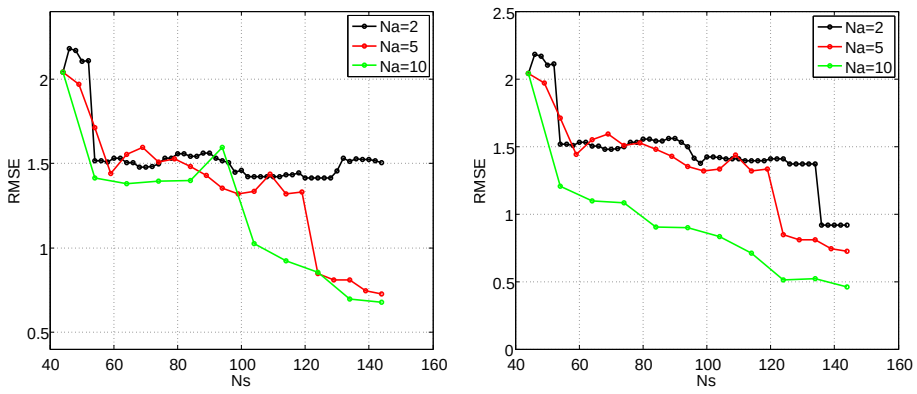

(a) brute, $\alpha = 0.8$

(b) fast, $\alpha = 0.8$

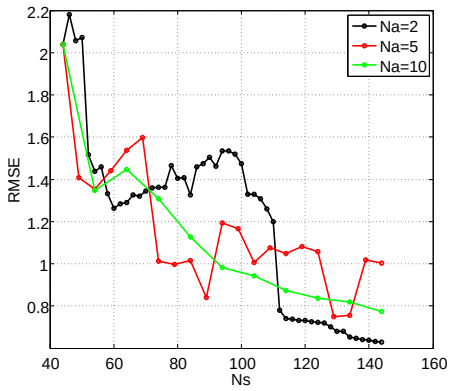

(c) brute, $\alpha = 0.5$

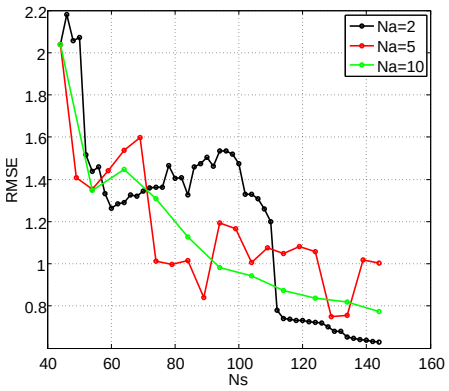

(d) fast, $\alpha = 0.5$

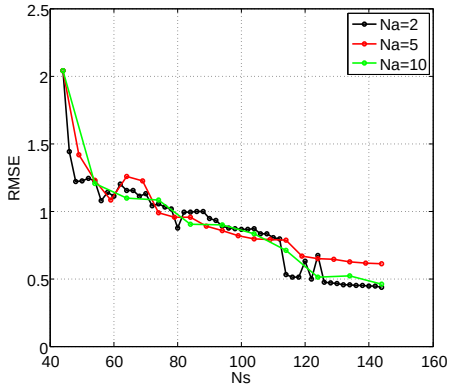

(e) brute, $\alpha = 0.2$

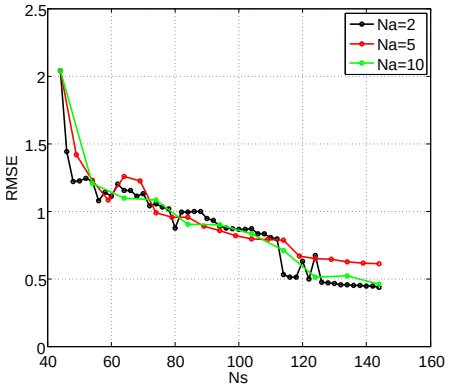

(f) fast, $\alpha = 0.2$

Figure 4.6: 2D testcase: Comparison between brute and fast approach, initial LHS of 44 points

convergence is systematically assessed by repeating the adaptation process starting from different LH designs of same size, and comparing then the obtained RMSE mean value and the standard deviation with the ones one would get with standard LHS designs of increasing size. Note also that the number of points added at each iteration is a choice of the user. A sensitivity over this parameter is provided in the following to illustrate the influence on the convergence.

TEST 2: 2D test function

It is first possible to state the convergence of the algorithm for the 2-dimensional test function described in Equation 3.45. The convergence test is done by repeating the adaptation process starting from 15 different LH design of same size, and comparing the obtained RMSE mean value and the standard deviation with the ones one would get with normal LHS design of increasing size.

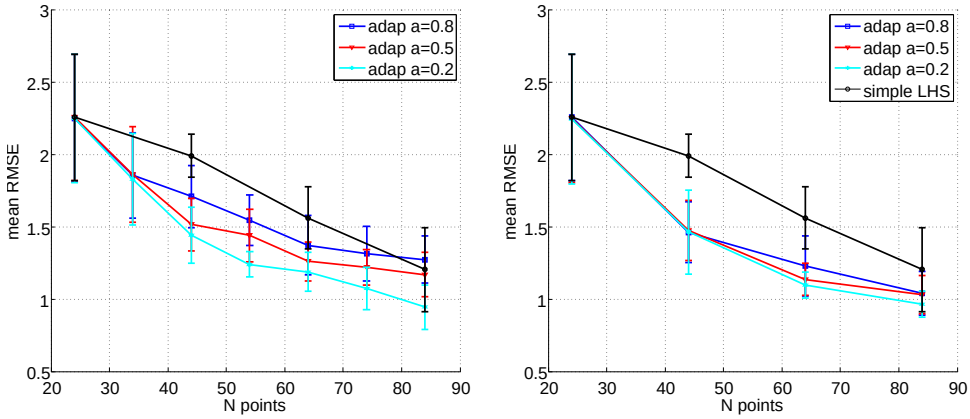

(a) 10 points per iteration

(b) 20 points per iteration

Figure 4.7: TEST 2: Convergence of the mean value of the RMSE and corresponding deviation computed with 15 different starting LHS DoE. The result of a simple increase of LHS point is compared with adaptation at different values of α coefficient

In Figure 4.7, it can be seen that, for this test case, the mean error related to the adaptive strategy converges faster than the the one of simple LHS, especially for $\alpha = 0.5$ and $\alpha = 0.2$, namely when taking into account also the Kriging estimation of the metamodeling error. Furthermore, the adaptation in this particular test case delivers more robust results, since variance of the RMSE is smaller. Note also that a consistent reduction is observed for both cases with 10 and 20 points added for each iteration.

TEST 3: Ishigami function

It is possible to repeat the same convergence test also for the TEST 3 function (see Table 3.2). Figure 4.8 shows the obtained results. Also for this test

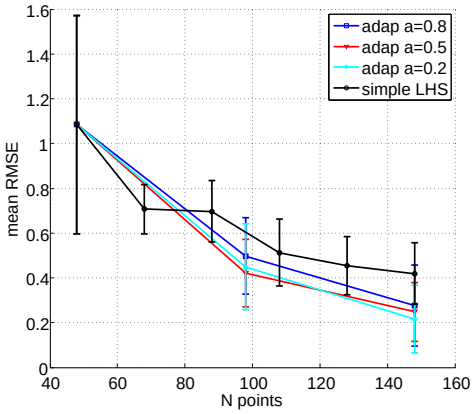

Figure 4.8: TEST 3: Convergence of the mean value of the RMSE and corresponding deviation computed with 15 different starting LHS DoE. The result of a simple increase of LHS point is compared with adaptation at different values of α coefficient

case, the adaptive strategy converges faster than the simple LHS, for the three selected values of the weight α. Notice also that here a fairly high number of points has been added at each iteration of the adaptation step, namely 50 points, and the resulting convergence curve is stable. However, in this test case, the RMSE variance of the adapted designs is not clearly smaller than the one of the simple LHS designs to which we compared.

TEST 4: 8D Sobol' function

Finally, a test is performed on the TEST 4 function introduced in Table 3.2, to verify if convergence is retained also on a higher-dimensional case. In this case, the extrapolation method presented in 4.4 is assessed. Results for this test-case are reported in Figures 4.9, 4.10 and 4.11. As it can be seen in 4.9a, the normal approach that puts nodes in the corners of the domain does not converge at least as fast as LHS, probably due to the fact that a relatively high number of training points with respect to the size of the initial DoE (256 over 320) needs to be put in the corners of the domain, leaving too little information to train an adequate metamodel inside the domain. Therefore, the adaptation is repeated with the extrapolating approach in Figure 4.9b, where all the training points are strictly inside the domain. This is able to improve results and to provide a convergence which is, for the first iteration, much better than the one obtained

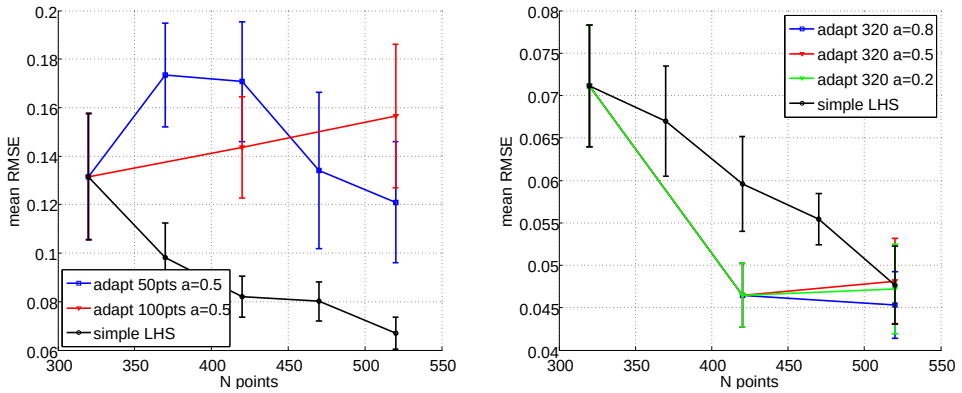

(a) without extrapolation (b) with extrapolation

Figure 4.9: TEST 4: Convergence of the mean value of the RMSE and corresponding deviation computed with 14 different starting LHS DoE of 320 points. The result of a simple increase of LHS points is compared with adaptation at different values of α coefficient. A comparison is done between the normal algorithm (a) and the one with extrapolation near the corners of the domain (b).

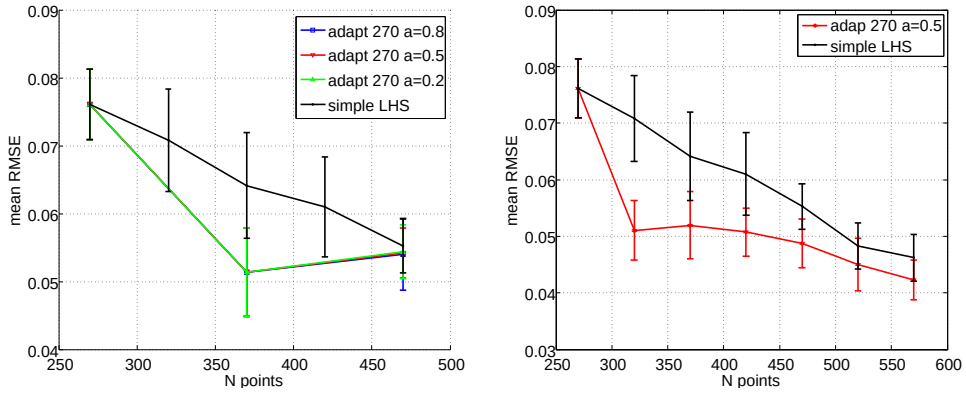

(a) 100 (b) 50

Figure 4.10: TEST 4: Convergence of the mean value of the RMSE and corresponding deviation computed with 7 different starting LHS DoE of 270 points. The result of a simple increase of LHS point is compared with adaptation at different values of α coefficient. A comparison is done between the addition of 100 and 50 points per iteration.

by just increasing in the size of the LHS plan. This extrapolating approach also allows to reduce the number of training point to a number which is lower

than (or very close to) the number of corners, as shown in Figure 4.10 and 4.11. It can be however noticed that the convergence of the adaptive approach

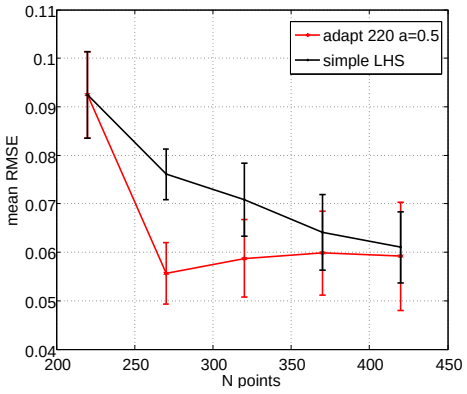

Figure 4.11: TEST 4: Convergence of the mean value of the RMSE and corresponding deviation computed with 7 different starting LHS DoE of 220 points. The result of a simple increase of LHS point is compared with adaptation at different values of α coefficient.

for this 8-dimensional case rapidly tends to be almost flat when adding 100 new points for each iteration. It is noticeable instead (Figure 4.10b and 4.11), when adding 50 samples per iteration, that the metamodeling error decreases generally faster than with the normal LHS: the first iteration decreases strongly the error, and, while the next iteration tends to realign to LHS, the trend is however better.

4.7 Application case: HEG cylinder

The final result presented in this chapter is about the application of the DoE adaptation technique to the application case of the HEG cylinder. The purpose is to test how the proposed approach behaves on a function issued from an engineering application, whose evaluation is quite expensive, since associated to CFD runs. Here we will concentrate only on the adaptation of an experimental design for the stagnation pressure, where the accuracy of the CFD simulations is higher. Since the results of the sensitivity analysis performed in Section 3.6.2 showed that only two variables contribute actively to the variation of the output (namely the freestream density and velocity), and given the fact that the construction of a Delaunay triangulation can be quite expensive in an 8-dimensional space, we decided to perform the adaptation only on the two-dimensional space constituted by ρ_∞ and u_∞. In view of the reduced dimensionality of the domain, and the fact that all the surrogate models analyzed in Chapter 3 were well converged even in the full space (see

Figure 3.8), we decided to start the adaptation process from a small initial design of experiments of only 10 training points, including the four corners of the domain constituted by the uniform prior bounds in Table 1.3. The computational model needs to be evaluated at each training point, obtaining the training set in Figure 4.12. A first PDD-UK surrogate is trained on the initial

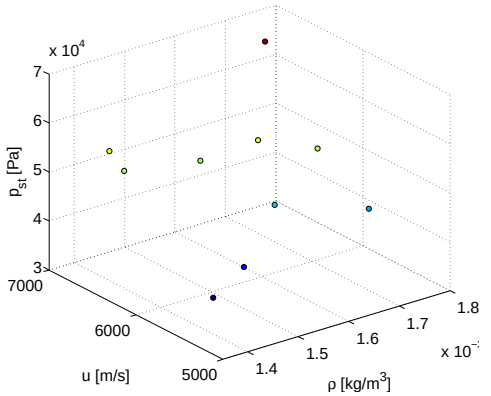

Figure 4.12: Evaluation of the quantity of interest, *i.e.* the stagnation pressure, in the 10 points composing the initial Latin Hypercube design.

experimental design. Plots of the prediction and the predictive variance can be seen respectively in Figures 4.13a and 4.13b. As it can be noticed from the prediction on this first surrogate model, the function of interest appears to be very simple and smooth, with a monotone trend. It is important to notice that it behaves as a ridge function, appearing almost constant along a certain direction. This will be useful in the next chapter.

It is now possible to run the adaptation algorithm. Firstly a triangulation is built on the existing training points. Gradient is evaluated at each training point and metamodeling error at each edge midpoint, and the weighted error criterion is computed for a value of the weight α chosen by the user. Then, the improved version of the brute approach is run to select the new training points. We chose to add 5 and 10 new training points to the existing DoE, to compare the results. Figure 4.14a shows the obtained triangulation and the location of the new training points, when adding 10 points for a choice of $\alpha = 0.2$, meaning that more importance is given to the reduction of the metamodeling error estimate. This choice can be motivated by the observation that the function of interest is monotone and does not present any complex feature. Just for comparison sake, a test with $\alpha = 0.8$ is also run.

At this point, the output of the computational model is evaluated at each new training point, and the whole augmented training set is used to build a new PDD-UK surrogate. It is then evaluated at 288 test points, where the actual model output is known, and the prediction output is used to compute

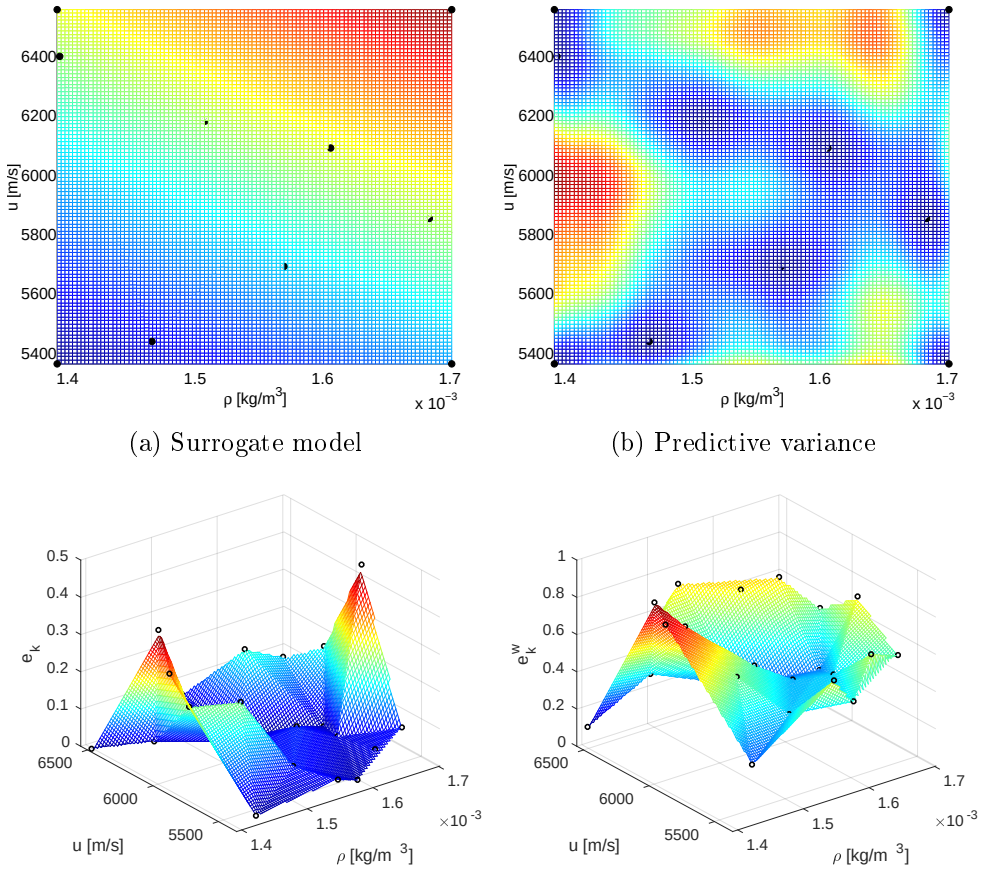

(a) Surrogate model

(b) Predictive variance

(c) Gradient-based error

(d) Weighted error

Figure 4.13: PDD-UK surrogate model trained on the initial design of experiments. The surrogate prediction is plotted in (a), and the predictive variance in (b). Subfigure (c) shows the gradient-based error criterion and (d) the weighted error for $\alpha = 0.2$ criterion at each edge center

the RMSE. Figure 4.14b shows the RMSE of the adapted design compared to the values obtained for different normal LHS designs of different sizes. It can be noticed that one step of the adaptation process is able to produce an experimental design with a lower metamodeling error than a simple Latin Hypercube training sample with the same number of points, and in the case of 5 new points, of almost the same value than with a training set twice as big. Curiously, when adding 5 points, the choice of $\alpha = 0.8$ performed better than $\alpha = 0.2$, while when adding 10 points the opposite is true.

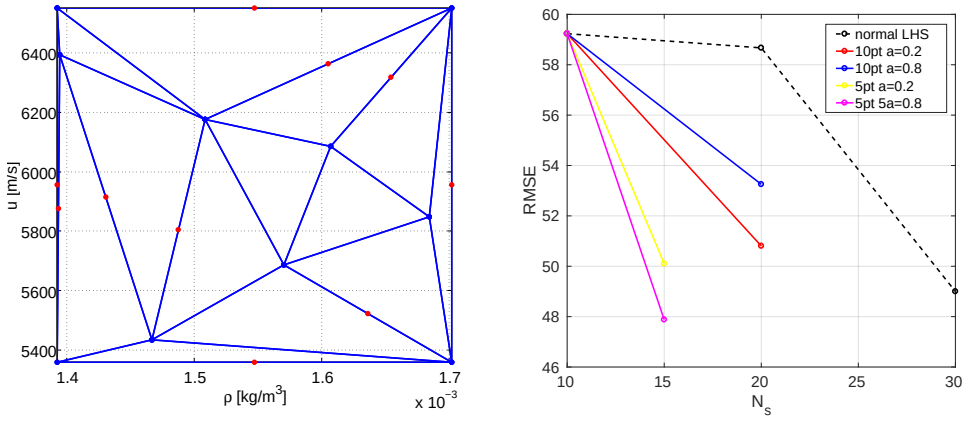

(a) Starting design (b) Surrogate model

Figure 4.14: Triangulation built on the starting experimental design and position of the new 10 training points added with $\alpha = 0.2$ (a). Subfigure (b) shows the comparison of the RMSE obtained with adaptation and the values associated to simple LHS design.

4.8 Conclusions

In this chapter, a technique derived from anisotropic mesh adaptation has been used to adaptively add new points to an exiting experimental design for the construction of a surrogate model. The method needs the construction of a simplex triangulation in the space of the uncertain inputs, using the existing training points as the nodes of the grid. It then exploits an error criterion, based on function gradients and surrogate modeling error, to adaptively add new training points along the edges of the grid maximizing the criterion. From several tests performed on analytic functions with the PDD-UK surrogate,this method produces, on average, more accurate surrogate models than a normal LHS design of the same size if the number of added points is not too large. When several iterations of the technique are performed, the accuracy tends to converge to the simple LHS designs. This methodology could be useful in case a surrogate trained on an initial experimental design is not accurate enough, and a relatively small number of new training points needs to be adaptively added to reduce the metamodeling error under a certain threshold.

Chapter 5

Dimension reduction by Active Subspaces for Bayesian inference

An emerging way to perform dimensionality reduction is by exploiting the active subspace of a function of interest. In this chapter, after defining active subspaces, they are exploited for dimensionality reduction applied to Bayesian inverse problems. A novel approach to use them for the problem of interest is proposed and compared to the one based on the misfit function, introduced in [Constantine et al., 2016b]. The two methodologies are compared on the HEG cylinder application case.

5.1 Introduction

Most of global sensitivity analysis methods usually measure the variation of the output along the input coordinates, and then use these measures to rank the coordinates. This is done, for example, when looking at first-order Sobol' sensitivity indices (see Chapter 2). Many multivariate functions in engineering models vary mainly along a reduced number of directions in the space of input parameters [Constantine *et al.*, 2016a]. When these directions correspond to coordinate directions, global sensitivity measures are very effective to determine the most influential parameters. However, some functions vary mostly along directions of the input space that are not aligned with the coordinate system of the input space. In these cases, these methods can perform poorly. Let us take, as a simple example, the following function:

$$f(x, y) = (0.32x + 0.68y)^2 \,,$$

with $x, y \in [-1, 1]$. As it can be noticed form figure 5.1, f varies the most along the direction $(0.32, 0.68)$, while it is constant along the direction $(-0.32, 0.68)$. This bivariate function can be actually consider univariate once the coordinate system has been rotated appropriately. Functions showing this behavior

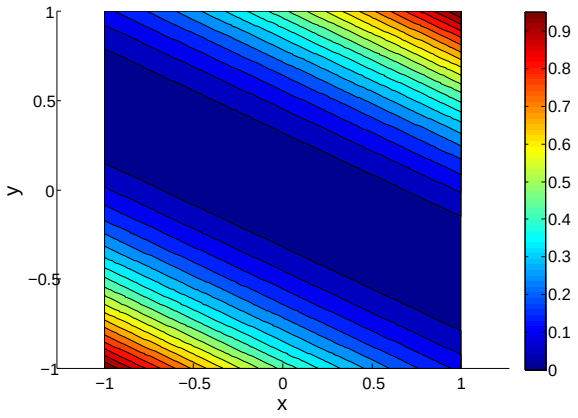

Figure 5.1: This function $f(x, y) = (0.32x + 0.68y)^2$ varies the most along the direction $(0.32, 0.68)$, while it is constant along the perpendicular direction $(-0.32, 0.68)$.

are often referred to as *ridge functions*. This suggests an alternative form of dimension reduction: rotate the coordinates such that the directions of the strongest variation are aligned with the rotated coordinates, and construct a response surface using only the most important rotated coordinates. Stagnation pressure and heat flux for the HEG cylinder as a function of freestream density and velocity, as can be seen in Figure 5.2, also behave like ridge function, as many other physical functions of interests, as discussed in [Constantine *et al.*, 2016a].

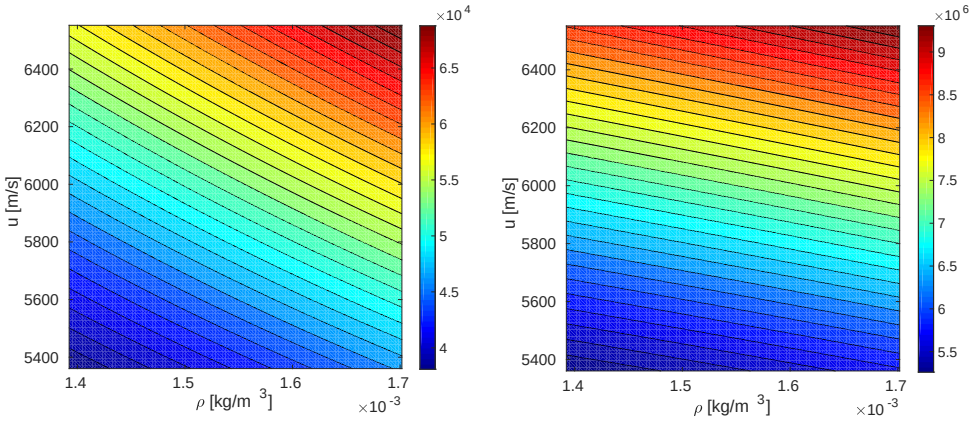

(a) Pressure (b) Heat Flux

Figure 5.2: Ridge behavior for stagnation pressure and heat flux as function of freestream density and velocity for the HEG cylinder.

[Constantine *et al.*, 2014; Constantine, 2015] proposed a method for detecting and exploiting the directions of strongest variability of a given function, called *active subspaces*, to construct an approximation of the function on a low-dimensional subspace of inputs. These directions are exploited by first projecting the input space to the low-dimensional subspace and then approximating the function on this active subspace. This kind of dimensionality reduction can be very effective if the function of interest shows a ridge behavior, allowing a smaller reduced input space compared to other more classical techniques like Sobol' indices.

Since the functions of interest for the study case of the HEG cylinder show a ridge behavior, we are interested in exploiting active subspaces to build a low-dimensional surrogate model and use it for direct and inverse uncertainty propagation. The possibility to work in a very low dimensionality is very advantageous for the training of a surrogate model, and also for the choice of an adequate set of proposal distribution widths ω_i (in Algorithm 2) allowing the MCMC algorithm used in the Bayesian inverse problem to efficiently explore the posterior space and converge in a number of iterations that is not too large.

In this chapter, active subspaces are firstly defined in 5.2. Then, in Section 5.3 a method for detecting active subspaces for computational models is presented. An approach to exploit active subspaces to accelerate Bayesian inference is proposed in 5.4 and compared with another approach presented in the recent literature [Constantine *et al.*, 2016b]. Finally, in Section 5.5.4, the two approaches are used for the freestream reconstruction in the HEG cylinder study case.

5.2 Active Subspaces

To review active subspaces, we closely follow [Constantine, 2015, Chapter 3] and [Constantine *et al.*, 2014]. We denote a given function of d input variables $f : \mathbb{R}^d \to \mathbb{R}$, where $\mathbf{x} \in \mathbb{R}^d$ is the vector of input parameters, with a joint probability density function $\sigma : \mathbb{R}^d \to \mathbb{R}$, and $f(\mathbf{x}) \in \mathbb{R}$ is the output of interest. Assume that f is continuous and differentiable in the support of σ, with continuous and square-integrable (with respect to σ) derivatives. Note that there is nothing inherently linked to stochastic inputs about active subspaces: we chose to perform the analysis using random inputs and tools from probability theory such as expectations since this work is focused on uncertainty quantification and probability notation gives interesting interpretations, but active subspaces can be found also for functions with deterministic inputs, and exploited in deterministic applications such as design optimization [Lukaczyk *et al.*, 2014].

Let us define the $d \times d$ symmetric, positive semidefinite matrix $\boldsymbol{C}$ as:

$$\boldsymbol{C} \;=\; \int \nabla f(\mathbf{x})\, \nabla f(\mathbf{x})^T\, \sigma(\mathbf{x})\, \mathrm{d}\mathbf{x}\,, \tag{5.1}$$

where the gradient of f is defined by the column vector $\nabla f(\mathbf{x}) = (\frac{\partial f}{\partial x_1} \dots \frac{\partial f}{\partial x_d})^T$. C can be interpreted as the uncentered covariance of the gradient vector. Since C is symmetric and positive semidefinite, it admits a real eigenvalue decomposition, that is:

$$\boldsymbol{C} \;=\; \boldsymbol{W}\Lambda\boldsymbol{W}^T\,, \tag{5.2}$$

where $\boldsymbol{W}$ is the orthogonal matrix of eigenvectors and Λ is diagonal matrix of non-negative eigenvalues $\Lambda = \mathrm{diag}(\lambda_1, \dots, \lambda_d)$ arranged in descending order $\lambda_1 \geq \dots \geq \lambda_d \geq 0$. The eigenpairs of this matrix are able to reveal structures in the function f, since (see [Constantine, 2015, Lemma 3.1]),

$$\lambda_i \;=\; \int \left(\mathbf{w}_i^T \nabla f(\mathbf{x})\right)^2 \sigma(\mathbf{x})\, \mathrm{d}\mathbf{x}, \qquad i = 1, \dots, d. \tag{5.3}$$

In words, the i-th eigenvalue measures the average, squared directional derivative of f along the corresponding eigenvector. Thus, if $\lambda_i > \lambda_j$, then perturbing $\mathbf{x}$ along $\mathbf{w}_i$ changes f more, on average, than perturbing $\mathbf{x}$ along $\mathbf{w}_j$. Moreover, if $\boldsymbol{C}$ is rank deficient, meaning that has some null eigenvalues, then its null space contains directions in the space of $\mathbf{x}$ along which f is constant.

With eigenvalues arranged in decreasing order, it is possible to separate them into a set that corresponds to greater average variation and a set corresponding to smaller average variation of f:

$$\Lambda = \begin{bmatrix} \Lambda_1 & 0 \\ 0 & \Lambda_2 \end{bmatrix} \qquad \text{and} \qquad \boldsymbol{W} = \begin{bmatrix} \boldsymbol{W}_1 & \boldsymbol{W}_2 \end{bmatrix}\,, \tag{5.4}$$

with $\Lambda_1 = \mathrm{diag}(\lambda_1, \dots, \lambda_n)$, with $n < d$, and $\boldsymbol{W}_1$ the collection of n eigenvectors corresponding to the eigenvalues Λ_1. Note that the eigenvectors $\boldsymbol{W}$ define a rotation of $\mathbb{R}^d$ and consequently of the domain of f. Therefore, it is possible to define the following rotated coordinates

$$\mathbf{y} = \boldsymbol{W}_1^T\mathbf{x} \tag{5.5}$$

$$\mathbf{z} = \boldsymbol{W}_2^T\mathbf{x}\,, \tag{5.6}$$

with $\mathbf{y} \in \mathbb{R}^n$ and $\mathbf{z} \in \mathbb{R}^{d-n}$. Thanks to this definition and the orthogonality of $\boldsymbol{W}$, it is possible to decompose $\mathbf{x}$ in the following way

$$\mathbf{x} = \boldsymbol{W}\boldsymbol{W}^T\mathbf{x} = \boldsymbol{W}_1\boldsymbol{W}_1^T\mathbf{x} + \boldsymbol{W}_2\boldsymbol{W}_2^T\mathbf{x} = \boldsymbol{W}_1\mathbf{y} + \boldsymbol{W}_2\mathbf{z}\,, \tag{5.7}$$

and the function can be rewritten showing its dependency on the rotated variables:

$$f(\mathbf{x}) = f(\boldsymbol{W}_1\mathbf{y} + \boldsymbol{W}_2\mathbf{z}). \tag{5.8}$$

An important property, taken from [Constantine *et al.*, 2014, Lemma 2.2], can be derived by this new description of the function:

$$\int (\nabla_{\mathbf{y}} f)^T \nabla_{\mathbf{y}} f \, \sigma(\mathbf{x}) \, \mathrm{d}\mathbf{x} = \sum_{i=1}^{n} \lambda_i \tag{5.9}$$

$$\int (\nabla_{\mathbf{z}} f)^T \nabla_{\mathbf{z}} f \, \sigma(\mathbf{x}) \, \mathrm{d}\mathbf{x} = \sum_{i=n+1}^{d} \lambda_i. \tag{5.10}$$

This property motivates the use of the name *active subspace* for the subset $\mathbf{y}$ of the rotated coordinates. In fact, $\mathbf{y}$ is the subset of directions defined by the columns of $\boldsymbol{W}_1$ along which f varies more on average, while along the directions $\mathbf{z}$ defined by the columns of $\boldsymbol{W}_2$ the function shows small average variations. Note that, in the extreme case where the eigenvalues $\lambda_{n+1}, \ldots, \lambda_d$ are all zero, equation (5.10) implies that the gradient along z is zero everywhere in $\mathbf{x}$ and therefore the function is $\mathbf{z}$-invariant.

Active subspaces can be exploited to find an approximation of reduced dimensionality for a function that is $\mathbf{z}$-invariant or nearly $\mathbf{z}$-invariant. They allow to find an n-dimensional, $\mathbf{z}$-invariant approximation of the original d-dimensional function. This is useful when d is too high to allow affordable UQ study or surrogate model training. For an arbitrarily fixed $\mathbf{y}$, the best guess one can make at the value of f is its average over all values of $\mathbf{x}$ that map to $\mathbf{y}$ [Constantine *et al.*, 2014]. This is the conditional expectation of f given $\mathbf{y}$. Therefore, we can define the function g that depends only on $\mathbf{y}$ by

$$g(\mathbf{y}) = \mathbb{E}(f|\mathbf{y}) = \int_z f(\boldsymbol{W}_1\mathbf{y} + \boldsymbol{W}_2\mathbf{z}) \, \pi_{\mathbf{z}|\mathbf{y}}(\mathbf{z}) \, \mathrm{d}\mathbf{z} \, , \tag{5.11}$$

with the conditional density $\pi_{\mathbf{z}|\mathbf{y}}(\mathbf{z})$ defined in the standard way from the joint density of the rotated variables $\pi(\mathbf{y}, \mathbf{z}) = \sigma_{\mathbf{x}}(\boldsymbol{W}_1\mathbf{y} + \boldsymbol{W}_2\mathbf{z})$. The function g can be used to approximate f at a given $\mathbf{x}$ with the following construction:

$$f(\mathbf{x}) \approx g(\mathbf{y}) = g(\boldsymbol{W}_1^T\mathbf{x}). \tag{5.12}$$

For definition, each evaluation of g requires an integral of the actual model with respect to the inactive variables $\mathbf{z}$. However, if f is nearly $\mathbf{z}$-invariant, it means that it is nearly constant along the coordinates $\mathbf{z}$. Thus, in many practical applications no integrations are needed to approximate the function, as will be shown in Section 5.3.

It is finally possible to build a surrogate model $\hat{g}$ of the lower-dimensional function g. This allows to construct a response surface with respect to the few variables $\mathbf{y} \in \mathbb{R}^n$ instead of the original variables $\mathbf{x} \in \mathbb{R}^d$.

$$f(\mathbf{x}) \approx g(\boldsymbol{W}_1^T\mathbf{x}) \approx \hat{g}(\boldsymbol{W}_1^T\mathbf{x}). \tag{5.13}$$

5.3 Finding active subspaces for dimension reduction

When simulation codes have gradient capabilities (*e.g.*, adjoint-based derivatives or algorithmic differentiation [Griewank et Walther, 2008]), then it is possible to estimate $\boldsymbol{C}$ from (5.1) with numerical integration such as by simple Monte Carlo. Then the eigenpairs of $\boldsymbol{C}$'s estimate provide estimates of the active subspaces [Constantine et Gleich, 2015]. However, many complex simulation codes do not have subroutines for gradients. In this case, we resort to modeling the gradients using function evaluations. For example, finite difference approximations of partial derivatives are the slope of a plane that interpolates two nearby function evaluations. The approach outlined in Algorithm 8, based on a least-squares-fit linear approximation of $f(\mathbf{x})$, has been surprisingly effective for uncovering one-dimensional active subspaces in a range of applications from integrated hydrological modeling [Jefferson *et al.*, 2015] to multiphysics scramjet modeling [Constantine *et al.*, 2015] to satellite system modeling [Hu *et al.*, 2016].

Algorithm 8 Linear model-based approach for estimating a one-dimensional active subspace; see [Constantine, 2015, Algorithm 1.3].

1. Choose $N > d+1$ sampling points $\mathbf{x}_j \in \mathbb{R}^d$ in the support of $\sigma(\mathbf{x})$.
2. For each $\mathbf{x}_j$, run the simulation model to compute $f_j = f(\mathbf{x}_j)$.
3. Find the coefficients $\hat{a}_0$ and $\hat{\mathbf{a}}$ of the least-squares-fit linear model such that
$$f_j \;\approx\; \hat{a}_0 + \hat{\mathbf{a}}^T \mathbf{x}_j, \quad j = 1, \ldots, N. \tag{5.14}$$
4. Compute the vector $\hat{\mathbf{w}}$ that is the normalized gradient of the linear model,
$$\hat{\mathbf{w}} \;=\; \hat{\mathbf{a}} / \|\hat{\mathbf{a}}\|, \tag{5.15}$$
where $\|\cdot\|$ is the vector 2-norm.

There are no eigenvalues computed in Algorithm 8, but the vector it computes often defines a one-dimensional active subspace. The algorithm is motivated as follows. Suppose that $f(\mathbf{x})$ is nearly linear and its gradient is nearly constant, *i.e.*, for some constants $a_0 \in \mathbb{R}$ and $\mathbf{a} \in \mathbb{R}^d$,

$$f(\mathbf{x}) \approx a_0 + \mathbf{a}^T \mathbf{x}, \quad \nabla f(\mathbf{x}) \approx \mathbf{a}. \tag{5.16}$$

Then $\boldsymbol{C}$ from (5.1) becomes

$$\boldsymbol{C} \approx \int \mathbf{a}\,\mathbf{a}^T \sigma(\mathbf{x})\, d\mathbf{x} = \mathbf{a}\,\mathbf{a}^T = \mathbf{w}\,\lambda\,\mathbf{w}^T, \tag{5.17}$$

where $\mathbf{w} = \mathbf{a}/\|\mathbf{a}\|$ and $\lambda = \|\mathbf{a}\|^2$. This linear model-based approach is closely related to the *ordinary least-squares* method [Li et Duan, 1989] for *sufficient dimension reduction* [Cook, 1998] in statistical regression. Although the algorithms across the two literatures are the same, the interpretation differs substantially between methods for data sets with random noise compared to methods for deterministic computer simulations.

To verify that the computed vector $\hat{\mathbf{w}}$ from Algorithm 8 has identified a one-dimensional active subspace, it is possible to make a *summary plot*, which is a scatter plot of f_j versus the rotated coordinate $\hat{\mathbf{w}}^T\mathbf{x}_j$. Such plots are common in regression graphics for identifying low-dimensional structures in regression data sets [Cook, 1998], and they are related to statistical techniques for *projection pursuit* [Huber, 1985]. If the plot reveals a strong univariate trend, then we can confidently approximate

$$f(\mathbf{x}) \;\approx\; \hat{g}(\hat{\mathbf{w}}^T\mathbf{x}), \tag{5.18}$$

where $\hat{g} : \mathbb{R} \to \mathbb{R}$ is fitted (*e.g.*, a least-squares-fit polynomial) with the pairs $(\hat{\mathbf{w}}^T\mathbf{x}_j, f_j)$, hence it is already usable as surrogate model of the function of interest with respect to the active variable. The plot enables the engineer to assess the quality of the fitted surface visually without the need to interpret complicated response surface quality metrics.

5.4 Exploiting Active Subspaces in MCMC for Bayesian inversion

The dimensional reduction enabled by active subspaces can be very useful in both forward and inverse UQ. The forward uncertainty propagation takes direct advantage of the presence of active subspace in the function of interest because this allows to train a surrogate model on a lower-dimensional space, reducing the drawbacks caused by the *curse of dimensionality*. Active subspaces can also be exploited to accelerate Markov Chain Monte Carlo (MCMC) algorithms (Section 2.5.1) to draw samples from the posterior distribution of Bayesian inference, even if more care has to be taken on some aspects. For this reason, in this section two approaches are detailed to exploit active subspaces in MCMC for Bayesian inversion. The first aims to reduce the input dimensionality in the so-called data misfit function 5.4.1, while the second in the parameter-to-observable map which the computational model constitutes 5.4.2.

5.4.1 Active subspace of the data misfit function

Let us recall the likelihood function $\ell(\boldsymbol{d}|\mathbf{x})$ for independent additive measurement noise, describe in equation (2.30). Assume the measurement noise

$\boldsymbol{\eta}$ to be a Gaussian vector with zero mean and diagonal covariance matrix $\mathrm{diag}(\sigma_1^2, \dots, \sigma_{n_m}^2)$, with σ_j^2 representing the amplitude of the measurement errors for each of the n_m independent measurements. In this case, the likelihood reads:

$$\ell(\boldsymbol{d}|\mathbf{x}) = \prod_{j=1}^{n_m} p_{\eta_j}(d_j - f_j(\mathbf{x})) \propto \exp\left(-\sum_{j=1}^{n_m} \frac{\big(d_j - f_j(\mathbf{x})\big)^2}{\sigma_j^2}\right). \tag{5.19}$$

As suggested by [Constantine *et al.*, 2016b] and also by [Cui *et al.*, 2014], to reduce the dimensionality of the MCMC related to a Bayesian inversion, it is possible to look for the active subspaces of the so-called *data misfit* function $m(\mathbf{x})$, or just *misfit*, that is the negative log-likelihood:

$$m(\mathbf{x}) = \sum_{j=1}^{n_m} \frac{\big(d_j - f_j(\mathbf{x})\big)^2}{\sigma_j^2}. \tag{5.20}$$

For a given point in the parameter space, the misfit measures how far the model observations are from the given data. When using the misfit to define the active subspace, the the inactive subspace identifies the directions along which the likelihood is relatively flat. This means that perturbing the parameters along the inactive variables changes the likelihood relatively little, on average, and so that the data will inform mostly the active directions.

From a theoretical point of view, to compute the averages defining the matrix C in (5.1) we need to integrate using the prior distribution $\sigma(\mathbf{x})$, which requires a careful interpretation of the data $\mathbf{d}$. In the measurement errors model (2.29) for Bayesian inference, $\mathbf{d}$ is a random variable whose mean depends on $\mathbf{x}$. Therefore $\mathbf{d}$ and $\mathbf{x}$ are not independent, and so we can not integrate against the prior without changing $\mathbf{d}$ as $\mathbf{x}$ varies. However, if we treat the realization $\mathbf{d}$ as a fixed and constant vector, then we can perform the integral defining C without any problem. By doing this, C and all derived quantities can not be interpreted anymore as random variables conditioned on $\mathbf{d}$, but they are functions of $\mathbf{d}$. Hence, in practice, when changing set of data, it is necessary to recompute the active subspace for the misfit.

Once the active subspace $\mathbf{y}$ for the misfit function have been identified and a surrogate $\hat{m}(\mathbf{y})$ have been trained, it is possible to exploit this low-dimensional structure in an MCMC. Algorithm 9 is a simple Metropolis-Hastings algorithm modified to run in the n-dimensional active subspace of the misfit function instead than in the $d > n$ original variables.

5.4.2 Active subspaces of the parameters-to-observables map

In this section, we introduce another way to use active subspaces for Bayesian calibration. It exploits the low-dimensional structure in the parameter-to-

Algorithm 9 A Metropolis-Hastings MCMC (see [Kaipio et Somersalo, 2005, Chapter 3.6.2]) on the active variables using the misfit surrogate $\hat{m}(\mathbf{y})$ and the kernel density estimate of the prior $\hat{\pi}_{\mathbf{y}}$.

Given an initial point $\mathbf{y}_0 \in \mathbb{R}^n$. For $k = 0, 1, 2, \ldots,$

1. Draw $\mathbf{y}' \in \mathbb{R}^n$ from a symmetric proposal distribution centered at $\mathbf{y}_k$.
2. Compute the acceptance ratio,

$$\alpha(\mathbf{y}', \mathbf{y}_k) \;=\; \text{minimum}\left(1, \frac{\exp(-\hat{m}(\mathbf{y}'))\,\hat{\pi}_{\mathbf{y}}(\mathbf{y}')}{\exp(-\hat{m}(\mathbf{y}_k))\,\hat{\pi}_{\mathbf{y}}(\mathbf{y}_k)}\right). \tag{5.21}$$

3. Draw t uniformly from $[0, 1]$. If $\alpha(\mathbf{y}', \mathbf{y}_k) > t$, set $\mathbf{y}_{k+1} = \mathbf{y}'$. Otherwise, set $\mathbf{y}_{k+1} = \mathbf{y}_k$.

observable map revealed by the active subspaces to enable efficient Bayesian inversion with MCMC. In contrast to the approach in Section 5.4.1, here n_m one-dimensional active subspaces in the parameter-to-observable maps are exploited, one for each output, corresponding to the measured quantities.

Let us suppose that each quantity of interest f_j, with $j = 1, \ldots, n_m$, depends on just one active variable. This hypothesis is reasonable for many engineering systems, as mentioned in Section 5.3. The directions $\hat{\mathbf{w}}_j$ that define these active variables are in general correlated but not identical. Define the matrix $\boldsymbol{W} \in \mathbb{R}^{d \times n_m}$ as the collection of the vectors defining the active directions of each output

$$\boldsymbol{W} \;=\; \begin{bmatrix} \hat{\mathbf{w}}_1 & \ldots & \hat{\mathbf{w}}_{n_m} \end{bmatrix}, \tag{5.22}$$

and let $\boldsymbol{V} \in \mathbb{R}^{d \times (d - n_m)}$ contain a basis for the null space of $\boldsymbol{W}^T$. For convenience, we orthogonalize the basis for the range of $\boldsymbol{W}$. Let

$$\boldsymbol{W} \;=\; \boldsymbol{U}\boldsymbol{R}, \qquad \text{with} \qquad \boldsymbol{U} \in \mathbb{R}^{d \times n_m},\ \boldsymbol{R} \in \mathbb{R}^{n_m \times n_m}, \tag{5.23}$$

be the tall QR factorization of $\boldsymbol{W}$, where $\boldsymbol{U}$ has orthogonal columns and $\boldsymbol{R}$ is upper triangular. Any parameter point $\mathbf{x} \in \mathbb{R}^d$ can be decomposed into a projection on the range of $\boldsymbol{W}$ and projection onto its orthogonal complement,

$$\mathbf{x} \;=\; \boldsymbol{U}\boldsymbol{U}^T\mathbf{x} + \boldsymbol{V}\boldsymbol{V}^T\mathbf{x} \;=\; \boldsymbol{U}\mathbf{y} + \boldsymbol{V}\mathbf{z}, \tag{5.24}$$

where $\mathbf{y} = \boldsymbol{U}^T\mathbf{x}$ and $\mathbf{z} = \boldsymbol{V}^T\mathbf{x}$. From the QR decomposition in (5.23), any point $\mathbf{y}$ in the active variables space can be written

$$\mathbf{y} \;=\; \boldsymbol{U}^T\mathbf{x} \;=\; \boldsymbol{R}^{-1}\boldsymbol{W}^T\mathbf{x}, \tag{5.25}$$

which implies

$$\begin{bmatrix} \mathbf{r}_1\mathbf{y} \\ \dots \\ \mathbf{r}_{n_m}\mathbf{y} \end{bmatrix} = \boldsymbol{R}\mathbf{y} = \boldsymbol{W}^T\mathbf{x} = \begin{bmatrix} \hat{\mathbf{w}}_1^T\mathbf{x} \\ \dots \\ \hat{\mathbf{w}}_{n_m}^T\mathbf{x} \end{bmatrix}, \tag{5.26}$$

where $\mathbf{r}_j$ are the rows of $\boldsymbol{R}$. In other words, given a sample of $\mathbf{y}$, we get the arguments to the response surfaces by a linear transformation with $\boldsymbol{R}$.

Let us denote with $\hat{g}_j(\hat{\mathbf{w}}_j^T\mathbf{x})$ the response surfaces of the form in equation (5.18) with vectors $\hat{\mathbf{w}}_j$ computed from Algorithm 8. The summary plots for one-dimensional active subspaces provide strong evidence that perturbing $\mathbf{z}$ in (5.24) has little-to-no effect on either quantity of interest. Therefore, such perturbations should not affect the likelihood (5.19). Then the likelihood in the active variables $\ell_{\mathbf{y}}(\mathbf{d}|\mathbf{y})$, derived from (5.19), is

$$\ell_{\mathbf{y}}(\mathbf{d}|\mathbf{y}) \;\propto\; \exp\left(-\sum_{j=1}^{n_m} \frac{\left(d_j - \hat{g}_j(\mathbf{r}_j\mathbf{y})\right)^2}{\sigma_j^2}\right). \tag{5.27}$$

In other words, we can ignore the variables $\mathbf{z}$ for the Bayesian inversion, since we cannot calibrate them anyway.

To exploit this lower-dimensional structure, we need to derive also a prior for the active variables as follows. For the prior probability density $\sigma(\mathbf{x})$ on the parameter space, we have

$$\begin{aligned} \sigma(\mathbf{x}) &= \sigma(\boldsymbol{U}\mathbf{y} + \boldsymbol{V}\mathbf{z}) \\ &= \pi(\mathbf{y}, \mathbf{z}) \\ &= \pi_{\mathbf{y}}(\mathbf{y})\, \pi_{\mathbf{y}|\mathbf{z}}(\mathbf{z}|\mathbf{y}), \end{aligned} \tag{5.28}$$

where $\pi(\mathbf{y}, \mathbf{z})$ is a joint density on the active and inactive variables, $\pi_{\mathbf{y}}$ is the marginal density on the active variables, and $\pi_{\mathbf{z}|\mathbf{y}}$ is the conditional density on the inactive variables given the active variables. The change of variables is straightforward since the determinant of the Jacobian $\begin{bmatrix} \boldsymbol{U} & \boldsymbol{V} \end{bmatrix}$ of the linear transformation is 1, by orthogonality. Note that the marginal prior of the active variables in some simpler cases can be computed analytically from the one of the physical parameters, but often only a numerical estimation $\hat{\pi}_{\mathbf{y}}$ is possible, for example by kernel density estimation [Silverman, 1986].

Knowing the marginal prior of the active variables $\hat{\pi}_{\mathbf{y}}$ and the likelihood $\ell_{\mathbf{y}}$, we can run a MCMC to draw samples of the posterior on the active variables $\mathbf{y}$. Algorithm 10 shows a Metropolis-Hastings MCMC algorithm (from Kaipio and Sommersalo [Kaipio et Somersalo, 2005, Chapter 3.6.2]) where the continuous state space for the Markov chain is the space of active variables $\mathbf{y}$.

This approach, the way it is currently formulated, requires the number of measured quantities to be smaller than the number of input parameters $n_m < d$. In general, it is also more computationally demanding in case several independent measurements are used for the inference, because an active subspace must be detected for each one. On the other hand, the surrogates built

Algorithm 10 A Metropolis-Hastings MCMC (see [Kaipio et Somersalo, 2005, Chapter 3.6.2]) on the active variables using the likelihood $\ell_{\mathbf{y}}$ from (5.27) and the kernel density estimate of the prior $\hat{\pi}_{\mathbf{y}}$.

Given an initial point $\mathbf{y}_0 \in \mathbb{R}^2$. For $k = 0, 1, 2, \ldots,$

1. Draw $\mathbf{y}' \in \mathbb{R}^2$ from a symmetric proposal distribution centered at $\mathbf{y}_k$.
2. Compute the acceptance ratio,

$$\alpha(\mathbf{y}', \mathbf{y}_k) \;=\; \text{minimum} \left(1, \frac{\ell_{\mathbf{y}}(\mathbf{d}|\mathbf{y}')\, \hat{\pi}_{\mathbf{y}}(\mathbf{y}')}{\ell_{\mathbf{y}}(\mathbf{d}|\mathbf{y}_k)\, \hat{\pi}_{\mathbf{y}}(\mathbf{y}_k)} \right). \tag{5.29}$$

3. Draw t uniformly from $[0, 1]$. If $\alpha(\mathbf{y}', \mathbf{y}_k) > t$, set $\mathbf{y}_{k+1} = \mathbf{y}'$. Otherwise, set $\mathbf{y}_{k+1} = \mathbf{y}_k$.

on the active subspaces are not specific for inverse problems and do not depend on the data, therefore they can be reused with different set of measurement and exploited also for direct UQ.

5.4.3 Sampling back to the original variables

With the two previous approaches in Sections 5.4.1 and 5.4.2, it is possible to efficiently draw MCMC samples from the posterior of the active variables $\mathbf{y}$ given the measurements. However, our goal is to estimate a posterior density of the original parameters $\mathbf{x}$ of the computational model. To achieve this goal, it is possible to exploit a relationship similar to (5.28). Let $\sigma^{\text{pos}}(\mathbf{x})$ be the desired posterior density on the input parameters $\mathbf{x}$. Then, for the output-based active subspaces, we have

$$\begin{aligned} \sigma^{\text{pos}}(\mathbf{x}|\mathbf{d}) &= \sigma^{\text{pos}}(\boldsymbol{U}\mathbf{y} + \boldsymbol{V}\mathbf{z}|\mathbf{d}) \\ &= \pi^{\text{pos}}(\mathbf{y}, \mathbf{z}|\mathbf{d}) \\ &= \pi^{\text{pos}}_{\mathbf{y}}(\mathbf{y}|\mathbf{d})\, \pi^{\text{pos}}_{\mathbf{z}|\mathbf{y}}(\mathbf{z}|\mathbf{y}, \mathbf{d}) \\ &= \pi^{\text{pos}}_{\mathbf{y}}(\mathbf{y}|\mathbf{d})\, \pi_{\mathbf{z}|\mathbf{y}}(\mathbf{z}|\mathbf{y}). \end{aligned} \tag{5.30}$$

The second line is a change of variables, where, similar to (5.28), the determinant of the linear transformation $\begin{bmatrix} \boldsymbol{U} & \boldsymbol{V} \end{bmatrix}$ is 1. The same expression can be obtained for the misfit-based case by just replacing $\boldsymbol{U}$ with $\boldsymbol{W}$. The last line uses the fact that the inactive variables are independent of the data, so the conditional posterior of $\mathbf{z}$ given $\mathbf{y}$ (and the measurements $\mathbf{d}$) is equal to the conditional prior on $\mathbf{z}$ given $\mathbf{y}$. Therefore, given $\mathbf{y}$ drawn according to the posterior on the active variables $\pi^{\text{pos}}_{\mathbf{y}}$ (*i.e.*, from the MCMC on the active variables), we can draw $\mathbf{z}$ according to the conditional prior $\pi_{\mathbf{y}|\mathbf{z}}$; then a sample $\mathbf{x}$ from the posterior σ^{pos} with the construction (5.24). Algorithm 11 shows a

simple Metropolis-Hastings MCMC for drawing $\mathbf{z}$ according to the conditional prior $\pi_{\mathbf{z}|\mathbf{y}}$.

Algorithm 11 A Metropolis-Hastings MCMC [Kaipio et Somersalo, 2005, Chapter 3.6.2] on the inactive variables $\mathbf{z}$ given a value for the active variables $\mathbf{y}$.

Given $\mathbf{y}$ and an initial point $\mathbf{z} \in \mathbb{R}^{d-n}$. For $k = 0, 1, 2, \ldots,$

1. Draw $\mathbf{z}' \in \mathbb{R}^{d-n}$ from a symmetric proposal distribution centered at $\mathbf{z}_k$.
2. Compute the acceptance ratio,

$$\alpha(\mathbf{z}', \mathbf{z}_k) \;=\; \text{minimum}\left(1, \frac{\sigma_{\mathbf{x}}(\boldsymbol{U}\mathbf{y} + \boldsymbol{V}\mathbf{z}')}{\sigma_{\mathbf{x}}(\boldsymbol{U}\mathbf{y} + \boldsymbol{V}\mathbf{z}_k)}\right). \tag{5.31}$$

3. Draw t uniformly from $[0, 1]$. If $\alpha(\mathbf{z}', \mathbf{z}_k) > t$, set $\mathbf{z}_{k+1} = \mathbf{z}'$. Otherwise, set $\mathbf{z}_{k+1} = \mathbf{z}_k$.

Note that Algorithm 11 should be run for every sample y_k, with $k = 1, \ldots, N_{MCMC}$, defining the posterior of the active variables $\mathbf{y}$. Since often thousands of samples are drawn with an MCMC, this operation can be very demanding from a computational point of view. However, a few details must be kept in mind. Fist of all, Algorithm 11 can be run just for the points of the first chain that remain after discarding the burn-in and taking into account a gap to reduce the autocorrelation of the chain. This may reduce substantially the number of run of the second chain. Furthermore, since normally the number of active variables to infer with the first MCMC is small, the first chain can be run with a relatively smaller number of points, at least when compared to higher dimensional reconstructions, and the visualization of the output of the chain and its convergence check is easier. Secondly, Algorithm 11 does not require the evaluation of any model or surrogate model, therefore it runs without a high computational demand.

5.5 Study case: HEG cylinder

In this section, the forward propagation of uncertainties on the HEG cylinder study case, already performed with the PDD-UK method in Chapter 3, will be repeated by exploiting the active subspaces of the two quantities of interest, namely the pressure and heat flux at the stagnation point. Furthermore, results of a Bayesian inference problem accelerated by surrogate models in the active variables are proposed. This is done to state the feasibility of the calibration of freestream density and velocity from stagnation pressure and heat flux data.

5.5.1 Active Subspaces for stagnation pressure and heat flux

As a first step, using the bounds in Table 1.3 for the two uncertain freestream parameters ρ_∞ and u_∞, and the standard deviations in Table 3.12 for the six uncertain chemical parameters, we shift and scale the parameter space to $[-1,1]^2 \times \mathbb{R}^6$, meaning that we want each uniform variable to be rescaled in the interval $[-1,1]$, and each normal to have zero mean and unity variance. This normalization is convenient for studying and exploiting the active subspaces. The thrust of active subspaces is to rotate high-dimensional surfaces until they reveal low-dimensional structure manifesting as directions along which the surface is flat, globally. Centering the parameter space at the origin ensures that all rotations occur about the origin. The prior densities on the normalized space are therefore $1/4$ (the uniform density on the box $[-1,1]^2$) times a multivariate standard Gaussian on $\mathbb{R}^6$.

Here we use the same 576 model evaluations at the training points, used for the PDD-UK surrogate in Chapter 3, to detect active spaces for the two quantities of interest. We use this training set within Algorithm 8 to compute the vectors $\hat{\mathbf{w}}_p$ and $\hat{\mathbf{w}}_q$. Figure 5.3 shows the summary plots and weight vector components for stagnation pressure p_{st} and heat flux q_{st}. The blue dots represent the 576 independent runs of COSMIC code with inputs drawn from the probability densities in Tables 1.3 and 3.12.

Figure 5.3a is the summary plot for pressure, and Figure 5.3b is the summary plot for heat flux. These summary plots reveal low-dimensional structure in the map from input parameters to output observables. The strong univariate trend in the blue dots for each output suggests that orthogonal to the active direction, the surface is relatively constant. The black lines show the one-dimensional polynomial response surfaces $\hat{g}$ from (5.18) fitted to the data pairs. Each surface is a simple univariate quadratic functions with three coefficients. Since the behavior of the rotated quantities of interest is very simple, and only one active variable is retained, it is not necessary to use the more complex PDD-UK surrogate model introduced in Chapter 3. Furthermore, a simple polynomial fit is suited for smoothing the projection errors that arise from the fact that the reduced structure of the functions are not exactly one-dimensional. The data varies roughly 1 or 2% from the fitted surface, but this variation is almost indistinguishable from numerical errors in the complex flow simulation, especially for heat flux values.

Figures 5.3c and 5.3d shows bar plots of the components of $\hat{\mathbf{w}}_p$ and $\hat{\mathbf{w}}_q$, respectively. The vector components give insight into the important input parameters. The relative insensitivity of pressure and heat flux to the reaction rates suggests that it is not possible to reliably calibrate the reaction rates using stagnation pressure and heat flux measurements, but at the same time that uncertainties on the chemical model will not influence strongly the rebuild

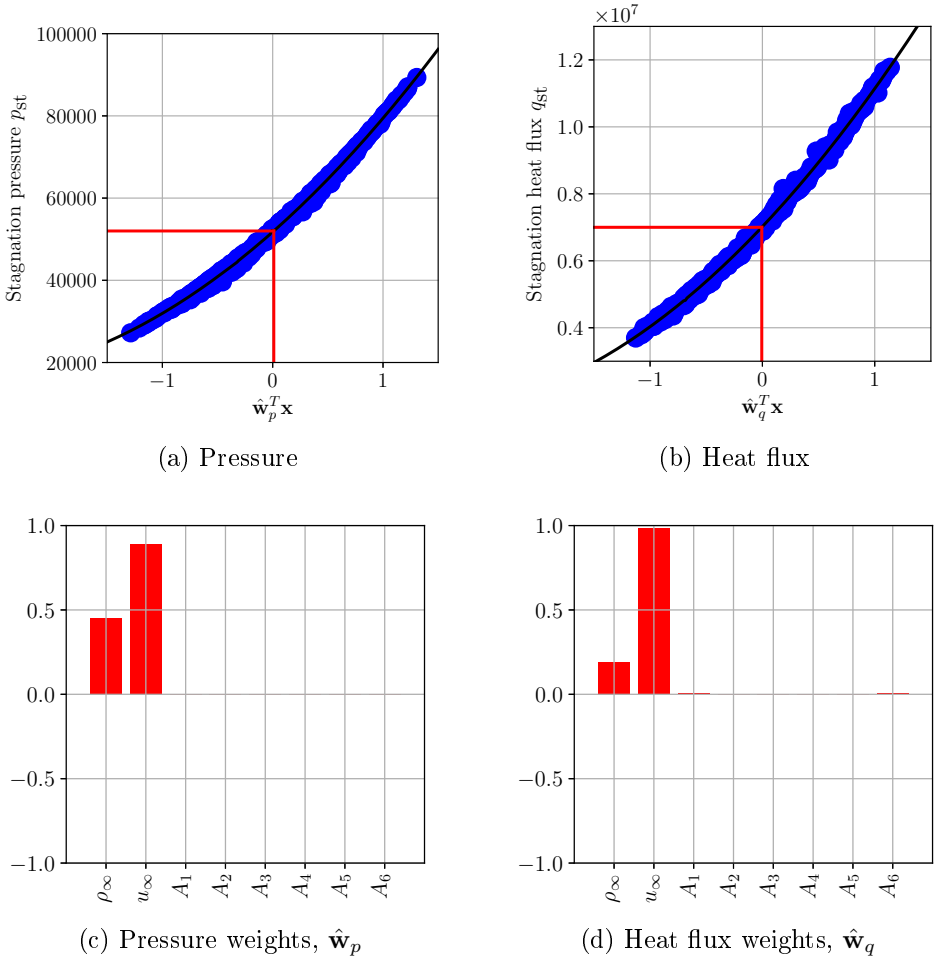

(a) Pressure

(b) Heat flux

(c) Pressure weights, $\hat{\mathbf{w}}_p$

(d) Heat flux weights, $\hat{\mathbf{w}}_q$

Figure 5.3: One-dimensional summary plots (top row) for pressure (left) and heat flux (right) using the vectors $\hat{\mathbf{w}}_p$ and $\hat{\mathbf{w}}_q$, respectively, from Algorithm 8, along with bar plots (bottom row) of the components of $\hat{\mathbf{w}}_p$ and $\hat{\mathbf{w}}_q$. The black lines show the one-dimensional response surfaces. The red horizontal lines are at the given measurements, p_{st}^* and q_{st}^*. The vertical red lines show the value of the respective active variables, $\hat{\mathbf{w}}_p^T\mathbf{x}$ and $\hat{\mathbf{w}}_q^T\mathbf{x}$, that maps to the measurements.

of freestream values and the variance of the quantities of interest.

5.5.2 Comparison with classical global sensitivity analysis

It is possible to compare vector components of the active directions in Figures 5.3c and 5.3d to the variance-based global sensitivity indices computed using the adaptive sparse PDD in Section 3.6.2.

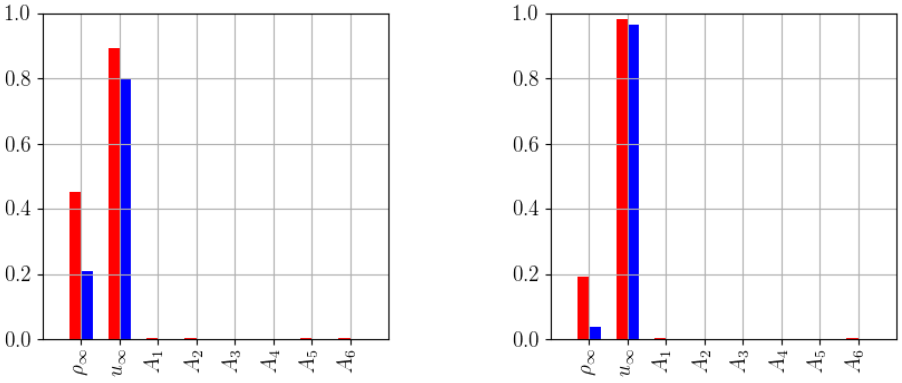

(a) Pressure weights and SI

(b) Heat flux weights and SI

Figure 5.4: Bar plots of the components of $\hat{\mathbf{w}}_p$ and $\hat{\mathbf{w}}_q$ (red) along with the global sensitivity indices (blue).

Figure 5.4 shows bar plots comparing the weights of vectors $\hat{\mathbf{w}}_p$ and $\hat{\mathbf{w}}_q$ (in red) with the Sobol' sensitivity indices computed with sparse PDD (in blue) for both outputs (see Tables 3.13 and 3.14). From the plots, it is possible to notice that global sensitivity indices show a hierarchy of input variables that is consistent with the one of vectors $\hat{\mathbf{w}}_p$ and $\hat{\mathbf{w}}_q$. For these two outputs, the weights suggest that neither pressure nor heat flux is sensitive to changes in the reaction rate coefficients, compared to their sensitivity with respect to free stream conditions.

When the summary plots (*i.e.*, Figures 5.3a and 5.3b) show such strong evidence of univariate structure, the components of the vectors $\hat{\mathbf{w}}_p$ and $\hat{\mathbf{w}}_q$ can be used as global sensitivity metrics. Since these weights are derived from the coefficients of the least-squares-fit linear model, they are similar to the *standard regression coefficients* [Saltelli *et al.*, 2008, Chapter 1.2.5] with different normalization, though their interpretation is significantly different. For more general connections between active subspaces and global sensitivity analysis, see [Constantine et Diaz, 2017].

5.5.3 Forward propagation of uncertainties

Exploiting the very reduced cost of evaluating the surrogate model, a simple Monte Carlo (MC) sampling technique can be applied to the two polynomial response surfaces in the active variables in order to perform a forward uncertainty propagation and compute the statistics of the quantities of interest. This will give the chance to compare to results obtained with PDD-UK surrogate model in Section 3.6.2.

In order to get a set of sampling points of the active variables, 100000

Monte Carlo samples are drawn from the priors of the physical variables and then projected on the active subspace by means of the linear transformation $\mathbf{y} = \hat{\mathbf{w}}^T\mathbf{x}$. Their kernel density estimate (KDE) is reported in Figure 5.5.

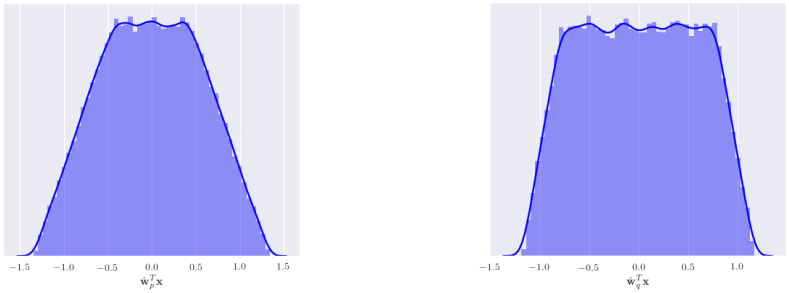

(a) Pressure active var. (b) Heat flux active var.

Figure 5.5: Probability densities of the first active variables for the stagnation pressure (left) and heat flux (right)

The two one-dimensional polynomial response surfaces in the active variables $\hat{g}_p(\hat{\mathbf{w}}_p\mathbf{x})$ and $\hat{g}_q(\hat{\mathbf{w}}_q\mathbf{x})$ are evaluated at the MC sampling points to propagate the input uncertainties to the two outputs. The probability density functions of the output quantities, estimated by means of kernel density estimations on the Monte Carlo samples, are reported in Figure 5.6. The figure shows the propagation of the PDF of the two active variables for p_{st} and q_{st} through the one-dimensional surrogate models and the obtained PDF. The fact of having reduced the input dimensionality of the problem makes the visualization of the uncertainty propagation process very easy. Comparison between results obtained on the active subspace metamodel (blue) and the ones of the physical variables metamodel (green and red) confirm a very good agreement.

Mean and variance of p_{st} and q_{st} are reported in Table 5.1. Differences between results of active subspace and physical variables are very small, being inferior to 1% for the means and up to 1% for variances. This means that the reduced order approximation of the functions of interest introduced by the active subspace (see Equation (5.18)) is able to conserve all the important information in the input-to-output map, as expected. Coefficients of variation are respectively about 26% for the pressure and 29% for the heat flux. It can be noticed that the forward propagation of prior probability densities produces coefficients of variation of the outputs that are bigger than the percentage measurement errors. This allows the posteriors to be mainly informed by the measurements and not by the priors, which in this work are just uninformative intervals chosen by the authors.

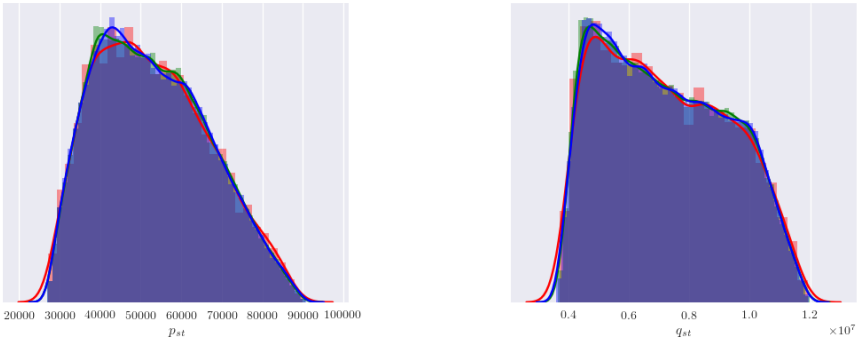

(a) Pressure (b) Heat flux

Figure 5.6: Uncertainty propagation process from the probability densities of the first active variables (top row) to the ones of the stagnation pressure and heat flux (bottom row) through the one-dimensional response surfaces built on the first active variable. Comparison between results obtained on the active subspace metamodel (blue) and the ones of the physical variables metamodel (green for the polynomial response surface and red for the PDD-UK) confirm a very good agreement.

5.5.4 Freestream calibration with Bayesian inference

This section is focused on the inverse UQ problem of rebuilding some uncertain parameters $\boldsymbol{m} = (\rho_\infty, u_\infty)$ starting from experimental (*i.e.* noisy) measurements $\boldsymbol{d} = (p^*_{\text{st}}, q^*_{\text{st}})$ of the stagnation quantities of interest at the wall of the cylinder. We also want to be able to account for other aleatory uncertainties in the physico-chemical model, namely the uncertainties on the chemical reaction rate coefficients $\boldsymbol{c} = \{(A_r)_{r=1,\dots,n_r}\}$. Results are presented by following the two sampling procedure based on MCMC in the active subspace presented in Section 5.4.

Misfit

Let us here follow the approach presented in Section 5.4.1, where the MCMC is run in the active variables of the misfit function. First of all, it is necessary to define the data misfit function $m(\mathbf{x})$ for this particular calibration problem. It reads:

$$m(\mathbf{x}) = \left(\frac{(p^*_{\text{st}} - p_{\text{st}}(\mathbf{x}))^2}{\sigma_p^2} + \frac{(q^*_{\text{st}} - q_{\text{st}}(\mathbf{x}))^2}{\sigma_q^2} \right). \tag{5.32}$$

The given artificial measurements are stagnation pressure $p^*_{\text{st}} = 5.2 \cdot 10^4$ Pa and stagnation heat flux $q^*_{\text{st}} = 7.0 \cdot 10^6$ W/m^2. The standard deviation model for the stagnation pressure noise is $\sigma_p = 0.02\, p^*_{\text{st}}$, and the standard deviation

		AS var.	8D polyn.	PDD-UK
p_{st} [Pa]	μ	53033	53050	53088
	σ	13782	13760	13925
	σ/μ	0.260	0.259	0.262
q_{st} [W/m^2]	μ	7.2029 e6	7.2054 e6	7.2093 e6
	σ	2.0586 e6	2.0596 e6	2.0703 e6
	σ/μ	0.286	0.286	0.287

Table 5.1: Mean value and standard deviation of the quantities of interest computed with the response surfaces built on the pressure and heat flux active variables. Values are computed with 100000 Latin Hypercubes samples and compared to results obtained with a propagation on a polynomial surrogate and the PDD-UK in the 8-dimensional physical input.

model for stagnation heat flux is $\sigma_q = 0.1\, q^*_{\text{st}}$. Once the misfit is defined, it is possible to compute the matrix C to detect if it shows an active subspace. In this case, it is not good to rely on Algorithm 8, since we know from its definition that the misfit function is not nearly-linear.

Figure 5.7 shows the summary plots and weight vector components for the active variable of the misfit function. This summary plot reveal low-dimensional structure in the map from input parameters to output observables. The strong univariate trend in the blue dots for each output suggests that orthogonal to the active direction, the surface is (relatively) constant. The black lines show the one-dimensional 4-th order polynomial response surfaces $\hat{g}$ from (5.18) fitted to the data pairs. Also for the misfit function, as expected, the

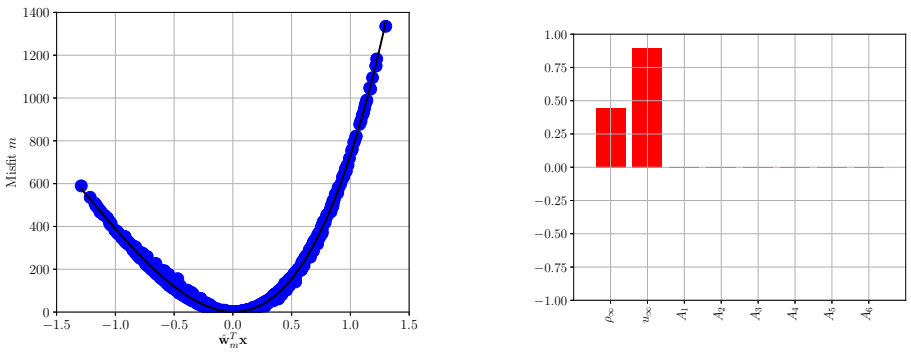

(a) Summary plot

(b) Vector weights

Figure 5.7: One-dimensional summary plots (left) for misfit function using the vectors $\hat{\mathbf{w}}_m$, along with bar plots of the components of $\hat{\mathbf{w}}_m$. The black lines show the one-dimensional response surfaces.

most influent vector components are the two freestream variables, meaning that the chemistry parameters will not be informed by the inference.

In Figure 5.8a a KDE of the prior of the active variable is shown. It is obtained bt projecting along the active direction the Monte Carlo samples of the physical variables. Figure 5.8b shows instead the KDE of the posterior

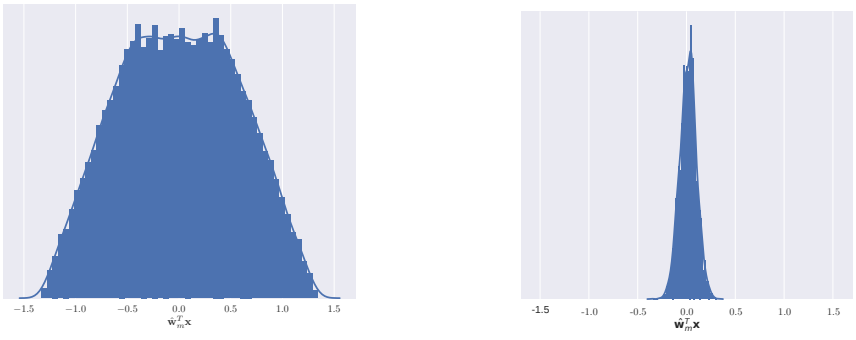

(a) Prior (b) Posterior

Figure 5.8: Prior (left) and posterior (right) distributions for the active variable $\mathbf{y}$ of the misfit function.

distribution of the active variable $\mathbf{y}$, obtained with the MCMC algorithm in Algorithm 9, using a Gaussian proposal distribution with an adapted exploration step. The chain has been run for 500000 iterations and 100000 were discarded as burn-in.

Parameters-to-observables map

In this section, we illustrate the results for the Bayesian calibration following the approach in Section 5.4.2. As seen in Section 5.5.1, stagnation pressure and heat flux each depend on one active variable. The two directions, $\hat{\mathbf{w}}_p$ and $\hat{\mathbf{w}}_q$, that define these two active variables are used to define the matrix $\boldsymbol{W}$ as

$$\boldsymbol{W} = \begin{bmatrix} \hat{\mathbf{w}}_p & \hat{\mathbf{w}}_q \end{bmatrix}, \tag{5.33}$$

that is orthogonalized for convenience in

$$\boldsymbol{W} = \boldsymbol{U}\boldsymbol{R}, \qquad \boldsymbol{U} \in \mathbb{R}^{8\times 2}, \ \boldsymbol{R} \in \mathbb{R}^{2\times 2}, \tag{5.34}$$

The next step that must be done to draw samples from the posterior of the active variables with Algorithm 10 is to define the prior $\pi_{\mathbf{y}}$ of the active variables starting from the one of the physical parameters $\sigma(\mathbf{x})$. If $\sigma(\mathbf{x})$ was Gaussian, then $\pi_{\mathbf{y}}$ would also have been a Gaussian density. However, prior components are not all Gaussian (see Table 1.3), hence $\pi_{\mathbf{y}}$ must be estimated

numerically. Since it is only a bivariate density and the forward map $\mathbf{y} = \boldsymbol{U}^T\mathbf{x}$ is simple (with no dependence on the complex physics model), we can estimate $\pi_{\mathbf{y}}$ to sufficient accuracy with a bivariate kernel density estimate. Figure 5.9b shows the contours of a bivariate kernel density estimate using the

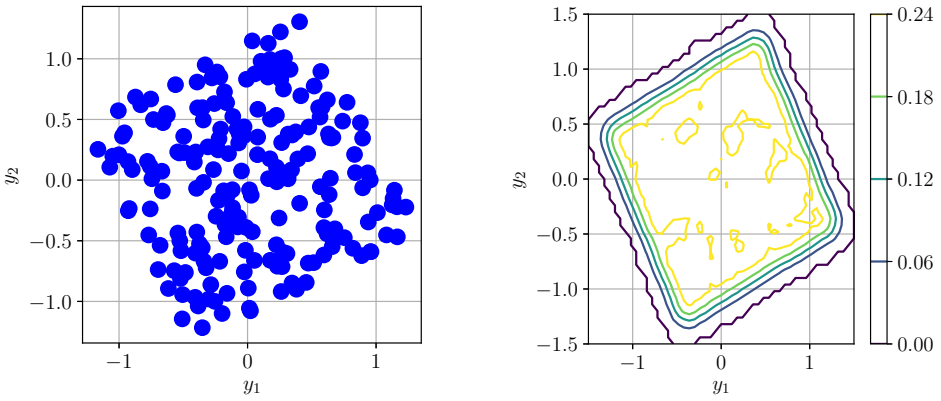

(a) Prior samples of active variables

(b) Kernel density of active variable prior

Figure 5.9: The left figure shows 200 samples of the active variables $\mathbf{y} = \boldsymbol{U}^T\mathbf{x}$ with $\mathbf{x}$ drawn from its normalized prior. The right figure shows the contours of the bivariate kernel density estimate for the active variables constructed from 50000 samples; it is essentially a rotate bivariate uniform density. The small scale fluctuations are a result of the finite sampling.

Python SciKit Learn's `KernelDensity` function [Pedregosa *et al.*, 2011] with parameters `bandwidth=0.15` and `kernel='tophat'` constructed from 50000 samples of $\mathbf{y} = \boldsymbol{U}^T\mathbf{x}$, where $\mathbf{x}$'s are drawn according to the normalized prior. Figure 5.9a shows a subset of 200 samples for reference. The small scale contour fluctuations near the center of the domain are due to finite sampling. Essentially, the marginal on the two active variables $\mathbf{y} = [y_1, y_2]^T$ is a rotated uniform density. This is consistent with the weights from Figures 5.3c and 5.3d, since the largest weights are associated with the two parameters (ρ_∞ and u_∞) that have uniform priors. Denote the kernel density estimate of $\pi_{\mathbf{y}}$ by $\hat{\pi}_{\mathbf{y}}$.

We use the same response surfaces shown in Figures 5.3a and 5.3b to build a likelihood function on the active variables. Hence, the likelihood in the active variables $\ell_{\mathbf{y}}(p^*_{\text{st}}, q^*_{\text{st}}|\mathbf{y})$, derived from (5.19), is

$$\ell_{\mathbf{y}}(p^*_{\text{st}}, q^*_{\text{st}}|\mathbf{y}) \;\propto\; \exp\left(\frac{-(p^*_{\text{st}} - g_p(\mathbf{r}_1\mathbf{y}))^2}{\sigma_p^2} + \frac{-(q^*_{\text{st}} - g_q(\mathbf{r}_2\mathbf{y}))^2}{\sigma_q^2}\right). \tag{5.35}$$

In our numerical implementation of Algorithm 10, we use a Gaussian proposal density centered at the current state ($\mathbf{y}_k$, see Step 1) with covariance

matrix $\mathrm{diag}(0.23^2, 1.02^2)$, where the two variance values are issue from an adaptation of the exploration step. We run one chain of 250000 steps, and, following the suggestion of Brooks et al. [Brooks *et al.*, 2011, Chapter 6.5], we discard the first part of the chain's samples as *burn in*, and we take in the final sample one sample eache 10 samples, which leaves us with 20000 samples. This is sufficient to cover the two-dimensional space of active variables.

Figure 5.10a shows 200 samples from the MCMC. The samples apparent alignment with the axes y_1 and y_2 is consistent with the rotation induced by $\boldsymbol{R}$ from (5.23) to create orthogonal coordinates (*i.e.*, the columns of $\boldsymbol{U}$ from (5.23) are orthonormal). The difference in the samples spread along the

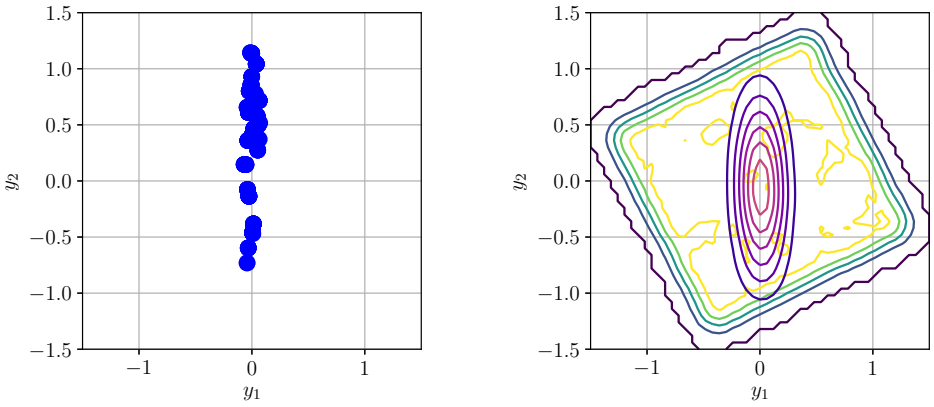

(a) Posterior samples of active variables

(b) Kernel density of posterior on active variables

Figure 5.10: The left figure shows 200 samples from the response surface-enabled MCMC on the active variables. The spread along coordinate axes is consistent with the different noise assumptions in the measurements. The right figure shows contours of a bivariate kernel density estimate of the MCMC samples compared to the prior contours.

axes is consistent with the different noise levels for each output. In effect, the relatively large noise (10%) in the heat flux measurement q^*_{st} permits a larger range of y_2 values that are consistent with the noisy measurements. The relatively low noise (2%) in the pressure measurement p^*_{st} leads to less spread in the y_1 samples. Figure 5.10b shows contours (purple) of a kernel density estimate of the posterior on $\mathbf{y}$ from the MCMC samples; the estimate uses a Gaussian kernel with bandwidth 0.15 implemented in SciKit Learn's `KernelDensity` [Pedregosa *et al.*, 2011]. The axis alignment is consistent with the discussion of the samples in Figure 5.10a. The apparent slight asymmetry about the y_2 axis results from the mild nonlinearity in the response surfaces. The same asymmetry appears in the y_1 axis, though it is not as apparent since the support of the contours is relatively narrow. The posterior contours are

superimposed on top of the contours from the density estimate of the prior $\hat{\pi}_{\mathbf{y}}$. The support of the posterior is smaller than the prior, which implies that the measurements (pressure p^*_{st} and heat flux q^*_{st}) have provided additional information about the parameter uncertainty in the active variables.

Note that the analysis of the posterior density on the active variables provides insights into the workings of the MCMC for Bayesian inversion, particularly since having only two active variables in this case permits helpful visualization.

Posteriors of the physical variables

The final goal of the study case is to have samples from the posterior densities of the physical parameters. It is possible to restore to this set of variables starting from the posteriors of the active variables by means of Eq. (5.30), for both the misfit approach and the parameters-to-observable map approach. If the joint prior on $(\mathbf{y}, \mathbf{z})$ was Gaussian, then the conditional $\pi_{\mathbf{z}|\mathbf{y}}$ would also have been Gaussian. Instead, in our case, the joint prior on $(\mathbf{y}, \mathbf{z})$ is not Gaussian (see section 1.6.1); hence the Metropolis-Hastings MCMC provides a general way to sample from the conditional PDF. In our implementation of Algorithm 11, we use a Gaussian proposal in Step 1 with covariance matrix $(0.8)^2\, \boldsymbol{I}$, where $\boldsymbol{I}$ is the 6×6 identity matrix. In our numerical experiments, we draw 100 samples of $\mathbf{z}$ per MCMC sample of $\mathbf{y}$ from Algorithm 10. From 20000 samples of $\mathbf{y}$, we get 2000000 samples of $\mathbf{x}$ with (5.24). Note that since $\mathbf{z}$ is independent of the measurements, the algorithm for drawing $\mathbf{z}$ given $\mathbf{y}$ does not call for the simulation model or its response surface approximation.

Figure 5.11 compares the univariate marginal posterior densities (blue, red and green lines) on the model parameters to the associated marginal prior densities (black lines) (see Tables 1.3 and 3.12). Notice that the MCMC in the physical variables (green line) used a simple second-order polynomial fit as surrogate. It has been preferred to the PDD-UK since it was already known from the previous analysis that the behavior of the function was easily approximated by such a polynomial representation, and this allowed a reduction in the computational effort involved in the MCMC run. It can be noticed that the only two parameters that are informed by the stagnation point measurements, p^*_{st} and q^*_{st}, (*i.e.*, their posteriors differ substantially from the priors) are the freestream conditions ρ_∞ and u_∞. Since the measurements cannot inform the reaction rates, the reaction rate posteriors are the same as the priors. A further comparison is proposed between the posteriors from the misfit approach (red lines), the ones from the parameters-to-observables approach (blue) and the ones obtained with a single-site updating Metropolis-Hastings MCMC sampling directly in the 8-dimensional physical parameters space (green lines), considering 8D quadratic regressions as metamodels for the stagnation pressure and heat flux. The chain ran for 500000 steps, with adapted explorations

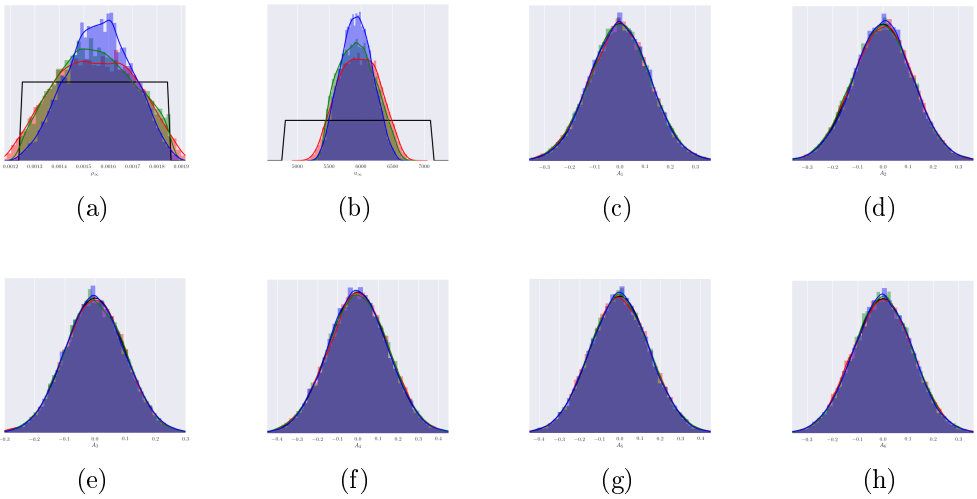

Figure 5.11: Posterior marginal densities from the parameter-to-observables approach (blue lines) on the eight model parameters compared to their marginal priors (black lines); see Tables 1.3 and 3.12. A comparison is shown also with the posteriors obtained with the misfit approach (red) and the ones by MCMC sampling directly in the physical space (green lines). The reaction rate parameters are not informed by the data, so their posterior is essentially the prior. Notice that that the MCMC in the physical variables used a simple second-order polynomial regression as surrogate.

steps for the Gaussian proposals in every dimension. It can be noticed that all the posteriors present a good qualitative agreement.

Figure 5.12 shows the most interesting bivariate marginal posterior, which is on the freestream parameters informed by the measurements, obtained with the parameters-to-observable results. The contours are the posterior and the red box is the joint prior. The freestream parameters are highly correlated in their posterior, so the univariate marginals alone can be misleading. Comparing the contours in Figure 5.12 to the posterior on the active variables in Figure 5.10b, the shapes are essentially the same but rotated; the correlation in the freestream parameters is related to the rotation induced by the matrix $\boldsymbol{R}$ from (5.23).

Posterior means and standard deviations of the free stream are then computed exploiting the MCMC samples of the posteriors and are reported in Table 5.2. A comparison is also performed with the posterior values sampled in the physical space. Values show a good agreement, with differences in the mean values smaller than 1% for both the density and the velocity.

Looking at the potential interest in using heat flux data for reconstruction, note that the coefficient of variation for freestream density and velocity are 8.3% and 4.1%, respectively. This shows how heat flux data could provide

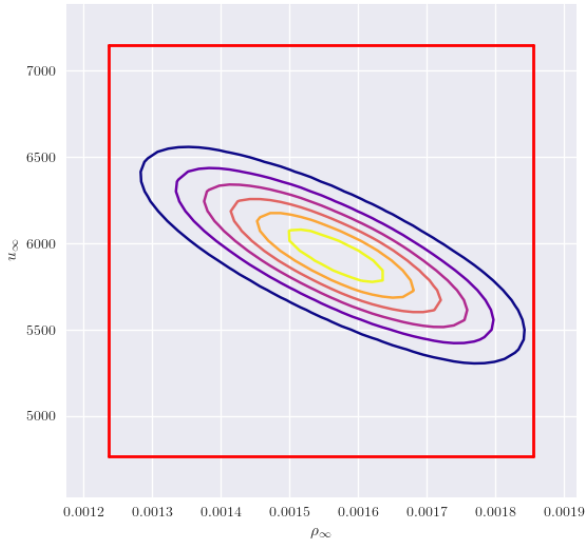

Figure 5.12: Bivariate marginal posterior contours for free stream parameters ρ_∞ and u_∞ compared to the joint marginal prior; see Table 1.3. Compare these contours to the posterior on the active variables in Figure 5.10b.

		AS	AS misfit	Physical var.
ρ_∞ [kg/m^3]	μ	1.5666e-03	1.5524e-03	1.5545e-03
	σ	1.2954e-04	1.6081e-04	1.4806e-04
u_∞ [m/s]	μ	5930.18	5967.83	5939.10
	σ	246.50	316.15	279.13

Table 5.2: Posterior mean value and standard deviation of the inferred free stream quantities computed with the MCMC samples. Comparison between values obtained for the regular chain directly run on the physical variables and the chains for the two different approaches in the active subspace.

additional insights towards the reconstruction of freestream conditions. However, the obtained posterior uncertainties are quite big if compared to other freestream reconstructions in literature (for example [Van Hove et Karatekin, 2017]). This is because the accuracy on velocity is much higher when rebuilt using IMU data, allowing also for a better estimation of the freestream density. Of course an improvement of results would be obtained assuming smaller noise associated with heat flux measurements. Another possibility would be to include IMU results in the Bayesian setting, to get a smaller uncertainty on the velocity, and using heat flux measurements to calibrate other uncertain freestream or model parameters. These aspects should clearly be tested in the

future, also in the context of a real space mission.

5.6 Conclusions

In this chapter, the input dimensionality of direct and inverse UQ problems has been reduced by exploiting active subspaces. In particular, a novel approach to exploit the active subspace in Bayesian inverse problems and MCMC has been introduced. It is based on the use of the active subspace of the actual function of interest, namely the input-to-output map, instead of the use of the active subspace of the log-likelihood (or misfit) function, as proposed in [Constantine *et al.*, 2016b]. This new approach is more versatile, in the sense that the surrogate model built on the active subspace of a function does not depend on measured data, and therefore can be exploited for different applications. Furthermore, it is able to provide direct information on low-dimensional structures of the function of interest, if they exist. The comparison showed that a very small loss of accuracy has to be expected when using active subspaces, with respect to the full-dimensional problem, and a valuable reduction of the input dimensionality. The only drawback of Bayesian inversion with active subspaces is the need to perform a second MCMC algorithm to sample the posterior of the physical variables, after having sampled the one of the active variables. This adds numerical complexity and cost, however, this operation does not require the evaluation of any computational model.

Chapter 6

Application: freestream characterization for EXPERT vehicle

The objective of this chapter is to assess the advantage of exploiting heat flux measurements at the heat shield of the vehicle, together with pressure measurements, to rebuild freestream parameters and other uncertain model parameters. In particular, we will focus on the reconstruction of freestream density, flow angles and catalytic recombination coefficient. Different tests are presented in which the reconstruction problem is solved in a Bayesian framework, exploiting the PDD-UK surrogate model previously introduced to accelerate the MCMC algorithm used to sample from the posterior distributions.

6.1 Introduction

This chapter is devoted to the study of an inverse uncertainty propagation problem within the framework of atmospheric entry of the EXPERT entry vehicle, by the European Space Agency (see Section 1.6.2 for details about the configuration under analysis). The goal is to understand the advantage of using heat flux measurements at the heat shield of the vehicle, together with pressure measurements, for rebuilding the freestream parameters and other uncertain model parameters.

Classical freestream characterization techniques, as reviewed in the introduction and briefly detailed in Appendix A, mostly rely on inertial and surface pressure measurements. Nevertheless, modern entry vehicles are equipped with many different types of sensors, able to provide further information about the air flow near the heat shield. Heat flux data is for example available for vehicles equipped with RAFLEX-like probes, *e.g.* used on the EXPERT vehicle.

However, to the author's knowledge, little effort has been done to try to include this data in the reconstruction process.

The statistical Bayesian approach introduced in Chapter 2 is adopted to solve the inverse problem of the reconstruction. This allows to account for measurement errors and other uncertain model parameters, and to consider complex forward models able to describe the phenomena occurring during the entry flight.

The chapter is structured as follows: in Section 6.2, some practical considerations are given about the choice of the inferred parameters. Then, in Section 6.3 we give a description about the hypothesis and the model used in order to consider the effect of flow angles in the case where only axisymmetric computational models are available. Section 6.4.1 describes the construction of the surrogate models for the quantities of interest, used to accelerate the Markov Chain Monte Carlo algorithm to sample the posterior distributions of the inferred quantities. Finally, in Section 6.5, results are shown for several cases of parameter calibrations: using only pressure measurements, to reproduce classical reconstruction techniques in the Bayesian framework (Sec. 6.5.1), using only heat flux measurements, to assess the advantage of using this kind of data (Sec. 6.5.2), and exploiting both pressure and heat flux (Sec. 6.5.3). All these explored configurations are summarized for clarity in Table 6.1.

	Measurements			Rebuilt variables		
	p stag.	p all	q all	ρ_∞	γ	angles
Case 1a	×			×		
Case 1b		×		×		
Case 2		×				×
Case 4		×		×		×
Case 5			×		×	
Case 5			×		×	×
Case 6		×	×	×		×
Case 7		×	×	×	×	×

Table 6.1: Reconstruction cases explored in this chapter for the EXPERT vehicle. Note that "p stag." refers to the use of only pressure measurement at the stagnation point, while "all" indicates that all the measurements are used, which are available in five locations on the forebody (see Figures 6.2 and 6.3).

6.2 Remark on the choice of the inferred parameters

Currently, freestream reconstruction for entry trajectories exploits mainly inertial data, provided by IMU (Inertial Measurement Unit) measurements, combined with pressure data from the FADS (Flush Air Data System), mounted in the thermal protection system (TPS) of the vehicle forebody. In general, inertial data are able to give a very accurate estimate of the vehicle velocity along the trajectory, with error bounds in the order of very few meters per second for velocities in the order of kilometers per second. For this reason, if neglecting the effect of wind gusts, it is possible to suppose that the freestream velocity is exactly known.

Classically, pressure measurements are used to reconstruct the atmospheric conditions at the freestream, especially the density of the gas mixture. In this work, we will consider the freestream temperature to be known and rebuild the density from wall pressure measurements. The third thermodynamic variable can be computed with the perfect gas law, knowing the value of the other two. Furthermore, the difference in pressure values at different sensor locations can be used to estimate the flow angles, as done in the literature [Häuser *et al.*, 2004].

Knowing these facts, we have to find a way to usefully exploit heat flux measurements in the reconstruction of other freestream or model parameters, whose value is usually known within a certain degree of uncertainty, or to improve the quality of the reconstruction for the previously mentioned quantities. It is important to keep in mind that, with current technologies, heat flux measurements are affected by much higher measurement errors than pressure ones. Therefore, the chosen rebuilt parameters should be well informed by heat flux measurements, or, in other words, the measured heat flux value should be strongly influenced by variations of those variables. Even though heat flux measurements could be very useful to inform many different flow quantities, for example freestream velocity, parameters related to the chemical mechanism of the gas mixture, wall catalycity and ablation parameters, and so on, in practice they are not commonly exploited in the literature, probably due to their elevated measurement error.

One possible choice could be to infer the freestream velocity, which is known to have a strong influence on the wall heating [Sutton et Graves, 1971]. The case study of the HEG cylinder, repetitively used in this work, although not being representative of a real entry problem, served as a preliminary analysis of the influence of stagnation heat flux with respect to velocity variations and to state the possibility of rebuilding this quantity starting from wall heating measurements. As seen in Section 5.5.4, freestream velocity was well informed by heat flux measurements. Nevertheless, the posterior coefficient of variation of about 4% tells us that the posterior uncertainty on the velocity obtained

by heat flux measurements is much higher that the one associated to IMU reconstructions. Given accurate heat flux models and measurements, velocity might be reconstructed. However this is not feasible, since models and sensors are not accurate enough, nor is required, since velocity is already accurately reconstructed from IMU measurements. However, heat flux measurements could be usefully exploited when inertial measurements are not available, for example in case of an IMU malfunctioning. In this case, the fact of having the ability to still be able to rebuild the velocity value can be very important, even if with a higher uncertainty level. However, in this chapter, we will not repeat the reconstruction of the velocity but we investigate the possibility of using forebody heat flux data to reconstruct the wall catalycity.

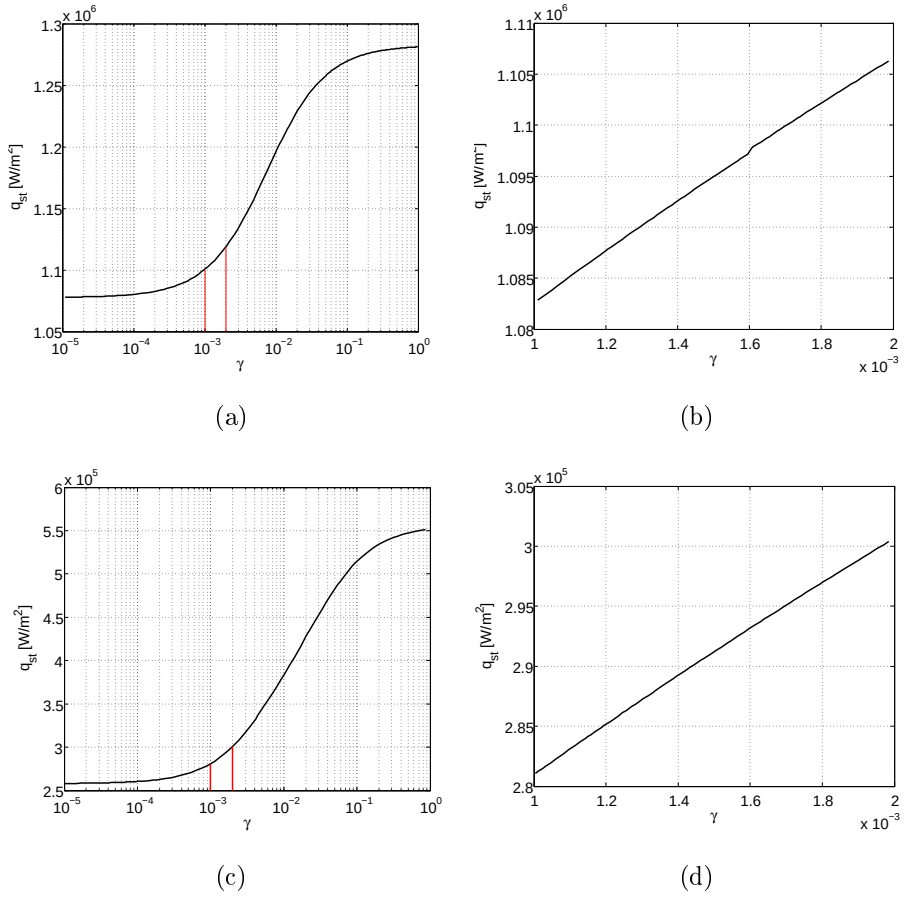

Figure 6.1: Stagnation heat flux as a function of γ values form 10^{-5} to 1 (left) and zoom on the interval of the prior (right) for the 30km (top line) and 60km (bottom line) trajectory points.

The quantity to be reconstructed from heat flux measurements is the coefficient γ, expressing the wall recombination probability due to catalysis at

the wall, called for simplicity catalycity coefficient. This is because it is well known that the heat exchange between the flow and the vehicle can be strongly influenced by the species recombination at the wall caused by catalysis [Sanson *et al.*, 2016]. This is shown in Figure 6.1. In Figure 6.1a and 6.1c, the variation of the stagnation heat flux value is shown versus the variation of the γ coefficient for both the 30km and 60km trajectory points. It can be seen that the stagnation heat flux has an increases by 18% from the value with a non-catalytic wall ($\gamma \to 0$) to the fully catalytic wall ($\gamma = 1$) for the 30km point, and it doubles for the other altitude. However, considering only variations of γ in the plausible prior interval for EXPERT vehicle (a uniform uncertainty of $\pm 33\%$ around the nominal value of 0.0015, as explained in Section 1.6.2), the resulting variation of the heat flux is much smaller (Figure 6.1b and 6.1d). Therefore, since the measurement error on heating data is quite big, with a standard deviation of 10% of the measured value, we do not expect the measurements to inform strongly the inferred parameter. A further practical reason that led us to explore this possibility is the fact that the numerical simulation code COSMIC accounts for wall catalysis phenomena.

6.3 Modeling the aerodynamic angles effect on measured quantities

Aerodynamic angles reconstruction is one of the classical applications for FADS problems. One of the goals is to exploit the different pressure and heat flux measurements to infer the value of the angles of attack α and sideslip β (referred to as flow or aerodynamic angles). However, since simulations are performed with the axisymmetric code COSMIC, it is not possible to directly simulate the change in pressure and heat flux at each sensor location due to changes of aerodynamic angles. Instead, it could be rigorously done by the use of a 3D computational code. Nevertheless, doing some hypothesis on the geometry of the EXPERT forebody, it is possible to exploit the output of the axisymmetric 2D simulation to evaluate the pressure and the heat flux at some measurement locations as a function of the aerodynamic angles.

The supporting geometrical hypothesis consists of assuming the nose of the EXPERT vehicle as a half sphere. While this is not its actual geometry, it consists in a relatively good approximation, from a geometrical point of view, as can be noticed from figure 6.2d. Since for a sphere the air flow does not change when changing the aerodynamic angles, a single axisymmetric simulation performed at α and β equal to zero can just be rotated and used to describe the behavior at different angle values. By geometrically treating the EXPERT forebody as a hemisphere, we assume that the flow field is invariant with respect to some small changes in the aerodynamic angles, and the surface pressure and heat flux from the axisymmetric simulation can just be rotated to

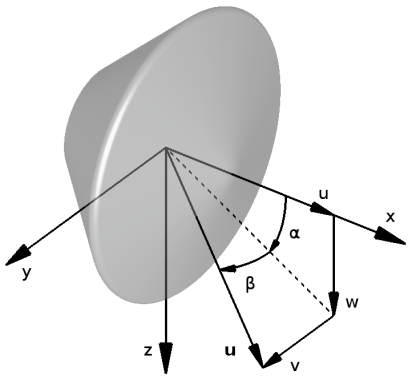

(a) Flow angles

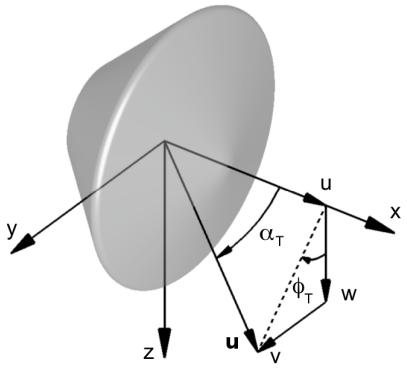

(b) Total aerodynamic angles

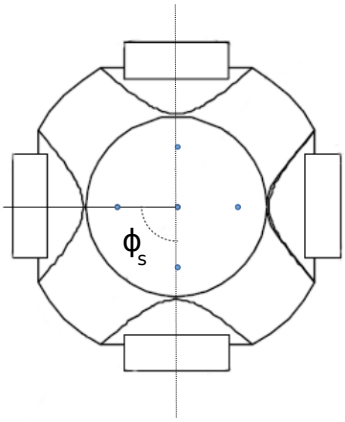

(c) Sensors clock angle

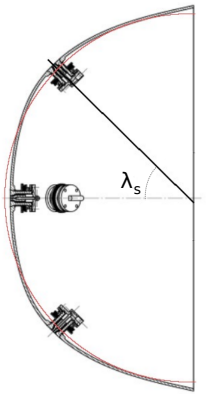

(d) Sensors cone angle

Figure 6.2: The first row gives a graphical representation of the flow angles (a) and total aerodynamic angles (b). In the second, there is a graphical definition of sensors clock (c) and cone (d) angles, together with a comparison between the actual EXPERT nose shape and the hypothesis of spherical nose (red line) (d).

describe the surface values with non-zero aerodynamic angles. This hypothesis allows to run only an axisymmetric simulations for the actual geometry of the nose, and then properly rotate the pressure and heat flux distributions according to the aerodynamic angles we want to account for.

When considering the forebody geometry as a sphere, it is practical to describe the position of a point on the surface, and particular sensors locations, by means of its cone λ_s and clock ϕ_s angles (see Figures 6.2c and 6.2d). With this convention, the locations of the $n_s = 5$ sensors on the EXPERT configuration are given by the values in Table 6.2. Then, the surface angle θ, namely

	Sensors				
	1 (stag.)	2 (top)	3 (left)	4 (bottom)	5 (right)
λ_s [deg]	0	45	45	45	45
ϕ_s [deg]	0	180	90	0	270

Table 6.2: Locations of the FADS sensors for the EXPERT vehicle expressed by means of the angles λ_s and ϕ_s.

the total angle from the sensor location to the velocity direction, can be computed from the flow angles and the sensor angles by means of the following trigonometric relation:

$$\begin{aligned}\cos(\theta) = &\cos(\alpha)\cos(\beta)\cos(\lambda_s)+\\ &+\sin(\beta)\sin(\phi_s)\sin(\lambda_s)+\\ &+\sin(\alpha)\cos(\beta)\cos(\phi_s)\sin(\lambda_s).\end{aligned} \tag{6.1}$$

This surface angle is used to rotate the axisymmetric solution at the wall to get the pressure and heat flux values at each sensor location. In practice, the axisymmetric solution, that is given at the Cartesian coordinates of the surface points, is rewritten with respect to the cone angle of this point, that coincides with the angle θ (see Figure 6.4). In fact, if $\theta = 0$ it means that the velocity and the sensor location vector are aligned, and therefore the sensor reads the stagnation values. When instead the sensor and the velocity are not aligned, the measurement will read a value of pressure or heat flux at an angle θ from the stagnation.

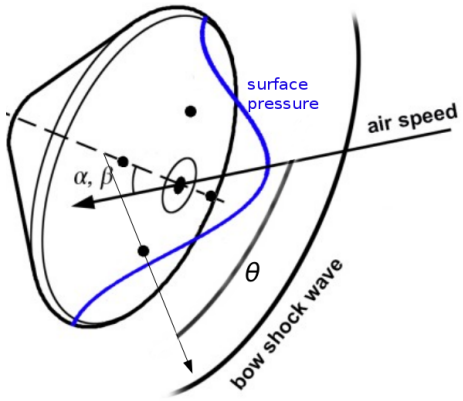

Figure 6.3: Graphical representation of the angle theta between the sensor location direction and the wind speed.

Proof for relation 6.1: In analogy with the definition of the sensors location, it is useful to describe the direction of the velocity vector by means of a total aerodynamic angle α_t and total aerodynamic clock angle ϕ_t (see figure 6.2b). From the definitions of the three components of the velocity vectors written in the two different sets of angles, it is possible to derive the following relations:

$$\cos(\alpha_t) = \cos(\alpha)\cos(\beta) \tag{6.2}$$

$$\tan(\phi_t) = \frac{\sin(\beta)}{\cos(\beta)\sin(\alpha)}\ , \tag{6.3}$$

and the inverse relations:

$$\sin(\beta) = \sin(\alpha_t)\sin(\phi_t) \tag{6.4}$$

$$\tan(\alpha) = \frac{\sin(\alpha_t)\cos(\phi_t)}{\cos(\alpha_t)}. \tag{6.5}$$

The surface angle θ between the vector defining the velocity direction and the one defining the position of the sensor on the sphere can be computed remembering the definition of scalar product between two vectors:

$$\boldsymbol{u} \cdot \boldsymbol{r}_s = |u||r_s|\cos(\theta). \tag{6.6}$$

The components of the two vectors $\boldsymbol{u}$ and $\boldsymbol{r}_s$ are defined as follows:

$$\boldsymbol{u} = \begin{Bmatrix} \cos(\alpha_t) \\ \sin(\alpha_t)\sin(\phi_t) \\ \sin(\alpha_t)\cos(\phi_t) \end{Bmatrix} \qquad \boldsymbol{r}_s = \begin{Bmatrix} \cos(\lambda_s) \\ \sin(\lambda_s)\sin(\phi_s) \\ \sin(\lambda_s)\cos(\phi_s) \end{Bmatrix}\ , \tag{6.7}$$

considering unit vectors, since we are interested only in θ and not the actual scalar product. Computing the scalar product between these two vectors, after some simple manipulation, it is possible to obtain the following expression

$$\cos(\theta) = \cos(\alpha_t)\cos(\lambda_s) + \sin(\alpha_t)\sin(\lambda_s)\cos(\phi_s - \phi_t). \tag{6.8}$$

Substituting in this expression the relations between total aerodynamic angles (α_t, ϕ_t) and aerodynamic angles (α, β), it is possible to obtain equation (6.1).

6.4 Methodology for Bayesian reconstruction

The statistical Bayesian approach introduced in Chapter 2 is adopted to solve the inverse problem that leads to the results of the reconstruction. All of the following reconstruction problems are solved in the framework of Bayesian inference (Section 2.5):

$$\sigma^{\text{pos}}(\mathbf{x}|\boldsymbol{d}) = \frac{\ell(\boldsymbol{d}|\mathbf{x})\,\sigma(\mathbf{x})}{\int \ell(\boldsymbol{d}|\mathbf{x})\,\sigma(\mathbf{x})\,\mathrm{d}\mathbf{x}}. \tag{6.9}$$

Bayes rule, here recalled, is able to provide the posterior joint PDF $\sigma^{\text{pos}}(\mathbf{x}|\boldsymbol{d})$ of the inferred parameters ($\mathbf{x} = \{\rho_\infty, \gamma, \alpha, \beta\}$ in the most general case here considered) given the measurements of pressure and heat flux at the sensors locations $\boldsymbol{d} = \{p_i; q_i\}_{i=1}^{n_s}$. Prior distributions described in Section 1.6.2 are used to describe the *a priori* knowledge $\sigma(\mathbf{x})$ about the parameters that we want to reconstruct. The likelihood function $\ell(\boldsymbol{d}|\mathbf{x})$ is modeled as in Section 2.5, and measurement errors are chosen to be respectively 2% for pressure and 10% for heat flux, as motivated in Section 1.6.2. The posterior distributions of the inferred parameters are sampled by means of Markov Chain Monte Carlo (MCMC) algorithms (see Sec. 2.5.1).

PDD-UK technique introduced in chapter 3 is used to train surrogate models for the quantities of interest, which coincide to pressure and heat flux at sensors locations. These surrogates are needed to accelerate the MCMC algorithms. Some technical aspects related to the training process are discussed in the following subsection 6.4.1, exploiting the relationship between flow angles and total surface angle modeled in Section 6.3. Once the metamodels for the quantities of interest are available, it is possible to tackle different inverse problems relative to the freestream reconstruction for the entry trajectory of the EXPERT vehicle. Different cases will be analyzed. In all the cases shown in the results, freestream velocity and temperature are assumed to be known exactly and therefore fixed to their nominal value, given in Table 1.5. For the velocity, this can be justified by the fact that it can be rebuilt usually from IMU measurement with a high accuracy, as explained in Section 6.2. Related measurement errors are in the order of few meters per second and they do not influence the results of the reconstruction.

Artificial measurements are produced by evaluating the surrogate models described in Section 6.4.1 at the values of ρ_∞, γ and corresponding to their nominal values. Regarding θ, the value is computed at each location of the sensors at the reference flow angles. No additional perturbation is added to the obtained value, because the main purpose of this chapter is to assess the interest of the reconstructions using heat flux measurement and not to reproduce a realistic case. Measurement errors are still accounted in the posterior distributions thanks to the formulation of the problem in the Bayesian framework.

For each case, a preliminary chain is run to adapt the values of the proposal distribution widths ω_i of the MCMC algorithm in Algorithm 2. They are chosen so that the resulting acceptance rate of the chain, namely the ratio between accepted and total steps, is close to an empirical optimal value, that is equal to 0.234 [Brooks *et al.*, 2011, Chapter 4]. After the adaptation process, MCMC chains are run for 250000 iterations. Then, for each final chain, the first 50000 iterations are discarded as burn-in time. The already small autocorrelation between samples of the obtained chain is already reduced by keeping in the final sampling point only one every 100 samples. These choices may seem too

conservative for the problems under analysis, but were adopted in order to have robust solutions. Of course, some more efficient setups are available, for example multiple short chains run in parallel [Brooks *et al.*, 2011, Chapter 7], and they could be exploited in these applications, after some testing and comparison with results given by longer chains.

6.4.1 Surrogate models

Surrogate models for the quantities of interest need to be constructed and used to accelerate the different MCMC algorithms involved in the different inverse problems described in the following sections. The coupled PDD-Kriging technique, introduced in Chapter 3, is used at this purpose.

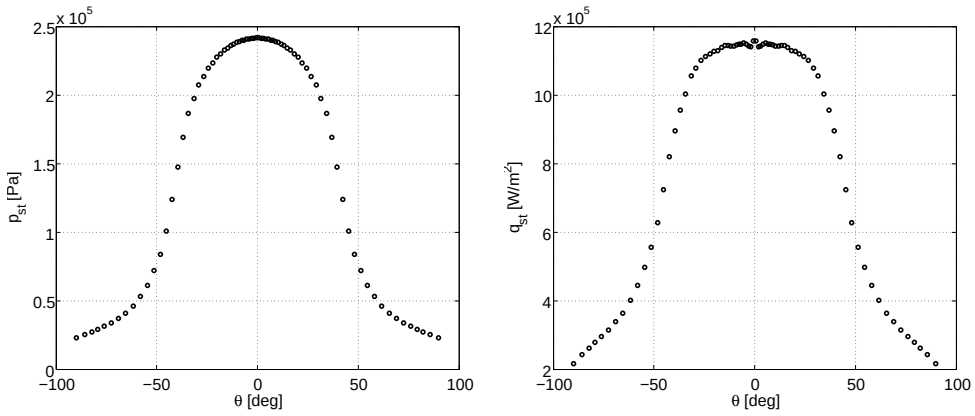

(a) Pressure (b) Heat flux

Figure 6.4: Output of the COSMIC simulations performed at nominal conditions for the 30km trajectory point. Axisymmetric simulations give results between 0° and 90°, and results for negative angles are obtained by symmetry.

Firstly, Latin Hypercube training points are drawn in the space of the uniform prior distributions of ρ_∞ and γ. Sets containing $N_s = 72$ training points are created for each individual uncertain variable and for the bi-dimensional case that arises when considering both of them. Simulations of the COSMIC code are run for every training point, exploiting the automated mesh adaptation approach described in Section 1.5. The output of each simulation is the value of pressure and heat flux at the wall, given at each cell center of the computational grid, a shown in Figure 6.4 for the output obtained using nominal input values at the 30km trajectory point.

When creating the surrogate model, a decision has to be made on whether building it with respect to the flow angles (α, β) or the surface angle θ. We decide to create the surrogate in the angle θ, because in this way it is possible

to reduce the input dimensionality and secondly for the simpler physical and graphical interpretation that this choice allows.

However, a practical issue arises if choosing θ as training variable. Let us take as example the case where a surrogate model is built in the variables (ρ_∞, θ). If one considered as training points all the points where the solution at

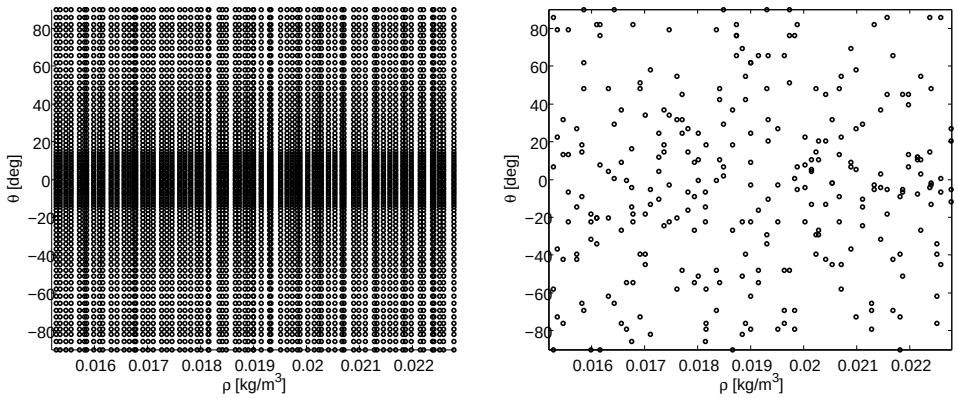

(a) Full (b) Reduced

Figure 6.5: Example of full (a) and reduced (b) set of training points for the EXPERT application case.

the surface is available, there would be $N_p \times 2N_s = 5472$ training points in two dimensions (see Figure 6.5a), since the number of cells of the computational domain along the surface is $N_p = 38$ for the considered grid. This number of training points is too big, and would lead to an excessive computational costs related to the training and the evaluation of the metamodel. Therefore, we made the decision to keep only four points in the direction θ for each of the 72 sample values of density, randomly chosen between the 32 available. This leads to a total number of 288 training points (Figure 6.5b), which is a good compromise between the level of information given to the surrogate and the training cost. Notice that the resulting training plan is not a Latin Hypercubes plan, and it will not be optimal in the sense of the point spacing, but this fact is not critical for the application, since the function we want to represent are sufficiently regular and simple. The same procedure is applied to build surrogates in (γ, θ) and $(\rho_\infty, \gamma, \theta)$. Notice, therefore, that surrogates are trained over either two or three dimensional inputs.

Finally, from this training set, it is possible to build a PDD-UK surrogate model for every quantity of interest. Figure 6.6 contains the plot of different surrogates, showing the variation of the quantities of interest with respect to (ρ_∞, θ) and (γ, θ) respectively. Notice that the quantities that contributes the most to the variation of the outputs are clearly the density and the surface

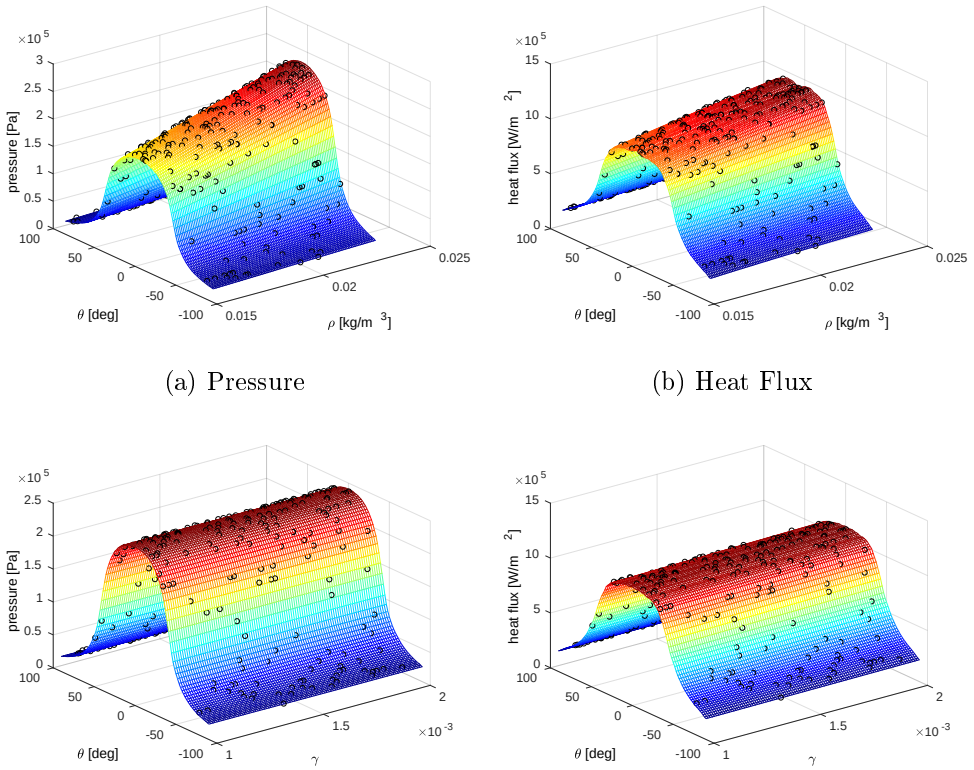

(a) Pressure

(b) Heat Flux

(c) Pressure

(d) Heat Flux

Figure 6.6: Plots of training points and surrogate models for the surface pressure and the heat flux as function of (ρ_∞, θ) (top row) and (γ, θ) (bottom row).

angle, while the catalytic coefficient does not show a strong contribution. This will suggest that it will probably be more difficult to have a good reconstruction of the value of γ. Notice also that in the following we will use different different metamodels for every set of input variables, but it could be possible to train a single global surrogate considering all three variables (ρ_∞,γ and θ), and to fix the ones that are temporarily not considered for the reconstruction to their nominal value.

One last remark needs to be made about the symmetry of the solution. In fact, since the response of the system is symmetrical with respect to the angle θ, it could be possible to train a surrogate model just in the domain $[0, 90]$ deg. However, we preferred to consider the whole domain $[-90, 90]$ deg, because this helped to have a more accurate surrogate at the symmetry point in $\theta = 0$ deg without having to introduce new constraints in the training phase.

6.5 Results of freestream parameters reconstructions

In this section, results are presented from the different reconstruction problems reported in Table 6.1. Each case represents a possible configuration of available measurements and quantities that are inferred exploiting the available information.

6.5.1 Reconstructions from pressure measurements

At first, the Bayesian approach is adopted to calibrate some freestream quantities, namely the atmospheric density and the flow angles, starting only from pressure measurements at the wall of the vehicle. This problem is equivalent to the typical reconstruction performed by means of FADS sensors. The difference is that the Bayesian approach naturally allows to account for priors uncertainties, error measurements and complex direct models (CFD) able to accurately describe the physics of entry flows.

Rebuilding freestream density

A first very simple test for the MCMC sampler of the posterior distribution is performed on the problem of rebuilding the freestream density solely from pressure measurements at the stagnation point, neglecting the other off-stagnation measurements and supposing γ and flow angles to be exactly known. This simple single-input-single-output problem is used mainly as a sanity check to verify correct functioning of the numerical setup. The MCMC algorithm is accelerated by the use of a surrogate model for the pressure as a function of the freestream density. The reference value of density is taken as $\rho_r = 1.9002 \cdot 10^{-2}$ kg/m^3 for the 30km trajectory point and $\rho_r = 2.8806 \cdot 10^{-4}$ kg/m^3 for the 60km one, corresponding to nominal values, where an exact evaluation of the model is available. Artificial measurements are produced by evaluating the surrogate model at ρ_r and values of θ corresponding to the location of the sensors at the imposed flow angles. Figure 6.7 shows the obtained posterior PDFs for the density at both trajectory points. As expected, the freestream density is well informed by stagnation pressure values, allowing a good calibration of its value at both analyzed configurations, since the posteriors are much narrower than the uniform prior, which is represented by the plot intervals on the abscissa. Mean values, standard deviations and coefficient of variation σ/μ of the posterior PDF are reported in table 6.3, together with the relative errors between the posterior mean and the reference measured density. Both present a variation of about 2% and a support that is noticeably smaller than the one of the prior. The fact that the posterior coefficient of variation is about 2% is expected from the fact that the model is nearly linear in an interval around

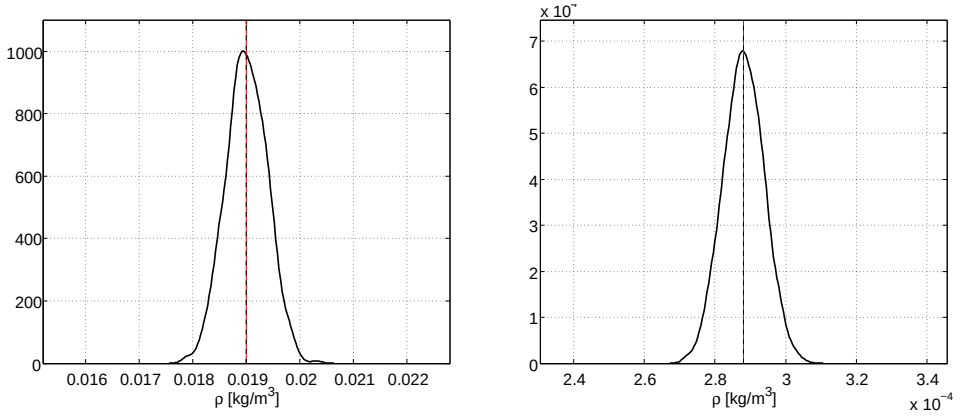

(a) 30km (b) 60km

Figure 6.7: PDFs of the density rebuilt from stagnation pressure measurements (solid black line). The dashed line represents the posterior mean value and the red line the reference value. The x axis width shows the uniform prior interval.

		30 km	60 km
ρ_∞ [kg/m^3]	μ	1.900741e-02	2.881030e-04
	σ	3.820336e-04	5.683209e-06
	σ/μ	2.010 %	1.973 %
	$\epsilon_\%$	0.028113 %	0.013997 %

Table 6.3: Posterior mean value, standard deviation and coefficient of variation of the freestream density inferred from stagnation pressure data for both trajectory points. The error $\epsilon_\%$ represents the relative error between the reference and the mean posterior values.

the reference value, and the measurement error on the stagnation pressure is considered to be of the order of the 2%.

The density reconstruction is then repeated using all of the five pressure measurements at the different sensors locations, expecting an improvement on the quality of the rebuilt solutions. The resulting posterior PDFs are shown in 6.8. It can be noticed that, as expected, using all of the available sensors output improves the quality of the reconstruction in the sense that the coefficient of variation of the posterior is smaller than the one obtained with just a single stagnation data (see Table 6.4). This allows for a less uncertain posterior density value. The obtained relative errors $\epsilon_\%$ from the reference density is very small, with a comparable order of magnitude as the one obtained from a single stagnation data.

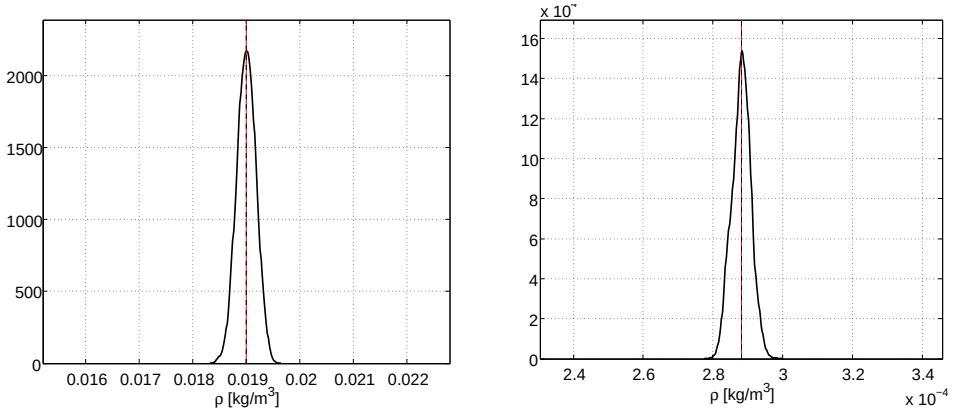

(a) 30km (b) 60km

Figure 6.8: PDFs of the density rebuilt from wall pressure measurements (solid black line). The dashed line represents the posterior mean value and the red line the reference value. The x axis width shows the uniform prior interval.

		30 km	60 km
ρ_∞ [kg/m^3]	μ	1.900424e-02	2.880628e-04
	σ	1.738477e-04	2.627332e-06
	σ/μ	0.91 %	0.912 %
	$\epsilon_\%$	0.011402 %	0.000055 %

Table 6.4: Posterior mean value, standard deviation and coefficient of variation of the inferred freestream density inferred from all pressure measurements for both trajectory points. The error $\epsilon_\%$ represents the relative error between the reference and the mean posterior values.

Rebuilding flow angles

The second calibration tested consists in the reconstruction of flow angles α and β from the five pressure measurements available, fixing all the other freestream quantities to their reference values. Reference values for the flow angles are arbitrarily supposed to be $\alpha_r = 5$ degrees and $\beta_r = -1$ degrees. Artificial measurements are created by evaluating the surrogate at θ values obtained at every sensor location for the reference values of flow angles. The surrogate-accelerated MCMC algorithm is run as in the previous case. Figure 6.9 shows the posterior probability distribution of the flow angles. Even in this case, as known in literature, the inferred quantities are well informed by the pressure data. Therefore, the support of their posteriors is noticeably smaller than their prior. Statistics of the posterior distribution are shown in table

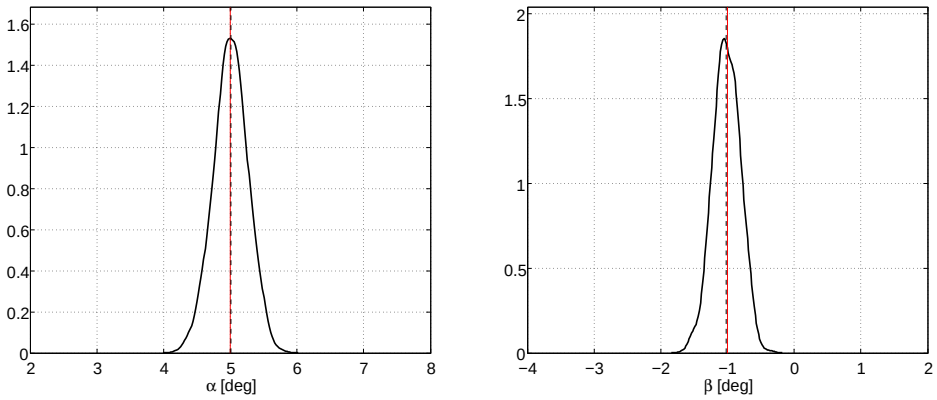

(a) Angle of attack (b) Sideslip angle

Figure 6.9: Posterior PDFs of the flow angles rebuilt from pressure measurements for the 30km trajectory point.

6.5, together with the error (in degrees) between the reference and the mean posterior values. Also in this case the calibration is able to lead to good results, with standard deviations of 0.2 degrees and small errors with respect to the reference value.

		30 km	60 km
α [deg]	μ	5.006348	4.998393
	σ	0.254892	0.2726189
	1σ interval	[4.751455, 5.261241]	[4.725774, 5.271011]
	ϵ_{deg}	0.006348	0.001607
β [deg]	μ	-1.015074	-0.982090
	σ	0.204631	0.203602
	1σ interval	[-1.219705, -0.810443]	[-1.185692 , -0.778488]
	ϵ_{deg}	0.015074	0.017910

Table 6.5: Posterior mean value, standard deviation and confidence intervals of the inferred flow angles computed with the MCMC samples for both trajectory points. The absolute error ϵ_{deg} represents the difference between the reference and the mean posterior values.

Rebuilding freestream density and flow angles

Finally, the global FADS problem of rebuilding freestream density and flow angles from wall pressure measurements is here performed. As in the previous

cases, the reference values for the inferred parameters are taken as $\rho_r = 1.9309 \cdot 10^{-2}$ kg/m^3, $\alpha_r = 5$ degrees and $\beta_r = -1$ degrees for the 30km trajectory point, and changing to $\rho_r = 2.8806 \cdot 10^{-4}$ kg/m^3 for the 60km point, and artificial measurements are created by evaluating the surrogate at those values for each sensor location. We will use this problem to verify if a loss of performance

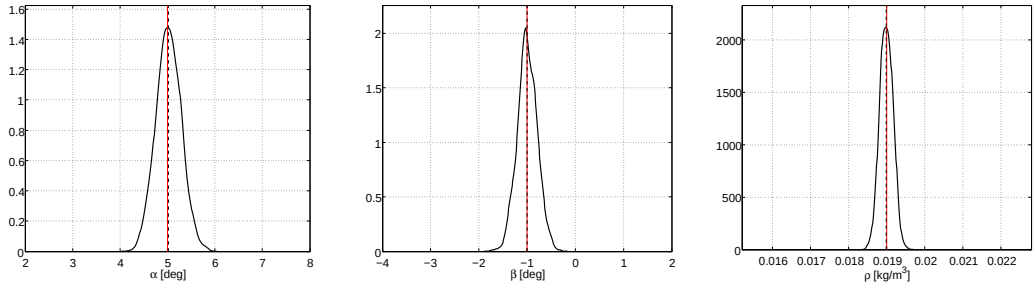

(a) Angle of attack (b) Angle of sideslip (c) Freestream density

Figure 6.10: PDFs of the freestream density and flow angles rebuilt from wall pressure measurements (solid black line) for the 30km trajectory points. The dashed line represents the posterior mean value and the red line the reference value. The x axis width shows the uniform prior interval.

occurs with respect to the two simpler cases previously shown. The posterior probability densities of the inferred parameters are plotted in Figure 6.10 for the trajectory point at 30km, and their statistics are displayed in Table 6.6. The comparison between these results with the ones respectively in Tables 6.4 and 6.5 does not show a significant increase in the variability or loss of accuracy of the inferred parameters. In fact the coefficient of variation of the freestream density is very close to the one obtained by the single-variable reconstruction (0.90% with respect to 0.87%). Comparing with the previous case, also the standard deviations values associated to the flow angles result very close. The differences in the errors respect to the reference values are more difficult to interpret, because the ones of the density and angle of attack are higher, while the one of the angle of sideslip is lower. It is possible that these errors are so small that these differences are mainly associated with the intrinsic variability of results related to the use of a MCMC algorithm than to physical aspects.

6.5.2 Reconstructions from heat flux measurements

In this subsection, we explore some calibration possibilities given by the availability of heat flux measurements at the wall of the entering vehicle.

		30 km	60 km
ρ_∞ [kg/m^3]	μ	1.899502e-02	2.880108e-04
	σ	1.710478e-04	2.638375e-06
	σ/μ	0.903937 %	0.916068 %
	$\epsilon_\%$	0.037084 %	0.018024 %
α [deg]	μ	4.999603	5.004188
	σ	0.2611465	0.2592601
	1σ interval	[4.738456, 5.260749]	[4.744927, 5.263448]
	ϵ_{deg}	0.000397	0.004188
β [deg]	μ	-0.995729	-0.982169
	σ	0.209720	0.197225
	1σ interval	[-1.199647, -0.791811]	[-1.179394, -0.784944]
	ϵ_{deg}	0.004271	0.017831

Table 6.6: Posterior mean value, standard deviation and coefficient of variation of the inferred freestream density and flow angles computed with the MCMC samples for both trajectory points. The error $\epsilon_\%$ represents the relative error between the reference and the mean posterior values.

Rebuilding the catalytic coefficient

For this Bayesian reconstruction, artificial measurements are produced by evaluating the surrogate models of heat flux at the sensors locations for the reference value of catalytic coefficient, chosen to be equal to the nominal value of $\gamma_r = 0.0015$ for both trajectory points. The posterior PDF resulting from the inference is shown in Figure 6.11. It is clear that the information added by the measurements is not sufficient to reduce the support of the probability density of γ, but it just slightly reduces its variance. However, better reconstruction results could be obtained if measurements with lower noise would be available, or the reconstruction could prove more useful in case of a wider prior distribution.

Rebuilding catalycity coefficient and flow angles

Now we want to asses the possibility of using heat flux measurements to rebuild flow angles, accounting also for the uncertainty on the catalycity coefficient. Even though the inverse problems is formulated as the reconstruction of the three quantities, it is already possible to know from the previous example that γ will not be properly inferred, because of the large measurement error, and will mainly act just as a small source of uncertainty for the characterization of the value of α and β. The same reference values as the previous examples for γ and the flow angles are used. As expected, results in Figure 6.12 show that the heat flux measurements are not able to improve the information on the value

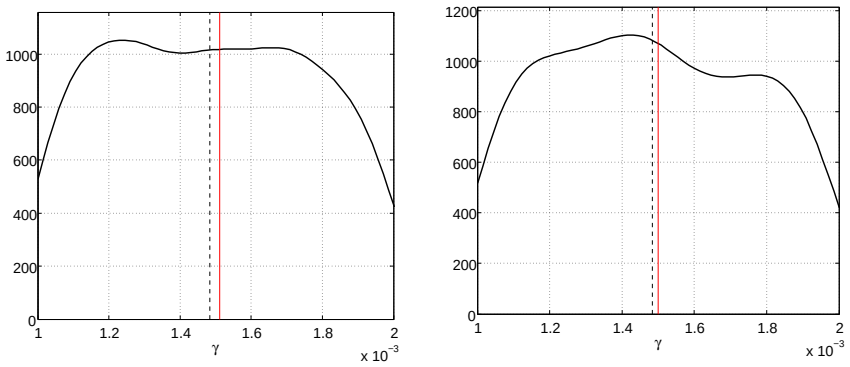

(a) 30km (b) 60km

Figure 6.11: PDFs of the coefficient γ rebuilt from wall heat flux measurements (solid black line). The dashed line represents the posterior mean value and the red line the reference value. The x axis width shows the uniform prior interval.

of catalycity coefficient with respect to its prior, but they can provide some information about the flow angles, even if with much bigger uncertainties than the reconstruction performed with pressure measurements (compared to Figure 6.9). Therefore, heat flux measurements alone, up to current measurement error values, are not able to adequately infer flow angle values.

6.5.3 Reconstructions from both pressure and heat flux measurements

In this final section, both pressure and heat flux measurements are exploited simultaneously. Some reconstructions previously performed with just pressure measurements, are repeated to see if the additional information added by heat flux measurement can improve the quality of the reconstruction. Finally, a complete case of reconstruction of density, flow angles and catalycity will be presented.

Rebuilding freestream density

First, the reconstruction of the density is repeated taking into account also heat flux measurements at the five sensors locations. The statistics obtained for the posteriors are shown in Table 6.7 for both trajectory points.

From these results, it is possible to observe a very slight reduction in the uncertainty associated with the rebuilt variable, with posterior coefficient of variations passing from 0.91% of the case with just pressure measurements (Tab 6.4) to 0.88% when considering also the heat flux for the 30km conditions, and from 0.91% to about 0.89% for the 60km case. It is a quite small

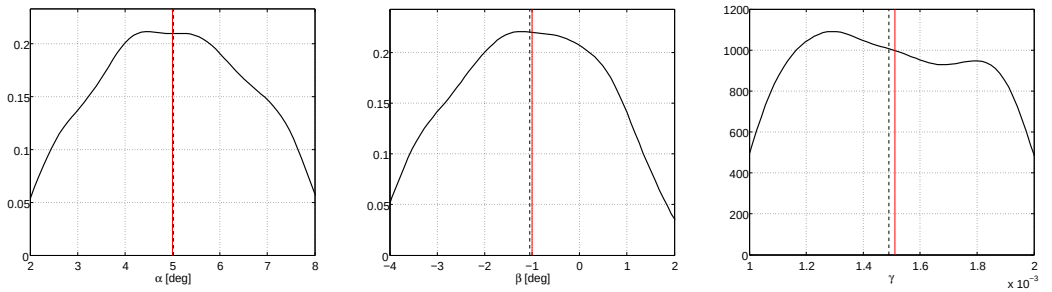

(a) Angle of attack (b) Angle of sideslip (c) Catalycity

Figure 6.12: PDFs of the γ coefficient and flow angles rebuilt from wall pressure measurements (solid black line) for the 30km trajectory points. The dashed line represents the posterior mean value and the red line the reference value. The x axis width shows the uniform prior interval.

improvement, but could be potentially more substantial if better measurements and prediction capabilities were available for the heat flux.

		30 km	60 km
ρ_∞ [kg/m^3]	μ	1.900850e-02	2.880591e-04
	σ	1.675554e-04	2.586513e-06
	σ/μ	0.881476 %	0.897910 %
	$\epsilon_\%$	0.033853 %	0.001255 %

Table 6.7: Posterior mean value, standard deviation and coefficient of variation of the freestream density inferred from pressure and heat flux measurements for both trajectory points. The error $\epsilon_\%$ represents the relative error between the reference and the mean posterior values.

Rebuilding flow angles

The reconstruction of flow angles is repeated considering both pressure and heat flux measurements. Since we already saw that heat flux alone was not able to adequately infer flow angles, we do not expect that it will add significant information with respect to the results already obtained with pressure measurements.

Results of means, standard deviations and 1σ intervals associated to the posteriors of α and β for both trajectory points are reported in Table 6.8. As expected, results are substantially equal to the ones obtained in Section 6.5.1, reported in Table 6.5. Posterior standard deviations are always of about the

		30 km	60 km
α [deg]	μ	5.001861	4.997776
	σ	0.263014	0.2660837
	1σ interval	[4.738846 , 5.264875]	[4.731692 , 5.263859]
	ϵ_{deg}	0.001861	0.002224
β [deg]	μ	-0.994782	-0.986635
	σ	0.206962	0.197795
	1σ interval	[-1.201744 , -0.787820]	[-1.184430 , -0.788839]
	ϵ_{deg}	0.005218	0.013365

Table 6.8: Posterior mean value, standard deviation and confidence intervals of the inferred flow angles computed with the MCMC samples for both trajectory points. The absolute error ϵ_{deg} represents the difference between the reference and the mean posterior values.

same amplitude, 0.26 deg for α and 0.2 deg for β, with no reduction of the uncertainties brought by the heat flux.

Complete reconstruction of density, flow angles and catalycity

This final section is about the global reconstruction of freestream density, flow angles and catalycity exploiting both pressure and heat flux measurements. The reconstruction is repeated for both the 30km and 60km trajectory points. The obtained posterior PDFs are shown in Figure 6.13 for the 30km case, and analogous plots, not reported here, are obtained for the other condition. Posterior statistics are shown in Table 6.9 for both trajectory points.

Comparing these results with the ones in Table 6.6, where just pressure had been used to reconstruct density and flow angles, it is possible to notice a small reduction in the coefficient of variation of the density, while the posterior variance associated with flow angles remains substantially the same. This confirms what was observed in the two former tests, where density and flow angles were independently reconstructed from pressure and heating data. Therefore, in the considered configuration, accounting for heat flux measurements does not seem to provide valuable improvements on reconstructions that can be done with only FADS pressure measurements.

A further test is here performed, repeating the global problem of reconstructing density, flow angles and catalycity coefficient in order to show how results would improve if measurement error of the heat flux were only at 2% of the measured quantity, that is the same level of accuracy than for pressure measurements. The obtained posterior distributions are shown in Figure 6.14 and statistics are reported in Table 6.10. From the figure, it is clear that there is an improvement in the estimate of the catalycity: even though the support

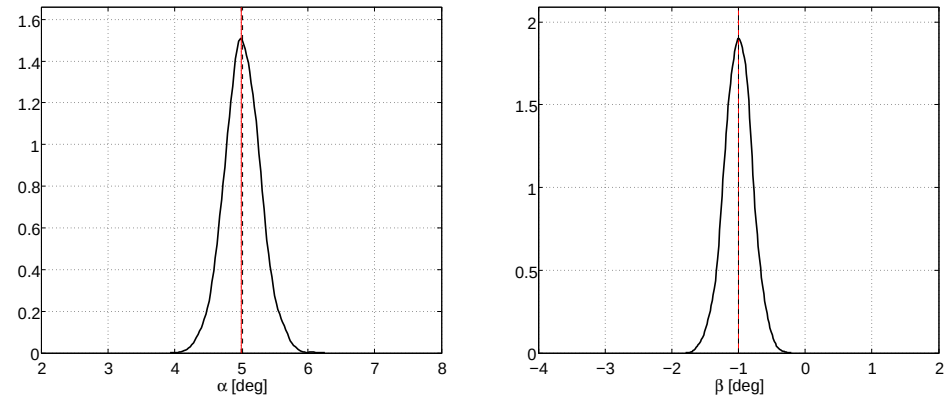

(a) Angle of attack

(b) Angle of sideslip

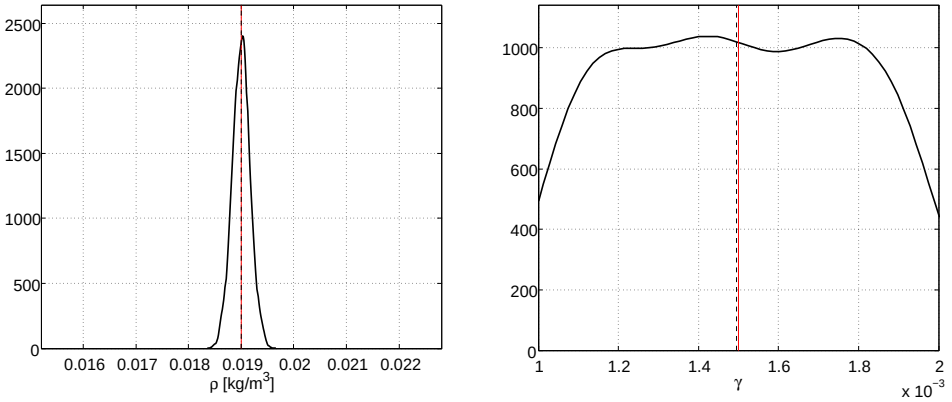

(c) Freestream density

(d) Freestream density

Figure 6.13: PDFs of the freestream density and flow angles rebuilt from wall pressure measurements (solid black line) for the 30km trajectory points. The dashed line represents the posterior mean value and the red line the reference value. The x axis width shows the uniform prior interval.

of the posterior is still as large as the prior, its variance is reduced. Looking at the quantitative results in Table 6.10, it is evident that the coefficient of variation of γ passed from about 19% (in Table 6.9) to respectively 14.8% and 12.5% when reducing the measurement error. It is more complicated to compare the other results, since for the 30km trajectory point it is possible to see an improvement especially on the reconstruction of the density, while for the 60km trajectory point the more noticeable improvement is on the reconstruction of flow angles.

		30km	60km
ρ_∞ [kg/m^3]	μ	1.900030e-02	2.886678e-04
	σ	1.676463e-04	2.597421e-06
	σ/μ	0.882 %	0.899796 %
	$\epsilon_\%$	0.009335 %	0.210063 %
γ	μ	1.495664e-03	1.484817e-03
	σ	0.000285	0.000283
	σ/μ	19.035 %	19.076693 %
	$\epsilon_\%$	0.289057 %	1.080869 %
α [deg]	μ	5.017937	4.945957
	σ	0.2672945	0.2673363
	1σ interval	[4.750642 , 5.285231]	[4.678620 , 5.213293]
	ϵ_{deg}	0.017937	0.054043
β [deg]	μ	-1.003269	-0.976203
	σ	0.203691	0.190685
	1σ interval	[-1.206960 , -0.799579]	[-1.166888 , -0.785518]
	ϵ_{deg}	0.003269	0.023797

Table 6.9: Posterior mean value, standard deviation and coefficient of variation of the inferred freestream density and flow angles computed with the MCMC samples for 30km and 60km trajectory point. The error $\epsilon_\%$ represents the relative error between the reference and the mean posterior values.

6.6 Conclusions

This chapter illustrated a study about the assessment of the interest in using forebody heat flux measurements on entry vehicles to reconstruct freestream values, namely the atmospheric density and the flow angles, and the uncertain wall catalycity coefficient, instead of just using surface pressure measurement, as usually done in the literature. All the reconstruction problems were done in a Bayesian framework, coupled with the PDD-UK surrogate modeling technique to emulate the response of expensive CFD simulations of the flow. The tests performed showed that, up to the current measurement errors for heat flux, this type of data is not able to bring much information to rebuilt freestream values, that are better characterized by pressure measurements. Heat flux data do not bring substantial information on the catalycity either, with respect to the fairly precise expert-based prior information considered for this variable. According to the results of a recent work [Sanson *et al.*, 2016], the expert-based prior distribution used for γ could be too optimistic, meaning that in practice wider prior PDFs could be expected for this parameter. In this case, it could be useful to show whether in-flight heat flux measurements could improve the characterization of γ. One last empirical test showed that the contribution

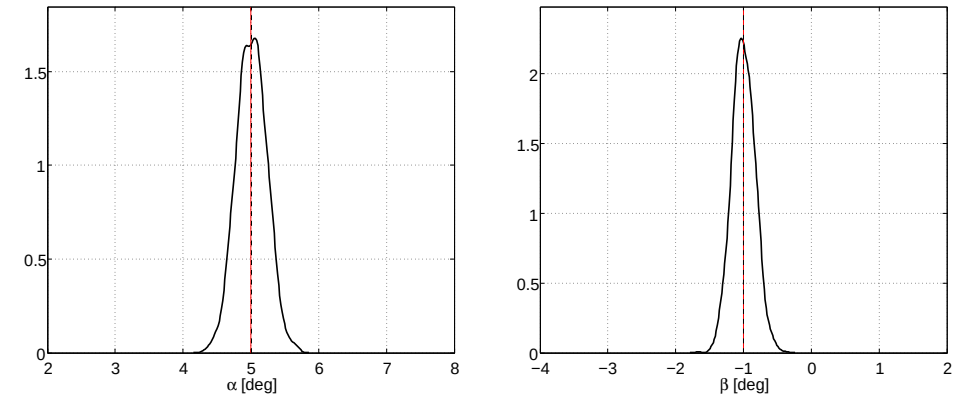

(a) Angle of attack

(b) Angle of sideslip

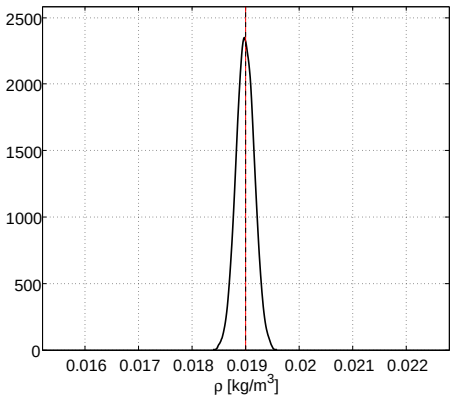

(c) Freestream density

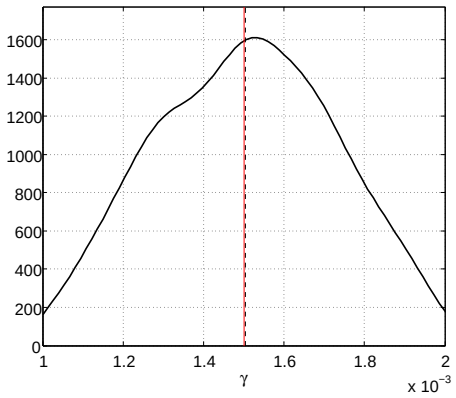

(d) Freestream density

Figure 6.14: PDFs of the freestream density and flight angles rebuilt from wall pressure measurements (solid black line) for the 30km trajectory points obtained with reduced measurement error for the heat flux.

of heat flux measurement could be more useful if measurement errors were substantially reduced. In a real-life scenario, benefits from including heat flux measurements will probably be obtained if, together with measurement accuracy, also prediction capabilities of numerical simulations were improved. In fact, when dealing with more complex flow, as the ones involved in Mars atmospheric entry, where ablation and radiation affect the surface heating, all these contributions to the global wall heat flux should also be accurately modeled, in order for the reconstruction to be meaningful.

		30km	60km
ρ_∞ [kg/m^3]	μ	1.899699e-02	2.887507e-04
	σ	1.626812e-04	2.592369e-06
	σ/μ	0.856 %	0.897788 %
	$\epsilon_\%$	0.026751 %	0.238849 %
γ	μ	1.504720e-03	1.485240e-03
	σ	0.000223	0.000186
	σ/μ	14.844634 %	12.555283 %
	$\epsilon_\%$	0.314693 %	1.333834 %
α [deg]	μ	5.017937	4.956571
	σ	0.2672945	0.2254609
	1σ interval	[4.750642 , 5.285231]	[4.731110 , 5.182032]
	ϵ_{deg}	0.017937	0.043429
β [deg]	μ	-1.003269	-0.996722
	σ	0.203691	0.161652
	1σ interval	[-1.206960 , -0.799579]	[-1.158374 , -0.835070]
	ϵ_{deg}	0.003269	0.003278

Table 6.10: Posterior mean value, standard deviation and coefficient of variation of the inferred freestream density and flight angles computed with the MCMC samples for 30km and 60km trajectory point. The error $\epsilon_\%$ represents the relative error between the reference and the mean posterior values.

Conclusions

This work focused on statistical forward and inverse uncertainty propagation problems applied to atmospheric entry flows, with a particular interest in the assessment of the possibility to exploit heat flux measurements at the forebody of the vehicle to rebuild values of freestream conditions and uncertain parameters of the model. The work contributed to improvements to mathematical tools used to perform propagation of uncertainties. Furthermore, some interesting conclusions can be drawn from the point of view of engineering and scientific applications. In the following list, some considerations are illustrated with respect to all the main objectives listed in the introduction, in addition global conclusions will be presented in the following discussion.

1. From a physical/application point of view, the reconstruction of freestream density, aerodynamic angles and catalytic coefficient has been performed in a Bayesian framework for the EXPERT vehicle, exploiting heat flux measurements at the forebody of the entry vehicle, together with the classically-available surface pressure measurements. It is found that, at the current level of accuracy for heat flux measurements (high measurement error, of the order of 10% the measured value), this kind of data does not provide enough information and, therefore, it does not reduce uncertainties on the rebuilt quantities with respect to reconstructions performed with only pressure measurements. The reconstruction of freestream velocity and density has also been tested, using pressure and heat flux measurements, for the HEG cylinder experimental configuration. The use of this kind of measurements leads to results for the velocity that are much more uncertain, *i.e.* with a higher 1σ variation, than the classical reconstruction by inertial data (provided by the IMU) as usually done in the literature. The only scenario where heat flux measurements would become more useful is in the case of IMU malfunctioning: in the absence of inertial data, a relatively uncertain reconstruction by heat flux would be better than the complete impossibility of rebuilding this variable.

2. Bayesian statistical framework was adopted to formulate direct and inverse uncertainty propagation problems related to hypersonic entry flows.

The framework worked as expected, for both direct and inverse uncertainty propagation problems. It proved to be very versatile, allowing to consider several sources of uncertainties, measurement errors and complex CFD models. The use of numerical models which are expensive to compute brings the need of replacing them by surrogate models, since several evaluations of the quantities of interest are required to fully characterize output uncertainties. This framework was particularly useful to perform robust prediction of hypersonic entry flows, rigorously quantifying output uncertainties related to pressure and heating at the stagnation point. It also allowed the rigorous statistical solution of the freestream reconstruction problem, applied only at single points of the entry trajectory. For this reason, the formulation used in this work is not suited for freestream reconstruction along the whole trajectory. However, it was not in the purpose of this work to find an alternative method to replace Kalman filters or other statistical techniques from the literature for atmospheric reconstruction.

3. From the point of view of numerical CFD simulations, it is important to remark that, in this work, a major unexpected challenge was to obtain accurate and robust numerical simulations for the heat flux, especially near the stagnation, even for relatively simple geometries like the HEG cylinder and EXPERT nose. The tested automated mesh adaptation strategy was not working universally, but it needed adjustments and modifications when changing a test case, geometry (2D or axisymmetric), numerical scheme and uncertain input parameters. If single computations needs to be performed, some more *ad hoc* strategies may be used, but this is very penalizing in the UQ framework, where several input configurations must be simulated and one needs to be able to automatically run the simulations.

4. Since uncertainty problems required a high number of evaluations of the function of interest, it was mandatory to exploit a surrogate model to replace the evaluations of the expensive computational CFD code for the simulation of hypersonic flows. With the methods introduced in this work, it has been possible to build an efficient and accurate surrogate model. In particular, three main algorithmic aspects have been investigated:

   (a) An improved surrogate modeling technique, denoted PDD-UK, has been introduced. It consists in the use of polynomial basis functions selected by an adaptive sparse-Polynomial Dimensional Decomposition algorithm as regression functions for a Universal Kriging surrogate. This improved approach proved to work well on several tests performed, both analytical and issued from applications in

the atmospheric entry field, providing an improved metamodeling accuracy with respect to both Ordinary Kriging and sparse-PDD. These tests showed that the proposed adaptive surrogate is able to handle problems with a relatively high number of uncertain inputs, in the case where the major contribution on the variability of the output is given by a limited subset of inputs. The performed tests also showed that, in order to have best results in terms of accuracy, it is necessary to choose an adequate set of input parameters (*i.e.* the maximum polynomial order m, the interaction order ν, etc.). This may require a preliminary analysis with error estimates (*e.g.* cross-validation error) to determine the best set of input parameters. Notice that the PDD-UK, although only accounting for polynomial basis functions, showed good performances even for test functions that did not possess an underlying polynomial trends. Other techniques, as Blind Kriging [Joseph *et al.*, 2008], allow the use of other different kind of functions, according to the features of the function of interest. Of course the possibility to include, for example, periodic bases in the case of periodic behaviors is very useful, but at the same time this would increase the complexity of the technique.

(b) A novel technique has been developed to adaptively add new training points to an existing experimental design, in case one wants to improve the accuracy of a surrogate built on this first ED. The technique relies on the construction of a Delaunay grid of simplex elements where the training points coincide with the vertices of the elements, and is able to account for the information on the function of interest acquired during the training process of the first surrogate model on the initial experimental design. In particular, it accounts for functions gradients and local estimates of the surrogate modeling error. The technique was able to add a fixed number of training points, chosen by the user, so that the new experimental design performed better than a normal LHS design in terms of average RMSE surrogate modeling error. The suggested use of this technique is to add a fixed and relatively small number of training points, when compared to the size of the ED, when new points are needed to improve the quality of the surrogate model built on the initial ED. This technique is not meant to be used iteratively in order to increase substantially the size of the ED. In such situation, its performance tends to converge to the one of a simple LHS, which has, however, the advantage of being computationally cheaper. The main drawback of the proposed methodology is that the construction of a simplex Delaunay grid becomes very computationally demanding when increasing the dimensionality of the input space. When it is not possible to decrease the dimensionality of the input by dimen-

sionality reduction techniques, this becomes a major problem that can prevent from the utilization of the proposed methodology. It is important to notice the difficulties associated to the construction of an adaptation technique that is as general as possible and does not rely on any assumption on the structure of the function in unexplored regions of the domain. In fact, a technique which relies too much on the information available about the function may miss to find new critical region in which it is worth adapting, and on the other hand, a technique which favors excessively the exploration of the domain is often not optimal.

(c) Active subspaces proved to be very effective for dimensionality reduction for direct propagation of uncertainties and sensitivity analysis, allowing to capture of information about low-dimensional structures hidden in the function of interest and to produce accurate output PDFs despite the highly-reduced dimensionality. We described an alternative way to exploit the low-dimensional structure in the parameter-to-observable map revealed by the active subspaces to enable efficient Bayesian inversion with MCMC. Instead of relying only on active subspaces of the log-likelihood (or misfit) function to reduce the dimension of the Markov chain as in [Constantine *et al.*, 2016b], here the two one-dimensional active subspaces in the parameter-to-observable maps have been exploited. If the structure of the functions of interest allows for the existence of active subspaces, they can be effectively exploited for Bayesian inverse problems. The proposed approach has one drawback that arises in cases where a non-Gaussian prior is present in the physical space. In order to have a sample of the posterior density in physical variables, one has to draw samples from the conditioned probability of the inactive variables given the active variables, which is not analytical when the joint prior on the active variables is not Gaussian. Hence, one must run a second MCMC to sample from the conditional pdf, which adds numerical efforts and complications. This makes the methodology more complicated and adds computational costs with respect to the full-dimensional counterpart, however the reduced dimensionality helps in curing the curse of dimensionality in both the construction of the surrogate and the convergence of the main MCMC. However, it must be noticed that the extra MCMC algorithm does not require any evaluation of the expensive simulation code nor of the surrogate model. Once a more efficient implementation of the double MCMC algorithm is available, the technique will be very usable even for real world applications, especially when the structure of the function of interest allows for a high dimensionality reduction. One advantage of the introduced strategy with

respect to the misfit-based method is that the active subspaces and metamodels for the functions of interest do not depend anymore on the measurements but just on the prior densities. This makes the approach more versatile as the surrogates can be used also for forward uncertainty propagation, and reused if changing measurements values. Furthermore, discovering and exploiting the active subspaces in the simulation model's parameter-to-observable map provides global sensitivity metrics, which give comparable rankings of the input as global variance-based sensitivity indices.

From the results of this work, freestream and parameter reconstruction possibilities given by heat flux forebody measurements were less useful than expected. Nevertheless, this does not mean that this kind of measurements are useless or that it is not worth trying to include different newly-available in-flight data in the trajectory and atmospheric reconstruction process. On the contrary, this partially disappointing result should motivate research on how to fully exploit the available in-flight data in a global framework to improve the information on uncertain parameters. Furthermore, the quality of surface heat flux measurements will probably improve in the future, since they are very useful for a direct monitoring of the TPS heating and performance. More accurate measurements will allow to improve also the predictive capabilities of numerical simulations. All these factors will eventually lead to progress in accuracy and robustness of predictions and freestream reconstruction.

As already noticed, the Bayesian framework for inverse problems was versatile and useful, and could be further exploited in direct and inverse UQ problems and sensitivity analysis for hypersonic entry flows and other aspects related to atmospheric entry. It must be kept in mind that it is especially suited for punctual analysis, and does not replace filtering methods to reconstruct the whole entry trajectory. It can instead be used in applications involving data from experimental facilities, as for example in [Sanson *et al.*, 2016]. Experimental configurations with stationary phenomena and adequate control over measurement errors could benefit from Bayesian inversion to characterize uncertain parameters which are not directly measurable. As a further remark, it is worth to stress the importance of the choice of the prior in a Bayesian setting. In fact, the quality of the results depends strongly on the prior. When weakly-informative (*i.e.* wide) priors are given, it is probably easy to obtain a posterior that improves the information over the prior, but at the same time, if model and measurement uncertainties are high, the posterior uncertainty will still be quite relevant. On the other hand, when very informative (*i.e.* narrow) priors are given, posteriors will be narrower too, but it may be very difficult to see an improvement over the prior. Furthermore, the result might be mainly influenced by the prior belief rather than learning from the data.

To conclude, we assessed atmospheric reconstruction performed with heat flux. Moreover, this work allowed to identify some critical aspects for UQ problems in hypersonic entry flows. In particular, mesh adaptation for numerical simulations of the flow was a very critical aspect, since it was causing major problems to get accurate yet automated simulations. While this may be obvious for experts in the field of numerical simulations of hypersonic flows, it becomes less evident when trying to perform a high number of simulations for UQ. This aspect needs an adequate collaboration between UQ people and experts in numerical simulations, in order to define a more general and rigorous operational framework. Another general conclusion that can be drawn from this work is that many further aspects in atmospheric entry are worth being analyzed in a UQ framework, for example the effect of ablation phenomena on surface heating, entry flows in atmospheres of different planets and entry trajectories of capsules and debris. All these problems involve complex models, with parameters that are difficult to estimate because of the lack of experimental data for a proper calibration, and therefore the whole validation and verification process could benefit from the quantification of uncertainties to robustly evaluate predictive capabilities of simulations.

6.7 Perspectives and future developments

This work has illustrated the developments for providing some solutions to some challenging points indicated in the objectives. We will illustrate now some perspectives, which may take advantage of the novelties introduced in the work, or others which could improve some of the weak points highlighted. From the point of view of the application to entry flows and freestream characterization, the following points are worth being explored.

- A short term improvement for the results of the freestream reconstruction for EXPERT would be to account for chemistry uncertainties, as done for the HEG cylinder.
- It would be definitively interesting to test Bayesian inversion for freestream reconstruction in a real-world case, where real in-flight data are available, containing also heat flux measurements. This would allow to verify the actual performance of both the methodology and heat flux measurements for freestream reconstruction. In such context, the discrepancy between measurements and model predictions would become more critical, thus the predictive capabilities of the computational model should be thoroughly assessed and the discrepancy with measured data adequately modeled in order to have representative inverse solutions.
- It could be very interesting to perform a forward propagation of uncertainties and sensitivity analysis for the entry in an atmospheric environ-

ment different than air, taking into account for example a Martian entry mission (*e.g.* MSL or EXOMARS missions), as done for example in [Bose *et al.*, 2004] for Titan's atmosphere. The higher uncertainty present on atmospheric models of other planets than Earth could produce more relevant uncertainties on the outputs of numerical simulations, therefore robust predictions would benefit from a rigorous attempt to quantify these variations. These extra-terrestrial entry missions would also probably require accounting for effects of the ablation of the heat shield for more predictive simulations. This would require to include uncertainties associated with parameters of the ablation model, that can affect the heating response, leading to different UQ results. This may become relevant also for the inverse UQ problem, where the usefulness of heat flux measurements might be higher.

- Another point that can be interesting to explore is the optimization of sensors position and accuracy in a Bayesian framework, in order to obtain a configuration which maximizes the accuracy of the reconstruction, by minimizing the variance of the posterior for example. Results might then be compared with more classically optimized sensors configuration, which may not take into account model uncertainties, but which may benefit from experimental tests and calibrations.

From a more mathematical point of view, different improvements could be tested for the methodologies proposed in the work.

- It would be interesting to test the implementation of sparse polynomial basis functions in the kernel (autocovariance) of a Gaussian process surrogate model with no regression trends. For example, [Duvenaud, 2014, Chapter 2] showed how to use different type of kernels to build surrogate models of functions of interest with many different structures. The implementation of features of the functions in the kernel of a Gaussian process is more common in the literature of machine learning [Duvenaud *et al.*, 2011; Bach, 2009] and should help fight against the curse of dimensionality [Bengio *et al.*, 2005], while it is less explored in the literature of uncertainty quantification. A natural comparison will be with the implementation proposed in this work, which uses polynomial basis in the regression term of the Universal Kriging surrogate.

- In order to improve the computational performance of the adaptation technique proposed in Chapter 4, the main interest is to get rid of the need of constructing a Delaunay simplex grid, which is one of the main features of the technique, but at the same time the bottleneck when increasing the input space dimensionality. Furthermore, other implementations of the error criterion could be explored, for example accounting for the average surrogate modeling error along the edge, instead of its

value in the edge midpoint. Although more complex and expensive, this implementations should be more representative of actual errors, since it is able to account for strong variations of surrogate modeling error along each edge.

- Since the use of active subspace was very effective, it is worth to improve the numerical efficiency of the proposed algorithm and use them for Bayesian inverse problem in practical applications. An intensive research is currently being carried out on active subspaces and their application, and the implementation of all the derived novelties will improve the effectiveness of this tool.

As already mentioned, more practical improvements should be carried out concerning the methodology for numerical simulations of hypersonic flows adopted in the work, in particular about mesh adaptation. Because of the difficulties in the mesh refinement, it could be interesting to exploit other more advanced mesh adaptation techniques for hypersonic flows as [Saunders *et al.*, 2007], to verify if they can produce more accurate and reliable results, without being too cumbersome to be adopted in the case of UQ applications.

Appendix A

Brief overview of conventional methods for atmospheric reconstruction

This appendix reviews the main ideas behind two classical techniques used for the reconstruction of the entry trajectory and the characterization of atmospheric quantities. The fist method infers all the unknown parameters starting from acceleration and rotation measurements given by the Inertial Measurement Unit (IMU), which is part of the normal equipment of a space vehicle. Then a second more advanced technique is described, which exploits also pressure measurements given by the FADS in the process of atmospheric rebuilding.

A.1 Conventional reconstruction method based on IMU data

An Inertial Measurement Unit (IMU) is a package of accelerometers and gyroscopes that measures linear accelerations and angular rotation rates. IMU flight data have to be numerically integrated to provide the vehicle positional state through time, i.e. its trajectory. Starting from an initial navigational state, the velocity and rotation rates can be integrated with a numerical integration scheme. This provides atmospheric entry trajectory in terms of altitude, velocity, angle of attack, etc. Trajectory reconstruction is described in more detail in [Withers *et al.*, 2003; Van Hove et Karatekin, 2013]. However, IMU alone does not provide direct information on wind velocity which affects the determination of air speed and flow angles, as will be discussed below.

In a second step, atmospheric profiles may be derived along the reconstructed trajectory. Atmospheric density is commonly estimated from the

drag equation:

$$D = m|\boldsymbol{a}_D| = \frac{1}{2}\rho_\infty u_\infty^2 A_{ref} C_D \ , \tag{A.1}$$

where D is the drag, which is equal the aerodynamic deceleration along the drag direction $|\boldsymbol{a}_D|$ times the vehicle mass m, ρ_∞ is the freestream density at a given altitude h, C_D the non-dimensional aerodynamic drag coefficient, u_∞ the air velocity and A_{ref} the reference surface area for a particular entry vehicle. This equation can be rearranged to calculate atmospheric density as a function of measured deceleration:

$$\rho_\infty = 2\frac{m|\boldsymbol{a}_D|}{C_D A_{ref} u_\infty^2}. \tag{A.2}$$

Note that C_D is computed from the predicted aerodynamic drag and cannot be constrained by IMU flight data. Any drag coefficient uncertainty, caused by inaccuracy of CFD simulations, is then propagated directly to the reconstructed atmospheric density.

Additional atmospheric quantities are derived from the density profile in two steps. First in Eq. (A.3), atmospheric pressure p_∞ is estimated by integrating density over altitude according to hydrostatic equilibrium. Second in Eq. (A.4), density and pressure are then combined in the ideal gas law to derive atmospheric temperature T_∞

$$p_\infty(h) = p_\infty(h_0) - \int_{h_0}^{h} g\rho_\infty \, dh \tag{A.3}$$

$$T_\infty = \frac{\mu p_\infty}{R\rho_\infty} \ , \tag{A.4}$$

with gravitational acceleration g, ideal gas constant $R = 8.3144621$ J/mol/K and the molecular weight μ of the atmospheric gas mixture. Uncertainties bounds on this deterministic method are typically estimated by Monte Carlo sampling, as, for example, in [Withers et Catling, 2010].

The main disadvantage of this IMU-based atmosphere reconstruction method is the reliance of Eq. (A.2) on the aerodynamic drag coefficient. C_D estimations from pre-flight wind tunnel testing and/or CFD simulations cannot be compared against real-flight coefficients, because they serve as an input for the calculations.

A.2 Reconstruction based on surface stagnation pressure

In recent decades, Flush Air Data Systems (FADS), consisting of a grid of heat shield integrated pressure sensors, have been developed for a variety of

high-speed vehicles, from jet fighters to planetary exploration vehicles. For the latter, this may also include heat flux measurements; but atmospheric reconstruction with FADS has so far been based on forebody pressure only [Dutta et Braun, 2014]. The derivation of the flow environment from forebody pressure is an inverse problem, as opposed to the more common forward calculation of the heat shield surface pressure distribution. While no aerodynamic coefficients are required in the pressure based reconstruction method, the forebody pressure must be predicted as function of atmospheric freestream conditions. The flow model can be constructed using CFD look-up tables, wind tunnel testing or approximate analytical relations. Here, the latter approach is used to obtain a FADS solver that is generally applicable to a wide range of blunt nosed entry vehicles.

Atmospheric conditions are classically derived from stagnation pressure p_{t2} with the analytical Rayleigh-pitot tube formula [Pruett *et al.*, 1983] in Eq. (A.5):

$$\frac{p_{t2}}{q_\infty} = \frac{2}{\gamma M_\infty}\left(\frac{(\gamma+1)^2 M_\infty^2}{4\gamma M_\infty^2 - 2(\gamma-1)}\right)^{\frac{\gamma}{\gamma-1}}\left(\frac{1-\gamma+2\gamma M_\infty^2}{\gamma+1}\right), \tag{A.5}$$

with Mach number M_∞ and the heat capacity ratio $\gamma = c_p/c_v$. Eq. (A.5) rests on the assumption that γ is constant along the stagnation streamline. In reality, the shock wave ahead of the vehicle significantly raises the temperature, modifying γ and making perfect non-reacting gas relations such as Eq. (A.5) invalid. To take high-temperature effects into account, it is possible to use equivalent values for γ derived from thermochemical equilibrium solutions of the shock conservation equations of mass, energy and momentum.

Once the freestream dynamic pressure has been determined, atmospheric density ρ_∞ can be derived according to Eq. A.6, where the required air speed is provided by IMU data:

$$\rho_\infty = \frac{2q_\infty}{V_\infty^2}. \tag{A.6}$$

Appendix B

Complements on Kriging and Gaussian Process regressions

B.1 Gaussian Process

Formally, a Gaussian process is a collection of random variables $Z(\mathbf{x})$ indexed by $\mathbf{x}$, any finite number of which have a joint Gaussian distribution.

A Gaussian process $Z(\mathbf{x})$ is a second-order stochastic process that is completely defined by its first and second-order statistical moments, namely by its mean function $\mu(\mathbf{x}) = \mathbb{E}[Z(\mathbf{x})]$ and its autocovariance function $C(\mathbf{x}, \mathbf{x}') = \mathbb{E}[(Z(\mathbf{x}) - \mu(\mathbf{x}))(Z(\mathbf{x}') - \mu(\mathbf{x}'))]$. Therefore, it is possible to denote a Gaussian process as:

$$Y(\mathbf{x}) \sim \mathcal{GP}(\mu(\mathbf{x}), C(\mathbf{x}, \mathbf{x}')). \tag{B.1}$$

B.1.1 Stationary Gaussian process

A *stationary* stochastic process is a process that is invariant by translation. Therefore, it follows that it has a constant mean function

$$\mu(\mathbf{x}) = \mu_0 \qquad \forall \mathbf{x} \,, \tag{B.2}$$

and an autocovariance function that depends only on the shift between $\mathbf{x}$ and $\mathbf{x}'$

$$C(\mathbf{x}, \mathbf{x}') = \sigma^2 k(\mathbf{x} - \mathbf{x}') \qquad \forall \mathbf{x}, \mathbf{x}' \,, \tag{B.3}$$

where σ^2 is a constant variance magnitude and $k(\mathbf{x} - \mathbf{x}')$ is called the autocorrelation function.

B.2 Universal Kriging and the BLUP problem

In this section, the analytical resolution of the best linear unbiased predictor (BLUP) is proposed. This problem arises in the formulation of the the

Universal Kriging predictor described in Section 3.2.1.

We recall that the main idea of Kriging method is to consider the output of the deterministic model $f(\mathbf{x})$ as a realization of a Gaussian stochastic process $F(\mathbf{x})$. In Universal Kriging (UK), the stochastic process is written in the form of the sum of a deterministic linear regression model and a stochastic departure term:

$$F(\mathbf{x}) = \sum_{j=1}^{n} \beta_j h_j(\mathbf{x}) + Z(\mathbf{x}) = \boldsymbol{h}^T(\mathbf{x})\boldsymbol{\beta} + Z(\mathbf{x}) \,, \tag{B.4}$$

where $h_j(\mathbf{x})$ are n linearly independent known regression functions, β_j are unknown weights, and $Z(\mathbf{x})$ is a stationary Gaussian process with zero mean function

$$\mathbb{E}[Z(\mathbf{x})] = 0 \qquad \forall \mathbf{x} \,, \tag{B.5}$$

and a stationary autocovariance function

$$\mathbb{E}[Z(\mathbf{x}), Z(\mathbf{x}')] = \sigma^2 k(\mathbf{x} - \mathbf{x}') \qquad \forall \mathbf{x}, \mathbf{x}'. \tag{B.6}$$

The autocovariance $\sigma^2 k(\mathbf{x}-\mathbf{x}')$ is assumed to be known. The Gaussian process assumption in Eq. (3.2) holds for both the unobserved values $f(\mathbf{x})$ and the observations of the model at the training points $\boldsymbol{f}_{obs} = (f(\mathbf{x}_1), \dots, f(\mathbf{x}_{N_s}))^T$.

The aim of Kriging is to build a *linear predictor* of the function of interest $F(\mathbf{x})$. This means that the predictor $\hat{F}(\mathbf{x})$ is written as a linear combination of the observations $\boldsymbol{F}_{obs} = (F(\mathbf{x}_1), \dots, F(\mathbf{x}_{N_s}))^T$ of the actual model at the N_s training points:

$$\hat{F}(\mathbf{x}) = \sum_{i=1}^{N_s} F(\mathbf{x}_i) a_i(\mathbf{x}) = \boldsymbol{a}^T(\mathbf{x}) \boldsymbol{F}_{obs}. \tag{B.7}$$

where $a_i(\mathbf{x})$ are unknown weights. We want the predictor to be the *best linear unbiased predictor* (BLUP) of the quantity of interest. This means that it has to minimize the mean-square prediction error (MSPE) between the model and the predictor

$$\mathrm{MSPE}(\mathbf{x}) = \mathbb{E}\Big[\big(F(\mathbf{x}) - \hat{F}(\mathbf{x})\big)^2\Big] \,, \tag{B.8}$$

while respecting the constraint of unbiasedness:

$$\mathbb{E}\big[F(\mathbf{x}) - \hat{F}(\mathbf{x})\big] = 0. \tag{B.9}$$

Therefore, the optimization problem consists in finding the optimal set of weights $\boldsymbol{a}^*(\boldsymbol{x})$ of the linear predictor with respect to the following optimization problem

$$\begin{aligned} &\boldsymbol{a}^*(\boldsymbol{x}) = \arg\min_{\boldsymbol{a}} \ \mathbb{E}\Big[\big(F(\mathbf{x}) - \boldsymbol{a}^T(\mathbf{x})\boldsymbol{f}_{obs}\big)^2\Big] \\ &\text{subject to} \qquad \mathbb{E}\big[F(\mathbf{x}) - \boldsymbol{a}^T(\mathbf{x})\boldsymbol{f}_{obs}\big] = 0. \end{aligned} \tag{B.10}$$

B.2.1 Resolution of the BLUP problem

The resolution of the BLUP problem is here proposed following the one in [Dubourg, 2011]. The stochastic error between the linear prediction $\hat{F}(\mathbf{x})$ and the model $F(\mathbf{x})$ can be rewritten by replacing $F(\mathbf{x})$ and $\boldsymbol{F}_{obs}$ with the Gaussian process model:

$$\begin{aligned}\hat{F}(\mathbf{x}) - F(\mathbf{x}) &= \boldsymbol{a}^T \boldsymbol{F}_{obs} - F(\mathbf{x}) = \\ &= \boldsymbol{a}^T (H\boldsymbol{\beta} + \boldsymbol{Z}) - (\boldsymbol{h}(\mathbf{x})^T \boldsymbol{\beta} + Z(\mathbf{x})) = \\ &= \boldsymbol{a}^T \boldsymbol{Z} - Z(\mathbf{x}) + (\boldsymbol{a}^T H - \boldsymbol{h}(\mathbf{x})^T)\boldsymbol{\beta}\ , \end{aligned} \tag{B.11}$$

with $\boldsymbol{Z} = (Z(\mathbf{x}_i)), \ldots, Z(\mathbf{x}_{N_s}))$ the vector of Gaussian departure at the training points, and where $\boldsymbol{h}(\mathbf{x}) = (h_1(\mathbf{x}), \ldots, h_n(\mathbf{x}))^T$ is the vector of basis functions, H is a $N_s \times n$ matrix whose elements are the evaluation of the j-th basis function at the i-th training point $H_{ij} = h_j(\mathbf{x}_i)$. Imposing the expectation of the error equal to zero for the unbiasedness, and putting $\mathbb{E}[\boldsymbol{a}^T Z - Z(\mathbf{x})] = 0$ for the zero-mean assumption on the Gaussian process, we obtain the constraint

$$\boldsymbol{a}^T H - \boldsymbol{h}(\mathbf{x})^T = 0. \tag{B.12}$$

Exploiting this relation, the mean-squared error can be simplified as follows:

$$\begin{aligned}\mathbb{E}\Big[\big(F(\mathbf{x}) - \hat{F}(\mathbf{x})\big)^2\Big] &= \mathbb{E}\Big[\big(\boldsymbol{a}^T \boldsymbol{F}_{obs} - F(\mathbf{x})\big)^2\Big] = \\ &= \mathbb{E}[\boldsymbol{a}^T \boldsymbol{Z}\boldsymbol{Z}^T \boldsymbol{a} + Z^2(\mathbf{x}) - 2\boldsymbol{a}^T Z Z(\mathbf{x})] = \\ &= \boldsymbol{a}^T \mathbb{E}[\boldsymbol{Z}\boldsymbol{Z}^T]\boldsymbol{a} + \mathbb{E}[Z^2(\mathbf{x})] - 2\boldsymbol{a}^T \mathbb{E}[Z Z(\mathbf{x})] = \\ &= \boldsymbol{a}^T \sigma^2 C \boldsymbol{a} + \sigma^2 - 2\boldsymbol{a}^T \sigma^2 \boldsymbol{c}(\mathbf{x})\ , \end{aligned} \tag{B.13}$$

with $\boldsymbol{c}(\mathbf{x})$ is a vector of length N_s whose elements $c_i = k(\mathbf{x} - \mathbf{x}_i)$ contain the correlations between the point $\mathbf{x}$ and each training point $\mathbf{x}_i$, and C is a $N_s \times N_s$ matrix of correlations among training points $C_{ij} = k(\mathbf{x}_i - \mathbf{x}_j)$. It follows that

$$\mathbb{E}\Big[\big(F(\mathbf{x}) - \hat{F}(\mathbf{x})\big)^2\Big] = \sigma^2\big(1 + \boldsymbol{a}^T C \boldsymbol{a} - 2\boldsymbol{a}^T \boldsymbol{c}(\mathbf{x})\big). \tag{B.14}$$

The BLUP optimization problem can now be solved exploiting the Lagrangian formalism. Introducing the vector of Lagrange multipliers $\boldsymbol{\lambda}$, the Lagrangian function for the constrained optimization problem is:

$$\mathcal{L}(\boldsymbol{a}, \boldsymbol{\lambda}) = \sigma^2\big(1 + \boldsymbol{a}^T (C\boldsymbol{a} - 2\boldsymbol{c}(\mathbf{x}))\big) + \boldsymbol{\lambda}\big(\boldsymbol{a}^T H - \boldsymbol{h}(\mathbf{x})^T\big). \tag{B.15}$$

As known, the optimal solution is found by putting to zero the gradients of the Lagrangian with respect to the unknowns and the multipliers. This leads to the following conditions:

$$\begin{cases} \nabla_{\boldsymbol{a}} \mathcal{L}(\boldsymbol{a}, \boldsymbol{\lambda}) = 2\sigma^2 (C\boldsymbol{a} - 2\boldsymbol{c}(\mathbf{x})) + H\boldsymbol{\lambda} = 0 \\ \nabla_{\boldsymbol{\lambda}} \mathcal{L}(\boldsymbol{a}, \boldsymbol{\lambda}) = H^T \boldsymbol{a} - \boldsymbol{h}(\mathbf{x}) = 0. \end{cases} \tag{B.16}$$

Being a linear system, it can be written in matrix form, calling $\tilde{\boldsymbol{\lambda}} = \frac{\boldsymbol{\lambda}}{2\sigma}$

$$\begin{bmatrix} C & H \\ H^T & 0 \end{bmatrix} \begin{Bmatrix} \boldsymbol{a} \\ \tilde{\boldsymbol{\lambda}} \end{Bmatrix} = \begin{Bmatrix} \boldsymbol{c}(\mathbf{x}) \\ \boldsymbol{h}(\mathbf{x}) \end{Bmatrix}. \tag{B.17}$$

Multiplying the first line by $H^T C^{-1}$ and subtracting to the second line, we obtain

$$\boldsymbol{\lambda}^*(\mathbf{x}) = \Big(H^T C^{-1} H\Big)^{-1} \Big(H^T C^{-1} \boldsymbol{c}(\mathbf{x}) - \boldsymbol{h}(\mathbf{x})\Big). \tag{B.18}$$

Then, substituting in the first line, it is possible to obtain the expression for the optimal coefficients

$$\boldsymbol{a}^*(\mathbf{x}) = C^{-1}\bigg(\boldsymbol{c}(\mathbf{x}) - H\Big(H^T C^{-1} H\Big)^{-1} \Big(H^T C^{-1} \boldsymbol{c}(\mathbf{x}) - \boldsymbol{h}(\mathbf{x})\Big)\bigg). \tag{B.19}$$

Replacing this optimal coefficients in the mean value of the linear predictor, it is possible to obtain the expression for the Universal Kriging predictor, that is the relation used for the surrogate model implementation:

$$\begin{aligned}
\mu_k(\mathbf{x}) = \mathbb{E}[\hat{F}(\mathbf{x})] &= \boldsymbol{a}^T \boldsymbol{f}_{obs} = \\
&= \bigg(\boldsymbol{c}(\mathbf{x}) - H\Big(H^T C^{-1} H\Big)^{-1} \Big(H^T C^{-1} \boldsymbol{c}(\mathbf{x}) - \boldsymbol{h}(\mathbf{x})\Big)\bigg)^T C^{-1} \boldsymbol{f}_{obs} = \\
&= \boldsymbol{c}(\mathbf{x})^T C^{-1} \boldsymbol{f}_{obs} - \Big[\big(H^T C^{-1} H\big)^{-1} H^T C^{-1} \boldsymbol{c}(\mathbf{x}) + \big(H^T C^{-1} H\big)^{-1} \boldsymbol{h}(\mathbf{x})\Big]^T H^T C^{-1} \boldsymbol{f}_{obs} = \\
&= \boldsymbol{h}(\mathbf{x})^T \underbrace{\big(H^T C^{-1} H\big)^{-1} H^T C^{-1} \boldsymbol{f}_{obs}}_{\boldsymbol{\beta}} + \boldsymbol{c}(\mathbf{x})^T C^{-1} \big(\boldsymbol{f}_{obs} - H \underbrace{\big(H^T C^{-1} H\big)^{-1} H^T C^{-1} \boldsymbol{f}_{obs}}_{\boldsymbol{\beta}}\big) = \\
&= \boldsymbol{h}^T(\mathbf{x})\boldsymbol{\beta} + \boldsymbol{c}(\boldsymbol{x})^T C^{-1} (\boldsymbol{f}_{obs} - H\boldsymbol{\beta}).
\end{aligned} \tag{B.20}$$

It is also possible to replace the optimal values of the linear predictor coefficients in the mean-squared error between the prediction and the actual function, to obtain a model-based metamodeling error estimator. Let us first call $\boldsymbol{u}(\mathbf{x}) = H^T C^{-1} \boldsymbol{c}(\mathbf{x}) - \boldsymbol{h}(\mathbf{x})$, it follows that $\boldsymbol{a}^*(\mathbf{x}) = C^{-1}\big(\boldsymbol{c}(\mathbf{x}) - H\big(H^T C^{-1} H\big)^{-1} \boldsymbol{u}\big)$. Replacing this expression in the definition of mean-squared error it is possible to obtain:

$$\begin{aligned}
s_k^2 &= \mathbb{E}\Big[\big(\hat{F}(\mathbf{x}) - F(\mathbf{x})\big)^2\Big] = \\
&= \sigma^2\big(1 + \boldsymbol{a}^T C \boldsymbol{a} - 2\boldsymbol{a}^T \boldsymbol{c}(\mathbf{x})\big) = \\
&= \sigma^2\big\{1 + (\boldsymbol{c}(\mathbf{x}) - H(H^T C^{-1} H)^{-1}\boldsymbol{u})^T C^{-1} [(\boldsymbol{c}(\mathbf{x}) - H(H^T C^{-1} H)^{-1}\boldsymbol{u}) - 2\boldsymbol{u}]\big\} = \\
&= \sigma^2\big[1 - (\boldsymbol{c}(\mathbf{x}) - H(H^T C^{-1} H)^{-1}\boldsymbol{u})^T C^{-1} (\boldsymbol{c}(\mathbf{x}) + H(H^T C^{-1} H)^{-1}\boldsymbol{u})\big] = \\
&= \sigma^2\big[1 - (\boldsymbol{c}(\mathbf{x})^T C^{-1} \boldsymbol{c}(\mathbf{x}) - (H(H^T C^{-1} H)^{-1}\boldsymbol{u})^T C^{-1} H (H^T C^{-1} H)^{-1}\boldsymbol{u})\big] = \\
&= \sigma^2\big[1 - \boldsymbol{c}(\mathbf{x})^T C^{-1} \boldsymbol{c}(\mathbf{x}) + \boldsymbol{u}^T (H^T C^{-1} H)^{-1} \boldsymbol{u}\big].
\end{aligned} \tag{B.21}$$

B.3 Universal Kriging and Gaussian process predictors, frequentist point of view

In this section, we will derive the Universal Kriging surrogate model in an alternative way, within the framework of the stochastic prediction methodology. The main assumption of stochastic predictions consists in considering the observation of the function of interest, gathered in the vector $\boldsymbol{f}_{obs}$, together with the value of the function at an unobserved point $f(\mathbf{x})$ to be a realization of a random vector $(F(\mathbf{x}), \boldsymbol{F}_{obs})^T$ distributed according to a joint probability distribution $\mathcal{P}$:

$$\begin{Bmatrix} F(\mathbf{x}) \\ \boldsymbol{F}_{obs} \end{Bmatrix} \sim \mathcal{P}. \tag{B.22}$$

By means of the stochastic prediction methodology, it is possible to derive a predictor $\hat{F}(\mathbf{x})$ for the unobserved values of the function by exploiting this statistical relation. At this purpose, the fundamental theorem of prediction [Santner *et al.*, 2003, Theorem 3.2.1] defines the optimal predictor minimizing the *mean squared prediction error* (MSPE $= \mathbb{E}_{\mathcal{P}}[(F(\mathbf{x}) - \hat{F}(\mathbf{x}))^2]$) as the conditional distribution of $F(\mathbf{x})$ given the observations:

$$\hat{F}(\mathbf{x}) = \mathbb{E}_{\mathcal{P}}[F(\mathbf{x})|\boldsymbol{F}_{obs}]. \tag{B.23}$$

A particular case of stochastic predictor is the Gaussian predictor, where the distribution $\mathcal{P}$ is a multivariate Gaussian distribution $\mathcal{N}$. In this case, the relationship between the input $\mathbf{x}$ and the model output $f(\mathbf{x})$ is a sample path from a Gaussian process $F(\mathbf{x})$ to be characterized. A common model for the Gaussian process is constituted by the linear regression model:

$$F(\mathbf{x}) = \sum_{j=1}^{n} \beta_j h_j(\mathbf{x}) + Z(\mathbf{x}) = \boldsymbol{h}^T(\mathbf{x})\boldsymbol{\beta} + Z(\mathbf{x}) \,, \tag{B.24}$$

where the stochastic process is written in the form of a deterministic linear regression model plus a stochastic departure term $Z(\mathbf{x})$, which is a Gaussian process with zero mean function $\mathbb{E}[Z(\mathbf{x})] = 0$ and a stationary autocovariance function $\mathbb{E}[Z(\mathbf{x}), Z(\mathbf{x}')] = \sigma^2 k(\mathbf{x} - \mathbf{x}')$, with $k(\mathbf{x} - \mathbf{x}')$ assumed to be known. Thanks to this model, it is possible to write the joint distribution between the predictions and the observations in the following way:

$$\begin{Bmatrix} F(\mathbf{x}) \\ \boldsymbol{F}_{obs} \end{Bmatrix} \sim \mathcal{N}\left(\begin{Bmatrix} \boldsymbol{h}^T(\mathbf{x})\boldsymbol{\beta} \\ H\boldsymbol{\beta} \end{Bmatrix}, \sigma^2 \begin{bmatrix} 1 & \boldsymbol{c}^T(\mathbf{x}) \\ \boldsymbol{c}(\mathbf{x}) & C \end{bmatrix} \right) , \tag{B.25}$$

where $\boldsymbol{h}(\mathbf{x}) = (h_1(\mathbf{x}), \ldots, h_n(\mathbf{x}))^T$ is the vector of basis functions, H is a $N_s \times n$ matrix whose elements are the evaluation of the j-th basis function at the i-th training point $H_{ij} = h_j(\mathbf{x}_i)$, $\boldsymbol{c}(\mathbf{x})$ is a vector of length N_s whose elements $c_i = k(\mathbf{x} - \mathbf{x}_i)$ contain the correlations between the point $\mathbf{x}$ and each

training point $\mathbf{x}_i$, and C is a $N_s \times N_s$matrix of correlations among training points $C_{ij} = k(\mathbf{x}_i - \mathbf{x}_j)$. From this normal joint distribution, the best MSPE predictor given by the theorem (B.23) becomes (see [Rasmussen et Williams, 2006, Appendix A.2] for the conditioned distribution of a Gaussian vector):

$$\begin{aligned}\hat{F}(\mathbf{x}) &= \mathbb{E}[F(\mathbf{x})|F_{obs}] \sim \\ &\sim \mathcal{N}\Big(\boldsymbol{h}^T(\mathbf{x})\boldsymbol{\beta} + \boldsymbol{c}(\mathbf{x})^T C^{-1}(\boldsymbol{f}_{obs} - H\boldsymbol{\beta}) \ , \ \sigma^2(1 - \boldsymbol{c}(\mathbf{x})^T C^{-1}\boldsymbol{c}(\mathbf{x}))\Big).\end{aligned} \tag{B.26}$$

Therefore, the predictive mean, used as surrogate model is simply the expectation of the predictor:

$$\mu_k(\mathbf{x}) = \mathbb{E}[\hat{F}(\mathbf{x})] = \boldsymbol{h}^T(\mathbf{x})\boldsymbol{\beta} + \boldsymbol{c}(\mathbf{x})^T C^{-1}(\boldsymbol{f}_{obs} - H\boldsymbol{\beta}). \tag{B.27}$$

B.3.1 Generalized least-squares by maximum likelihood estimation

In order to compute the regression coefficients $\boldsymbol{\beta}$ for the predictor, we will solve a generalized least-squares problem in a frequentist approach. The Gaussian linear model (B.24) is valid for the observations of the function at the training points, therefore we can write:

$$F_i^{obs} = \sum_{j=1}^{n} \beta_j h_j(\mathbf{x}_i) + Z_i \qquad i = 1, \dots, N_s \ , \tag{B.28}$$

where Z_i are the Gaussian deviation terms at the training points, which are collected in the vector $\boldsymbol{Z}$, leading to $\mathbb{E}[\boldsymbol{Z}] = 0$ and $\mathbb{E}[\boldsymbol{Z}\boldsymbol{Z}^T] = \sigma^2 C$. Due to the general linear regression model in (B.28), the random vector of the observations is distributed with the following multivariate normal distribution:

$$\boldsymbol{F}_{obs} \sim \mathcal{N}\big(H\boldsymbol{\beta} \ , \ \sigma^2 C\big) \ , \tag{B.29}$$

where H is a $N_s \times n$ matrix whose terms are defined as $H_{ij} = h_j(\mathbf{x}_i)$.

The solution to the regression problem in the least squares sense consists in finding the optimal values for $\boldsymbol{\beta}$ that maximizes the likelihood of the observations given $\boldsymbol{\beta}$. In the Gaussian linear model framework, the likelihood is defined as follows from the multivariate normal probability density function of the observations:

$$\ell(\mathbf{f}_{obs}|\boldsymbol{\beta}) = \frac{1}{\sqrt{(2\pi\sigma^2)^{N_s}\det[C]}} \exp\left(-\frac{(\mathbf{f}_{obs} - H\boldsymbol{\beta})^T C^{-1}(\mathbf{f}_{obs} - H\boldsymbol{\beta})}{2\sigma^2}\right). \tag{B.30}$$

Normally, instead of directly maximizing the likelihood, it is simpler to solve the equivalent problem of minimizing the negative log-likelihood. Therefore the *maximum likelihood estimation* (MLE) problem can be expressed as:

$$\boldsymbol{\beta}^* = \arg\min_{\boldsymbol{\beta}} \big(-\log \ell(\mathbf{f}_{obs}|\boldsymbol{\beta})\big) \ , \tag{B.31}$$

where log is the natural logarithm. The optimality condition for this unconstrained optimization problem can be found by putting to zero the derivatives of the likelihood with respect to the design parameters $\boldsymbol{\beta}$

$$\nabla_{\boldsymbol{\beta}} \log \ell(\mathbf{f}_{obs}|\sigma^2, \boldsymbol{\beta}) = 0. \tag{B.32}$$

By computing the derivatives, we obtain the following linear system of equations:

$$\frac{1}{\sigma^2}\big(H^T C^{-1}\mathbf{f}_{obs} - H^T C^{-1} H\boldsymbol{\beta}\big) = 0 \qquad \forall \sigma^2. \tag{B.33}$$

This system can be easily solved, obtaining the generalized least-squares estimate for the regression weights

$$\boldsymbol{\beta}^* = \big(H^T C^{-1} H\big)^{-1} H^T C^{-1} \boldsymbol{f}_{obs}. \tag{B.34}$$

B.4 Stationary autocorrelation functions

In this section, some stationary autocorrelation functions (also called kernels) for Gaussian process are reported. These are well-known examples of autocorrelation functions present in many Kriging predictor implementations.

B.4.1 Exponential

A first simple model is given by the (anisotropic) exponential autocorrelation function, defined as:

$$k(\mathbf{x} - \mathbf{x}') = \exp\left\{ - \sum_{i=1}^{d} \frac{|x_i - x_i'|}{\theta_i} \right\}. \tag{B.35}$$

The sample path resulting from a Gaussian process with this autocorrelation function are continuous but non-differentiable functions. This means that a predictor obtained using this kernel will present discontinuous derivative.

B.4.2 Squared exponential

Similarly, the (anisotropic) squared exponential autocorrelation function is defined as follows:

$$k(\mathbf{x} - \mathbf{x}') = \exp\left\{ - \sum_{i=1}^{d} \left(\frac{x_i - x_i'}{\theta_i} \right)^2 \right\}. \tag{B.36}$$

In this case, the correlation function provides a sample path with infinite degree of differentiability, meaning that all its derivatives are continuous.

B.4.3 Matérn

Another very common autocorrelation function is given by the Matérn kernel:

$$k(\mathbf{x}-\mathbf{x}') = \prod_{i=1}^{d} \frac{1}{2^{\nu-1}\Gamma(\nu)} \left(2\sqrt{\nu}\frac{|x_i - x_i'|}{\theta_i}\right)^{\nu} K_\nu \left(2\sqrt{\nu}\frac{|x_i - x_i'|}{\theta_i}\right) , \tag{B.37}$$

where $\nu \geq 1/2$ is called shape parameter, Γ is the Euler Gamma function and K_ν the modified Bessel function of the second kind. A characteristic of this correlation function is that sample paths from the corresponding Gaussian process are $\lceil \nu - 1 \rceil$ times differentiable [Dubourg, 2011], with $\lceil \cdot \rceil$ the ceiling operator. Therefore, when $\nu = 1/2$ the Matérn correlation function coincides with the exponential function. on the other limiting case, when $\nu \to \infty$, the Matérn correlation function tends to the squared exponential function. In practice, three classical implementations of the function are given by:

$$k(\mathbf{x}-\mathbf{x}') = \prod_{i=1}^{d} \begin{cases} e^{-r_i} & \text{for } \nu = 1/2, \\ \left(1+\sqrt{3}r_i\right) e^{-\sqrt{3}r_i} & \text{for } \nu = 3/2, \\ \left(1+\sqrt{5}r_i + \frac{5}{3}r_i^2\right) e^{-\sqrt{5}r_i} & \text{for } \nu = 5/2, \end{cases} , \tag{B.38}$$

with $r_i = \frac{|x_i - x_i'|}{\theta_i}$.

B.4.4 Nugget

The nugget autocorrelation function is called in this way for historical reasons associated to early applications of Kriging in geology and mining. It is defined as a Dirac delta function:

$$k(\mathbf{x}-\mathbf{x}') = \delta(\mathbf{x}-\mathbf{x}') , \tag{B.39}$$

which is equal to one if $\mathbf{x} = \mathbf{x}'$ and zero otherwise. This means that all points are characterized by the lack of any correlation. It is often used as an additive term to other autocorrelation models to be able to account for noise in the training data and to improve the numerical conditioning.

B.5 Empirical estimation of the autocorrelation model by maximum likelihood

When deriving the Kriging Gaussian predictor, the autocovariance model is assumed to be known. In practice, in the context of computer codes, normally this assumption is not true. Therefore, the user needs to choose a family of stationary autocorrelation function, for example between one of the classical

models reported in Section B.4, and then estimate the unknown hyperparameters, that for the models in B.4 consist in the covariance magnitude σ^2 and the correlation length scales $\boldsymbol{\theta}$.

Several approaches can be used to determine a suitable value of the hyperparameters. Some examples are given by the variogram [Cressie, 1993], mainly used in the field of geostatistcs, cross validation and bayesian estimation [Rasmussen et Williams, 2006, Chapter 5]. In this work we will follow another common approach, that consists in maximizing the likelihood of the observations with respect to the hyperparameters. By picking the hyperparameters that maximize this probability, a Kriging model that best describes the data can be constructed. The likelihood is defined the probability of the Gaussian process describing the training data given the hyperparameters, and can be written as follows:

$$\ell(\mathbf{f}_{obs}|\sigma^2,\boldsymbol{\theta},\boldsymbol{\beta}) = \frac{1}{\sqrt{(2\pi\sigma^2)^d \det[C(\boldsymbol{\theta})]}} \exp\left(-\frac{(\mathbf{f}_{obs}-H\boldsymbol{\beta})^T C(\boldsymbol{\theta})^{-1}(\mathbf{f}_{obs}-H\boldsymbol{\beta})}{2\sigma^2}\right). \tag{B.40}$$

As done in B.3.1, the problem is restated by minimizing the negative log-likelihood:

$$(\boldsymbol{\beta}^*,\sigma^{*2},\boldsymbol{\theta}) = \arg\min_{\boldsymbol{\beta},\sigma^2,\boldsymbol{\theta}} \big(-\log \ell(\mathbf{f}_{obs}|\sigma^2,\boldsymbol{\theta},\boldsymbol{\beta})\big). \tag{B.41}$$

Note that the maximum likelihood estimates of $\boldsymbol{\beta}$ and σ^2 can be found analytically by solving the optimality conditions of the likelihood:

$$\begin{cases} \nabla_{\boldsymbol{\beta}} \log \ell(\mathbf{f}_{obs}|\sigma^2,\boldsymbol{\beta}) = 0 \\ \frac{\partial}{\partial\sigma^2} \log \ell(\mathbf{f}_{obs}|\sigma^2,\boldsymbol{\beta}) = 0. \end{cases} \tag{B.42}$$

This leads to the following system of equations:

$$\begin{cases} \frac{1}{\sigma^2}\big(H^T C^{-1}\mathbf{f}_{obs} - H^T C^{-1} H\boldsymbol{\beta}\big) = 0 \\ \frac{N_s}{2\sigma^2} - \frac{(\mathbf{f}_{obs}-H\boldsymbol{\beta})^T C^{-1}(\mathbf{f}_{obs}-H\boldsymbol{\beta})}{2\sigma^4} = 0. \end{cases} \tag{B.43}$$

This system can be easily solved, obtaining the generalized least-squares estimate for the regression weights

$$\boldsymbol{\beta}^* = \big(H^T C^{-1} H\big)^{-1} H^T C^{-1} \boldsymbol{f}_{obs}\ , \tag{B.44}$$

and for the variance estimate

$$\sigma^{*2} = \frac{(\mathbf{f}_{obs}-H\boldsymbol{\beta}^*)^T C^{-1}(\mathbf{f}_{obs}-H\boldsymbol{\beta}^*)}{N_s}. \tag{B.45}$$

Plugging this two solutions in the likelihood, it is possible to obtain the so-called reduced likelihood function, depending only on $\boldsymbol{\theta}$. The maximum likelihood estimate of the correlation lengths is therefore obtained by minimizing

the reduced likelihood function. This global optimization problem can not be solved analytically, requiring the use of some numerical optimization technique. Notice that some numerical difficulties are associated to the solution of this optimization problem, as shown in [Marrel *et al.*, 2008].

Note that this method is valid for noiseless data. It is also valid when a pseudo-noise prescribed by the user is considered to ensure proper conditioning of the covariance matrix, thus making numerically more robust the computation of the hyperparameters and of $\boldsymbol{\beta}$. In this case, the noise ratio σ_n^2/σ^2 can be fixed by the user and therefore the covariance matrix $C_{(n)}(\boldsymbol{\theta}) = C(\boldsymbol{\theta}) + \frac{\sigma_n^2}{\sigma^2} I$ is still a function of only $\boldsymbol{\theta}$. In the more general case of noisy data, when σ_n^2 is directly imposed or considered as a further hyperparameter to be optimized from the likelihood, the covariance matrix becomes a function of both $\boldsymbol{\theta}$ and σ^2, and equation B.45 is not valid anymore. In such cases, hyperparameters can be obtained by direct numerical optimization of the negative log-likelihood.

Appendix C

Surrogate models assessment

Several error measures can be found in literature [Queipo *et al.*, 2005] to state the quality of a metamodel $\hat{f}(\mathbf{x})$, that is its accuracy at representing the actual function of interest $f(\mathbf{x})$. A first distinction that can be done is between *local* (or pointwise) and *global* error estimates. As it is clearly understandable, local estimates provide a value for the metamodeling error at a specific location $\mathbf{x}$, while global estimates provide and indication of the accuracy of the metamodel over the whole domain. A second distinction can be made between *model-based* and *model-independent* estimates. In the firsts, the method to compute the estimate relies on the structure and on some assumptions done to train the surrogate, while the seconds are independent on the kind of metamodeling technique. Model-dependent estimates can be very inaccurate when the assumptions are not respected, while model-independent estimates are normally associated to a higher computational cost.

In this paper, we rely mainly on two different global and model-independent techniques, in particular, a cross validation estimate and the root mean squared error. They will be briefly described in this appendix, where also other definitions will be given of estimates used for sake of comparison with previous works.

C.1 Root mean-squared error

If one can afford to compute the actual value of the quantity of interest in different points of the stochastic space other than the training points, it is easy then to compute the point wise metamodeling error $e(\mathbf{x})$, defined as the difference at those points between the actual solution and the prediction given by the surrogate:

$$e(\mathbf{x}) = f(\mathbf{x}) - \hat{f}(\mathbf{x}). \tag{C.1}$$

By integrating this local error measure on the whole domain Ω, it is possible to obtain the global Root Mean Squared Error (RMSE), which is often used

as a measure of the accuracy of the approximation.

$$\mathrm{RMSE} = \sqrt{\frac{1}{V}\int_{\Omega} e^2(\mathbf{x})\,\mathrm{d}\mathbf{x}}\,, \tag{C.2}$$

with $V = \int_{\Omega} \mathrm{d}\mathbf{x}$ the volume of the domain. In practice, since normally only a limited number of evaluations of the true model can be afforded, the integration is done numerically [Goel *et al.*, 2009]. by evaluating the function in a finite set of N_t test points, and then the integral can be expressed as

$$\mathrm{RMSE} = \sqrt{\frac{\sum_{i=1}^{N_t} e_i^2 \xi_i}{\sum_{i=1}^{N_t} \xi_i}}\,, \tag{C.3}$$

where $e_i = e(\mathbf{x}_i)$ is the error evaluation at the N_t test point and ξ_i are the integration weights. It is possible to use the collocation points of a quadrature method as test points. Hence a quadrature formula can be exploited to compute the integral in eq. C.3. Another possibility is to compute the integral via Monte Carlo sampling, leading to the following expression

$$\mathrm{RMSE} = \sqrt{\frac{1}{N_t}\sum_{i=1}^{N_t}\big(f(\mathbf{x}_i) - \hat{f}(\mathbf{x}_i)\big)^2}. \tag{C.4}$$

Notice that the RMSE tends to the actual metamodeling error for a large enough number of test points.

The same information can be used to compute a normalized measure called relative mean square error MSE_r, used for example in [Kersaudy *et al.*, 2015]:

$$\mathrm{MSE}_r = \frac{\sum_{i=1}^{N_t}\big(f(\mathbf{x}_i) - \hat{f}(\mathbf{x}_i)\big)^2}{\sum_{i=1}^{N_t}\big(f(\mathbf{x}_i) - \hat{\mu}_y\big)^2}\,, \tag{C.5}$$

where $\hat{\mu}_y$ is the estimated mean of the output variable.

Often, in practical applications the computational cost associated to the evaluation of the model solution is too high, hence the RMSE can not be directly computed. In this cases an estimate of the error measure is instead required.

C.1.1 RMSE for Kriging surrogates

As already mentioned in section 3.2.1 and Appendix B, for Kriging metamodels, the predictive variance of the process (eq. (3.12)) can be used as an estimate of the pointwise mean squared error, hence it follows that:

$$e(\boldsymbol{x}) = \sqrt{s_k^2(\boldsymbol{x})}. \tag{C.6}$$

It is possible to integrate this local model-based error estimate to obtain an estimate of the global root mean squared error (RMSE). In practice, also here the integration is done by a numerical integration technique.

It has to be noticed that this error measure is a model based estimate, because it is based on some assumptions on which the metamodeling technique relies. For example the computations of s_k^2 depends on the assumption on the covariance $k(\boldsymbol{u}, \boldsymbol{v})$ to be of a certain functional form. This fact can lead sometimes to poor error evaluations, especially when the chosen covariance model is not well representative of the behavior of the real function.

C.2 Cross-validation error

In literature there can be found many model independent error measures, that are able to deal with many kinds of surrogate models [Queipo *et al.*, 2005]. One of the most popular among these methods is *k-fold cross validation*, also called *leave-k-out cross-validation*. In particular, as suggested in [Goel *et al.*, 2009] and [Meckesheimer *et al.*, 2002], one recommended choice is to use *leave-one-out cross validation* (often abbreviated as LOOCV) to estimate the Kriging metamodel error. This method consists in fitting a surrogate model on $N_s - 1$ points, by leaving out one training point at a time, then the response is predicted at this point with the metamodel. Then the cross validation error (CV) can be defined as following, in analogy with the RMSE error

$$\mathrm{CV} = \sqrt{\frac{1}{N_s} \sum_{i=1}^{N_s} \left(f_i - \hat{f}_i^{(-i)} \right)^2} , \tag{C.7}$$

where f_i is the training point observed response, while $\hat{f}_i^{(-i)}$ is the prediction at the left-out point using the surrogate built from all the other points. The CV error can be used to estimate the actual root mean squared error of the approximation. Although being relatively expensive, since the training of the surrogate must be repeated at each left out point, this error estimate is supposed to perform quite well. Moreover, being a model independent error measure, it does not depend on the structure and the parameters of the metamodeling technique, since it only needs the output of the prediction, hence it can be used for black-box metamodeling codes. However, as can be seen from its definition, the LOOCV acts more as an indicator of the influence of each training point in the training of the surrogate. For this reason, in some cases it can bring to inaccurate error estimations.

Notice that one way to reduce the computational cost of leave-one-out cross-validation error for Kriging metamodels, often used in literature, is to keep the same hyperparameters for all the reduced training plans, since the exclusion on just one single point is not strongly influencing the output of the

optimization problem, and since the covariance model should be considered as a known input for the training of the Kriging surrogate.

An easier way to interpret the CV error as accuracy indicator can be achieved by computing the determination coefficient Q^2, as done in [Tang *et al.*, 2016]

$$\mathrm{Q}^2 = 1 - \frac{\mathrm{CV}^2}{\hat{V}[\mathcal{Y}]} \,, \tag{C.8}$$

where $V[\mathcal{Y}]$ is the estimated output variance associated to the training set, computed as:

$$\hat{V}[\mathcal{Y}] = \frac{1}{N_s - 1} \sum_{i=1}^{N_s} (y_i - \bar{y})^2 \qquad \text{with} \quad \bar{y} = \frac{1}{N_s} \sum_{i=1}^{N_s} y_i. \tag{C.9}$$

Therefore, if Q^2 is close to unity it means that the metamodel is accurate, and it is able to well fit the function of interest.

Bibliography

Abgrall, Rémi et Congedo, Pietro Marco, 2013. A semi-intrusive deterministic approach to uncertainty quantification in non-linear fluid flow problems. *Journal of Computational Physics*, 235(Supplement C):828 – 845.

Ajdari, Ali et Mahlooji, Hashem, 2014. An adaptive exploration-exploitation algorithm for constructing metamodels in random simulation using a novel sequential experimental design. *Communications in Statistics - Simulation and Computation*, 43(5):947–968.

Alekseev, A. K. et Pavlov, G. A., 1998. Estimation of entry parameters from heat flux measurements. *Journal of Spacecraft and Rockets*, 35(4):575–577.

Anderson, J. D., 2000. *Hypersonic and High Temperature Gas Dynamics*. McGraw-Hill series in aeronautical and aerospace engineering. American Institute of Aeronautics and Astronautics. ISBN 9781563474590.

Anderson, J. D., 2005. *Introduction to Flight*. McGraw-Hill.

Anderson, J. D., 2010. *Fundamentals of Aerodynamics*. McGraw-Hill Education. ISBN 9780073398105.

Andrianakis, Ioannis et Challenor, Peter G., 2012. The effect of the nugget on gaussian process emulators of computer models. *Computational Statistics & Data Analysis*, 56(12):4215 – 4228. doi: http://dx.doi.org/10.1016/j.csda.2012.04.020.
URL http://www.sciencedirect.com/science/article/pii/S0167947312001879

Babuska, Ivo, Nobile, Fabio et Tempone, Raúl, 2007. A stochastic collocation method for elliptic partial differential equations with random input data. *SIAM Journal on Numerical Analysis*, 45(3):1005–1034.

Bach, Francis R., 2009. High-dimensional non-linear variable selection through hierarchical kernel learning. *CoRR*, abs/0909.0844.
URL http://arxiv.org/abs/0909.0844

Barbante, P., 2001. *Accurate and efficient modelling of high temperature non-equilibrium air flows*. Thèse de doctorat, Von Karman Institute for Fluid Dynamics.

Barbante, P. F. et Magin, T. E., 2004. Fundamentals of hypersonic flight–properties of high temperature gases. Dans *RTO-EN-AVT-116*, RTO AVT Lecture Series on Critical Technologies for Hypersonic Vehicle Development. Von Karman Institute for Fluid Dynamics.

Bellas-Chatzigeorgis, G., Villedieu, N., Panesi, M., Congedo, P. M. et Magin, T. E., 2013. Work package 2.2: Propagation of uncertainties related to a complex detailed chemical mechanism. Rapport technique, Von Karman Institute for Fluid Dynamics.

Bellas-Chatzigeorgis, Georgios, Turchi, Alessandro, Viladegut, Alan, Chazot, Olivier, Barbante, Paolo F. et Magin, Thierry E., 2017. Development of catalytic and ablative gas-surface interaction models for the simulation of reacting gas mixtures. Dans *23rd AIAA Computational Fluid Dynamics Conference*, AIAA AVIATION Forum. American Institute of Aeronautics and Astronautics.

Bengio, Y., Delalleau, O. et Le Roux, N., 2005. The curse of highly variable functions for local kernel machines. *Advances in Neural Information Processing Systems*, 18:107–114.

Birolleau, Alexandre, Poëtte, Gaël et Lucor, Didier, 2014. Adaptive bayesian inference for discontinuous inverse problems, application to hyperbolic conservation laws. *Communications in Computational Physics*, 16(1):1–34. doi: 10.4208/cicp.240113.071113a.

Bishop, C., 1995. *Neural Networks for Pattern Recognition*. Clarendon Press.

Blanchard, R. C. et Desai, P. N., 2011. Mars phoenix entry, descent, and landing trajectory and atmosphere reconstruction. *Journal of Spacecraft and Rockets*, 48(5):511–518.

Blatman, Géraud et Sudret, Bruno, 2010a. An adaptive algorithm to build up sparse polynomial chaos expansions for stochastic finite element analysis. *Probabilistic Engineering Mechanics*, 25(2):183 – 197. doi: http://dx.doi.org/10.1016/j.probengmech.2009.10.003.
URL http://www.sciencedirect.com/science/article/pii/S0266892009000666

Blatman, Géraud et Sudret, Bruno, 2010b. Efficient computation of global sensitivity indices using sparse polynomial chaos expansions. *Reliability Engineering & System Safety*, 95(11):1216 – 1229. doi:

http://dx.doi.org/10.1016/j.ress.2010.06.015.
URL http://www.sciencedirect.com/science/article/pii/S0951832010001493

Bonfiglioli, A., Grottadaurea, M., Paciorri, R. et Sabetta, F., 2013. An unstructured, three-dimensional, shock-fitting solver for hypersonic flows. *Computers & Fluids*, 73(Supplement C):162 – 174.

Borgonovo, Emanuele et Plischke, Elmar, 2016. Sensitivity analysis: A review of recent advances. *European Journal of Operational Research*, 248(3):869 – 887. doi: http://dx.doi.org/10.1016/j.ejor.2015.06.032.
URL http://www.sciencedirect.com/science/article/pii/S0377221715005469

Bose, D., Wright, M. et Gokçen, T., 2004. Uncertainty and Sensitivity Analysis of Thermochemical Modeling for Titan Atmospheric Entry. *37th AIAA Thermophysics Conference, Portland, Oregon*.

Bose, Deepak, Brown, James L., Prabhu, Dinesh K., Gnoffo, Peter, Johnston, Christopher O. et Hollis, Brian, 2013. Uncertainty assessment of hypersonic aerothermodynamics prediction capability. *Journal of Spacecraft and Rockets*, 50(1):12–18.

Bose, Deepak, Wright, Michael J. et Palmer, Grant E., 2006. Uncertainty analysis of laminar aeroheating predictions for mars entries. *Journal of Spacecraft and Rockets*, 20(4):652–662.

Bottin, B., Chazot, O., Carbonaro, M., Van Der Haegen, V. et Paris, S., 2000. *The VKI Plasmatron Characteristics and Performance*. Defense Technical Information Center.

Bottin, Benoît, Abeele, David Vanden, Carbonaro, Mario et Degrez, Gérard, 1999. Thermodynamic and Transport Properties for Inductive Plasma Modeling. *Journal of Thermophysics and Heat Transfer*, 13(3):343–350.
URL https://doi.org/10.2514/2.6444

Box, G. E. P. et Draper, N. R., 1987. *Empirical Model-Building and Response Surfaces*. Wiley.

Braun, Robert D. et Manning, Robert M., 2007. Mars exploration entry, descent, and landing challenges. *Journal of Spacecraft and Rockets*, 44(2):310–323.

Brooks, Steve, Gelman, Andrew, Jones, Galin et Meng, Xiao-Li, 2011. *Handbook of Markov Chain Monte Carlo*. Chapman & Hall / CRC, Boca

Raton.
URL http://www.mcmchandbook.net/

Buhmann, M., 2003. *Radial Basis Functions*. Cambridge University Press.

Bursztyn, Dizza et Steinberg, David M., 2006. Comparison of designs for computer experiments. *Journal of Statistical Planning and Inference*, 136(3):1103 – 1119.

Caflisch, Russel E., 1998. Monte carlo and quasi-monte carlo methods. *Acta Numerica*, 7:1–49. doi: 10.1017/S0962492900002804.

Calvetti, Daniela et Somersalo, Erkki, 2007. *Introduction to Bayesian Scientific Computing: Ten Lectures on Subjective Computing*. Springer, New York.
URL https://link.springer.com/book/10.1007/978-0-387-73394-4

Candler, Graham, 1998. High enthalpy flow simulation challenges. Dans *29th AIAA, Plasmadynamics and Lasers Conference*. American Institute of Aeronautics and Astronautics.

Candler, Graham, Mavriplis, Dimitri et Trevino, Loretta, 2009. Current status and future prospects for the numerical simulation of hypersonic flows. Dans *47th AIAA Aerospace Sciences Meeting including The New Horizons Forum and Aerospace Exposition*. American Institute of Aeronautics and Astronautics.

Chapman, S. et Cowling, T. G., 1970. *The Mathematical Theory of Non-Uniform Gases*. Cambridge University Press.

Chikhaoui, A., Dudon, J.P., Kustova, E.V. et Nagnibeda, E.A., 1997. Transport properties in reacting mixture of polyatomic gases. *Physica A: Statistical Mechanics and its Applications*, 247(1):526 – 552. doi: http://dx.doi.org/10.1016/S0378-4371(97)00392-0.
URL http://www.sciencedirect.com/science/article/pii/S0378437197003920

Chkifa, Abdellah, Cohen, Albert, Passaggia, Pierre-Yves et Peter, Jacques, 2013. A comparative study between kriging and adaptive sparse tensor-product methods for multi-dimensional approximation problems in aerodynamics design. Dans *CEMRACS 2013*, tome 48 de *ESAIM: Proceedings and Surveys*, pages 248–261. Marseille, France. doi: 10.1051/proc/201448011.
URL https://hal.archives-ouvertes.fr/hal-01353245

Christian, J., Verges, A. et Braun, R., 2007. Statistical reconstruction of mars entry, descent, and landing trajectories and atmospheric profiles. Dans *AIAA SPACE Conference and Exposition, AIAA 2007-6192*.

Cobleigh, Brent R., Whitmore, Stephen A., Haering, Edward A. Jr., Borrer, Jerry et Roback, V. Eric, 1999. Flush Airdata Sensing (FADS) System Calibration Procedures and Results for Blunt Forebodies. Rapport technique NASA-TP-1999-209012, NASA.

Colombatti, G., Withers, P., Ferri, F., Aboudan, A., Ball, A.J., Bettanini, C., Gaborit, V., Harri, A.M., Hathi, B., Leese, M.R., Makinen, T., Stoppato, P.L., Towner, M.C., Zarnecki, J.C., Angrilli, F. et Fulchignoni, M., 2008. Reconstruction of the trajectory of the huygens probe using the huygens atmospheric structure instrument (hasi). *Planetary and Space Science*, 56:586–600.

Congedo, P.M., Corre, C. et Martinez, J.-M., 2011. Shape optimization of an airfoil in a bzt flow with multiple-source uncertainties. *Computer Methods in Applied Mechanics and Engineering*, 200(1):216–232.

Constantine, P. G., 2015. *Active Subspaces: Emerging Ideas in Dimension Reduction for Parameter Studies*. SIAM, Philadelphia.

Constantine, P. G., Doostan, A., Wang, Q. et Iaccarino, G., 2011. A surrogate accelerated bayesian inverse analysis of the HyShot II supersonic combustion data. Dans *Proceedings of the 49th Aerospace Meeting*.

Constantine, P. G., Dow, E. et Wang, Q., 2014. Active subspace methods in theory and practice: applications to kriging surfaces. *SIAM Journal on Scientific Computing*, 36(4):A1500–A1524.
URL http://dx.doi.org/10.1137/130916138

Constantine, P. G., Emory, M., Larsson, J. et Iaccarino, G., 2015. Exploiting active subspaces to quantify uncertainty in the numerical simulation of the HyShot II scramjet. *Journal of Computational Physics*, 302:1–20. doi: https://doi.org/10.1016/j.jcp.2015.09.001.

Constantine, Paul, del Rosario, Zachary et Iaccarino, Gianluca, 2016a. Many physical laws are ridge functions. *arXiv preprint arXiv:1605.07974*.

Constantine, Paul et Gleich, David, 2015. Computing active subspaces with Monte Carlo. *arXiv preprint arXiv:1408.0545v2*.

Constantine, Paul G et Diaz, Paul, 2017. Global sensitivity metrics from active subspaces. *Reliability Engineering & System Safety*, 162:1–13.
URL https://doi.org/10.1016/j.ress.2017.01.013

Constantine, Paul G., Kent, Carson et Bui-Thanh, Tan, 2016b. Accelerating Markov chain Monte Carlo with active subspaces. *SIAM Journal on Scientific Computing*, 38(5):A2779–A2805.
URL https://doi.org/10.1137/15M1042127

Cook, R. Dennis, 1998. *Regression Graphics: Ideas for Studying Regression through Graphics*. John Wiley & Sons, New York.

Coquel, Frédéric et Liou, Meng-Sing, 1995. Hybrid upwind splitting (hus) by a field-by-field decomposition. Rapport technique NASA-TM-106843, NASA Lewis Research Center.

Cortesi, A. F. et Congedo, P. M., 2016a. A kriging-pdd surrogate model for uncertainty quantification. Dans *VII European Congress on Computational Methods in Applied Sciences and Engineering*, ECCOMAS 2016. ECCOMAS.

Cortesi, A. F., Congedo, P. M., Magin, T. E., Hove, B. Van et Karatekin, O., 2016. Rebuilding freestream atmospheric conditions using surface pressure and heat flux data. Dans *8th AIAA Atmospheric and Space Environments Conference*, AIAA AVIATION Forum. American Institute of Aeronautics and Astronautics.

Cortesi, A. F., Constantine, P. G., Magin, T. E. et Congedo, P. M., submitted. Forward and backward uncertainty quantification with active subspaces: application to hypersonic flows around a cylinder. *Journal of Computational Physics*.

Cortesi, A. F., Jannoun, G. et Congedo, P. M., 2017. Adaptive refinement of the design of experiment for metamodels through anisotropic mesh adaptation. Dans *2nd International Conference on Uncertainty Quantification in Computational Sciences and Engineering*, UNCECOMP 2017. ECCOMAS.

Cortesi, A. F., Jannoun, G. et Congedo, P. M., Submitted. Kriging-sparse polynomial dimensional decomposition surrogate model with adaptive refinement. *Journal of Computational Physics*.

Cortesi, A. F., Magin, T. E. et Congedo, P. M., 2015a. About the Construction of a Robust Metamodel to Estimate the Stagnation Heat Flux for the EXPERT Vehicle. Dans *The 5th International ARA Days*.

Cortesi, A. F., Magin, T. E. et Congedo, P. M., 2015b. Surrogate model with conservative error measure for the stagnation heat flux in atmospheric entry flows. Dans *1st International Conference on Uncertainty Quantification in Computational Sciences and Engineering*, UNCECOMP 2015. ECCOMAS.

CORTESI, Andrea F. et CONGEDO, Pietro M., 2016b. A kriging-PDD surrogate model for low-cost sensitivity analysis. Dans *17th AIAA/ISSMO Multidisciplinary Analysis and Optimization Conference*, AIAA AVIATION Forum. American Institute of Aeronautics and Astronautics.

COUPEZ, T., 2011. Metric construction by length distribution tensor and edge based error for anisotropic adaptive meshing. *Journal of Computational Physics*, 230:2391 – 2405.

COUPEZ, T., JANNOUN, G., NASSIF, N., NGUYEN, H.C., DIGONNET, H. et HACHEM, E., 2013. Adaptive time-step with anisotropic meshing for incompressible flows. *Journal of Computational Physics*, 241:195 – 211.

COWLES, Mary Kathryn et CARLIN, Bradley P., 1996. Markov chain monte carlo convergence diagnostics: A comparative review. *Journal of the American Statistical Association*, 91(434):883–904.

CRAWFORD, Ian A., 2016. The long-term scientific benefits of a space economy. *Space Policy*, 37(Part 2):58 – 61.

CRESSIE, N. A. C., 1993. *Statistics for spatial data*. John Wiley & Sons.

CRESTAUX, T., LE MAÎTRE, O. P. et MARTINEZ, J. M., 2009. Polynomial chaos expansion for sensitivity analysis. *Reliability engineering and system safety*, **94**(7):1161 – 1172.

CROMBECQ, Karel, GORISSEN, Dirk, DESCHRIJVER, Dirk et DHAENE, Tom, 2011. A novel hybrid sequential design strategy for global surrogate modeling of computer experiments. *SIAM Journal on Scientific Computing*, 33(4):1948–1974.

CUI, T, MARTIN, J, MARZOUK, Y M, SOLONEN, A et SPANTINI, A, 2014. Likelihood-informed dimension reduction for nonlinear inverse problems. *Inverse Problems*, 30(11):114015.
URL http://stacks.iop.org/0266-5611/30/i=11/a=114015

CURRIN, Carla, MITCHELL, Toby, MORRIS, Max et YLVISAKER, Don, 1991. Bayesian prediction of deterministic functions, with applications to the design and analysis of computer experiments. *Journal of the American Statistical Association*, 86(416):953–963.

DELAUNAY, B., 1934. Sur la sphere vide. *Izv. Akad. Nauk SSSR, Otdelenie Matematicheskii i Estestvennyka Nauk*, 7:793–800.

DELMAS, Jean-François, 2010. *Introduction au calcul des probabilités et á la statistique*. Les Presses de l'ENSTA.

Desai, P. N., Blanchard, R. C. et Powell, R. W., 2003. Entry trajectory and atmosphere reconstruction methodologies for the mars exploration rover mission. Dans *Proceedings of the International Workshop Planetary Probe Atmospheric Entry and Descent Trajectory Analysis and Science*.

Desai, P. N. et Knocke, P. C., 2007. Mars exploration rovers entry, descent, and landing trajectory analysis. *Journal of the Astronautical Sciences*, 55(3):311 – 323.

Desai, P. N., Prince, J. L., Queen, E. M., Schoenenberger, Mark M., Cruz, J. R. et Grover, M. R., 2011. Entry, descent and landing performance of the mars phoenix lander. *Journal of Spacecraft and Rockets*, 48(5):798 – 808.

Dick, Steven J. et Launius, Roger D., 2007. *Societal Impact of Spaceflight*. National Aeronautics and Space Administration, Office of External Relations, History Division.

Donoho, D. L., 2000. High-dimensional data analysis: The curses and blessings of dimensionality. Dans *AMS Conference on Math Challenges of the 21st Century*.
URL http://www-stat.stanford.edu/~donoho/Lectures/CBMS/Curses.pdf

Draper, N.R. et Guttman, I., 1992. Treating bias as variance for experimental design purposes. *Ann. Inst. Statist. Math*, 44:659–671.

Druguet, Marie-Claude, Candler, Graham V. et Nompelis, Ioannis, 2005. Effects of numerics on navier-stokes computations of hypersonic double-cone flows. *AIAA Journal*, 43(3):616–623.

Dubourg, Vincent, 2011. *Adaptive surrogate models for reliability analysis and reliability-based design optimization*. Thèse de doctorat, Université Blaise Pascal, Clermont-Ferrand.

Dutta, S. et Braun, R. D., 2014. Statistical entry, descent, and landing performance reconstruction of the mars science laboratory. *Journal of Spacecraft and Rockets*, 51(4):1048 – 1061.

Dutta, S., Braun, R. D. et Karlgaard, C. D., 2014. Uncertainty quantification for mars entry, descent, and landing reconstruction using adaptive filtering. *Journal of Spacecraft and Rockets*, 51(3):967–977.

Dutta, Soumyo, Braun, Robert D., Russell, Ryan P., Striepe, Scott A. et Clark, Ian G., 2013. Comparison of statistical estimation techniques for mars entry, descent, and landing reconstruction. *Journal of Spacecraft and Rockets*, 50(6):1207–1221.

DUVENAUD, D., 2014. *Automatic model construction with Gaussian processes*. Thèse de doctorat, University of Cambridge.

DUVENAUD, David K., NICKISCH, Hannes et RASMUSSEN, Carl E., 2011. Additive gaussian processes. Dans J. Shawe-Taylor, R. S. Zemel, P. L. Bartlett, F. Pereira et K. Q. Weinberger, rédacteurs, *Advances in Neural Information Processing Systems 24*, pages 226–234. Curran Associates, Inc. URL http://papers.nips.cc/paper/4221-additive-gaussian-processes.pdf

ENZIAN, A., DEVEZEAUX, D., MOHAMED, A., THIVET, F., TRAN, P. et TRIBOT, J.-P., 2002. Flight experiments to address unsolved aerothermodynamic issues for a future european reusable space launcher. Rapport technique ESA SP-487, ESA.

EULER, E.A., ADAMS, G.L. et HOPPER, F.W., 1978. Design and reconstruction of the viking lander descent trajectories. *Journal of Guidance, Control, and Dynamics*, 1(5):372–378.

FALCHI, Alessandro, MINISCI, Edmondo, VASILE, Massimiliano et KUBICEK, Martin, 2017. Aero-thermal re-entry sensitivity analysis using DSMC and a high dimensional model representation-based approach. Dans *7th European Conference on Space Debris, Darmstadt, Germany*.

FERSON, Scott, OBERKAMPF, William L. et GINZBURG, Lev, 2008. Model validation and predictive capability for the thermal challenge problem. *Computer Methods in Applied Mechanics and Engineering*, 197(29):2408 – 2430. doi: https://doi.org/10.1016/j.cma.2007.07.030. Validation Challenge Workshop.

FISHMAN, G. S., 1996. *Monte Carlo: Concepts, Algorithms, and Applications*. Springer.

FRAUHOLZ, Sarah, BEHR, Marek, REINARTZ, Birgit et MÜLLER, Siegfried, 2012. Numerical simulation of hypersonic air intake flow in scramjet propulsion using a mesh-adaptive approach. Dans *18th AIAA/3AF International Space Planes and Hypersonic Systems and Technologies Conference*. American Institute of Aeronautics and Astronautics.

GARUD, Sushant S., KARIMI, Iftekhar A. et KRAFT, Markus, 2017. Design of computer experiments: A review. *Computers & Chemical Engineering*, 106(Supplement C):71 – 95. ESCAPE-26.

GELMAN, J. B., CARLIN, A., STERN, H.S. et RUBIN, D.B., 2003. *Bayesian data analysis*. Chapman and Hall/CRC.

GERACI, Gianluca, 2013. *Schemes and Strategies to Propagate and Analyze Uncertainties in Computational Fluid Dynamics Applications*. Thèse de doctorat, Université Sciences et Technologies - Bordeaux I.

GERACI, Gianluca, CONGEDO, Pietro Marco, ABGRALL, Rémi et IACCARINO, Gianluca, 2016. A novel weakly-intrusive non-linear multiresolution framework for uncertainty quantification in hyperbolic partial differential equations. *Journal of Scientific Computing*, 66(1):358–405.

GHANEM, R.G. et SPANOS, S. D., 1991. *Stochastic Finite Elements: A Spectral Approach*. Springer Verlag.

GILKS, W. R., RICHARDSON, S. et SPIEGELHALTER, D. J., 1996. *Markov Chain Monte Carlo in practice*. Chapman & Hall/CRC Interdisciplinary Statistics.

GLIMM, J et SHARP, D.H, 1999. Prediction and the quantification of uncertainty. *Physica D: Nonlinear Phenomena*, 133(1):152 – 170. doi: https://doi.org/10.1016/S0167-2789(99)00103-7.

GNOFFO, P.A., GUPTA, R.N. et SHINN, J.L., 1989. Conservation equations and physical models for hypersonic air flows in thermal and chemical nonequilibrium. Rapport technique NASA-TP-2867, NASA Langley Research Center.
URL https://ntrs.nasa.gov/archive/nasa/casi.ntrs.nasa.gov/19890006744.pdf

GNOFFO, Peter, JOHNSTON, Christopher et THOMPSON, Richard, 2009. Implementation of radiation, ablation, and free energy minimization modules for coupled simulations of hypersonic flow. Dans *47th AIAA Aerospace Sciences Meeting including The New Horizons Forum and Aerospace Exposition*, Aerospace Sciences Meetings. American Institute of Aeronautics and Astronautics.

GNOFFO, Peter A., 1999. Planetary-entry gas dynamics. *Annual Review of Fluid Mechanics*, 31(1):459–494. doi: 10.1146/annurev.fluid.31.1.459.

GOEL, T., HAFKTA, R. T. et SHYY, W., 2009. Comparing error estimation measures for polynomial and kriging approximation of noise-free functions. *Structural and multidisciplinary optimization*, **38**:429 – 442.

GRAMACY, Robert B. et LEE, Herbert K. H., 2012. Cases for the nugget in modeling computer experiments. *Statistics and Computing*, 22(3):713–722. doi: 10.1007/s11222-010-9224-x.
URL https://doi.org/10.1007/s11222-010-9224-x

GRIEWANK, Andreas et WALTHER, Andrea, 2008. *Evaluating Derivatives: Principles and Techniques of Algorithmic Differentiation*. SIAM, Philadelphia.
URL https://doi.org/10.1137/1.9780898717761

HAMMERSLEY, J.M. et HANDSCOMB, D.C., 1964. *Monte Carlo Methods*. Fletcher & Son Ltd.

HARTMANN, Ralf et HOUSTON, Paul, 2002. Adaptive discontinuous galerkin finite element methods for the compressible euler equations. *Journal of Computational Physics*, 183(2):508 – 532.

HASTIE, T., TIBSHIRANI, R. et FRIEDMAN, J., 2009. *The elements of statistical learning: data mining, inference and prediction*. Statistics, Springer.

HASTINGS, W. K., 1970. Monte carlo sampling methods using markov chains and their applications. *Biometrika*, 57(1):97–109.

HÄUSER, J., DAI, W., KOPPENWALLNER, G. et MUYLAERT, J., 2004. Inverse problem solution for determining spacecraft orientation from pressure measurements. *Proceedings of the Fifth European Symposium on Aerothermodynamics for Space Vehicles*, ESA SP-563:1 – 30.

HELTON, J.C. et DAVIS, F.J., 2003. Latin hypercube sampling and the propagation of uncertainty in analyses of complex systems. *Reliability Engineering & System Safety*, 81(1):23 – 69. doi: http://dx.doi.org/10.1016/S0951-8320(03)00058-9.
URL http://www.sciencedirect.com/science/article/pii/S0951832003000589

HIRSCH, C., 1990. *Numerical Computation of Internal and External Flows*, tome vol. 2. John Wiley & Sons.

HOMMA, T. et SALTELLI, A., 1996. Importance measures in global sensitivity analysis of nonlinear models. *Reliability Engineering and System Safety*, 52(1):1–17.

HOSDER, Serhat, WALTERS, Robert et PEREZ, Rafael, 2006. A non-intrusive polynomial chaos method for uncertainty propagation in cfd simulations. Dans *44th AIAA Aerospace Sciences Meeting and Exhibit*. American Institute of Aeronautics and Astronautics.

HU, Xingzhi, PARKS, Geoffrey T., CHEN, Xiaoqian et SESHADRI, Pranay, 2016. Discovering a one-dimensional active subspace to quantify multidisciplinary uncertainty in satellite system design. *Advances in Space Research*, 57(5):1268–1279.
URL https://doi.org/10.1016/j.asr.2015.11.001

HUBER, Peter J., 1985. Projection pursuit. *The Annals of Statistics*, 13(2):435–475.

IACCARINO, Gianluca, 2014. Uncertainty quantification in computational science. Dans *STO-AVT-VKI Lecture Series 2013/2014 - AVT 235*, Lecture Series on Uncertainty Quantification in computational fluid dynamics. Von Karman Institute for Fluid Dynamics.

IOOSS, Bertrand, DORPE, François Van et DEVICTOR, Nicolas, 2006. Response surfaces and sensitivity analyses for an environmental model of dose calculations. *Reliability Engineering & System Safety*, 91(10):1241 – 1251. doi: https://doi.org/10.1016/j.ress.2005.11.021. The Fourth International Conference on Sensitivity Analysis of Model Output (SAMO 2004).
URL http://www.sciencedirect.com/science/article/pii/S0951832005002334

IOOSS, Bertrand et LEMAÎTRE, Paul, 2015. *A Review on Global Sensitivity Analysis Methods*, pages 101–122. Springer US, Boston, MA. ISBN 978-1-4899-7547-8. doi: 10.1007/978-1-4899-7547-8_5.
URL https://doi.org/10.1007/978-1-4899-7547-8_5

ISECG, 2013. Benefits stemming from space exploration. Rapport technique, NASA.

JEFFERSON, J. L., GILBERT, J. M., CONSTANTINE, P. G. et MAXWELL, R. M., 2015. Active subspaces for sensitivity analysis and dimension reduction of an integrated hydrologic model. *Computers & Geosciences*, 83:127–138.
URL https://doi.org/10.1016/j.cageo.2015.07.001

JIN, R., CHEN, W. et SUDJIANTO, A., 2002. On sequential sampling for global metamodeling in engineering design. tome 2, pages 539–548.

JONES, D.R, 2001. A taxonomy of global optimization methods based on response surfaces. *Journal of Global Optimization*, 21:345 – 383.

JONES, D.R, SCHONLAU, M. et WELCH, W. J., 1998. Efficient global optimization of expensive black-box functions. *Journal of Global Optimization*, 13:455 – 492.

JONES, L. M., PETERSON, J. W., SCHAEFER, E. J. et SCHULTE, H. F., 1959. Upper-air density and temperature: some variations and an abrupt warming in the mesosphere. *Journal of Geophysical Research*, 64(12):2331–2340. doi: 10.1029/JZ064i012p02331.
URL http://dx.doi.org/10.1029/JZ064i012p02331

Joseph, V. Roshan, Hung, Ying et Sudjianto, Agus, 2008. Blind Kriging: A new method for developing metamodels. *ASME Journal of Mechanical Design*, (130).

Kaipio, J. et Somersalo, E., 2005. *Statistical and computational inverse problems*, tome 160 de *Applied Mathematical Sciences*. Springer.

Karl, Sebastian, Schramm, Jan Martinez et Hannemann, Klaus, 2003. High enthalpy cylinder flow in HEG: A basis for CFD validation. Dans *33rd AIAA Fluid Dynamics Conference and Exhibit*, Fluid Dynamics and Co-located Conferences. American Institute of Aeronautics and Astronautics.

Karlgaard, Christopher D., Kutty, Prasad, Schoenenberger, Mark, Munk, Michelle M., Little, Alan, Kuhl, Christopher A. et Shidner, Jeremy, 2014a. Mars science laboratory entry atmospheric data system trajectory and atmosphere reconstruction. *Journal of Spacecraft and Rockets*, 51(4).

Karlgaard, Christopher D., Norman, John Van, , Siemers, Paul M., Schoenenberger, Mark et Munk, Michelle M., 2014b. Mars entry atmospheric data system modeling, calibration, and error analysis. Rapport technique NASA/TM–2014–218535, NASA Langley Research Center.

Kawai, Soshi et Shimoyama, Koji, 2014. Kriging-model-based uncertainty quantification in computational fluid dynamics. Dans *32nd AIAA Applied Aerodynamics Conference*. American Institute of Aeronautics and Astronautics.

Kazeminejad, Bobby, Atkinson, David H., Pérez-Ayúcar, Miguel, Lebreton, Jean-Pierre et Sollazzo, Claudio, 2007. Huygens' entry and descent through titan's atmosphere—methodology and results of the trajectory reconstruction. *Planetary and Space Science*, 55:1845–1876.

Kersaudy, P., Sudret, B., Varsier, N., Picon, O. et Wiart, J., 2015. A new surrogate modeling technique combining Kriging and polynomial chaos expansions - Application to uncertain analysis in computational dosimetry. *Journal of Computational Physics*, 286:103 – 117.

Knight, Doyle, Chazot, Olivier, Austin, Joanna, Badr, Mohammad Ali, Candler, Graham, Celik, Bayram, de Rosa, Donato, Donelli, Raffaele, Komives, Jeffrey, Lani, Andrea, Levin, Deborah, Nompelis, Ioannis, Panesi, Marco, Pezzella, Giuseppe, Reimann, Bodo, Tumuklu, Ozgur et Yuceil, Kemal, 2017. Assessment of predictive capabilities for aerodynamic heating in hypersonic flow. *Progress in Aerospace Sciences*, 90(Supplement C):39 – 53. doi: https://doi.org/10.1016/j.paerosci.2017.02.001.

KNIGHT, Doyle, LONGO, José, DRIKAKIS, Dimitris, GAITONDE, Datta, LANI, Andrea, NOMPELIS, Ioannis, REIMANN, Bodo et WALPOT, Louis, 2012. Assessment of CFD capability for prediction of hypersonic shock interactions. *Progress in Aerospace Sciences*, 48 - 49:8 – 26.

KOEHLER, J.R. et OWEN, A.B., 1996. 9 computer experiments. Dans *Design and Analysis of Experiments*, tome 13 de *Handbook of Statistics*, pages 261 – 308. Elsevier.

KOPPENWALLNER, G., 2003. Definition of requirements and operational specifications for fads. *Technical note WP1: Flush and Laser Air Data System*, HTG TN-03-6.

KOPPENWALLNER, G., 2007. Controlled hypersonic flight air data system and flight instrumentation. *Flight Experiments for Hypersonic Vehicle Development,*, Educational Notes RTO-EN-AVT-130(17):1 – 30.

KRIGE, Daniel G., 1951. A Statistical Approach to Some Basic Mine Valuation Problems on the Witwatersrand. *Journal of the Chemical, Metallurgical and Mining Society of South Africa*, 52(6):119–139.
URL http://dx.doi.org/10.2307/3006914

KUTTY, Prasad M., 2014. *RECONSTRUCTION AND UNCERTAINTY QUANTIFICATION OF ENTRY, DESCENT AND LANDING TRAJECTORIES USING VEHICLE AERODYNAMICS*. Thèse de maître, Georgia Institute of Technology.

LACHAUD, J., MARTIN, A., COZMUTA, I., et LAUB, B., 2010. Ablation testcase series 1. Dans *4th AFOSR/SNL/NASA Ablation Workshop*.

LACHAUD, Jean, MAGIN, Thierry E., COZMUTA, Ioana et MANSOUR, Nagi N., 2011. A short review of ablative-material response models and simulation tools. Dans *7th aerothermodynamics symposium; 9-12 May 2011; Brugge Belgium*.

LACHAUD, Jean et MANSOUR, Nagi N., 2014. Porous-material analysis toolbox based on openfoam and applications. *Journal of Thermophysics and Heat Transfer*, 28(2):191–202.

LARSON, Terry J., WHITMORE, Stephen A., EHERNBERGER, L. J., JOHNSON, J. Blair et SIEMERS, Paul M. III, 1987. Qualitative evaluation of a flush air data system at transonic speeds and high angles of attack. Rapport technique NASA-TP-2716, NASA.

LE MAÎTRE, O. P. et KNIO, O. M., 2010. *Spectral Methods for Uncertainty Quantification: With Applications to Computational Fluid Dynamics*. Springer.

Le Maître, Olivier P, Knio, Omar M, Najm, Habib N et Ghanem, Roger G, 2001. A stochastic projection method for fluid flow. *Journal of Computational Physics*, 173(2):481 – 511.

LeVeque, Randall J, 2002. *Finite volume methods for hyperbolic problems*, tome 31. Cambridge university press.

Li, Ker-Chau et Duan, Naihua, 1989. Regression analysis under link violation. *The Annals of Statistics*, 17(3):pp. 1009–1052.
URL http://www.jstor.org/stable/2241708

Liu, Haitao, Ong, Yew-Soon et Cai, Jianfei, 2017. A survey of adaptive sampling for global metamodeling in support of simulation-based complex engineering design. *Structural and Multidisciplinary Optimization*.

Lockwood, B. A., ???? http://w3.uwyo.edu/~blockwoo/ForKlib/index.html.

Lockwood, Brian et Mavriplis, Dimitri, 2013. Gradient-based methods for uncertainty quantification in hypersonic flows. *Computers & Fluids*, (85):27 – 38.

Loehle, Stefan, 2016. Review of heat flux measurements for high enthalpy flows. Dans *32nd AIAA Aerodynamic Measurement Technology and Ground Testing Conference*. American Institute of Aeronautics and Astronautics.

Loeppky, Jason L., Moore, Leslie M. et Williams, Brian J., 2010. Batch sequential designs for computer experiments. *Journal of Statistical Planning and Inference*, 140(6):1452 – 1464.

Longo, J. M. A., 2004. Modelling of hypersonic flow phenomena. Dans *Critical Technologies for Hypersonic Vehicle Development Technology*, RTO-EN-AVT-116.

Lophaven, S. N., Nielsen, H. B. et Søndergaard, J., 2002. DACE: a MATLAB kriging toolbox, version 2.0. Rapport technique, Technical University of Denmark.

Lucor, Didier, 2011. *Stochastic Spectral Approach to Uncertainty Quantification of Computational Fluid Dynamics*. Habilitation à diriger des recherches, Université Pierre et Marie Curie.

Lukaczyk, Trent W., Constantine, Paul, Palacios, Francisco et Alonso, Juan J., 2014. Active subspaces for shape optimization. Dans *10th AIAA Multidisciplinary Design Optimization Conference*, AIAA SciTech Forum. American Institute of Aeronautics and Astronautics. doi: doi:10.2514/6.2014-1171.
URL https://doi.org/10.2514/6.2014-1171

LYNCH, Scott M., 2007. *Introduction to Applied Bayesian Statistics and Estimation for Social Scientists*. Springer.

MAGIN, T. E., CAILLAULT, L., BOURDON, A., et LAUX, C. O., 2006a. Nonequilibrium radiative heat flux modelling for the huygens entry probe. *Journal of Geophysical Research*, 111.

MAGIN, T. E., CAILLAULT, L., BOURDON, A. et LAUX, C. O., 2006b. Nonequilibrium radiative heat flux modeling for the huygens entry probe. *Journal of Geophysical Research: Planets*, 111(E7). E07S12.

MARGHERI, Luca et SAGAUT, Pierre, 2016. A hybrid anchored-ANOVA – POD/kriging method for uncertainty quantification in unsteady high-fidelity CFD simulations. *Journal of Computational Physics*, 324:137 – 173.

MARREL, Amandine, IOOSS, Bertrand, LAURENT, Béatrice et ROUSTANT, Olivier, 2009. Calculations of sobol indices for the gaussian process metamodel. *Reliability Engineering & System Safety*, 94(3):742 – 751. doi: http://dx.doi.org/10.1016/j.ress.2008.07.008.

MARREL, Amandine, IOOSS, Bertrand, VAN DORPE, Francois et VOLKOVA, Elena, 2008. An efficient methodology for modeling complex computer codes with Gaussian processes. *Computational Statistics and Data Analysis*, 52:4731–4744. doi: 10.1016/j.csda.2008.03.026.
URL https://hal.archives-ouvertes.fr/hal-00239492

MARSEGUERRA, Marzio, MASINI, Riccardo, ZIO, Enrico et COJAZZI, Giacomo, 2003. Variance decomposition-based sensitivity analysis via neural networks. *Reliability Engineering & System Safety*, 79(2):229 – 238. doi: https://doi.org/10.1016/S0951-8320(02)00234-X. SAMO 2001: Methodological advances and innovative applications of sensitivity analysis.
URL http://www.sciencedirect.com/science/article/pii/S095183200200234X

MARZOUK, Youssef M. et NAJM, Habib N., 2009. Dimensionality reduction and polynomial chaos acceleration of bayesian inference in inverse problems. *Journal of Computational Physics*, 228(6):1862 – 1902. doi: https://doi.org/10.1016/j.jcp.2008.11.024.
URL http://www.sciencedirect.com/science/article/pii/S0021999108006062

MARZOUK, Youssef M., NAJM, Habib N. et RAHN, Larry A., 2007. Stochastic spectral methods for efficient bayesian solution of inverse problems. *J. Comput. Physics*, 224:560–586.

MATHERON, G., 1971. *The theory of regionalised variables and its applications*. Thèse de doctorat, École Nationale Supérieure des Mines.

MAYER, J. E. et MAYER, M. G., 1946. *Statistical Mechanics*. John Wiley & Sons.

MCKAY, M. D., BECKMAN, R. J. et CONOVER, W. J., 1979. A comparison of three methods for selecting values of input variables in the analysis of output from a computer code. *Technometrics*, 21(2):239 – 245.

MECKESHEIMER, M., BARTON, R. R., SIMPSON, T. W. et BOOKER, A., 2002. Computationally inexpensive metamodel assessment strategies. *AIAA Journal*, **40**(10):2053 – 2060.

MEHTA, Piyush M., KUBICEK, Martin, MINISCI, Edmondo et VASILE, Massimiliano, 2016a. Debris re-entry modeling using high dimensional derivative based uncertainty quantification. Dans *Astrodynamics 2015*, Advances in Astronautical Sciences. American Astronautical Society.

MEHTA, Piyush M., KUBICEK, Martin, MINISCI, Edmondo et VASILE, Massimiliano, 2016b. Surrogate model for probabilistic modeling of atmospheric entry for small neo's. pages 1807–1822.

MEHTA, Piyush M., KUBICEK, Martin, MINISCI, Edmondo et VASILE, Massimiliano, 2017. Sensitivity analysis and probabilistic re-entry modeling for debris using high dimensional model representation based uncertainty treatment. *Advances in Space Research*, 59(1):193 – 211. doi: https://doi.org/10.1016/j.asr.2016.08.032.

MIKI, Kenji, PANESI, Marco et PRUDHOMME, Serge, 2015. Systematic validation of non-equilibrium thermochemical models using bayesian inference. *Journal of Computational Physics*, 298(Supplement C):125 – 144. doi: https://doi.org/10.1016/j.jcp.2015.05.011.

MORRIS, Max D., 1991. Factorial sampling plans for preliminary computational experiments. *Technometrics*, 33(2):161–174.
URL http://www.jstor.org/stable/1269043

MOYER, C. B. et RINDAL, R. A., 1968. An Analysis of the Coupled Chemically Reacting Boundary Layer and Charring Ablator: Part II. Rapport technique NASA 1061, NASA manned spacecraft center.

MÜLLER-EIGNER, R. et KOPPENWALLNER, G., 2001. RAFLEX-an air data system for re-entry vehicles. *Fourth European Symposium on Aerothermodynamics for Space Vehicles*, ESA SP-487.

Müller-Eigner, R., Koppenwallner, G. et Fritsche, B., 1999. Pressure and heat flux measurement with RAFLEX II during MIRKA re-entry. *Third European Symposium on Aerothermodynamics for Space Vehicles*, ESA SP-426:685 – 694.

Muylaert, J., Walpot, L., Ottens, H. et Cipollini, F., 2007. Aerothermodynamic reentry flight experiments EXPERT. Rapport technique RTO-EN-AVT-130, NATO OTAN.

NASA, 2012. Mars Science Laboratory - Mission Timeline: Entry, Descent and Landing. https://www.nasa.gov/audience/forstudents/nasaandyou/home/edl_bkgd_en.html.

Neal, R.M., 1997. Monte carlo implementation of gaussian process models for bayesian regression and classification. Rapport technique Tech. Rep. 9702, Department of statistics, University of Toronto, Toronto, Ontario, Canada.

Oberkampf, William L. et Roy, Christopher J., 2010. *Verification and Validation in Scientific Computing*. Cambridge University Press.

Onofri, M., Paciorri, R., Cardillo, D., Grottadaurea, M. et Bonfiglioli, A., 2011. Numerical simulations of flows past ixv re-entry vehicle at cras. Dans *3rd International ARA days*.

Osher, S. et Solomon, F., 1982. Upwind Difference Schemes for Hyperbolic Systems of Conservation Laws. *Mathematics of Computation*, 38(158):339–374.

Paciorri, Renato et Bonfiglioli, Aldo, 2009. A shock-fitting technique for 2d unstructured grids. *Computers & Fluids*, 38(3):715 – 726. doi: http://dx.doi.org/10.1016/j.compfluid.2008.07.007.
URL http://www.sciencedirect.com/science/article/pii/S0045793008001503

Pandolfi, Maurizio et D'Ambrosio, Domenic, 2001. Numerical instabilities in upwind methods: Analysis and cures for the carbuncle phenomenon. *Journal of Computational Physics*, 166(2):271 – 301. doi: http://dx.doi.org/10.1006/jcph.2000.6652.
URL http://www.sciencedirect.com/science/article/pii/S002199910096652X

Panesi, M., Miki, K., Prudhomme, S. et Brandis, A., 2012. On the assessment of a bayesian validation methodology for data reduction models relevant to shock tube experiments. *Computer Methods in Applied Mechanics and Engineering*, 213-216(Supplement C):383 – 398. doi: https://doi.org/10.1016/j.cma.2011.11.001.

PANESI, Marco, MIKI, Kenji, PRUDENCIO, Ernesto, SCHULZ, K. et PRUDHOMME, Serge, 2011. Calibration of rates parameters for multi-temperature models using bayesian formulation. Dans *42nd AIAA Thermophysics Conference*. American Institute of Aeronautics and Astronautics.

PARK, C., JAFFE, R. et PARTRIDGE, H., 2001. Chemical-kinetic parameters of hyperbolic earth entry. *Journal of Thermophysics and Heat Transfer*, **15**(1):76 – 90.

PARK, Chul, HOWE, John T., JAFFE, Richard L., et CANDLER, Graham V., 1994. Review of chemical-kinetic problems of future NASA missions. II - Mars entries. *Journal of Thermophysics and Heat Transfer*, 8(1):9–23.

PARK, Jeong-Soo, 1994. Optimal latin-hypercube designs for computer experiments. *Journal of Statistical Planning and Inference*, 39(1):95 – 111.

PEDREGOSA, F., VAROQUAUX, G., GRAMFORT, A., MICHEL, V., THIRION, B., GRISEL, O., BLONDEL, M., PRETTENHOFER, P., WEISS, R., DUBOURG, V., VANDERPLAS, J., PASSOS, A., COURNAPEAU, D., BRUCHER, M., PERROT, M. et DUCHESNAY, E., 2011. Scikit-learn: Machine learning in Python. *Journal of Machine Learning Research*, 12:2825–2830.
URL http://www.jmlr.org/papers/volume12/pedregosa11a/pedregosa11a.pdf

PICHENY, V., 2009. *Improving accuracy and compensating for uncertainty in surrogate modeling*. Thèse de doctorat, École Nationale Supérieure des Mines.

POWELL, M. J. D., 1987. Algorithms for approximation. chapitre Radial Basis Functions for Multivariable Interpolation: A Review, pages 143–167. Clarendon Press, New York, NY, USA. ISBN 0-19-853612-7.
URL http://dl.acm.org/citation.cfm?id=48424.48433

PRUETT, C. D., WOLF, H., HECK, M. L. et P. M. SIEMERS III, 1983. Innovative air data system for the space shuttle orbiter. *Journal of Spacecraft and Rockets*, 20(1):61 – 69.

QUAN, Aaron, 2014. *Batch Sequencing Methods for Computer Experiments*. Thèse de doctorat, The Ohio State University.

QUEIPO, Nestor V., HAFTKA, Raphael T., SHYY, Wei, GOEL, Tushar, VAIDYANATHAN, Rajkumar et TUCKER, P. Kevin, 2005. Surrogate-based analysis and optimization. *Progress in Aerospace Sciences*, 41(1):1 – 28. doi: https://doi.org/10.1016/j.paerosci.2005.02.001.
URL http://www.sciencedirect.com/science/article/pii/S0376042105000102

Quirk, James J., 1994. A contribution to the great riemann solver debate. *International Journal for Numerical Methods in Fluids*, 18(6):555–574. doi: 10.1002/fld.1650180603.
URL http://dx.doi.org/10.1002/fld.1650180603

Raftery, Adrian et Lewis, Steven, 1970. The number of iterations, convergence diagnostics and generic metropolis algorithms.

Rahman, S., 2008. A polynomial dimensional decomposition for stochastic computing. *International Journal for Numerical Methods in Engineering*, 76:2191 – 2116.

Ramshaw, J. D., 1990. Self-consistent effective binary diffusion in multicomponent gas mixtures. *Journal of Non-Equilibrium Thermodynamics*, 15:295–300. doi: 10.1515/jnet.1990.15.3.295.

Rasmussen, C. E. et Williams, C. K. I., 2006. *Gaussian processes for machine learning*. The MIT Press.

Ratti, F., Gavira, J., Thirkettle, A. C., Thoemel, J. et Ritter, H., ???? Instrumentation on board the european experimental re-entry test bed expert. ESA-ESTEC.

Reagan, Matthew T., Najm, Habib N., Ghanem, Roger G. et Knio, Omar M., 2003. Uncertainty quantification in reacting-flow simulations through non-intrusive spectral projection. *Combustion and Flame*, 132(3):545 – 555. doi: http://dx.doi.org/10.1016/S0010-2180(02)00503-5.
URL http://www.sciencedirect.com/science/article/pii/S0010218002005035

Roy, C. J. et Oberkampf, W. L., 2011. A comprehensive framework for verification, validation and uncertainty quantification in science computing. *Comput. Methods Appl. Mech. Engrg.*, **200**:2131 – 2144.

Sacks, J., Schiller, S. B. et J., Welch W., 1989a. Designs for computer experiments. *Technometrics*, 31(1):41–47.

Sacks, J., Welch, W. J., Mitchell, T. J. et Wynn, H. P., 1989b. Design and analysis of computer experiments. *Statistical sciences*, **4**(4):409 – 435.

Salehi, Saeed, Raisee, Mehrdad, Cervantes, Michel J. et Nourbakhsh, Ahmad, 2017. Efficient uncertainty quantification of stochastic cfd problems using sparse polynomial chaos and compressed sensing. *Computers & Fluids*, 154(Supplement C):296 – 321. ICCFD8.

SALTELLI, Andrea, RATTO, Marco, ANDRES, Terry, CAMPOLONGO, Francesca, CARIBONI, Jessica, GATELLI, Debora, SAISANA, Michaela et TARANTOLA, Stefano, 2008. *Global Sensitivity Analysis. The Primer*. John Wiley & Sons, Inc., Hoboken.

SAMY, Ihab, POSTLETHWAITE, Ian, GU, Da-Wei et GREEN, John, 2010. Neural-network-based flush air data sensing system demonstrated on a mini air vehicle. *Journal of Aircraft*, 47(1).

SANSON, Francois, MAGIN, Thierry E., PANERAI, Francesco et CONGEDO, Pietro Marco, 2016. Bayesian Reconstruction of Catalytic Properties of Thermal Protection Materials for Atmospheric Reentry. Dans *SIAM UQ*. Lausanne, Switzerland.

SANSON, François, BOUILLY, Jean-Marc et CONGEDO, Pietro M., 2017a. Uncertainty quantification in orbital debris reentry for reliable ground footprint estimation. Dans *7th European Conference on Space Debris, Darmstadt, Germany*.

SANSON, François, VILLEDIEU, Nadège, PANERAI, Francesco, CHAZOT, Olivier, CONGEDO, Pietro M. et MAGIN, Thierry E., 2017b. Quantification of uncertainty on the catalytic property of reusable thermal protection materials from high enthalpy experiments. *Experimental Thermal and Fluid Science*, 82:414 – 423.

SANTNER, Thomas J., WILLIAMS, Brian J. et NOTZ, William I., 2003. *The Design and Analysis of Computer Experiments*. Springer-Verlag New York.

SARMA, G.S.R., 2000. Physico–chemical modelling in hypersonic flow simulation. *Progress in Aerospace Sciences*, 36(3):281 – 349.

SAUNDERS, David, YOON, Seokkwan et WRIGHT, Michael, 2007. An approach to shock envelope grid tailoring and its effect on reentry vehicle solutions. Dans *45th AIAA Aerospace Sciences Meeting and Exhibit*. American Institute of Aeronautics and Astronautics.

SEIFF, A., 1991. Atmospheres of earth, mars, and venus, as defined by entry probe experiments. *Journal of Spacecraft and Rockets*, 28(3):265–275.

SEIFF, A. et REESE, D. E. Jr., 1965. Use of entry vehicle responses to define the properties of the mars atmosphere. Rapport technique, NASA Ames Research Center.

SERMEUS, Kurt, 2013. *Multi-Dimensional Upwind Discretization and Application to Compressible Flows*. Thèse de doctorat, Von Karman Institute for Fluid Dynamics.

SHAFER, Glenn, 1976. *A mathematical theory of evidence*. Princeton Univ. Press.

SHAGHAGHI, Azam et ANTONAKOPOULOS, Konstantinos, 2012. The societal impacts of a mars mission in the future of space exploration. *Physics Procedia*, 38(Supplement C):176 – 185.

SHEWRY, M. C. et WYNN, H. P., 1987. Maximum entropy sampling. *Journal of Applied Statistics*, 14(2):165–170.

SILVERMAN, Bernard W, 1986. *Density estimation for statistics and data analysis*, tome 26. CRC press.

SIMPSON, T.W., POPLINSKI, J.D., KOCH, P. N. et ALLEN, J.K., 2001. Metamodels for computer-based engineering design: Survey and recommendations. *Engineering with Computers*, 17(2):129–150.

SINHA, Krishnendu, 2010. Computational fluid dynamics in hypersonic aerothermodynamics. *Defence Science Journal*, 60(6):663–671.

SINHA, Krishnendu et REDDY, D. Siva K., 2011. Effect of chemical reaction rates on aeroheating predictions of reentry flows. *Journal of Thermophysics and Heat Transfer*, 25(1):21–33.

SMOLYAK, S. A., 1963. Quadrature and interpolation formulas for tensor products of certain classes of functions. *Soviet Mathematics Doklady*, 4:240–243.

SOBOL', I. M., 1993. Sensitivity estimates for nonlinear mathematical models. *Mathematical modelling & Computational Experiments*, 1:407–414.

SOBOL', I. M., 2001. Global sensitivity indices for nonlinear mathematical models and their Monte Carlo estimates. *Mathematics and Computers in Simulations*, 55:271–280.

SOBOL', I. M. et MYSHETSKAYA, E. E., 2008. Monte carlo estimators for small sensitivity indices. *Monte Carlo Methods and Applications*, 13.

SOBOL', I.M, 1967. On the distribution of points in a cube and the approximate evaluation of integrals. *USSR Computational Mathematics and Mathematical Physics*, 7(4):86 – 112.

SPENCER, David A., BLANCHARD, Robert C., BRAUN, Robert D., KALLEMEYN, Pieter H. et THURMAN, Sam W., 1999. Mars pathfinder entry, descent, and landing reconstruction. *Journal of Spacecraft and Rockets*, 36(3):357–366.

SRIVASTAVA, Ankur et MEADE, Andrew J., 2015. A comprehensive probabilistic framework to learn air data from surface pressure measurements. *International Journal of Aerospace Engineering*, 2015.

SRIVASTAVA, Ankur, MEADE, Andrew J. et LONG, Kurtis R., 2012. Learning air-data parameters for flush air data sensing systems. *Journal of Aerospace Computing, Information, and Communication*, 9(3):110–124.

STEIN, Michael, 1987. Large sample properties of simulations using latin hypercube sampling. *Technometrics*, 29(2):143–151.
URL http://www.jstor.org/stable/1269769

STERN, F., WILSON, R. V., COLEMAN, H. W. et PATERSON, E. G., 2001. Comprehensive Approach to Verification and Validation of CFD Simulations—Part 1: Methodology and Procedures. *ASME. J. Fluids Eng.*, 123(4).

STUART, A. M., 2010. Inverse problems: A bayesian perspective. *Acta Numerica*, 19:451–559.

SUDRET, Bruno, 2008. Global sensitivity analysis using polynomial chaos expansions. *Reliability Engineering & System Safety*, 93(7):964 – 979. doi: http://dx.doi.org/10.1016/j.ress.2007.04.002. Bayesian Networks in Dependability.
URL http://www.sciencedirect.com/science/article/pii/S0951832007001329

SUN, M. et TAKAYAMA, K., 2003. An artificially upstream flux vector splitting scheme for the euler equations. *Journal of Computational Physics*, 189(1):305 – 329. doi: http://dx.doi.org/10.1016/S0021-9991(03)00212-2.
URL http://www.sciencedirect.com/science/article/pii/S0021999103002122

SUTTON, K. et GRAVES, R. A., Jr., 1971. A general stagnation-point convective heating equation for arbitrary gas mixtures. Rapport technique NASA-TR-R-376, L-7885, NASA.

TALAY, T. A., WHITE, N. H. et NAFTEL, J. C., 1985. Impact of atmospheric uncertainties and viscous interaction effects on the performance of aeroassisted orbital transfer vehicles. *Progress in Astronautics and Aeronautics*, 96:198–229. Thermal Design of Aeroassisted Orbital Transfer Vehicles.

TANG, K., CONGEDO, P. M. et ABGRALL, R., 2016. Adaptive surrogate modeling by ANOVA and sparse polynomial dimensional decomposition for global sensitivity analysis in fluid simulation. *Journal of Computational Physics*, 314:557–589.

Tarantola, A., 2005. *Inverse Problem Theory and Methods for Model Parameter Estimation*. Society for Industrial and Applied Mathematics. URL http://epubs.siam.org/doi/abs/10.1137/1.9780898717921

Thoemel, Jan, Muylaert, Jean-Marie, Ratti, Francesco et Gavira, José, 2009. In-flight testing of critical technologies and experimentation of aerothermodynamic phenomena. Dans *16th AIAA/DLR/DGLR International Space Planes and Hypersonic Systems and Technologies Conference*. American Institute of Aeronautics and Astronautics.

Tolson, R. H., Dwyer, A. M., Hanna, J. L., Keating, G. M., George, B. E., Escalera, P. E. et Werner, M. R., 2005. Application of accelerometer data to mars odyssey aerobraking and atmospheric modeling. *Journal of Spacecraft and Rockets*, 42(3):435–443. doi: https://doi.org/10.2514/1.15173.

Tolson, R. H., Keating, G. M., Zurek, R. W., Bougher, S. W., Justus, C. J. et Fritts, D. C., 2007. Application of accelerometer data to atmospheric modeling during mars aerobraking operations. *Journal of Spacecraft and Rockets*, 44(6):1172–1179.

Tolson, Robert H., Bemis, Eammon, Zaleski, Kristina, Keating, Gerald, Shidner, Jeremy D., Brown, Shaun, Brickler, Angela, Scher, Michael, Thomas, Paige et Hough, S., 2008. Atmospheric modeling using accelerometer data during mars reconnaissance orbiter aerobraking operations. *Journal of Spacecraft and Rockets*, 45(3):511–518.

Tripathy, Rohit, Bilionis, Ilias et Gonzalez, Marcial, 2016. Gaussian processes with built-in dimensionality reduction: Applications to high-dimensional uncertainty propagation. *Journal of Computational Physics*, 321(Supplement C):191 – 223.

Tryoen, J., Congedo, P. M., Abgrall, R., Villedieu, N. et Magin, T.E., 2014. Bayesian-based method with metamodels for rebuilding freestream conditions in atmospheric entry flows. *AIAA Journal*, **52**(10):2190 – 2197.

Van Albada, GD, Van Leer, Bram et Roberts Jr, WW, 1982. A comparative study of computational methods in cosmic gas dynamics. *Astronomy and Astrophysics*, 108:76–84.

Van Hove, B. et Karatekin, Ö., ???? Mars entry, descent, and landing reconstruction from flight data: uncertainty quantification.

Van Hove, B. et Karatekin, Ö., 2013. Mars atmosphere reconstruction using a flush air data system on the exomars entry, descent and landing demonstrator module. *10th International Planetary Probe Workshop*.

Van Hove, B. et Karatekin, Ö., 2017. Atmospheric reconstruction with stagnation pressure flight data from mars science laboratory. *Journal of Spacecraft and Rockets*, 54(3):609 – 620. doi: 10.2514/1.A33627.

Van Leer, B., 1979. Towards the ultimate conservative difference scheme. V. A second-order sequel to godunov's method. *Journal of Computational Physics*, 32(1):101–136.

Van Leer, Bram, 1977. Towards the ultimate conservative difference scheme. iv. a new approach to numerical convection. *Journal of Computational Physics*, 23(3):276 – 299. doi: http://dx.doi.org/10.1016/0021-9991(77)90095-X.
URL http://www.sciencedirect.com/science/article/pii/002199917790095X

Van Leer, Bram, 1982. *Flux-vector splitting for the Euler equations*, pages 507–512. Springer Berlin Heidelberg, Berlin, Heidelberg. ISBN 978-3-540-39532-4. doi: 10.1007/3-540-11948-5_66.
URL https://doi.org/10.1007/3-540-11948-5_66

Villedieu, N., Panerai, F., Chazot, O. et Magin, T.E., 2012. Uncertainty quantification for gas-surface interaction in plasmatron. Rapport technique, ESA.

Wan, Xiaoliang et Karniadakis, George Em, 2005. An adaptive multi-element generalized polynomial chaos method for stochastic differential equations. *Journal of Computational Physics*, 209(2):617 – 642. doi: https://doi.org/10.1016/j.jcp.2005.03.023.
URL http://www.sciencedirect.com/science/article/pii/S0021999105001919

Wang, G. G., 2003. Adaptive response surface method using inherited latin hypercube design points. *Journal of Mechanical Design*, 125:210 – 220.

Wang, Li et Mavriplis, Dimitri, 2009. Adjoint-based h-p adaptive discontinuous galerkin methods for the compressible euler equations. Dans *47th AIAA Aerospace Sciences Meeting including The New Horizons Forum and Aerospace Exposition*. American Institute of Aeronautics and Astronautics.

Wang, Xiaoyong, Yan, Chao, Ju, Shengjun, Zheng, Yongkang et Yu, Jian, 2017. Uncertainty analysis of laminar and turbulent aeroheating predictions for mars entry. *International Journal of Heat and Mass Transfer*, 112(Supplement C):533 – 543. doi: https://doi.org/10.1016/j.ijheatmasstransfer.2017.04.126.

West, Thomas K. IV et Hosder, Serhat, 2015. Uncertainty quantification of hypersonic reentry flows with sparse sampling and stochastic expansions. *Journal of Spacecraft and Rockets*, 52(1):120–133.

Whitmore, Stephen, Davis, Roy et Fife, John, 1995. In-flight demonstration of a real-time flush airdata sensing (rt-fads) system. Dans *20th Atmospheric Flight Mechanics Conference*. American Institute of Aeronautics and Astronautics.

Whitmore, Stephen A. et Ellsworth, Joel C., 2008. Simulation of a flush air-data system for transatmospheric vehicles. *Journal of Spacecraft and Rockets*, 45(4):716–732.

Withers, P. et Catling, D. C., 2010. Production of reduced data records for the phoenix atmospheric structure experiment. *NASA Planetary Data System*, PHX-M-ASE-5-EDL-RDR-V1.0.

Withers, Paul et Smith, Michael D., 2006. Atmospheric entry profiles from the mars exploration rovers spirit and opportunity. *Icarus*, 185(1):133 – 142. doi: https://doi.org/10.1016/j.icarus.2006.06.013.
URL http://www.sciencedirect.com/science/article/pii/S0019103506002302

Withers, Paul, Towner, M.C., Hathi, B. et Zarnecki, J.C., 2003. Analysis of entry accelerometer data: A case study of mars pathfinder. *Planetary and Space Science*, 51(9):541 – 561. doi: https://doi.org/10.1016/S0032-0633(03)00077-1.
URL http://www.sciencedirect.com/science/article/pii/S0032063303000771

Witteveen, J. A.S. et Iaccarino, G., 2012. Simplex stochastic collocation with random sampling and extrapolation for nonhypercube probability spaces. *SIAM J. Sci. Comput.*, 34(2):A814 – A838.

Witteveen, J. A.S. et Iaccarino, G., 2013. Simplex stochastic collocation with ENO-type stencil selection for robust uncertainty quantification. *Journal of Computational Physics*, 239:1 – 21.

Xiong, Ying, Chen, Wei, Apley, Daniel et Ding, Xuru, 2007. A non-stationary covariance-based kriging method for metamodelling in engineering design. *International Journal for Numerical Methods in Engineering*, 71(6):733–756. doi: 10.1002/nme.1969.
URL http://dx.doi.org/10.1002/nme.1969

Xiu, D. et Karniadakis, G. E., 2002. The wiener-askey polynomial chaos for stochastic differential equations. *SIAM J Sci Comput*, 24(2):619 – 644.

Xiu, Dongbin, 2009. Fast Numerical Methods for Stochastic Computations: A Review. *Communications in computational physics*, 5(2).

Xiu, Dongbin, 2010. *Numerical methods for stochastic computations: a spectral method approach*. Princeton university press.

Xiu, Dongbin et Hesthaven, Jan S., 2005. High-order collocation methods for differential equations with random inputs. *SIAM Journal on Scientific Computing*, 27(3):1118–1139.

Xiu, Dongbin, Lucor, Didier, Su, C. H. et Karniadakis, George Em, 2002. Stochastic modeling of flow-structure interactions using generalized polynomial chaos. *Journal of Fluids Engineering, Transactions of the ASME*, 124(1):51–59.

Xu, Shengli, Liu, Haitao, Wang, Xiaofang et Jiang, Xiaomo, 2014. A robust error-pursuing sequential sampling approach for global metamodeling based on voronoi diagram and cross validation. *Journal of Mechanical Design*, 136(7).

Yadav, Vaibhav et Rahman, Sharif, 2014. Adaptive-sparse polynomial dimensional decomposition methods for high-dimensional stochastic computing. *Computer Methods in Applied Mechanics and Engineering*, 274(Supplement C):56 – 83.

Zimmermann, H.-J., 1996. *Fuzzy set theory and its applications*. Kluwer Academic Publishers.

zur Nieden, P. et Olivier, H., 2007. Determination of atmospheric densities from reentry data flight data. *Journal of Spacecraft and Rockets*, **44**(2):332 – 337.

List of Figures

List of Tables

List of symbols

$\boldsymbol{a}(\mathbf{x})$	weights BLUP
A_r	pre-exponential Arrhenius factor
b	burn-in
$\boldsymbol{c}$	uncertain parameters
$\boldsymbol{c}(\mathbf{x}), C$	Correlation functions for Kriging
c_p, c_v	specific heats
C_i	expansion coefficients
C	uncentered covariance matrix of gradients
d	input dimensionality
$\boldsymbol{d}$, $\boldsymbol{D}$	measurements
D_T	active dimension PDD
D_{ij}	multicomponent diffusion coefficient
E	total energy per unit mass
e	internal energy
e_k	gradient-based edge error
$e_k^{(m)}$	surrogate-based edge error
$e_k^{(w)}$	weighted edge error
E_d	activation energy
$\mathbb{E}[\cdot]$	expectation
F	conserved fluxes
$f(\cdot)$,$F(\cdot)$	model
$\hat{f}(\cdot)$,$\hat{F}(\cdot)$	surrogate model
$\boldsymbol{f}_{obs}$	observations at training points
H	transport fluxes
h	enthalpy
$\mathbf{h}(\cdot)$, $H(\cdot)$	regression functions for Kriging
$\boldsymbol{J}$	diffusion flux
$k(\cdot,\cdot)$	covariance function
k	Boltzmann constant
$\underline{\underline{K}}$	permeability tensor
K_e	chemical equilibrium constant
k_f, k_b	forward and backward reaction rates
$\ell_{\mathbf{y}}(\cdot\|\cdot)$	likelihood function

M	molar mass
m	maximum PDD polynomial order
$\boldsymbol{m}$	inferred parameters
$m(\cdot)$	misfit function
n	number of basis functions
n_s	number of MC samples / number of sensors
N_a	number of additional training points
N_s	number of sampling points
N_{MCMC}	number of MCMC samples
p	pressure / threshold for truncated ANOVA
$\mathcal{Q}$	partition function
q	heat flux (intensity)
$\boldsymbol{q}$	heat flux vector
$q(\cdot,\cdot)$	proposal distribution for MCMC
Q^2	surrogate accuracy
R	specific gas constant
$\mathcal{R}$	universal gas constant
$\boldsymbol{S}$	source terms
S, S^{tot}	sensitivity indices
s	number of species
s_k^2	predictive variance
s_k	edge stretching
T	temperature
t	time
$\boldsymbol{U}$	vector of conserved variables
$\boldsymbol{u}$	average air mixture speed vector
$\boldsymbol{U}$	active directions
u	flow velocity
$\mathbf{x}, X$	input variables
$\boldsymbol{V}$	inactive directions
$\boldsymbol{W}$, $\mathbf{w}$	eigenvectors
x_i	molar fraction of the i-th species
$\mathbf{x}_{obs}$	observation points
$\mathbf{y}$	active variables
y, Y	model response
y_i	mass fraction of the i-th species
$\mathbf{z}$	inactive variables
$Z(\cdot)$	Gaussian process departure term
α	angle of attack / error weight
α_T	total aerodynamic angle
$\alpha(\cdot,\cdot)$	acceptance rate
β	angle of sideslip
$\boldsymbol{\beta}$	Kriging regression coefficients

γ	wall recombination probability (catalytic coefficient)
γ_i	normalization constant
Γ_p	polynomial chaos of order p
Δ, δ	metamodeling error
ϵ	volume fraction
ε_{Q^2}	error-based adaptation threshold for PDD
H, η	measurement error
η	volume viscosity coefficient
θ	total surface angle / variance-based adaptation threshold for PDD
$\boldsymbol{\theta}$	correlation lengths
λ	thermal conductivity / Lagrangian multiplier
Λ, λ	eigenvalues
λ_s	sensor location cone angle
μ	shear viscosity coefficient / mean value
ν	stoichiometric coefficient/ maximum ANOVA interaction
$\boldsymbol{\mathcal{V}}$	diffusion velocity
$\pi(\cdot)$	probability density function
Π	pyrolysis gas production term
ρ	density
σ	standard deviation
σ^2	variance
$\sigma(\cdot)$	prior distribution
$\sigma^{pos}(\cdot)$	posterior distribution
$\underline{\underline{\tau}}$	viscous stress tensor
$\phi(\cdot)$	objective function
ϕ_s	sensor location clock angle
ϕ_T	total aerodynamic clock angle
$\psi(\cdot)$	orthogonal polynomial basis function
$\dot{\omega}_i$	rate of chemical production
ω_i	MCMC proposal distribution width